CIRCULATION AND TRANSPORT WITHIN A SYSTEM OF SHALLOW,
INTERCONNECTED BARRIER ISLAND LAGOONS

By

STEVEN J. PEENE

A DISSERTATION PRESENTED TO THE GRADUATE SCHOOL
OF THE UNIVERSITY OF FLORIDA IN
PARTIAL FULFILLMENT OF THE REQUIREMENTS
FOR THE DEGREE OF DOCTOR OF PHILOSOPHY

UNIVERSITY OF FLORIDA

1995

UMI Number: 9607429

UMI

This is an authorized facsimile, made from the microfilm master copy of the original dissertation or master thesis published by UMI.

The bibliographic information for this thesis is contained in UMI's Dissertation Abstracts database, the only central source for accessing almost every doctoral dissertation accepted in North America since 1861.

INFORMATION TO USERS

ACKNOWLEDGEMENTS

I would like to express my gratitude to my advisor and supervisory committee chairman, Dr. Y. Peter Sheng, for his guidance and support throughout my doctoral program. The freedom he allowed me in the development of the field measurement program provided an education I could not have gotten anywhere else. I would also like to thank the members of my committee, Dr. Robert G. Dean, Dr. Max Sheppard, Dr. Daniel Hanes and Dr. Clay Montague, for their advice and support.

I must thank everyone out at the Coastal Laboratory where I spent the best parts of my years in the program. Special thanks to Vernon Sparkman and Jim Joiner who not only provided most of the brain power for the field work but also friendship, patience, guidance and fun. Special thanks also to Sidney Schoefield, Danny Brown, Don Mueller, Mark Southerland, Chuck Broward, Vik Adams and George Chappel. I will never forget volleyball the Cypress Lodge, redneck preppies, tower ramming, gator skiing, mutiny on the Munson, the sinking of the Anna Capri and all my friends at the lab.

As my time in the program was rather lengthy, I was fortunate to make many good friends. I owe them a lot because they helped make my time at the University fun. Thanks to Tom B., Rick, Victor, Yuming, Sam, Jeff, Barry, Gusty, Mike and Sheila, Phil and Lynn, Becky and Terry, Sandra, Lucy, Laura, Paul, Jei Kok, Dave, H.K. Lee, Phil H., Mark P., and Eduardo. A special thanks to all the members of L.A.S. whom I will always count as my good friends.

Thanks to my parents for always believing in me and supporting me in whatever endeavor I undertook. Also to my sister C.J. for her love and support through this

ii

whole craziness.

Finally, my wife Christina, whom I met at the start of this program, fell in love with and married as a doctoral candidate. She always stood by me and supported me. She went through all the tough times and always told me I could make it. She never lost faith in me.

TABLE OF CONTENTS

LIST OF FIGURES

ix

LIST OF TABLES

Abstract of Dissertation Presented to the Graduate School
of the University of Florida in Partial Fulfillment of the
Requirements for the Degree of Doctor of Philosophy

CIRCULATION AND TRANSPORT WITHIN A SYSTEM OF SHALLOW,
INTERCONNECTED BARRIER ISLAND LAGOONS

By

STEVEN J. PEENE

August 1995

Chairman: Dr. Y. Peter Sheng
Major Department: Coastal and Oceanographic Engineering

Data of water surface elevations, currents, winds, discharges and salinities collected
throughout a system of interconnected shallow barrier island lagoons are analyzed
to describe the circulation and transport processes. In addition, a three-dimensional
curvilinear model, representing the Sarasota Bay System, is calibrated to the data,
tested for sensitivity and used to isolate the forcing mechanisms driving the flow.

Spectral and harmonic analysis of the tides and currents quantified the distribu-
tion of energy across five frequency bands, the sub-tidal, diurnal, semi-diurnal, third
diurnal and fourth diurnal. The analyses showed that the inlets and constrictions act
as low pass filters for the tides reducing the semi-diurnal energies, while increasing
the semi-diurnal energy within the currents. The shift in current energy is driven by
the change from rotational flow within the Gulf to more unidirectional flow.

Currents within lagoons which receive tidal forcing from opposite directions ex-
hibit similar characteristics, such as increased residual flow energy, and equivalent
distribution of energy between the semi-diurnal and diurnal. Regions which are
forced more unidirectionally exhibit opposing characteristics. All regions no mat-
ter the depth exhibit some level of three-dimensionality in the currents, both in the
short term and residual flows.

Filtering of the winds, water levels and currents identified the driving mechanisms for the residual fluctuations as Ekman Transport and local wind forcing. The Ekman Transport acts within the lower frequency bands (7 to 10 days) while the local wind forcing acts within higher bands (3 to 4 days).

The three-dimensional numerical model is calibrated to the collected data by comparing the simulated energy distribution with those described above. The model accurately simulates the short term tides and currents and captures the general characteristics of the residual water level fluctuations and currents. The model is unable to accurately simulate the absolute transport of salinity but succeeds in capturing some of the general trends.

Finally, a term by term analysis of the equations of motion identified the primary forcing mechanisms driving residual flow throughout the lagoons as wind and mean water surface gradients.

The level of detail in the data analyses, the determination of the distribution of energies and forcing mechanisms, as well as the quantification of the model accuracy is largely unprecedented. This approach provides insight into the physics of the overall circulation and transport within the shallow lagoons as well as quantifying the capability of three-dimensional numerical models to simulate the complex flow patterns.

CHAPTER 1
INTRODUCTION

The study presented herein investigates the circulation and transport within a multi-inlet barrier island lagoon system. The study focuses upon all aspects of the processes which drive flow and transport utilizing collected data and a three-dimensional numerical model.

1.1 Barrier Island Lagoons

Barrier islands and their associated lagoon systems can be found within coastal plain environments throughout the world. They exist under varying morphologic configurations along the east and west coasts of the United States, the northern coast of Alaska, the Mediterranean Sea and even within the Great Lakes. The geologic forces which created these protected lagoons have been the subject of debate within the scientific community for many years. The first widely accepted theory was presented by deBeaumont in 1845 (King, 1972) which stated that barrier islands (and therefore the lagoons) were formed as offshore bar deposits which built up due to wave breaking and eventually became islands trapping the waters behind them. In the early 1900's this theory was tested and supported by Johnson (1919) and remained popular until Hoyt (1967) proposed the idea that barrier lagoons were created by the most recent sea level rise as lands behind former beach dunes and ridges were inundated.

Although the exact forces which created the lagoons remain in question, it is generally accepted that barrier island lagoons exist within a wide range of tidal and wave energy environments, and their morphology is highly dependent upon that environment. Hayes (1979) provides a generalized model of barrier islands and barrier island lagoon morphology based upon the amount of hydrologic (tide and wave) en-

1

ergy expended upon a coastline. The classifications are: a macrotidal coast (tide range greater than 4 meters), a mesotidal coast (tide range 2 - 4 meters), and a microtidal coast (tide range less than 2 meters).

In general, barrier island lagoons do not exist along macrotidal coastlines. Bays and estuaries along macrotidal coasts are instead dominated by wide openings and broad expanses of salt marshes and mud flats. Lagoons along mesotidal coastlines are characterized by tightly spaced multiple inlets due to the short stunted nature of the barrier islands. Spacings between inlets within this environment are on the order of 3 to 20 kilometers. Mesotidal lagoon formation and evolution are predominantly driven by tidal forces which overshadow the effects of the waves. Microtidal lagoons are generally very long and narrow with fewer inlet connections to the open ocean. Spacings between inlets along microtidal coastlines are on the order of 30 to 100 kilometers, and their formation and evolution are predominantly driven by wave forces.

1.2   General Circulation and Transport within Barrier Island Lagoons

As with morphology, the circulation and transport patterns observed within barrier island lagoons are the product of the energy imparted by the forcing mechanisms acting therein. These mechanisms include water surface gradients, wind stress, vertical and horizontal density gradients and bottom friction. Acting in conjunction with these forcing mechanisms, the multiple inlets, the varying bathymetry and geometry all add to the overall complexity.

Generally the most visible forcing mechanism within barrier island lagoons is the rise and fall of the water surface due to the tides. Tidal waves enter through the multiple openings and create surface gradients which in turn drive flow. At first glance tidal currents may appear to be symmetrical and a net transport nonexistent, but tidal transport can be significant under the proper geometric conditions. Analytic and numerical studies have shown this phenomena under idealized conditions (e.g., van

de Kreeke and Dean, 1975). Fisher (1979) defines two causes of net tidal transport, "tidal pumping" and "tidal trapping." Tidal pumping occurs when the arrival of a tidal wave to one opening proceeds the arrival at another within the same system. The asymmetrical damping of the flow by bottom friction at high tide versus low creates a net current from the leading inlet toward the lagging inlet. Tidal trapping is a phenomenon which occurs due to the presence of side embayments and small branching channels. During a flooding tide waters are trapped within these off-channel features and separated from the main flow. Upon reversal of flow, the trapped waters rejoin the flow in a new location and mixing occurs.

During normal weather conditions the magnitude of wind driven currents in bays and estuaries are generally much smaller than their tidally driven counterparts, except in locations which are far from an opening to the ocean. In contrast, the magnitude of the wind driven residual currents can be of the same order of magnitude or greater than the tidal residual. The application of winds over a water body can induce vertical and horizontal circulation gyres. In the vertical, the wind stress acting at the surface transports water in the direction of the wind creating a setup. To balance this force, a return current which flows against the wind occurs along the bottom and a vertical gyre is created. In a basin with a channel cut through the middle, the application of wind stress upon the surface would create a horizontal gyre with flow traveling with the wind along the shallow sides and return flow in the channel. Fischer (1979) explains the physics behind this phenomena using a simplified estuary with a deep channel running along one side. "The wind induces an approximately uniform stress everywhere on the water surface. Therefore the line of action of the wind-induced force is through the centroid of the water surface. The center of mass of the water in the basin is displaced towards the deeper side, since there is more water there. Hence the line of action of the force passes on the shallow side of the center of mass of the water, and a torque is induced causing the water mass to rotate."[35].

Density currents occur when waters of different temperature or salinity meet. The gravitational force causes the higher density fluid to displace the other. The classical circulation pattern occurs when higher density ocean waters move into a drowned river valley and proceed upstream along the bottom as the fresher water flows outward at the surface (Hansen and Rattray, 1967, van de Kreeke and Zimmerman, 1990). An excellent example of this situation exists within the Mississippi River where it meets the Gulf of Mexico. Although in general vertical density gradients are not primary forcing mechanisms within shallow barrier island lagoons, horizontal density gradients may drive residual flows. This phenomena has been found to be significant within Tampa Bay, a relatively shallow bay along the west coast of Florida.

1.3 Study Area Description

The focus of the studies presented herein is the circulation and transport within a series of shallow interconnected barrier island lagoons situated along the western coast of central Florida. Referred to for the purposes of this study as the "Sarasota Bay System", the lagoons consist of Anna Maria Sound, Sarasota Bay, Roberts Bay, Little Sarasota Bay and Blackburn Bay. Figure 1.1 presents a map showing the location of the Sarasota Bay System relative to the State of Florida and the Gulf of Mexico.

The west coast of Florida has generally been classified as a mixed energy, wave dominated environment, exhibiting an increased number of tidal inlets over classic microtidal wave dominated systems (Hayes, 1979). For the Sarasota Bay System, five barrier islands, totaling 54 kilometers in length, separate the interior lagoons from the Gulf of Mexico. These are, from north to south, Anna Maria Island, Longboat Key, Lido Key, Siesta Key and Casey Key. Examination of their shapes shows both mesotidal (short stunted islands, Lido Key) and microtidal (long linear islands, Longboat Key) characteristics. The four inlets which connect the lagoons to the Gulf of Mexico (Longboat Pass, New Pass, Big Pass and Venice Inlet) have spacings which
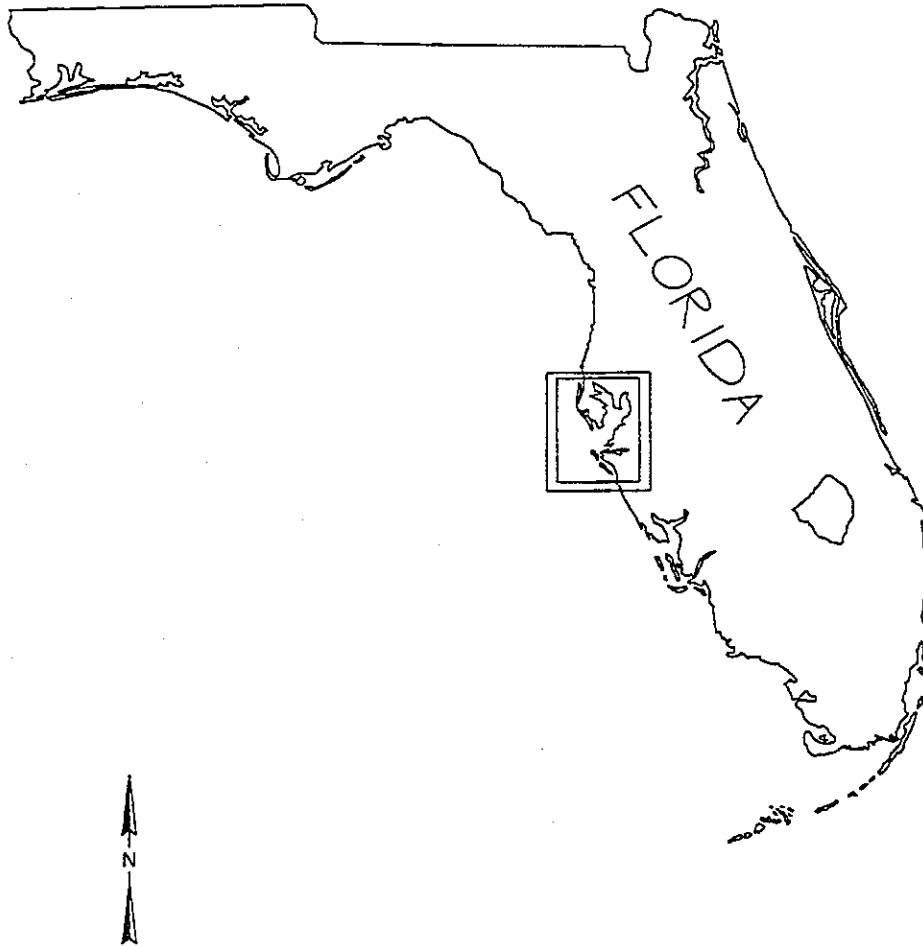
Figure 1.1: A site map of the Sarasota Bay System and its location relative to the State of Florida and the Gulf of Mexico

range from less than 3 kilometers (New Pass to Big Pass) to more than 25 kilometers (Big Pass to Venice Inlet). A fifth inlet (Midnight Pass) existed as recently as 1980 between Venice Inlet and Big Pass but it closed due to migration and infilling. Another tidal openning exists at the north end of the system where Anna Maria Sound meets the southwest side of Tampa Bay.

The bathymetry within the Sarasota Bay System varies from lagoon to lagoon. Anna Maria Sound is characterized by shallow waters and sea grass flats with average depths ranging from 1 to 2 meters at mean water level. The deepest waters are found within the Intracoastal Waterway (3 to 4 meters) and these must be maintained by dredging.

The most open water body water is Sarasota Bay with an average width of 4 kilometers and depths ranging from 3 to 4 meters. Much of the shoreline has been modified through the construction of seawalls, infilling of seagrass flats and excavation of canals and channels. This is most pronounced immediately south of Sarasota Bay where the islands of Bird Key and St. Armands were originally extensive seagrass beds but were filled in for development purposes and their shorelines hardened.

South of Big Pass; Roberts Bay, Little Sarasota Bay and Blackburn Bay have similar bathymetric and geometric features. All three lagoons are characterized by very shallow tidal flats (0.5 to 1.5 meters at mean water level) and narrow widths with the Intracoastal Waterway running longitudinally along their north-south axes. These lagoons are in essence a self-contained system with only two tidal openings, one at the north end which opens toward Big Pass, and one at the south end which opens into the Gulf of Mexico.

1.4 Statement of Purpose

The Sarasota Bay System, as with many other coastal waters, has come under increasing development pressure due to man's desire to live near or on the water.

As urbanization of the lands surrounding the lagoons increases, pollutant loadings from residential, commercial and industrial runoff as well as sewage discharges from the many package treatment plants, also increases. In the past it was assumed that these systems were able to assimilate the waste loads without deterioration, but recent studies have shown that water quality within the system is degrading with an associated decline in fisheries and other habitats.

The first step in any study of water quality is the quantification of the circulation and transport mechanisms. These determine the assimilative capacity of the water body through flushing and transport of contaminants. Other aspects of the water quality which are directly linked to the currents and tides include reaeration of the water column, resuspension and deposition of bottom material, and many other phenomena.

Since 1990, the Coastal and Oceanographic Engineering Department of the University of Florida, under the supervision of Dr. Y. Peter Sheng, embarked on a field and modeling study of the circulation and transport in the Sarasota Bay system. The study was supported by the Sarasota Bay National Estuary Program (SBNEP) through the United States Geological Survey (USGS) (Sheng and Peene, 1992). The purpose of the Sarasota Bay System Study included the general circulation, the effect of openning Midnight Pass on the circulation and flushing of the southern lagoons and the effect of freshwater inflow from the Manatee River on the circulation and transport. The focus of this dissertation, which is part of the overall study, is a detailed and comprehensive investigation of the tides and currents within the entire Sarasota Bay System.

As was stated earlier, the water surface elevation fluctuations and the currents within the Sarasota Bay System have multiple components which may be driven by the actions of the tides, wind, density gradients and other forcing mechanisms. In addition, each component is altered by the interaction of the flowing waters with the

complex geometry and bathymetry throughout the lagoons. These multiple compo-
nents superimpose upon one another to create the overall circulation and transport
patterns which are observed. The goal of this study, therefore, is to develop an im-
proved understanding of the overall circulation and transport within the Sarasota Bay
System through the quantification of these individual components and the determi-
nation of the relative influence of the forcing mechanisms defined above.

Field data and a numerical model are utilized to achieve this goal. An extensive
data set was collected by the Coastal and Oceanographic Engineering Department of
the University of Florida in 1991. Other data utilized for this study were collected by
USGS and the National Oceanographic and Atmospheric Administration (NOAA).
Chapter 3 presents a description of the data collected by UF and USGS. In Chapter
4 the data are systematically analyzed to isolate and quantify the relative impacts of
the individual forcing mechanisms.

The second tool is a three-dimensional numerical circulation and transport model
developed by Dr. Y. Peter Sheng. The model was modified and applied to the study
area described above. Once calibrated to the data, it allows a more spatially intensive
determination of the circulation and transport. In addition, the relative impacts of
the forcing mechanisms can be isolated and tested through iterative and sensitivity
runs of the model.

1.5 Presentation Outline

The following chapter highlights past efforts, both analytical and numerical, which
attempt to quantify the circulation and transport patterns within shallow barrier
island lagoons. Chapter 3 describes the data collection methodologies utilized by the
University of Florida and the United States Geological Survey. Chapter 4 presents
the analysis of the data. Chapter 5 presents a brief summary of the formulation of the
equations used in the model. Chapter 6 presents the calibration and sensitivity testing

of the numerical model along with applications of the model to define the overall circulation patterns and the relative impacts of the individual forcing mechanisms. Chapter 7 presents a summary of the work performed and conclusions drawn from this study.

CHAPTER 2
LITERATURE REVIEW

A large body of literature exists concerning studies of circulation and transport

phenomena in estuarine systems, including drowned river valleys, fjords, lagoons and

bays in macro-, meso- or micro-tidal environments. These studies include the devel-

opment and application of numerical and analytical models as well as the collection

and analyses of field data of winds, tides, currents, temperature, salinity and other

physical parameters. In an effort to limit the review of literature, and to focus upon

those papers which relate directly to the work within this study, this review will

concentrate on research related to the physics of circulation and transport within

shallow, micro/mesotidal barrier island lagoons. Papers whose primary focus is the

development of numerical or analytical models, instead of quantification of the phys-

ical processes of circulation and transport, are not included.

2.1 Analyses of Field Measurements

Kjerfve (1975) studied the response of the water surface elevation within a Louisiana

bar-built estuary to tidal and fair weather wind inputs. Water levels were measured

at three stations, while winds were measured at a single station. The wind station

historically contained a six-level anemometer system which allowed detailed quantifi-

cation of the vertical wind profile. The initial study used the logarithmic law of the

wall to define the friction velocity at the water surface. The relationship between the

wind velocity at 6.77 meters and the friction velocity was developed through analysis

of 386 wind profiles. This relationship was used to quantify the wind stress due to

winds measured at 6.77 meters in the 1975 study. This later study found that tidal

10

dynamics dominate the flow for short term fluctuations, but for the sub-tidal variations it was found that the wind, through the creation of Ekman transport toward the coastline, created water level variations on the order of 24 cm inside the estuary.

Smith (1979) measured and analyzed currents, water levels and winds in the region of Aransas Pass, Texas, over a 45 day period to describe the tidal and low frequency motions within the bay. The data showed that tides in that region are mixed diurnal/semi-diurnal with dominance in the diurnal tides. The measured currents showed a stronger diurnal signal in percentage than the measured tides. The data were filtered using a low pass filter with a cutoff frequency equivalent to a 48-hour period. The resulting long term fluctuations in water level showed a strong coherence with cross-shore winds indicating the presence of wind set-up and set-down. Some coherence between the alongshore winds and the fluctuations within the bay were found but at very long time scales (greater than 10 days). This indicated portions of the variations in mean tide were due to the propagation of low frequency waves within the Gulf of Mexico driven by Ekman transport.

During the 1980s Smith conducted a series of field studies to quantify the tides and currents within Indian River Lagoon, which is a micro-tidal barrier island lagoon along the east coast of Florida. Smith (1980) compared tides measured offshore to tides measured just inside Fort Pierce Inlet. The data showed that as the tidal wave propagates toward and through the inlet, the semi-diurnal harmonic constituent (M_2) is damped to a greater degree than the diurnal constituents (K_1 and O_1), i.e. the inlet acts as a low pass filter for the tidal wave. Similar results were found in a study of water level dynamics over a 25 year period at 23 stations along the Indian River Lagoon (Smith, 1987). The results were presented in terms of the "form number" at various locations within the lagoon. The form number represents the ratio of the diurnal to semi-diurnal tidal amplitudes and was calculated using the formula,

$$F = \frac{O_1 + K_1}{M_2 + S_2} \tag{2.1}$$

where O_1 and K_1 are the amplitudes of the principal diurnal harmonic constituents, and M_2 and S_2 are the amplitudes of the principal semi-diurnal constituents. The results showed that the semi-diurnal constituents were damped to a greater degree and the form numbers increased as the tidal waves traveled through the inlets and further into the lagoon.

In another study, Smith (1983) analyzed 32 days of current data from 4 stations along the Intracoastal Waterway between Ft. Pierce Inlet and Sebastian Inlet. The stations were spaced evenly 8 km apart. The current data, along with winds measured at the Vero Beach Municipal Airport, were filtered using a low pass filter with a cutoff frequency equivalent to a 48 hour period. The filtered currents showed significant coherence with the along channel winds and Smith surmised that local wind forcing was a significant transport mechanism within this portion of the Indian River lagoon. Comparison of the percent sub-tidal (more than 48 hour period) energies from the station nearest to Ft. Pierce Inlet with the station farthest interior to the bay showed a percentage increase ranging from 1 to 27 percent.

A similar study was performed using data from a single current meter moored within the Intracoastal Waterway between St. Lucie Inlet and Ft. Pierce Inlet (Smith, 1985). The station was 25 kilometers from the nearest inlet. The data were analyzed using a harmonic analysis program and the purely tidal currents were subtracted from the raw data to provide the wind driven currents. Additionally, the influence of the tidal currents upon the wind stress (i.e. alterations in wind stress due to tidal currents opposing or flowing with the winds) were removed along with the nonlinear interactions due to bottom friction. The remaining currents were the pure nontidal components. Comparison of data with a simple one-dimensional wind model produced a correlation coefficient of 0.66. The results indicated that tidal forcing accounted for 45 percent of the total variance at the study site, while local wind forcing constituted 45 percent. The remaining energies were attributed to freshwater inflow and non-local

forcing mechanisms.

van de Kreeke and Wang (1984) analyzed data from 4 tide gages installed within the northern portion of Biscayne Bay. The northern part of the bay is characterized by shallow waters with the Intracoastal Waterway running longitudinally along its axis. Multiple causeways cross the bay, effectively separating it into 5 water bodies interconnected by narrow openings. Harmonic analyses of the tides were performed and the results analyzed to define the relative contributions from the various harmonic constituents. The data showed the M_2 constituent to be the dominant harmonic with some measured higher harmonic overtides at the M_4 frequency. A net 3-4 cm set-up was measured in the bay and this was attributed to interaction between the incoming tidal wave and the reflected tidal wave from the northern end of the bay. The correlation coefficient between the measured tides and the tides calculated from the harmonic constituents indicated that the tidal harmonics account for 95 percent of the tidal energy within the bay. The remaining 5 percent of the variations were attributed to longer scale meteorological forcings.

In addition to the tidal measurements, currents were measured within Bakers Haulover Inlet and Government Cut which connect Biscayne Bay to the Atlantic Ocean. The conveyance factors (C) were calculated for each inlet based upon the equations

$$\frac{Q}{A_I} = C\sqrt{RS} \tag{2.2}$$

$$C = \sqrt{\frac{2gL}{2fL + mR}} \tag{2.3}$$

where Q is the flow rate, A_I is the cross-sectional area of the inlet, S is the hydraulic gradient, R is the hydraulic radius, L is the inlet length, m is the entrance and exit loss friction coefficient, and f is the friction factor

$$f = \frac{\tau_b}{\rho U_x^2} \tag{2.4}$$

where, τ_b is the bottom shear stress, U_x is the cross-sectionally averaged velocity and ρ is the fluid density. Based upon the magnitude of the conveyance factors it was determined that tidal asymmetry existed at the two inlets. This asymmetry favored a net flow from Bakers Haulover Inlet to Government Cut.

The tidal amplitude to depth ratio has been found to be a critical parameter determining the significance of non-linear interactions for tides and currents (Aubrey and Speer, 1985, Aubrey and Friedrichs, 1988). In lagoons where this ratio is relatively large, the non-linearity created through bottom friction, inertial forcing and other sources can become significant. A number of field studies (Aubrey and Speer, 1985, Aubrey and Friedrichs, 1988) have been conducted to determine the significance of non-linear interactions upon the tides and currents within micro/mesotidal barrier island lagoons. The following presents results from those studies.

Harmonic analysis of tides and currents collected at multiple stations within the Nauset Harbor Estuary system in Massachusetts (Aubrey and Speer, 1985) was performed to determine the spatial variations in the M_4/M_2 amplitude ratio and the $(2M_2\text{-}M_4)$ phase relation. Along coastlines where the dominant tidal constituent is the semi-diurnal M_2 component, the predominant overtide or higher harmonic is the M_4 constituent. Consequently the M_4/M_2 ratio is an indication of the level of non-linearity or asymmetry. The $2M_2\text{-}M_4$ phase relation in this case indicates the sense of the asymmetry. For $2M_2\text{-}M_4$ between 0 degrees and 180 degrees, the falling or ebbing tide is longer than the rising or flood tide. For a phase relationship between 180 degrees and 360 degrees, the rising or flood tide is longer than the ebb. Considering an inlet, if the ebb tide lasts longer the flooding tide will have stronger velocities in order to maintain continuity; this situation is termed flood dominance. The opposite situation is termed ebb dominance.

Analyses of the tides and currents within Nauset Harbor indicated flood dominance throughout the entire system. This flood dominance is phase locked in that the

$2M_2$-M_4 phase relationship remains constant at 60-70 degrees throughout the system. Additionally, Speer and Aubrey found a fortnightly tidal component MS_f with a 10 cm amplitude. This component created lower mean water levels during neap tide as versus spring tide. It was surmised that this variation in water level will impact the degree of non-linearity as the depth to tidal amplitude ratio (a/h) will change.

Boon (1988) utilized complex demodulation of predicted and measured tides at Wachapreague, Virginia, to determine the temporal variations in the amplitudes of the tidal asymmetries (M_4/M_2 ratio) and the phase relationships ($2M_2$-M_4). The predicted tidal signals were generated from harmonic constituents calculated from the measured data. The amplitude ratio was shown to have a significant seasonal variation with a range of values from 0.02 to 0.08. The phase relationships did not, however, show significant temporal variations. The demodulation showed that the amplitude of the quarter-diurnal tide (M_4) varies as the square of the amplitude of the semi-diurnal tide (M_2).

Aubrey and Friedrichs (1988) used recorded sea level data over a 16 month period at Murrells, South Carolina along with a simple one-dimensional numerical model to study the changes in tidal asymmetry due to variations in mean sea level and tidal amplitudes of the primary harmonic constituents. Analyses of the data showed that as the tidal amplitude to depth ratio increased, as the result of increased tidal amplitude, the tidal distortion became more flood dominant. For long term sea level fluctuations they showed that the tidal asymmetry changes were highly dependent upon the extent of tidal flats adjacent to the channel. In areas with extensive tidal flats, as a/h decreased, the tidal asymmetry or flood dominant nature of the system increased. In areas with small tidal flats, as a/h increased, the flood dominance increased.

Seim and Sneed (1988) performed harmonic analysis of current and tidal data collected within the Mississippi Sound and the adjacent continental shelf from 1980

to 1981. They computed the form numbers using equation 2.1, and calculated the ratios of the form numbers for the tides and currents measured on the continental shelf with those measured inside the inlets. The ratios for the currents were as low as 0.5, i.e., the inlets showed a much higher predominance of semi-diurnal tidal energy in the currents. The tides showed little change from offshore to the inlets. Inside of the bay the form number ratio for the currents increased back toward that found from the offshore data. This phenomenon was examined through theoretical derivations of the form numbers derived for Sverdrup waves and uniform flow through an inlet. The theoretically derived form numbers indicated that maintaining continuity through the inlet caused the semi-diurnal currents to increase relative to the diurnal as the tidal wave progressed from a 2-D rotational region to a 1-D unidirectional region. The authors speculated that this phenomenon will occur in all regions with narrow inlets and mixed offshore tides.

2.2 Simplified Analytic Solutions and Numerical Models

A series of studies conducted in the 1970s (van de Kreeke 1971, Cotter 1974, van de Kreeke and Cotter 1974, van de Kreeke and Dean 1975) quantified the net discharge in a simplified canal open to tidal forcing at two ends; the tides at the two ends were forced through idealized inlets. The canal/inlets are a representation of the many multiple inlet lagoon systems throughout the State of Florida. Figure 2.1 presents the geometry of the idealized system. The basic equations solved for in the canal are the simplified one-dimensional equations of motion and transport

$$b\frac{\partial \zeta}{\partial t} + \frac{\partial Q}{\partial x} = 0 \tag{2.5}$$

$$\frac{\partial Q}{\partial t} + gA_I\frac{\partial \zeta}{\partial x} + \frac{1}{A_I}\frac{\partial Q^2}{\partial x} = \frac{-fQQb}{A_I^2} \tag{2.6}$$

where b is the width of the lagoon, ζ is the water surface elevation, Q is the discharge, g is the acceleration due to gravity, A_I is the cross-sectional area $b(h + \zeta)$, h is the

depth, and f is the friction factor.

Within the inlets the equation used to describe the flow is the semi-empirical equation

$$gA_I \frac{\partial \zeta}{\partial x} = \frac{-f_I Q Q b}{A_I^2} \tag{2.7}$$

where, f_I is the friction coefficient for the inlet and accounts for lateral and bottom friction as well as the entrance and exit losses.

In each of the studies listed above, the equations were solved numerically using finite difference techniques for the net discharge, Q_*, through the canal such that

$$Q_* = \frac{1}{T} \int_0^T Q dx \tag{2.8}$$

The forcing of the tides occurs at the ocean side of the idealized inlets and is defined as

$$\zeta_1 = a_1 cos(\sigma t + \delta) \tag{2.9}$$

$$\zeta_4 = a_4 cos(\sigma t) \tag{2.10}$$

where ζ is the water surface elevation, σ is the frequency of the forcing tide (generally 12.42 hours, M_2), a is the amplitude of the forcing tide and δ is a phase lag in degrees.

To determine the impacts of various geometric conditions on the net discharge, specific parameters were varied while all others were held constant. Figure 2.1 presents the results for varying relative depth, width and length of the two inlets. The plots show that transport occurs toward the inlet with the lesser depth, the lesser width and longer length. For a phase lag between the two inlets the transport is toward the lagging inlet. The tide induced transport is shown to be proportional to (a^2/h^2), therefore a significant net transport will only occur for a large tidal amplitude to depth ratio, i.e. in shallow lagoons.

In order to allow for analytic solutions of these simplified equations, the friction term is linearized. Comparison of the analytic solutions to the numerical solutions
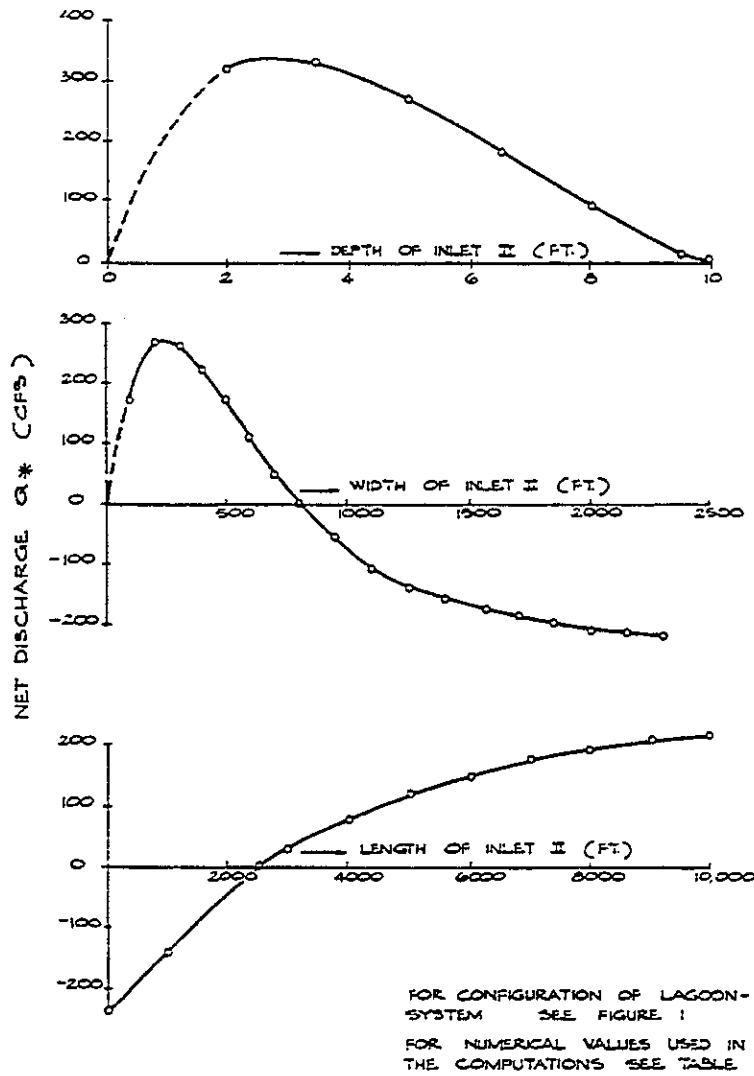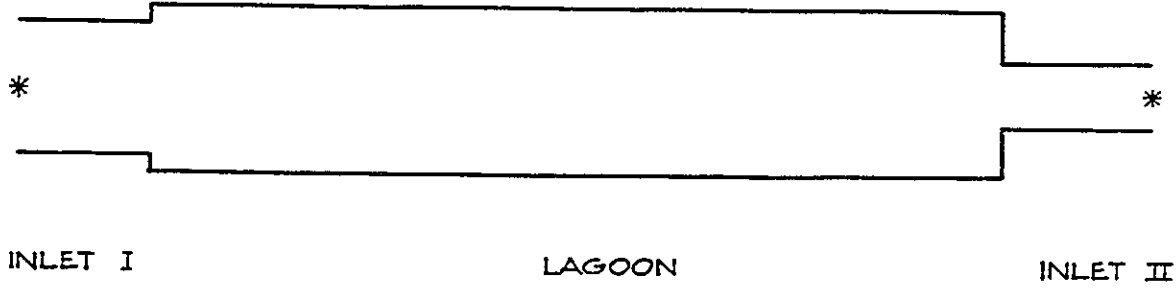
Figure 2.1: The idealized geometry for the canal/inlet system utilized in the study by van de Kreeke, along with the variation in the net discharge as a function of inlet depth, width and length (van de Kreeke and Cotter, 1974)

indicates that while the results maintain the same general form, linearization of the friction terms introduces significant error in systems with large amplitude to depth ratios (a/h much greater than 0).

Johnson and Lee (1977) investigated the influence of horizontal density gradients on residual velocities and flushing within Biscayne Bay and Card Sound. They solved simplified versions of the momentum, continuity and conservation of density equations within an idealized representation of the two water bodies. The results indicated that residence times for density induced motion was on the order of 20 to 1000 years. Comparison with residence times calculated from wind and tide induced flow (3 months) showed that density induced motion plays a very small part in the flushing of Biscayne Bay.

Dronkers (1978) studied the longitudinal dispersion created by the filling and draining of tidal flats alongside of dredged navigation channels. He found that in estuaries which have significant tidal flats the dispersion is the result of three phenomena. The first is mixing of waters propagating over the shallow tidal flat areas. The geometric variability, presence of sea grasses and marsh grass, and bottom friction combine to create significant mixing. The second phenomenon is the exchange of water between the tidal flats and the channel due to means other than the rise and fall of the tides, i.e. density currents and horizontal eddies. The third and final method is due to a phase shift between the tides and the currents; this causes the channel to flow out prior to drainage of the tidal flats, which creates mixing similar to the "trapping" phenomena presented in Chapter 1.

Moody (1988) integrated a simplified form of the 1-D equation of motion ignoring the inertial terms. He defined an equation which relates the square of the ratio of the bay amplitude to the ocean amplitude to a dimensionless number

$$L^2 = CQ_I \qquad (2.11)$$

where

$$L = \frac{\zeta_b}{\zeta_o} \tag{2.12}$$

is termed the amplitude response; it relates the bay amplitude (ζ_b) to the ocean amplitude (ζ_o), and

$$Q_I = \left(\frac{2g}{\zeta_o \omega^2} \right) \left(\frac{A_I}{A_b} \right)^2 \tag{2.13}$$

is a dimensionless parameter in which A_I is the inlet cross-sectional area, A_b is the surface area of the bay, and ω is the frequency of the tidal wave. The author calculated the value of Q_I for six inlets on or near Cape Cod, Massachusetts, and for 12 tidal constituents ($O_1, K_1, N_2, M_2, S_2, MK_3, MN_4, M_4, MS_4, MK_4, M_6, M_8$) and fit the results by linear regression to the equation:

$$ln(L^2) = ln(cQ^m) \tag{2.14}$$

Three separate linear regressions were performed. The first only included the diurnal and semi-diurnal constituents, which gave a value of m = 0.59 and c = 0.11, with a correlation coefficient of 0.808. The second was for all of the constituents, which gave a value of m = 0.92 and c = 0.09 with a correlation coefficient of 0.839. The third was made excluding overtides within inlets which had an excessive area of tidal flats, which gave a value of m = 0.72 and c = 0.07. The study concluded that small-scale inlets act as amplitude and frequency dependent tidal filters and the bay response can be closely simulated by a simple quadratic response function.

Speer and Aubrey (1985), Aubrey and Friedrichs (1988), Friedrichs and Aubrey (1988), and Speer, Aubrey and Friedrichs (1991) examined the tidal asymmetry in shallow inlet/bay systems using numerical solutions of the simplified 1-D equations of continuity and momentum. The equations include flooding and drying of tidal flats and are of the form

$$\frac{\partial U_x}{\partial t} + \frac{\partial}{\partial x} \frac{U_x^2}{A_I} = gA_I \frac{\partial \zeta}{\partial x} - \frac{\tau_b}{\rho} P \tag{2.15}$$
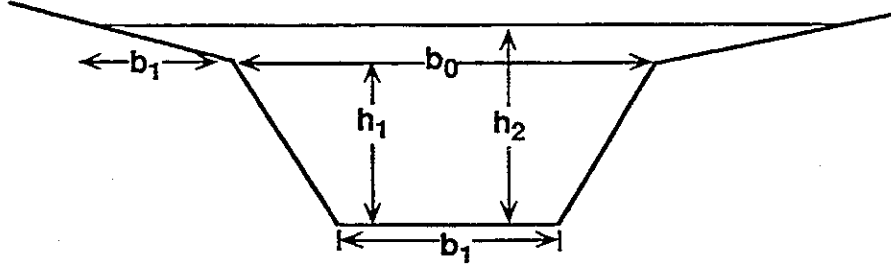
Figure 2.2: The idealized channel geometry used in the solution of the 1-D Equations of Momentum and Continuity (Speer and Aubrey, 1985)

$$\frac{\partial \zeta}{\partial t} + \frac{1}{b}\frac{\partial U_x}{\partial x} = 0 \qquad (2.16)$$

where ζ is the sea surface elevation, g is the acceleration of gravity, b is the channel width, U_x is the cross-sectional flux, τ_b is the average shear stress on the boundaries, P is the wetted channel perimeter, A is the channel cross-sectional area and ρ is the water density. The bottom friction, τ_b, is calculated using the quadratic stress law

$$\tau_b = \frac{\rho f U U}{A_f^2} \qquad (2.17)$$

where, f is a dimensionless friction factor. Figure 2.2 shows the idealized channel used in the solutions.

Speer and Aubrey (1985) found that for a/h less than 0.3 all systems were flood dominant. For a/h = 0.1 to 0.2 the systems were flood dominant if tidal flats were not extensive. The addition of tidal flats to the system when a/h = 0.1 to 0.2 brought the system from flood dominance to ebb dominance.

Friedrichs and Aubrey (1988) analyzed the estuary length, depth, ocean M_2 amplitude, a/h and marsh storage volume to channel volume ratio (V_s/V_c) for 26 separate systems and applied the one-dimensional numerical solution. Based upon these solu-

tions, the authors determined that a/h is the primary determining factor in the type of estuary (flood or ebb dominant), i.e. for a/h less than 0.2 it is an ebb dominant system, for a/h greater than 0.2 and a/h less than 0.3 the type of system can be determined by the channel volume to marsh storage volume ratio, for a/h greater than 0.3 the systems are flood dominant.

Speer, Aubrey and Friedrichs (1991) extended the application of the simplified 1-D equations to a special class of flood-dominant estuaries in which estuarine channels shoal over short distances to depths less than the offshore tidal amplitude. The tidal asymmetry within these types of systems exhibit high M_4/M_2 ratios (0.3 to 0.4) and low M_2 to M_4 relative phases (5 to 35 degrees).

Friedrichs and Madsen (1992) solved the equations of motion and continuity assuming the non-linear terms are negligible. They utilized a channel similar to that shown in Figure 2.2. Solving for the velocity within the simplified momentum equation, and inserting it into the continuity equation, gave a non-linear diffusion equation of the form

$$\frac{\partial \zeta}{\partial t} - \frac{1}{b}\frac{\partial}{\partial x}\left(\frac{b_c h^{\frac{5}{3}}}{n|\frac{\partial \zeta}{\partial x}|^{\frac{1}{2}}}\frac{\partial \zeta}{\partial x}\right) = 0 \tag{2.18}$$

where n is Manning's friction coefficient and b_c is the channel width. The term within the parenthesis and to the left of the spatial derivative is comparable to the diffusion coefficient seen in the standard equations of motion. This equation was solved analytically and numerically and compared with numerical solutions of the 1-D continuity and momentum equations. The first-order solutions to the equation were obtained by assuming a constant diffusion coefficient. The second order solution was obtained by assuming that the diffusion coefficient is variable in time but constant in space. Comparison of the analytic solutions of the zero-inertia equations of motion with numerical solutions of the full 1-D equations showed that this equation reproduced the main features of the nonlinear tidal signal observed in shallow lagoons.

Sheng, Peene and Liu (1991) applied a one-dimensional numerical model over the entire Indian River Lagoon to determine the tide and wind driven circulation. The model was forced through the multiple inlets within the system and defined the currents under the conditions of no wind and along channel wind forcing.

2.3 Multidimensional Modeling

Wang and Swakon (1977) applied a 2-D finite element model in the study of tides and currents within the southern portion of Biscayne Bay. The model utilized tidal and wind forcing to drive the simulations. The model was used to study the advective transport within the bay. The results indicated that, although tides define the primary transport mechanisms for short term fluctuations, the wind is the primary driving mechanism in the long term transport and therefore the flushing of the system.

Sheng (1983) used a three-dimensional numerical model to study the tidal and wind-driven circulation and sediment transport in Mississippi Sound, a shallow barrier island lagoon along the Mississippi coast of the Gulf of Mexico. The model domain included an area approximately 220 kilometers by 120 kilometers. To produce the open boundary condition for the circulation model, Sheng used the tidal constituents simulated by Reid and Whittaker's (1981) Gulf tide model along the deep offshore water which is 60 kilometers offshore of the barrier islands. The model was able to accurately simulate the measured dynamics of the water level and currents in the Mississippi Sound. Significant currents inside the tidal inlets were found to be sufficient to cause sediment erosion and resuspension.

van de Kreeke and Wang (1984, 1986) investigated the flow within the northern portion of Biscayne Bay using a nested 1-D/2-D numerical model. The one-dimensional model was applied over the entire bay, while the two-dimensional model was applied to the individual bodies of water connected through the causeways. The one-dimensional model was used to develop tidal forcings at the causeway openings for the two-dimensional model while maintaining conservation of energy and mass

throughout the system. The model results verified the existence of a net residual flow from Bakers Haulover Inlet toward Government Cut as discussed in the earlier field measurement section. The residual was attributed to phase and amplitude differences between the two inlets. Flushing of the various interconnected water bodies was calculated using the model. The results indicated an exchange period of 1-2 weeks which is highly dependent upon local wind forcing, i.e. whether or not the winds oppose or enhance the residual flow.

Smith (1990a) studied the residual flow in the Indian River Lagoon utilizing a two-dimensional laterally averaged numerical model. The model contained four layers within the Intracoastal Waterway and communicated with two-layer zones along the tidal flats on either side. Simulations were conducted for a 161 day period in 1983. The model results indicated cumulative transport within the shallow regions in the direction of net winds while the bottom layers within the Intracoastal Waterway show return flow.

A two-dimensional, four-layer numerical model of tidally induced residual flow was applied and calibrated to a 65 day data set of tides and currents from the summer of 1991 within the Indian River Lagoon (Smith, 1990b). Water depths and surface slopes at the approximate midpoint between Ft. Pierce and St. Lucie inlet were calculated by assuming that the tide inside the lagoon is the superposition of exponentially damped sine waves representing six tidal constituents. The tidal wave moving south from Ft. Pierce Inlet was modified by a tidal wave of the same six constituents moving north from St. Lucie Inlet. The net slope as the two waves passed through one another defined the barotropic pressure gradient and the net tidal residual flow. The results showed a depth averaged tidally induced residual flow of 0.8 cm/sec at the point where measured data were available. The residual flow varied from 0.1 to 1.2 cm/sec over a synodic lunar month. Examination of the mechanisms driving the residual flow indicated that just under two-thirds of the total is explained by Stokes

transport, with the remainder attributed to Eulerian mass transport.

Sheng et al. (1993) used a one-dimensional model and a three-dimensional model to simulate the circulation and flushing in Indian River Lagoon under the forcings of tide, wind, and density gradients.

2.4 Studies Relative to Sarasota Bay

Although much research within the Sarasota Bay system has been conducted relative to water quality and ecology, few studies have focused upon the circulation and transport processes. The following describes all studies found which relate to the hydrodynamic processes within the entire Sarasota Bay system.

A simplified analytic model was applied to the Big Sarasota Bay system in order to define the residence times and flushing characteristics (Chiu, T.Y., J. van de Kreeke and R.G. Dean, 1970). The model considered the forcing from Longboat Pass, New Pass and Big Pass. The results were inconclusive relative to the flushing within the system as residual velocities predicted were very low.

A link-node model was applied to Little Sarasota Bay and Blackburn Bay in order to quantify the impacts of the closure of Midnight Pass on the circulation and flushing characteristics within that system (Dendrou, S.A., C.I. Moore and R. Walton, 1983). The model defined the tidal currents and predicted the flushing times within Little Sarasota Bay under the conditions of Midnight Pass open and closed. The model was forced at the north end of Little Sarasota Bay and the south end of Blackburn Bay.

A number of publications related to Sarasota Bay circulation preceeded the publication of this report. Sheng and Peene (1991) presented some data and simulation of tidal circulation inside Big Sarasota Bay. The simulations were conducted without including Little Sarasota Bay and Tampa Bay. Peene, Sheng and Houston (1991) simulated the circulation in Sarasota Bay and Tampa Bay during the passage of a tropical storm in 1990. Sheng and Peene (1992) presented a study on the flushing in-

side the Sarasota Bay system. Sheng and Peene (1993) presented a preliminary study on the residual circulation in Sarasota Bay. This report presents the results of an enhanced and more comprehensive study on Sarasota Bay Circulation by performing a more quantitative analysis of data and more detailed model simulations.

2.5 Chapter Summary

The studies presented herein, focused predominantly upon simplified one-dimensional solutions pertaining to individual characteristics of circulation and transport. Although these simplified studies were able to quantify some of the mechanisms driving the flow, few addressed the complete circulation and the relative influences of one mechanism versus another. Those studies which did address the multidimensional nature of the flow focus primarily upon the verification of the numerical models applied therein, and did not present a comprehensive analysis of the physics of the circulation.

The studies presented relative to Sarasota Bay provided little or no knowledge of the physics of the circulation and the interactions between the multiple lagoons and inlets. Additionally, the spatial distribution of net transport, and the relative influence of the forcing mechanisms of wind, tides and density gradients have not been thoroughly investigated.

Table 2.1 presents a summary of the investigations presented herein highlighting the type of study (data analysis, model simulation) along with the forcing mechanisms considered. No study presented examines all the forcing mechanisms and their relative influence utilizing both measured data and multidimensional modeling. In the subsequent chapters, an attempt is made to further the understanding of the physics of circulation within the Sarasota Bay System through data analysis and multidimensional modeling. The study considers all of the forcing mechanisms listed within Table 2.1 and the relative influence each has upon the short term periodic, and long term residual, tides and currents.

Table 2.1: A Summary of Historic Studies of Tides and Currents within Shallow Barrier Island Lagoons

Study	Method	Tidal Forcing	Wind Forcing	Residual Transport	Non-Linear Forcing	Density Grad.
Kjerfve (1975)	Data	yes	yes	yes	no	no
Smith (1979)	Data	yes	yes	yes	no	no
Smith (1980)	Data	yes	no	no	no	no
Smith (1983)	Data	no	yes	yes	no	no
Smith (1985)	Data, 1-D Model	yes	yes	yes	no	no
van de Kreeke and Wang(1984)	Data 2-D Model	yes	no	no	yes	no
Speer, Aubrey Friedrichs (1985-1992)	Data 1-D Model	yes	no	no	yes	no
Boon (1988)	Data	yes	no	no	yes	no
Seim and Sneed (1988)	Data	yes	no	no	yes	no
van de Kreeke Dean, Cotter (1971-1975)	1-D Model	yes	no	yes	yes	no
Johnson, Lee (1977)	1-D Model	yes	yes	yes	no	yes
Dronkers (1978)	1-D Model	yes	no	no	yes	no
Moody (1988)	1-D Model	yes	no	no	yes	no
Wang, Swakon (1977)	2-D Model	yes	yes	yes	no	no
Smith (1990a,b)	2-D Model	yes	yes	yes	no	no
Sheng (1983)	3-D Model	yes	yes	no	yes	no
Sheng (1993)	3-D Model	yes	yes	yes	yes	yes

CHAPTER 3
FIELD DATA COLLECTION

3.1 Introduction

As part of a cooperative agreement, the Coastal and Oceanographic Engineering Department of the University of Florida (UFL) and the Water Resources Division of the United States Geologic Survey (USGS) collected hydrodynamic data throughout the Sarasota Bay system during the years 1990 to 1992. The data collection effort involved 13 locations at which tides, currents, salinity, temperature and wind speed were measured (not all were measured at each station). In conjunction, intra-tidal discharge measurements were taken at critical cross sections within the lagoons and across the inlets connecting the lagoons to the Gulf of Mexico. This chapter describes the locations where the data were collected, the periods over which the data were collected, the types of instruments used and their relative accuracy, the instrument maintenance and any possible instrument errors.

3.2 University of Florida Data Collection Stations

The Coastal and Oceanographic Engineering Department of the University of Florida deployed a total of six sets of instruments in Anna Maria Sound, Sarasota Bay, Little Sarasota Bay, Blackburn Bay and offshore in the Gulf of Mexico. Figures 3.1 and 3.2 show the locations.

The UFL stations are defined in two categories, bay stations and offshore stations. On Figures 3.1 and 3.2 the offshore stations are prefixed by an "O" and the bay stations prefixed by a "B". The offshore stations were installed to obtain data on the

tidal and salinity conditions in the Gulf of Mexico. These data are used to produce boundary conditions for the circulation and transport model the results of which are presented in Chapter 6. In addition, these data are analyzed in Chapter 4 to compare the nature of the offshore tides with those measured inside the lagoons and how the offshore forcings impact the interior circulation.

The bay stations were installed to measure currents, water surface elevation, conductivity, water temperature and wind at discrete positions throughout the interior lagoons. These data are first analyzed in Chapter 4 to provide some insight into the physics of the circulation and transport, and later used to calibrate and verify the numerical model.

3.2.1 Bay Stations

At the bay stations, UFL-B1, UFL-B2, UFL-B3, and UFL-B4 the instruments were mounted on surface piercing platforms. A schematic of the platforms is shown in Figure 3.3.

Platform Design and Installation

The platforms were designed and constructed at the University of Florida Coastal and Oceanographic Engineering Department. They are made of lightweight aluminum; a 4 meter high platform weighs approximately 125 kg without instrumentation. The platforms were designed such that they could be broken apart and transported as joints and connecting pipes. The corner joints for each platform are the same and the height is determined by varying the lengths of the connecting pipes. This allowed for deployment over a range of depths, and allowed the sizes to be altered simply by cutting new connecting pipes. The conning tower, where the data logger and power supply were mounted, is the same for each platform.

The deployment procedure consisted of the following. The platforms were assembled at a dockside location without the instrumentation. A transport saddle, which
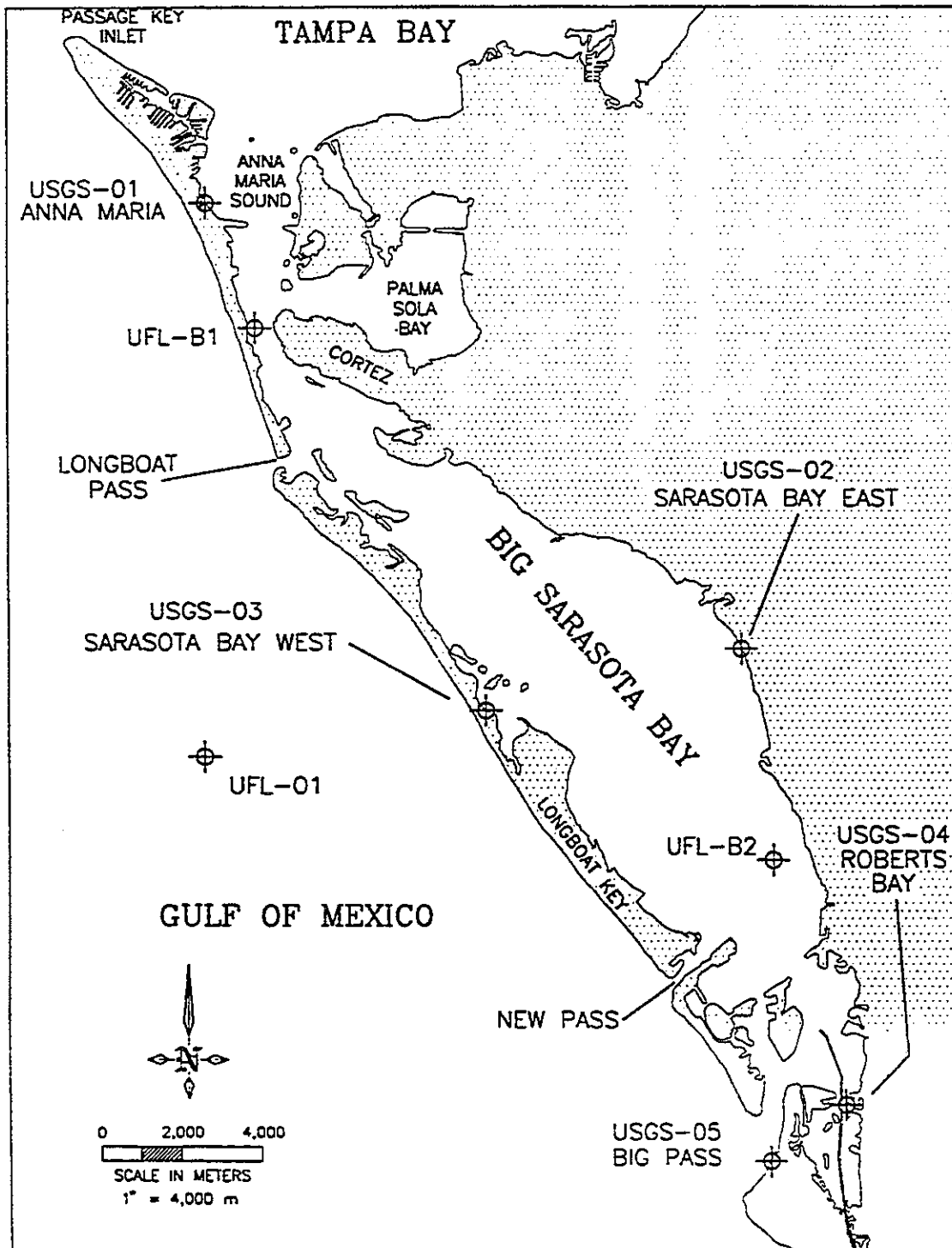
Figure 3.1: The locations of the UFL and USGS data collection stations within Anna Maria Sound and Big Sarasota Bay, 1991 deployment.
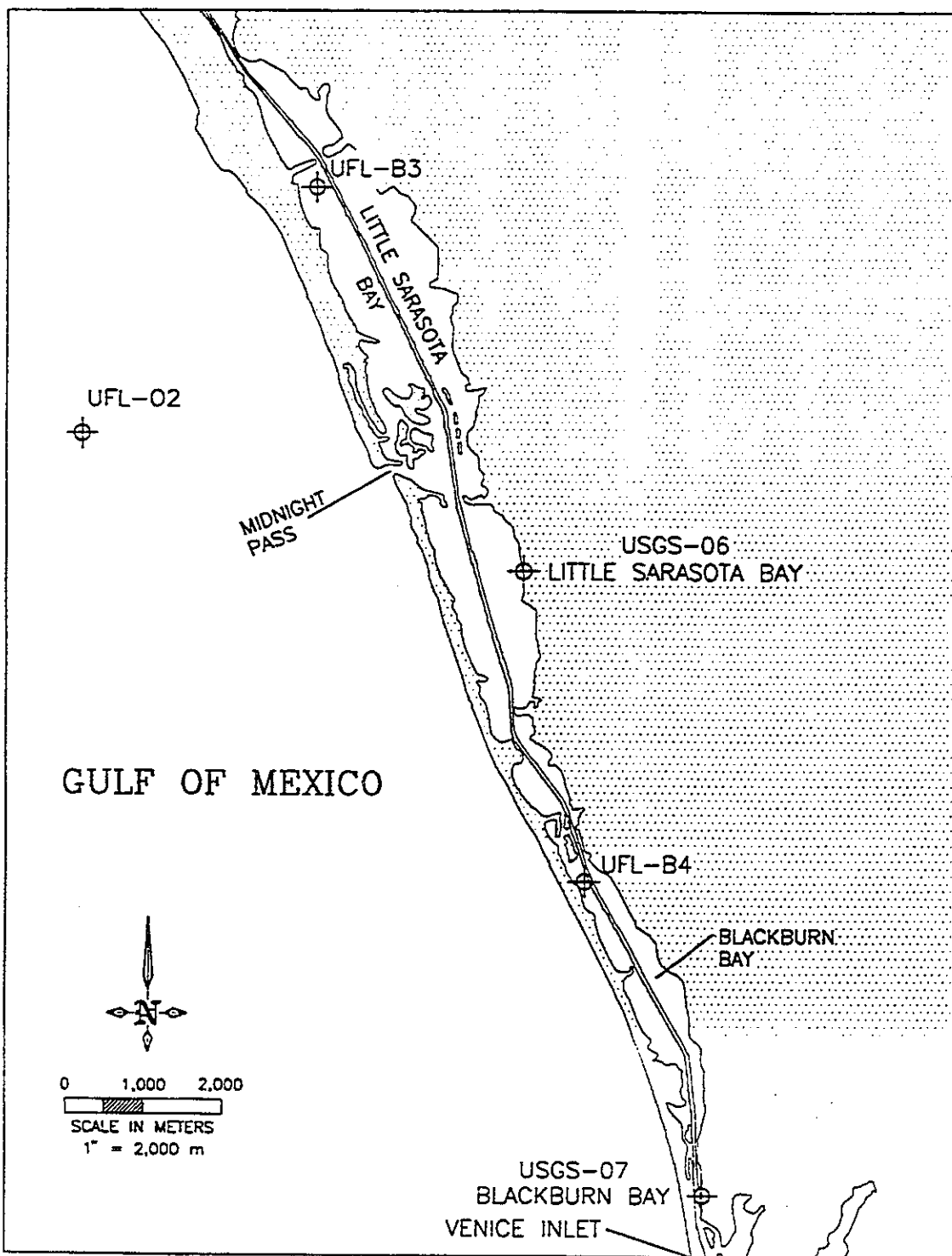
Figure 3.2: The locations of the UFL and USGS data collection stations in Little Sarasota Bay and Blackburn Bay, 1991 deployment.
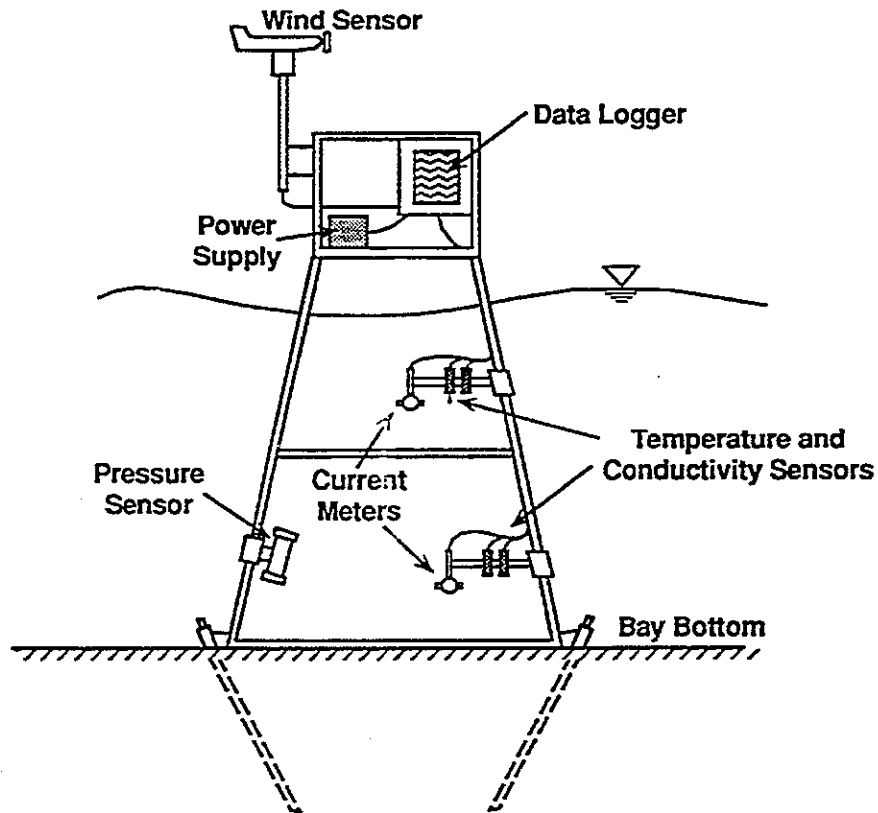
Figure 3.3: A schematic of the University of Florida instrument platforms.

was designed and constructed for this project, was mounted on the Coastal Vessel Munson and allowed the platforms to be transported to their predetermined locations and easily lowered into the water. The stations were secured to the bay bottom by jetting in pipes at the three corners of the base and clamping the corner joints to the jet pipes. The instruments were then mounted onto the frame along with the data logging system and the power supply. The complete installation procedure for each station lasted approximately 6 hours. The station locations in latitude and longitude, the water depth at mean sea level, and the deployment durations are given in Table 3.1. The station locations were determined by triangulation to known land references.

Table 3.1: The locations and depths of the University of Florida Stations

Station I.D.	Latitude	Longitude	Depth(cm)	Duration
UFL-B1	27 28.50	82 41.80	240.0	07/18/91 - 09/23/91
UFL-B2	27 21.00	82 33.50	330.0	07/17/91 - 09/23/91
UFL-B3	27 14.20	82 31.15	210.0	07/19/91 - 09/23/91
UFL-B4	27 09.30	82 28.92	210.0	07/20/91 - 09/23/91
UFL-O1	27 12.63	82 33.02	900.0	07/15/91 - 09/14/91
UFL-O2	27 22.57	82 42.52	900.0	07/15/91 - 09/14/91

Instruments

Each station had instruments mounted at two elevations below the low water mark on arms which extended toward the center of the frame (see Figure 3.3). This was done to prevent snagging on the anchor lines of boats mooring near the platforms. The platforms were designed such that the diameter of the connecting pipes was as small as possible (2 inches), this reduced any possible wake interference on the current readings. In addition, where possible, the platforms were oriented such that no support pipes were directly upstream or downstream of the current sensors.

Table 3.2: Instrument elevations on the University of Florida platforms, 1991 deployment

Station	Arm Number	Current	Conductivity	Temperature
UFL-B1	1	25 cm	55 cm	55 cm
	2	145 cm	175 cm	175 cm
UFL-B2	1	55 cm	85 cm	85 cm
	2	225 cm	255 cm	255 cm
UFL-B3	1	25 cm	55 cm	55 cm
	2	115 cm	145 cm	145 cm
UFL-B4	1	25 cm	55 cm	55 cm
	2	115 cm	145 cm	145 cm

Each instrument arm had an electromagnetic current sensor, a conductivity sensor and a temperature sensor. In addition, each platform had a wind sensor mounted approximately 4 feet above the top of the conning tower and a pressure sensor mounted

below the lower low water datum. The instrument elevations for each platform are given in Table 3.2.

The electromagnetic current sensors utilize Faraday's principle which states that any conductor passing through a magnetic field will produce a voltage, and the voltage is proportional to the speed at which the conductor passes. To make use of this principle, the current sensors have an electromagnet inside their head which produces a magnetic field. As water (a conductor) moves past the head, a voltage is induced within the field which is sensed by elements on the outside of the sensor. The magnitude of the voltage measured, along with the polarity, determines the velocity vector components. The sensing elements are positioned along orthogonal axes of a plane radiating outward from the sensor, therefore only two-dimensions of the velocity field can be measured. In our case these were the horizontal velocity vector components.

Electromagnetic current sensors have a good tilt response factor, i.e. the measurements of the horizontal vector components are not contaminated by vertical velocity fluctuations which may be present. They are also accurate sensors, capable of measuring velocities as low as 1-2 cm/sec. This was important in this study as the amplitude of the tidal currents at some of the stations were as low as 5 to 10 cm/sec.

One disadvantage of these instruments is that the current sensing elements can be prone to fouling. The head has an antifoulant coating everywhere except at the tips of the sensing elements. This means that frequent cleanings, on the order of a week, were required to prevent inaccurate readings. The other disadvantage is that the sensors can drift, i.e. the voltage which corresponds to zero current can change slowly over time. To monitor this problem the sensors have a setting (calibrate) which corresponds to a specific voltage and can be scanned to spot any drift. The calibrate voltage was scanned on a weekly basis throughout the deployment.

The current sensors were calibrated prior to deployment in the USGS flow tank at the Stennis Space Center in Slidel, Louisiana. The calibrations are presented and

discussed in Appendix A.

The conductivity and temperature sensors were manufactured by Sea Bird Technologies. They were designed to be used to measure vertical profiles of conductivity and temperature in the open ocean and are accurate enough to resolve minor changes. The temperature probes are accurate to within .002 Degrees C. The conductivity sensors are accurate to within .0002 siemens/meter. The calibrations of these sensors were conducted by the manufacturer and the sensors were deployed for the first time on this project. The manufacturers calibrations are presented in Appendix A.

The temperature sensors were unaffected by fouling, while the conductivity sensors were susceptible to fouling. The three electrodes used in the conductivity probes are housed in a Plexiglas tube which allows the sea water to pass through it. In order to prevent growth within this tube, antifoulant sleeves were place on both ends. These sleeves, which allowed seawater to pass through, were lined with tributyl-tin which dissolved slowly throughout the deployment. They effectively prevented growth within the tubes and eliminated all fouling due to algal and barnacle growth. The only fouling which occurred was caused by fine silty material settling inside the tubes at stations with low velocities. Pre and post cleaning readings showed the error, after conversion to salinity, to be at most 0.2 parts per thousand (ppt).

The wind sensors were R.M. Young anemometers which measured speed and direction. The speed is measured as a voltage induced by a spinning propeller and the direction is measured by a potentiometer as the sensor moves to face the wind direction. The wind sensors were calibrated prior to the deployment in a wind tunnel at the Aerospace Engineering Department of the University of Florida. The calibration curves for the wind sensors are included in Appendix A.

The pressure sensors were deployed to measure the water surface elevation at the stations. The pressure transducers were purchased from Transmetrics Corporation and placed in a housing designed and manufactured at the Coastal and Oceanographic

Engineering Laboratory of the University of Florida. The sensing element sits in a pool of oil and is separated from the water by a diaphragm which is free to transfer any pressure changes through the oil.

All data collected were recorded using Onset Tattletale data loggers. These loggers are programmed in BASIC to allow the sampling to be tailored to the users needs. For this deployment the loggers were programmed to record ten minute averages of data taken at a 1 hertz rate on the quarter hour. All data were collected with time set to Eastern Standard Time. This standard was maintained for all data collected either by the University of Florida or the United States Geological Survey.

Overall the data loggers operated well. Stations UFL-B1, UFL-B2 and UFL-B4 had short periods of down time in the data logging system, station UFL-B3 operated continuously throughout the study. Station UFL-B4 had the longest periods of down time as the result of battery failures. Stations UFL-B1 and UFL-B2 only had short periods of down time.

All the individual instruments except the pressure transducers performed well throughout the study. Barnacle growth on the rubber diaphragm created false pressure readings. The barnacles were frequently cleaned off but their rapid regrowth created contamination of the data which was unresolvable. Given the number and spacing of the USGS tide stations, the loss of this data was not deemed critical. A description of the tidal data collected by the USGS is presented in section 3.3.

3.2.2 Offshore Stations

Stations UFL-O1 and UFL-O2 were deployed approximately 4 kilometers offshore in the Gulf of Mexico. The instruments consisted of a bottom mounted Sea Data Package which recorded pressure, and two conductivity sensors mounted on a buoy tether. Figure 3.4 presents a schematic of the offshore data stations. Table 3.1 lists the lengths of time that data were collected at the offshore stations, the water depth
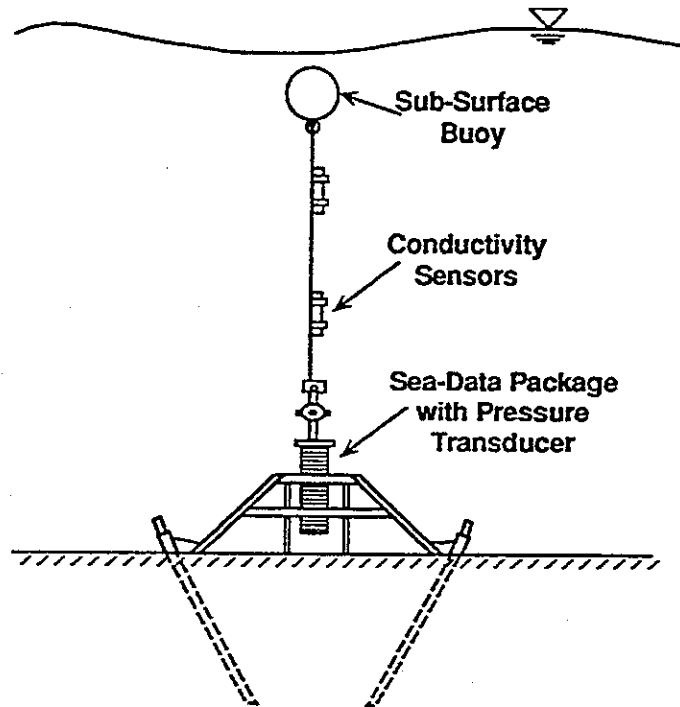
Figure 3.4: A schematic diagram of the offshore data collection stations

at mean tide and the station locations in latitude and longitude. The station locations were chosen to be evenly spaced across the offshore open boundary to the model.

The Sea Data Loggers were programmed to perform 5 minute averages of the pressure every 10 minutes and store the results. The pressure was then transformed into water surface elevation using the hydrostatic equations. Given that the Sea Data Instruments were bottom mounted, in a depth of 10 meters, it was impossible to reference the tidal fluctuations to a specific datum. Therefore, these data were demeaned and detrended prior to use. The Sea Data packages operated properly throughout the study period and provided a continuous record of offshore tidal fluctuations.

The conductivity sensors along with separate data loggers were deployed by USGS

at two levels along the buoy tether at each of the stations. The gages were installed to measure conductivity and temperature throughout the study. The data logging systems on both stations did not operate properly and no reliable data were obtained from these gages.

3.3 Tide and Discharge Measurements Taken by the USGS

3.3.1 Tidal Data

The Water Resources Division of the USGS established 7 stations throughout the project area, Table 3.3 gives the latitudes and longitudes. Each station consisted of a data logger in an aluminum shelter over a PVC stilling well attached to a dock. Pressure sensors measured the changes in water level and the data were stored on the logger. The data consisted of instantaneous pressure readings taken every 15 minutes. The pressure was converted into water surface elevation using hydrostatic equations. The stations were established on August 2nd and 3rd, 1990 and maintained on an intermittent basis until October 1992. The station at Big Sarasota Pass (USGS-05) was maintained for the entire period. The stations at Roberts Bay (USGS-4), Little Sarasota Bay (USGS-06) and Blackburn Bay (USGS-07) were maintained from August 1990 to January 1992. The stations at Anna Maria Sound (USGS-01), Sarasota Bay East (USGS-02) and Sarasota Bay West (USGS-03) were maintained from August 1990 to January 1991 and from January 1992 to October 1992. Periodic power failures and instrument malfunctions created gaps in the data.

Initial elevations on the instruments were established using a Trimble Global Positioning System (GPS). The datum corrections to NGVD, determined from the GPS system, are listed in Table 3.3 under "GPS". Examination of the data indicated some possible errors in the initial survey work. As a check, 4 of the 7 stations were releveled using standard techniques tied to existing benchmarks. The revised datum corrections are listed under "Level". Table 3.4 lists the reference benchmarks used to

Table 3.3: The locations of the USGS tidal data stations.

Location	Latitude	Longitude	GPS (feet)	Level (feet)	Settling (feet)
Anna Maria Sound (USGS-01)	27 30.08	82 42.60	-5.181	-5.280	.02
Sarasota Bay East (USGS-02)	27 24.13	82 43.32	-6.610	-6.311	.02
Sarasota Bay West (USGS-03)	27 23.25	82 38.28	-6.640	-6.252	.01
Roberts Bay (USGS-04)	27 18.00	82 32.65	-5.416	None	.02
Big Sarasota Pass (USGS-05)	27 17.22	82 33.78	-7.745	-7.279	.00
Little Sarasota Bay (USGS-06)	27 11.73	82 29.60	-5.745	None	.03
Blackburn Bay (USGS-07)	27 07.50	82 28.13	-5.465	None	.03

establish the revised datum for each station.

The releveling indicated that the error is different for each of the stations and for the purposes of analysis the datum established by the standard methods was used. Based upon this, the corrections to NGVD established for the Roberts Bay, Little Sarasota Bay and Blackburn Bay stations are not reliable.

As well as setting the elevations for each station, USGS periodically ran optic levels from the established reference marks to the instrument. This was done to determine the amount of settling of the stilling well over the study period. The amount of settling for each station is listed in Table 3.3.

Table 3.4: Benchmarks used to verify elevations of USGS tide gauges

Station	Benchmark (BM)
Anna Maria Sound (USGS-01)	USCGS N-254, 1965 DNR 13 85 A15 DOT 13 85 A15 REF
Sarasota Bay East (USGS-02)	Manatee County BM FEMA BM
Sarasota Bay West (USGS-03)	Sarasota County BM R-2, 1985 17-84 A02
Big Sarasota Pass (USGS-05)	DNR R-44A (reset 1985)

3.3.2 <u>Discharge Measurements</u>

Measurements of discharge were taken by USGS at critical cross sections within the lagoon system and at the inlets. In 1991 the discharge at the Siesta Bridge in Roberts Bay and the Nokomis Bridge in Blackburn Bay were measured (see figures 3.1 and 3.2). These two cross sections are the only two entrances to the Roberts Bay/Little Sarasota Bay/Blackburn Bay system. The purpose was to quantify the relative flow from the north and south into Little Sarasota Bay and Blackburn Bay. The discharge was measured at both stations over an ebb as well as a flood tide.

The method utilized to measure the flows was as follows. The cross-section directly below the bridge was divided into sections of even area. Current meters were lowered from the bridge and measurements were taken at 20 and 80 percent of the depth at the centerline of each section. Where the depth was too shallow, readings were taken at 60 percent of the depth only. The measurements were taken over the entire cross section as rapidly as possible to obtain instantaneous discharges. The longest time for the completion of one cycle was 30 minutes, while the average time was approximately 15 minutes. The discharge was then calculated by multiplying the average velocity within each section by the area and summing over the cross section. Results presented later show the measurements as instantaneous readings.

In 1992 an Acoustic Doppler Current Profiler (ADCP) was made available to USGS to perform the discharge measurements. This instrument allowed measurements to be taken from a boat. The profiler was mounted off of the boat and pulled across the cross section. The time to profile in this manner was much quicker than the 1991 method and the results represent a more instantaneous measurement. The 1992 discharge measurements were taken across the inlets connecting the lagoons to the Gulf of Mexico. Data were collected at Big Pass, New Pass, Longboat Pass, Anna Maria Sound and Roberts Bay.

CHAPTER 4
FIELD DATA ANALYSIS

4.1 Introduction

In Chapter 2, studies were presented which isolated the response of shallow barrier island lagoons to the forcing by the tides, wind and density gradients. In conjuction, the studies examined how the varying bathymetry and geometry within the lagoons modified their response. Within this chapter, the response of the Sarasota Bay System to these "forcing mechanisms" is examined through analysis of the data set described in Chapter 3.

The first part of this chapter includes spectral analysis, filtering, and harmonic analysis of the data of water surface elevation, current and wind. The continuous signals are decomposed into sub-components and separated into portions driven by single forcing mechanisms. These separated signals are analyzed comparatively to define the relative energy in each, and correlated to one another to isolate and identify the forcing.

The second part of this chapter presents the results from the discharge measurements conducted by the USGS in 1991 and 1992. The discharges are analyzed to quantify the relative flows through each of the multiple inlets connecting the lagoons with the Gulf of Mexico, as well as defining the flows through critical cross sections separating sub-bays within the system.

The final section presents the salinity measurements taken at the University of Florida bay stations along with representative measurements of freshwater inflow to the system. These data are analyzed to define the levels and variations in salinity under the inflow of freshwater from the tributaries. These data provide a qualitative

evaluation of transport and the level of flushing within the individual lagoons. Additionally, these data provide information on the spatial and temporal variations of stratification.

The data collection effort spanned two years, from 1990 to 1992. From this data set two 60 day periods are focused upon. The first period coincides with the time when the University of Florida deployed its platforms (July 17, 1991 to September 15, 1991). This period reflects summer conditions with its associated localized thunderstorms and low overall wind energy. The second period (September 15, 1990 to November 15, 1990) reflects fall to winter conditions with higher sustained wind energy. As the University of Florida platforms, which contained the current meters and salinity sensors, were not deployed during 1990, the available tide and wind data are analyzed in order to compare and quantify the effects of the differing weather patterns on the circulation throughout the system.

4.2   Decomposition of Water Surface Elevations, Currents and Wind

The water surface elevations and the currents can each be represented in equation form as (Pugh, 1987),

$$X(t) = Z_0(t) + T(t) + S(t) \qquad (4.1)$$

where $X(t)$ is either the measured water surface elevation or current, $Z_0(t)$ is the slowly varying mean water level or mean current, $T(t)$ is the short term tidally driven portion of the signal and $S(t)$ is the short term portion of the signal driven by the meteorological forcing.

Within the terms on the right hand side of the equation, various sub-components exist. For instance, the tidally driven portion of the signal is actually the superposition of a number of harmonic constituents each with its own amplitude and period. These include the semi-diurnal (M_2 and N_2) the diurnal (K_1 and O_1) and other higher and lower frequency harmonics. These variations, which are associated with the pull of

the sun and moon, are termed gravitational tides or currents.

The short term meteorological variations are normally associated with wind stress acting upon the water surface creating surge and flow. These forcings may occur locally or may, as in the case of a lagoon connected to the ocean, occur in a larger body of water and propagate into the lagoon through the inlets. Certain periodic constituents, such as the S_2 harmonic, may be partially driven by meteorological forcing, i.e. the effects of the sea breeze. When meteorological forcings result in periodic fluctuations, they are termed radiational tides or currents.

The long-term variations in the mean water level may contain both gravitational and radiational forcings. The S_a harmonic constituent for instance is the annual variation in mean water level due to the relative positions of the sun and moon. The long period gravitational forcings in general are small in relation to the long term variations in water level associated with meteorological forcings.

Inside of a lagoon or bay, gravitational tides are considered to be remotely forced, i.e. the variations occur in larger bodies of water such as the Gulf of Mexico and propagate into the bay through the inlets. The currents are then locally driven by water surface elevation gradients. Radiational tides or currents may be either locally (i.e. wind driven currents or surge) or remotely forced, i.e. due to Ekman transport propagating in from the offshore.

All of the mechanisms described above act simultaneously to produce the measured tidal and current fluctuations. In the following sections the relative energies imparted by these mechanisms will be examined through decomposition of the raw data signals and comparison and correlation between the measured water surface elevations, currents and winds. Prior to decomposition, the raw data will be presented and discussed relative to the bathymetry and geometry of the lagoons.

4.2.1   Presentation and Discussion of Raw Data

Water Surface Elevation Data

Figures 4.1 and 4.2 present example data of water surface elevation measured from Julian day 255 to 285 in 1990 and from Julian day 200 to 230 in 1991. On both figures the data are presented with the offshore stations in the top plot progressing farther interior to the lagoons going down. The complete water surface elevation data sets for the seven USGS stations are plotted in Appendix B.

The plots demonstrate the mixed semi-diurnal/diurnal tides characteristic of the Gulf of Mexico. These mixed tides create an irregular pattern in the amplitudes and periods. The damping of the tidal wave can be seen by comparing the offshore tides (UFL-01, NOAA-01) with the Little Sarasota Bay tides (USGS-06). The effects of the wind, as shown by the short term fluctuations in the water level data (day 270 to 272 in Figure 4.1), are less pronounced at the more interior stations. Additionally there is an increase in the non-linearity of the wave. Figure 4.3 presents a comparison between tides measured at USGS-05 (Big Pass) and USGS-06 (Little Sarasota Bay) over a five day period. The tidal wave at the interior station (USGS-06) has a more peaked non-linear shape. Although the data indicate a super elevation at the interior stations, errors associated with the leveling of the tide gages, described in Chapter 3, make any conclusions unreliable.

Current Data

This section will present the north-south and east-west velocity vector components measured from Julian Day 200 to 230 in 1991. Plots of the remaining data set (beyond Julian Day 230) for the four University of Florida stations are included in Appendix B.

Visual examination of the plots is the first step towards an understanding of the circulation patterns within the bay. As the geometry and bathymetry of a lagoon or estuary can have a significant influence on the circulation and transport patterns, a

Offshore (NOAA-01) (a)

Elevation (cm)

Julian Day (1990)

USGS-05 (Big Pass) (b)

Elevation (cm)

Julian Day (1990)

USGS-04 (Roberts Bay) (c)

Elevation (cm)

Julian Day (1990)

USGS-06 (Little Sarasota Bay) (d)

Elevation (cm)
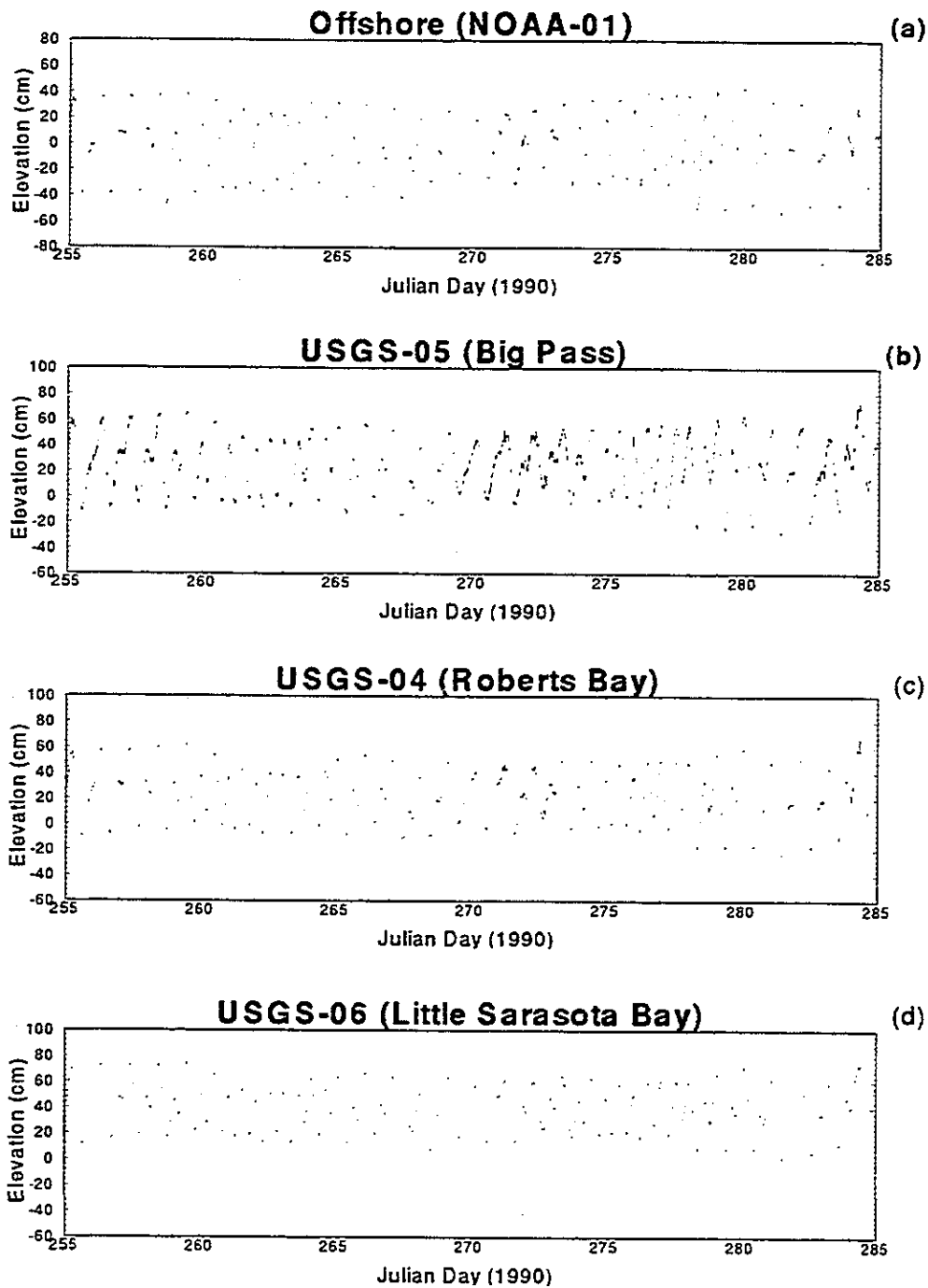
Julian Day (1990)

Figure 4.1: The measured water surface elevations from Julian Day 255 to 285, 1990. a) offshore; b) USGS-05 (Big Pass); c) USGS-04 (Roberts Bay); d) USGS-06 (Little Sarasota Bay).
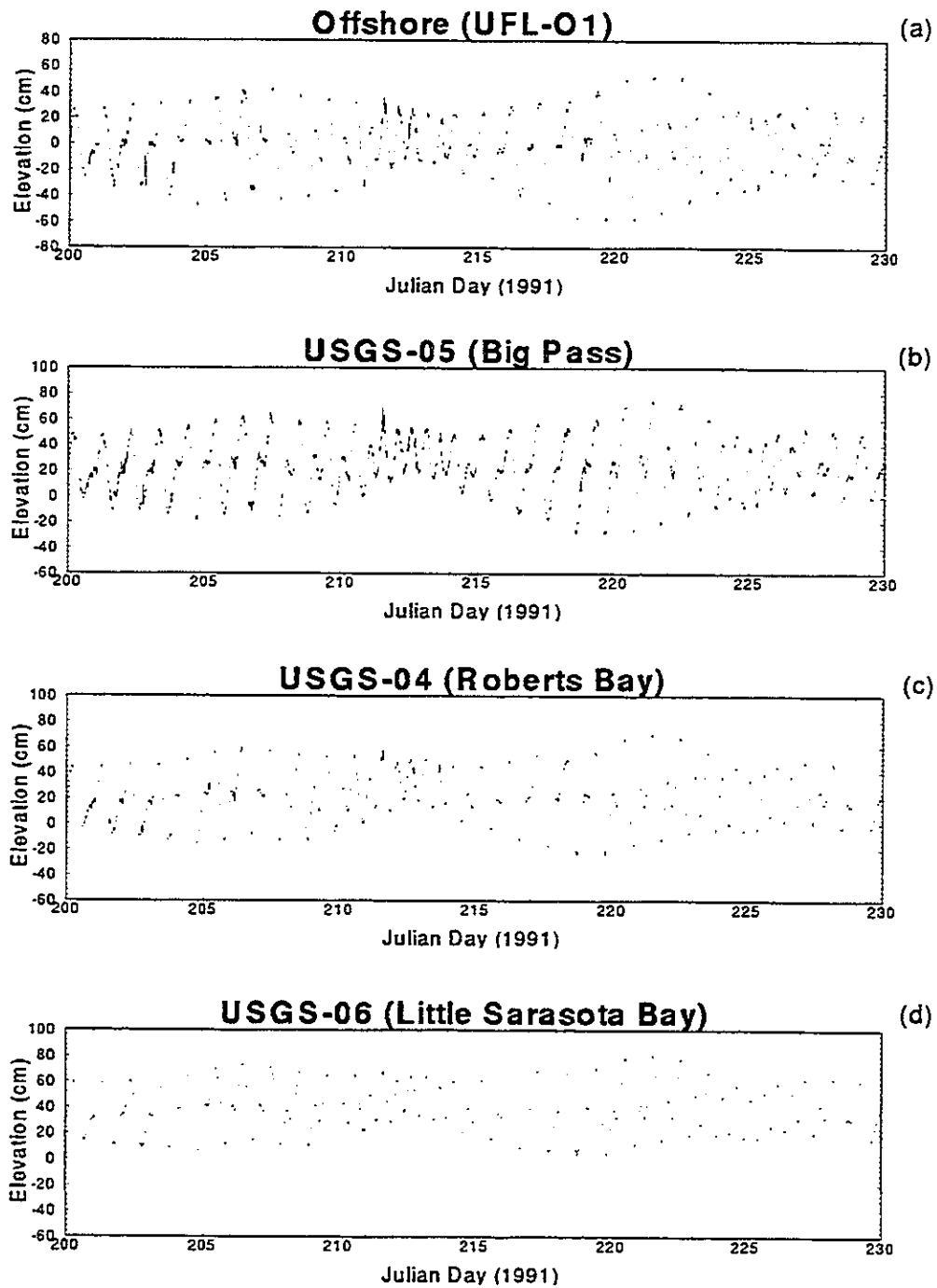
Figure 4.2: The measured water surface elevations from Julian Day 200 to 230, 1991. a) UFL-O1; b) USGS-05 (Big Pass); c) USGS-04 (Roberts Bay); d) USGS-06 (Little Sarasota Bay).
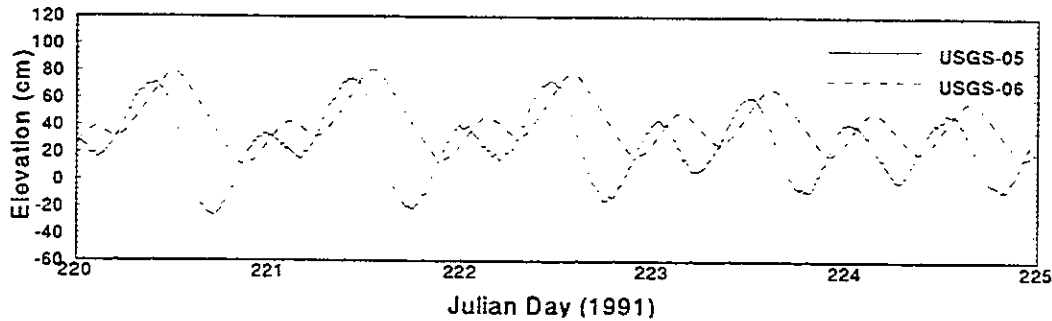
Figure 4.3: A comparison of measured water surface elevations from Julian Day 220 to 225, 1991 at USGS-05 (Big Pass) and USGS-06 (Little Sarasota Bay)

discussion of the geometry and bathymetry surrounding each station is included.

Station UFL-B1

Station UFL-B1 is located within a constriction which connects Anna Maria Sound and Palma Sola Bay with the northern end of Sarasota Bay and Longboat Pass (see Figure 3.1). This constriction is approximately 700 meters wide and is oriented at 330 degrees. The nearest inlet is Longboat Pass which is 3 kilometers to the south. Anna Maria Sound opens into the southwest corner of Tampa Bay which immediately opens out to the Gulf of Mexico through Passage Key Inlet.

The bathymetry near UFL-B1 is characterized by shallow flats (1 to 2 meters) intersected longitudinally by the Intracoastal Waterway and other maintained channels. Looking from east to west across the constriction where UFL-B1 was located, the cross-section goes from deep water on the eastern side of the channel (3 to 4 meters) sloping upward to the west with a 300 meter wide shallow region (approximately 1 meter) on the western side (Figure 4.4). The instrument platform was located in the transition region between the deep and shallow waters, the station depth at mean water level was presented in Table 3.1.
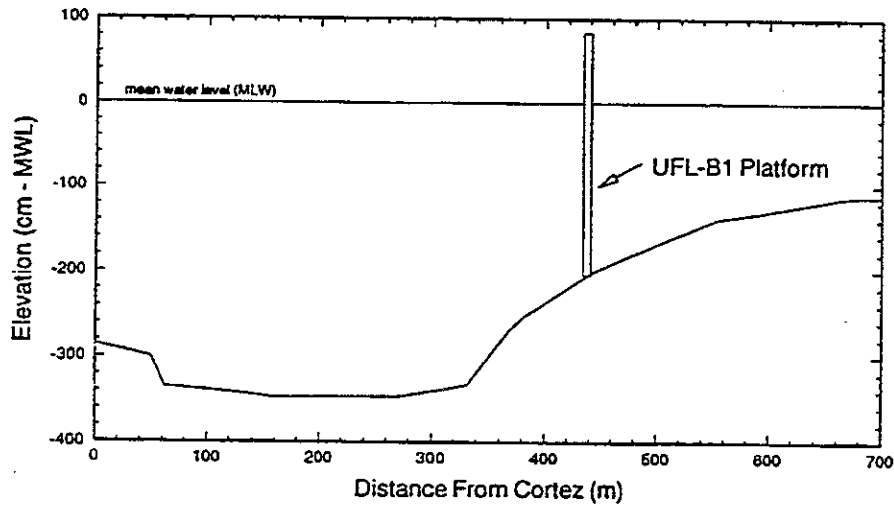
Figure 4.4: The bathymetric cross-section at station UFL-B1

The measured currents (Figure 4.5) show a distinct SSE directed residual. Taking the means from each of the signals gives residual current magnitudes of 3.0 and 4.4 cm/sec for the bottom and surface east-west velocity components respectively, and -6.0 and -8.5 cm/sec for the bottom and surface north-south velocity components respectively. The resultant vectors are a 6.7 cm/sec residual oriented at 154 degrees near the bottom, and a 9.6 cm/sec residual oriented at 153 degrees near the surface.

Some simplified analyses were described in Chapter 2 which defined the net transport between two inlets in a multi-inlet lagoon system (van de Kreeke 1971, Cotter 1974, van de Kreeke and Cotter 1974, van de Kreeke and Dean 1975). As UFL-B1 is essentially between two inlet openings, Tampa Bay (Passage Key Inlet) and Longboat Pass, it is possible to explain qualitatively some possible driving mechanisms for this residual. Figure 2.1 presented the net flow for the simplified geometry under varying inlet widths, depths and amplitudes of the tidal forcing. The results showed that net flow is toward the inlet which is narrower, shallower and has the smaller tidal amplitude. Examining each of these characteristics in relation to the two openings, Longboat Pass is narrower and shallower than the openings to Tampa Bay. Addi-
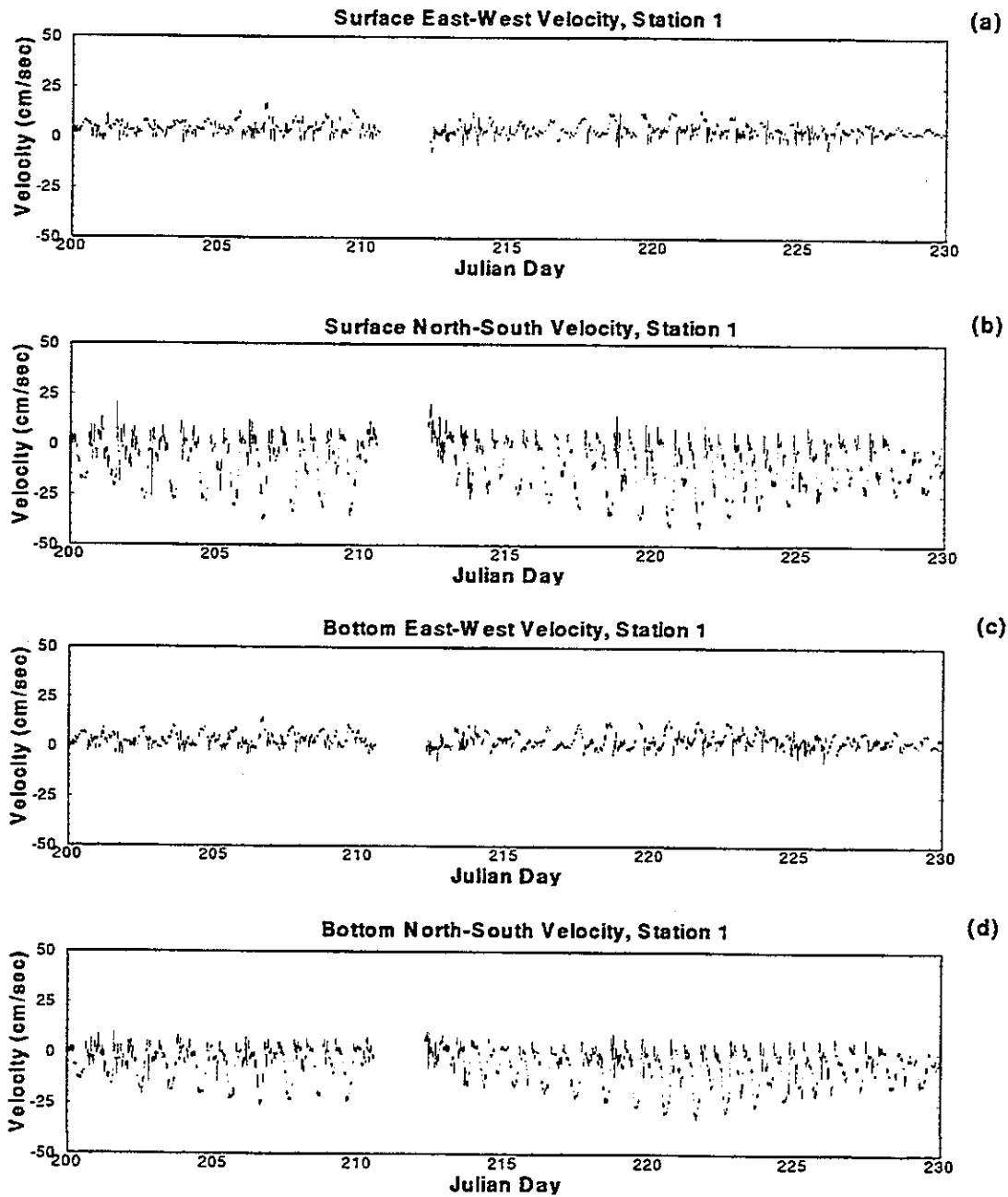
Figure 4.5: The current vector components measured from Julian Day 200 to 230, 1991 at UFL-B1. a) Surface East-West Velocity; b) Surface North-South Velocity; c) Bottom East-West Velocity; d) Bottom North-South Velocity.

tionally, it will be shown later that the tidal amplitude in the offshore regions is reduced moving from north to south, and therefore the tidal amplitude at Longboat Pass may be lower than that entering Tampa Bay. Each of these characteristics supports a residual flow from north to south across UFL-B1. These explanations will be examined in later parts of this chapter and through application of the numerical model.

<u>Station UFL-B2</u>

Station UFL-B2 is located on the southern end of Sarasota Bay. Sarasota Bay is the most open body of water within the system and is approximately 5 kilometers wide and 15 kilometers long. The depths are relatively uniform and range from 8.0 feet to 13.0 feet, the deepest portions are at the center. Tidal velocities at this station are driven by the wave propagating through New Pass and Big Pass (see Figure 3.1).

The measured currents (Figure 4.6) exhibit primarily north-south flow. The current magnitudes range from 30 cm/sec during spring tides to 15 cm/sec during neap tides. Current magnitudes are highest during flood tide which occurs over a shorter duration. Using terminology introduced in Chapter 2, this type of system would be termed flood dominant as transport would be greater during flood tide. The flood tides at this station may also be stronger due to the nature of the flood and ebb patterns near an inlet. The flooding currents enter the bay through New Pass and Big Pass as a jet and reach farther in than the ebbing currents which tend to flow from all directions.

Taking the mean values for each component gives 2.7 cm/sec and 1.1 cm/sec for the bottom and surface east-west residual velocities and 2.2 cm/sec and 2.8 cm/sec for the bottom and surface north-south residual velocities. The resultant vectors are a 3.4 cm/sec residual at an angle of 51 degrees on the bottom and a 3.0 cm/sec residual at an angle of 21 degrees on the surface. The residual currents exhibit a counterclockwise rotation from the bottom to the surface.
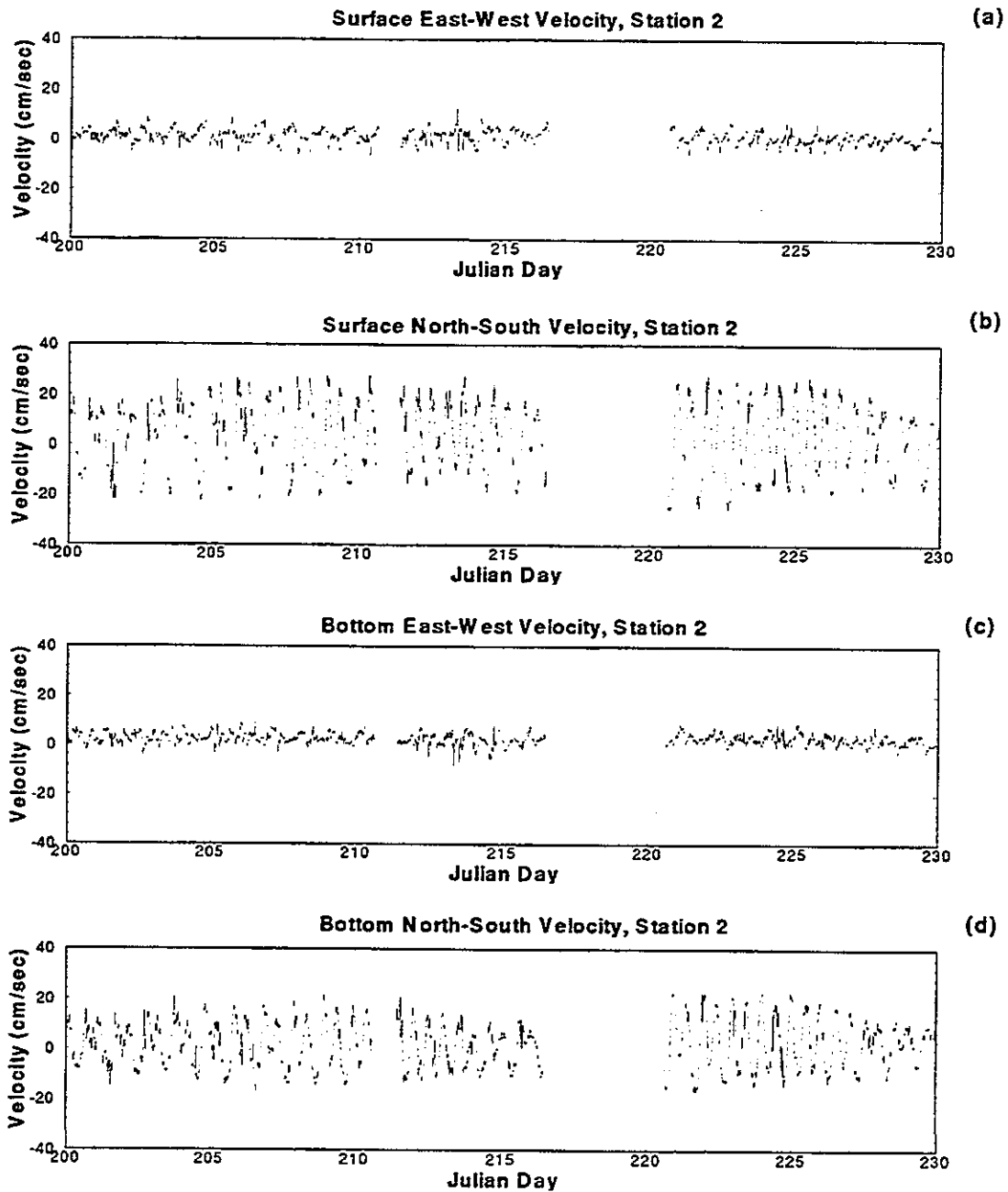
Figure 4.6: The current vector components measured from Julian Day 200 to 230, 1991 at UFL-B2. a) Surface East-West Velocity; b) Surface North-South Velocity; c) Bottom East-West Velocity; d) Bottom North-South Velocity.

Station UFL-B3

Station UFL-B3 is located in the northern end of Little Sarasota Bay. Little Sarasota Bay is a narrow lagoon approximately 20 kilometers long with numerous constrictions. The average width is 1000 to 1500 meters. The bathymetry within Little Sarasota Bay is shallow with an average depth of 1 to 2 meters at low water. The Intracoastal Waterway runs down the center of the bay and is an artificially maintained channel 70 to 100 meters wide and 3 meters deep. The connections from Little Sarasota Bay to the Gulf of Mexico are narrow and highly restrictive. To the north, the tidal wave propagates through Roberts Bay and then through a long narrow artificial channel which at some points reduces to less than 100 meters in width. To the south the wave enters through Venice Inlet and propagates through the narrow passage from Venice Inlet into Blackburn Bay and finally to Little Sarasota Bay.

The instrument platform was located approximately 100 meters to the west of the Intracoastal Waterway in approximately 2 meters or water. This station was located the greatest distance from any opening to the Gulf of Mexico, the nearest inlet was Big Pass 16 kilometers to the north.

The velocities presented in Figure 4.7 reflect the distance to the Gulf of Mexico and the restricted flow into Little Sarasota Bay. The highest recorded current magnitudes were near 15 cm/sec flowing predominantly to the north-south. Although the two current sensors were only one meter apart in the vertical, there was a more significant top-to-bottom reduction in the current magnitudes in comparison with the other stations. One explanation for this increased damping is that the bottom boundary layer within this region may be laminar, whereas at the other stations it may be turbulent. Figure 4.8 shows a comparison between two ideal velocity profiles under laminar and turbulent flow. The thickness of the boundary layer under laminar flow is greater and therefore there is a larger top-to-bottom velocity gradient.

Calculation of the mean velocities gives -1.2 cm/sec and -3.7 cm/sec in the bottom
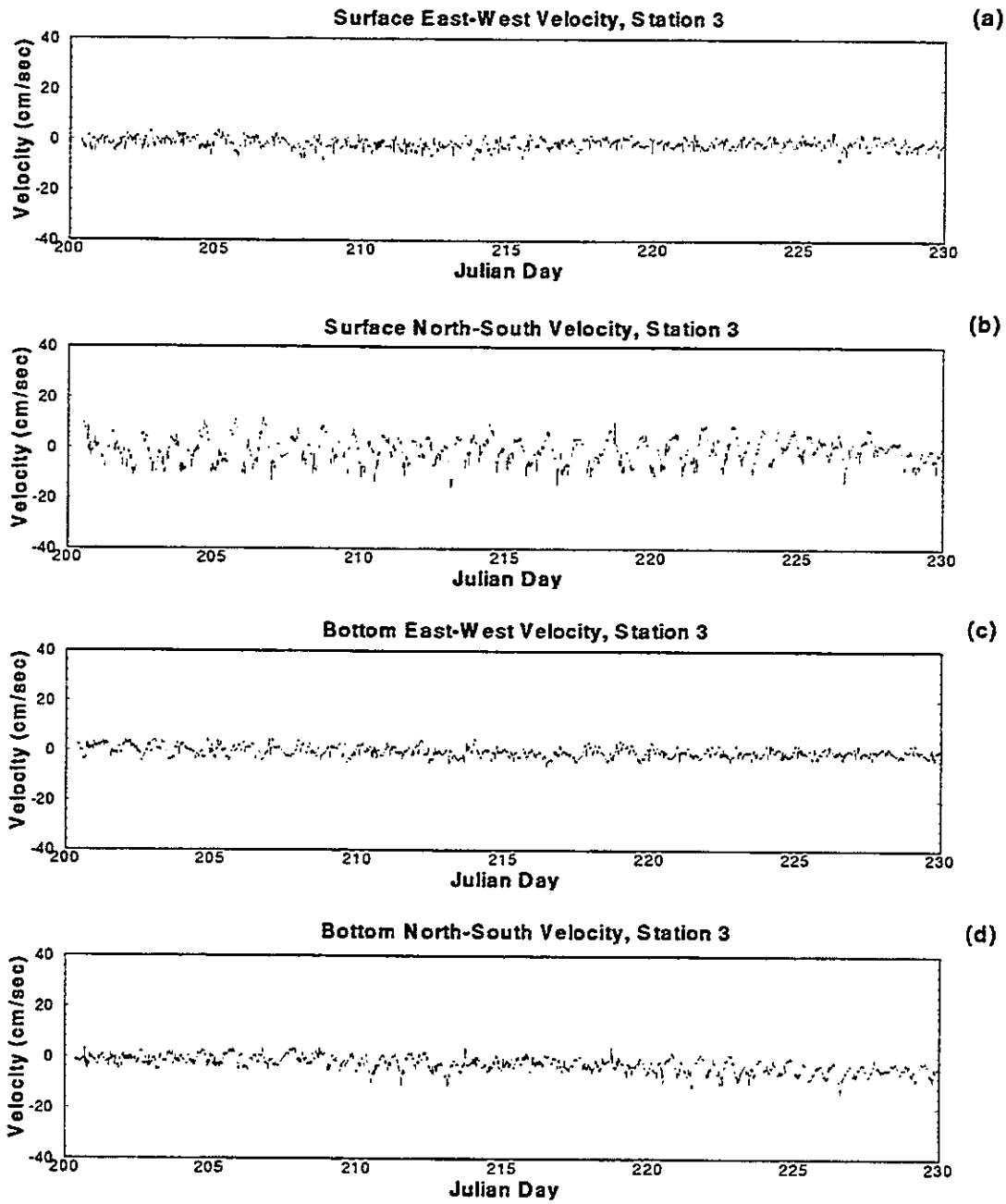
Figure 4.7: The current vector components measured from Julian Day 200 to 230, 1991 at UFL-B3. a) Surface East-West Velocity; b) Surface North-South Velocity; c) Bottom East-West Velocity; d) Bottom North-South Velocity.
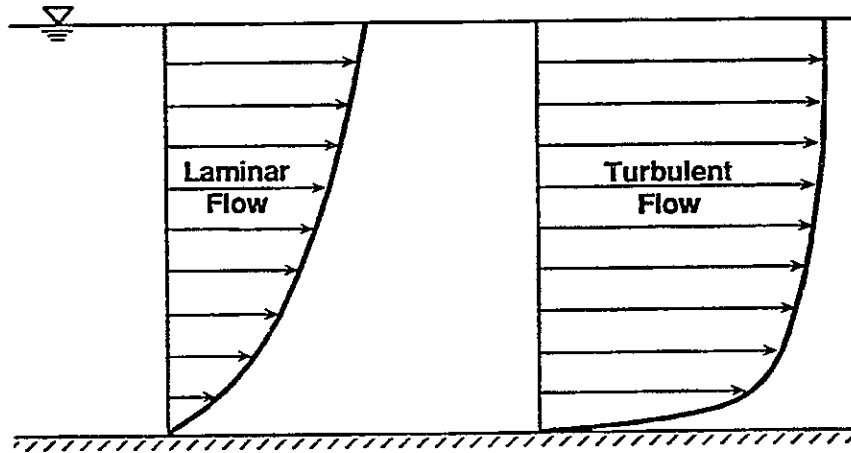
Figure 4.8: Idealized velocity profiles under laminar and turbulent boundary layers

east-west and north-south velocities respectively, and -1.9 and -1.3 in the surface east-west and north-south velocities respectively. The resultant vectors are a 3.4 cm/sec residual at 198 degrees on the bottom, and a 2.3 cm/sec residual at 235 degrees at the surface. The residual velocities show a 37 degree clockwise rotation from top to bottom.

Station UFL-B4

Station UFL-B4 was located in the northern end of Blackburn Bay. Blackburn Bay is a narrow lagoon oriented predominantly north-south. The bathymetry is similar to UFL-B3, i.e. shallow with depths from 1 to 2 meters with the Intracoastal Waterway running longitudinally along its axis. The instrument platform was located 75 meters to the west of the Intracoastal Waterway in approximately 2 meters of water. The nearest opening to the Intracoastal Waterway is through Venice Inlet 8 kilometers to the south.
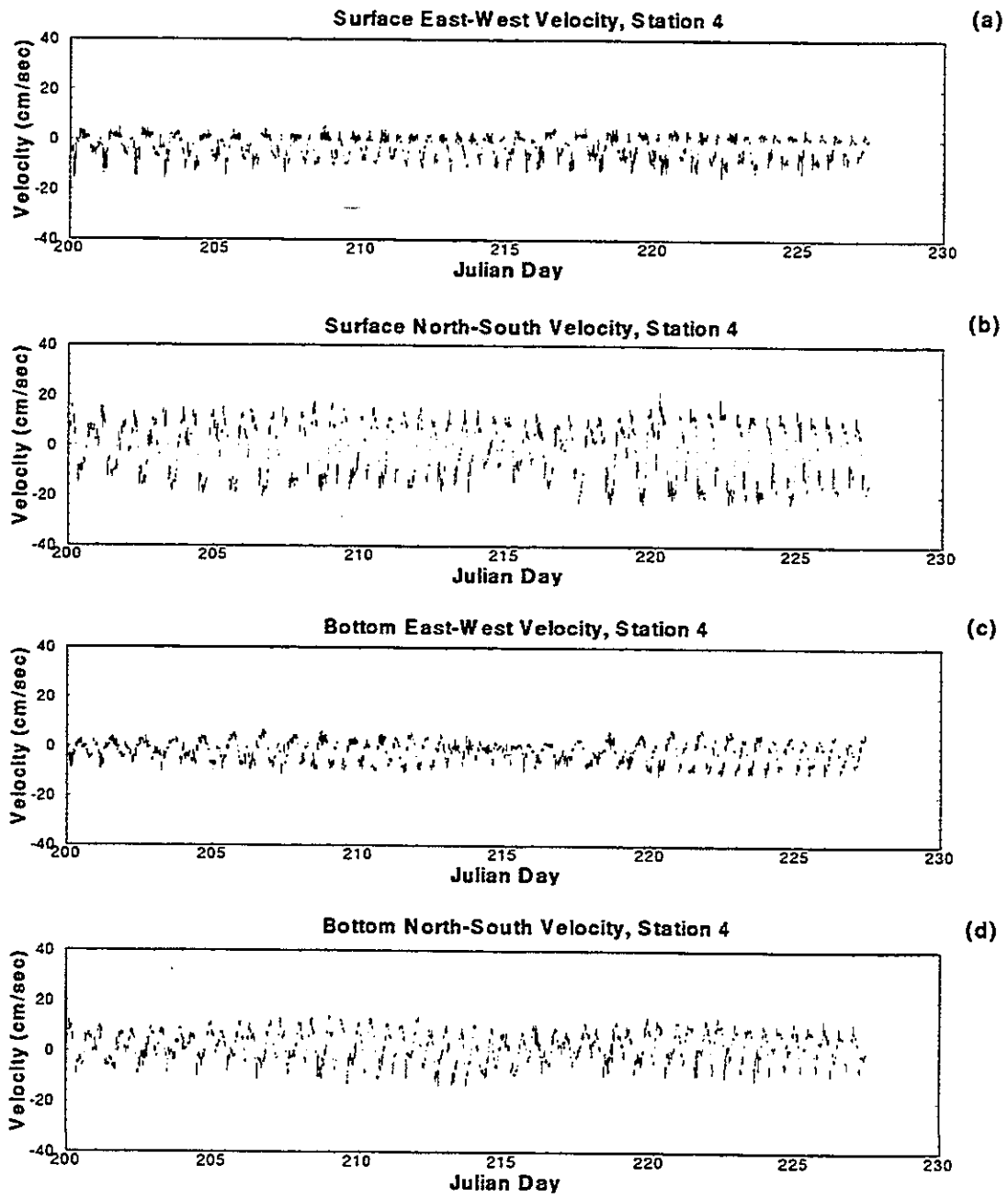
Figure 4.9: The current vector components measured from Julian Day 200 to 230, 1991 at UFL-B4. a) Surface East-West Velocity; b) Surface North-South Velocity; c) Bottom East-West Velocity; d) Bottom North-South Velocity.

The velocity components presented in Figure 4.9 show the influence of Venice Inlet on the flows. Current magnitudes are as high as 25 to 30 cm/sec during neap conditions. The residual velocities in the surface meter are not considered reliable due to a calibration problem with the surface north-south component on the sensor. The residual velocities measured at the bottom show -1.8 cm/sec in the east-west and 2.2 cm/sec in the north-south. The resultant vector is a 2.8 cm/sec residual at 319 degrees.

Although Stations UFL-B3 and UFL-B4 were in nearly identical bathymetric conditions, and sensor elevations were identical, the vertical variations in velocity were different. Visual comparison of the surface and bottom velocity components for both stations indicates that UFL-B4 does not have as high a vertical velocity gradient. This supports the assertion made earlier that the bottom boundary layer at Station UFL-B3 may be laminar (due to the low velocity conditions) as versus turbulent at UFL-B4. A more quantitative analysis of this phenomena will be made in Section 4.2.3 entitled "Harmonic Analysis of the Intertidal and Intratidal Frequency Bands".

Wind Data

Figure 4.10 presents the measured east-west and north-south components of the wind speed for the 1990 and 1991 data periods. The 1990 data were obtained from a permanent weather station positioned atop the Sunshine Skyway Bridge in the middle of Tampa Bay. This station is maintained by NOAA. The University of Florida stations were not installed during this period and therefore no wind measurements were available for Sarasota Bay. The 1991 data were taken from the winds measured at UFL-B3. The measured winds from UFL-B1, UFL-B2, and UFL-B4 are presented in Appendix B.

Visual examination of the plots shows the difference in the wind conditions between the summer months and the fall. During the summer (bottom plots) the winds are dominated by the sea breeze which is caused by the relative heating of the land
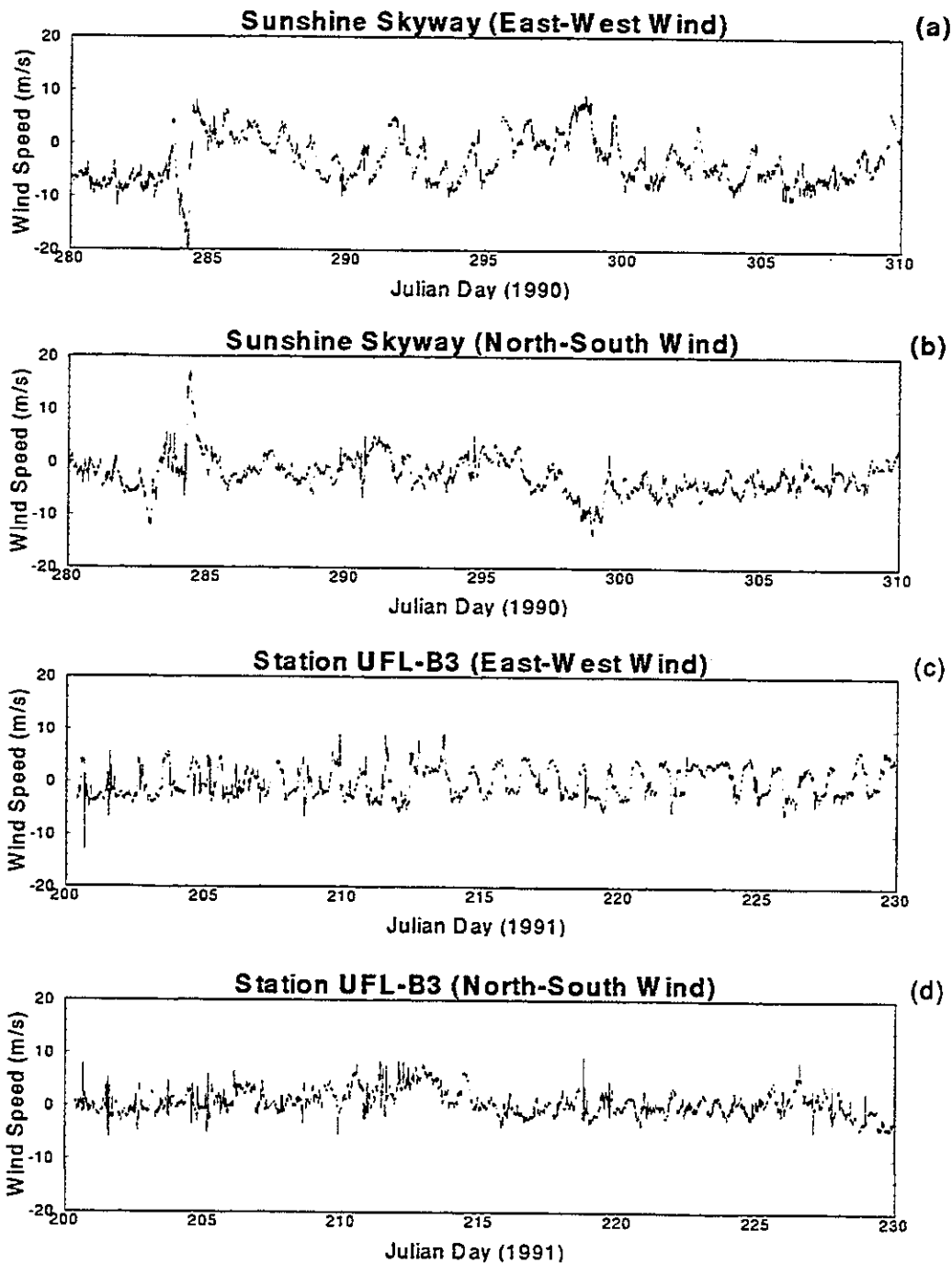
Figure 4.10: The wind velocity vector components. a) East-west component measured at the Sunshine Skyway (Julian Day 280 to 310, 1990); b) north-south component measured at the Sunshine Skyway (Julian Day 280 to 310, 1990); c) east-west component measured at UFL-B3 (Julian Day 200 to 230, 1991); d) north-south component measured at UFL-B3 (Julian Day 200 to 230, 1991).

mass versus the waters of the Gulf. The shoreline along Sarasota Bay is oriented nearly north-south therefore the sea breezes are most pronounced in the east-west wind components. Typical conditions during the summer have the wind coming out of the east during the late evening and early morning hours, switching over to the west during the daytime. The fall season (top plots) also shows sea breezes, but superimposed upon this are the effects of frontal systems. As fronts begin to propagate as far south as Sarasota, the wind becomes dominated by these systems creating sustained wind from one direction over several days.

Around day 284 in 1990, tropical storm Marco passed by Sarasota and Tampa Bays. The storm moved into the Gulf of Mexico and ran along the coastline just offshore over a period of 8 to 10 hours. The eye of the storm remained just offshore as the storm passed, and the resulting winds are clearly seen in the 1990 measurements taken at the Skyway Bridge.

4.2.2 Spectral Analysis of Tides, Currents and Wind

The first step in the decomposition of the water surface elevations and the currents is to define where the energy within each of the signals resides. This is accomplished through spectral analysis. The spectral density is a measure of the energy of a given signal within a specific frequency band.

Analysis Method

Fourier Analysis was performed upon the water surface elevation, current, and wind data to determine the variance or spectral density. The total variance (area under the spectral density curve) represents the total energy of the signal. Therefore the breakdown of the spectral density as a function of frequency will define the relative energies within each frequency band.

The basic idea of Fourier analysis is that any function may be represented as the sum of a series of sines and cosines of frequencies which are multiples of a fundamental

frequency $\sigma = (2\pi/M\Delta t)$. The series can be expressed in equation form as:

$$X(t) = Z_0 + \sum_{m=1}^{M/2} A_m cos(m\sigma t) + \sum_{m=1}^{M/2} B_m sin(m\sigma t) \qquad (4.2)$$

where, A_m and B_m may be determined by evaluating M values of $X(t)$ sampled at a constant interval Δt. Once these values are determined the variance can be calculated for each frequency band.

The data analysis program MATLAB was utilized to develop the power spectra or spectral density curves. For this application the data consisted of 60 days of measurements taken at 15 minute intervals, therefore each data set contained 5760 discrete samples. In calculating the spectral density, MATLAB utilizes Welch's method which performs an FFT transformation over a series of overlapping or non-overlapping data sets (Krauss, Shure and Little, 1993). For this study, it was desired to resolve the spectral densities at frequencies as low as 0.1 cycles per day (10 day period). To accomplish this, data sets of 2048 points were analyzed with sufficient overlap to cover the entire 60 days of data. The data sets were demeaned and broken into 3 statistically independent sets of 2048 each. The sets overlapped each other by 200 data points. This methodology was utilized in all the subsequent spectral analyses.

One note on the use of the MATLAB spectral analysis subroutines is that due to internal non-dimensionalization, which occurs within the MATLAB subroutines, the absolute energy levels are not calculated. These can be corrected, but for this study the energies were only utilized in a relative sense to determine the distribution of the spectral energies. Therefore so long as the data sets compared are at identical sampling intervals and durations the non-dimensionalization may be ignored when performing comparative analyses.

Spectral Analysis of Water Surface Elevation Data

Figures 4.11 and 4.12 present plots of the spectral density function for three of the USGS tidal stations during the 1990 and 1991 data periods. The stations plotted represent a transition from conditions at an inlet (USGS-05) to a station well
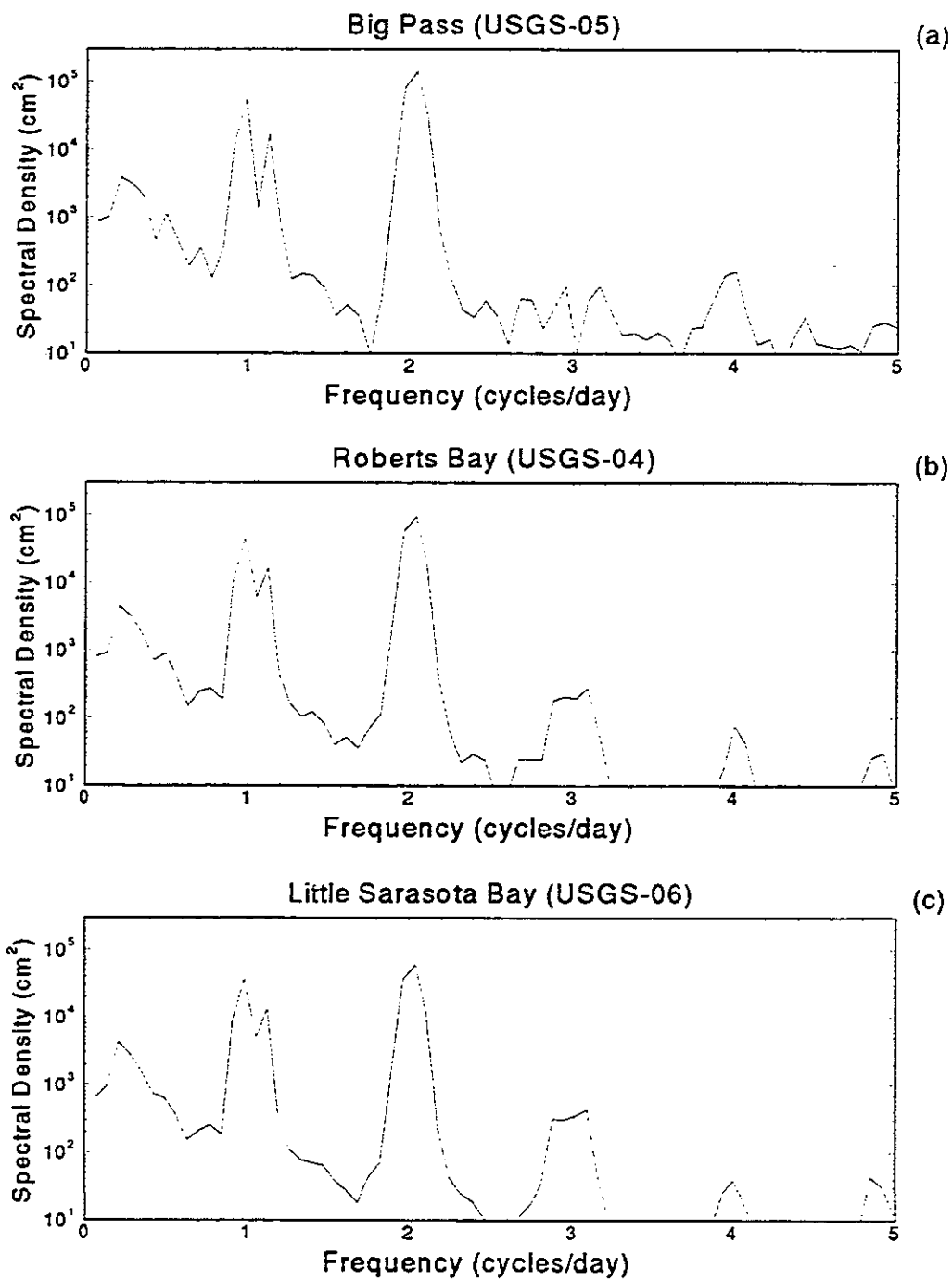
Figure 4.11: Spectral density of water surface elevations measured from Julian Day 255 to 315, 1990. a) USGS-05; b) USGS-04; c) USGS-06

Big Pass (USGS-05)

(a)

Roberts Bay (USGS-04)

(b)

Little Sarasota Bay (USGS-06)

(c)
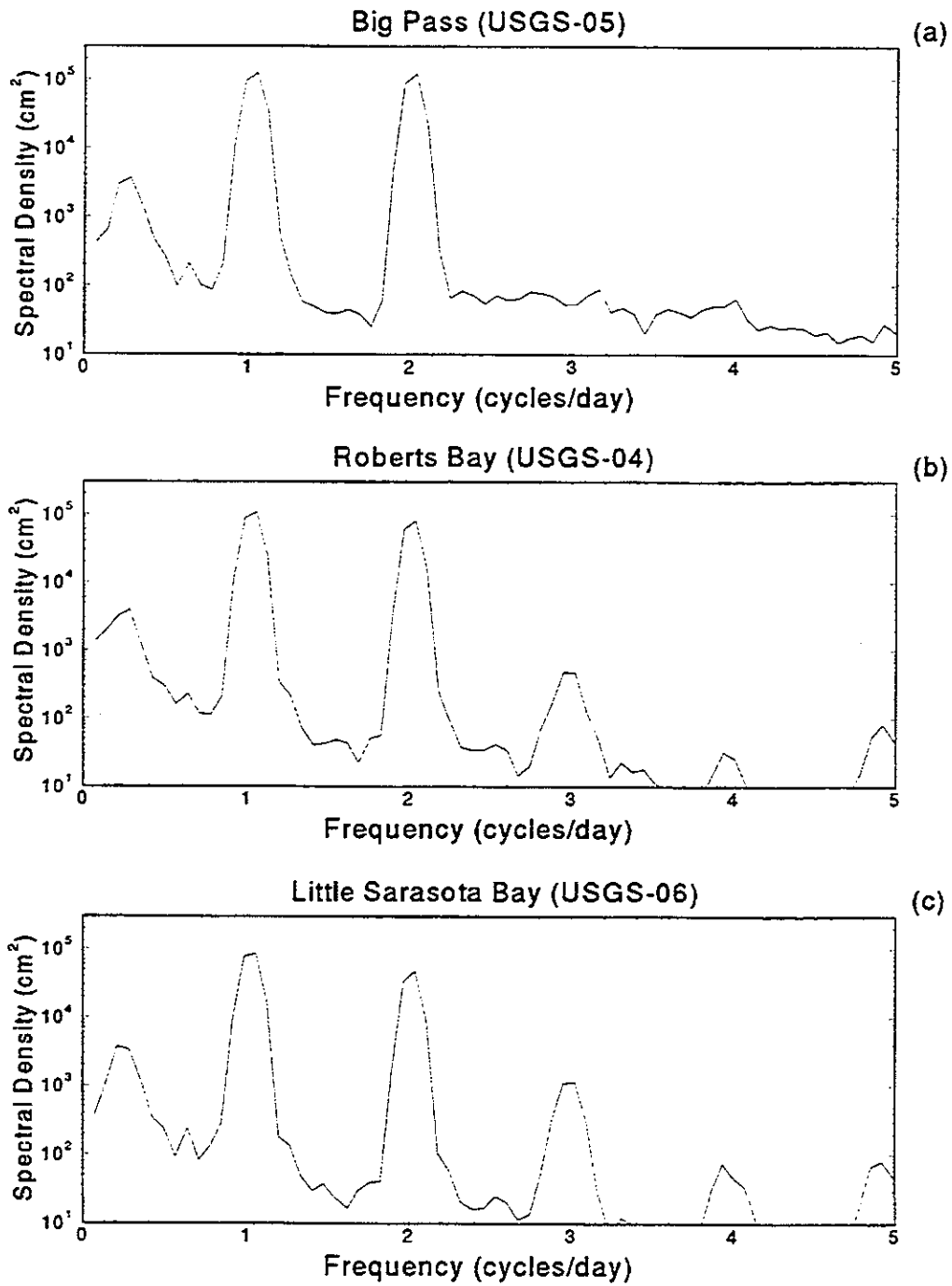
Figure 4.12: Spectral density of water surface elevations measured from Julian Day 200 to 260, 1991. a) USGS-05; b) USGS-04; c) USGS-06

inside the system far from any inlet (USGS-06). The Roberts Bay station (USGS-04) represents the transition region. The spectral density functions for all other stations are presented in Appendix B.

The data exhibit three primary energy bands and three secondary energy bands. The primary bands occur below 0.5 cycles per day (greater than 2 day period), 1 cycle per day (1 day period) and 2 cycles per day (12 hour period). The term subtidal will be applied to those frequencies below 0.5 cycles per day (Wong and Garvine, 1984) as these are outside of the classic diurnal/semi-diurnal tidal periods. The other two primary energy bands surround the diurnal and semi-diurnal harmonic constituents, these are termed intertidal frequencies. The three bands are primary because they are not generated locally (for the most part) but propagate into the system from the Gulf of Mexico.

The secondary bands occur around 3 cycles per day (8 hour period) and 4 cycles per day (6 hour period), and are termed respectively the third and fourth-diurnal. These higher frequency signals are weak in the offshore but increase in magnitude traveling into the lagoons. They are generated by the non-linear interaction between the primary harmonic constituents (Pugh, 1987). These "intratidal" frequency bands or "overtides" are generated locally and do not propagate in through the inlets.

The area under the spectral density curve represents the total energy within the signal. Concurrently, the area under the curve within the individual energy bands represents the energy within that particular range. Utilizing the range of frequencies over which the harmonic constituents within a particular band are found to define the frequency ranges (Pugh, 1987), the relative energy within the primary and secondary bands are determined. The subtidal band is defined as ranging from 0 to 0.5 cycles per day, the diurnal band is defined from 0.8 to 1.2, the semi-diurnal from 1.8 to 2.2, the third-diurnal from 2.8 to 3.2 and the fourth-diurnal from 3.8 to 4.2.

Tables 4.1 and 4.2 present the distribution of energy found in the 1990 and 1991

Table 4.1: The distribution of tidal energy across the primary and secondary frequency bands, 1990 data

Station	Total Energy $cm^2 - s$	Sub Tidal percent	Diurnal percent	Semi Diurnal percent	Third/Fourth Diurnal percent	Percent Total
USGS-01	26941.5	3.0	22.6	72.6	1.0	99.2
USGS-02	23432.9	4.4	24.0	69.5	.8	98.8
USGS-03	23677.4	3.3	24.1	70.4	1.1	98.9
USGS-04	19533.1	4.7	26.9	66.5	.5	98.6
USGS-05	25398.8	3.2	23.7	71.4	.6	98.9
USGS-06	13481.7	6.3	31.4	60.0	.8	98.5
USGS-07	12996.1	5.6	31.6	60.9	1.0	99.1

Table 4.2: The distribution of tidal energy across the primary and secondary frequency bands, 1991 data

Station	Total Energy $cm^2 - s$	Sub Tidal percent	Diurnal percent	Semi Diurnal percent	Third/Fourth Diurnal percent	Percent Total
NOAA-O1	50578.0	.8	52.2	46.1	.5	99.6
UFL-O1	48090.5	.9	53.8	44.2	.5	99.5
UFL-O2	42795.8	.8	54.3	43.6	.6	99.3
USGS-04	28392.2	2.5	56.8	39.4	.4	99.1
USGS-05	35738.2	1.8	51.3	45.6	.3	99.0
USGS-06	20825.6	3.2	64.0	30.9	1.3	99.3
USGS-07	19870.0	3.0	60.5	35.3	.3	99.1

water surface elevations. The tables list the station locations, the total energy (area under the spectral density curve) and the percent energies within each of the frequency bands. The final number is the percent of the total energy accounted for by adding the sub-tidal, diurnal, semi-diurnal and the third/fourth diurnal energy percentages.

It is important to note that although the frequency bands are defined based upon the tidal harmonics (i.e. gravitational forcing) all of the energy within the band may not be forced by gravity. Meteorological forcings with associated frequencies may contribute to the energy.

Within the Primary Bands, damping of the tidal wave as it propagates from the offshore into the lagoons is highly dependent upon the associated frequency. Smith (1980) showed that tidal inlets act as low pass filters. This can be carried one step further and shown that restrictions within the lagoons also act as low pass filters, and as the wave moves further into the lagoons the energies in the higher frequencies are damped. This trend can be seen from the spectral analysis of the 1990 and the 1991 tidal data (Tables 4.1 and 4.2). The data show a decrease in the semi-diurnal percentages going from USGS-05 to USGS-04 as well as from USGS-04 to USGS-06. Coincident with this decrease in the semi-diurnal energy is an increase in the diurnal and sub-tidal energy percentages. Going from USGS-05 to USGS-04 to USGS-06 represents movement from within an inlet further into the lagoons.

Comparison of the 1991 offshore data indicates that the tidal energy lessens from north to south with the Tampa station showing the highest energy. This will affect the interior stations as each is influenced by different inlets along the barrier islands. For instance, the total energy at Blackburn Bay (USGS-07) is lower than the total energy at Little Sarasota Bay (USGS-06). This result is unexpected based upon the location of the two stations relative to their nearest forcings. The most likely explanation is that the wave propagating in through Venice Inlet has less energy than that passing through Big Pass. As these two waves combine to create the tides at Little Sarasota Bay, the tides at Little Sarasota Bay are higher. Additionally, the total energy at the station inside of Anna Maria Sound which is forced from Longboat Pass and Tampa Bay is higher than that found within Big Pass. Were the offshore forcings constant, this result would not be expected due to damping of the wave prior to reaching Anna Maria Sound.

The energy residing in the secondary bands (Third/Fourth Diurnal) were combined as they are relatively insignificant in comparison to the energies in the primary bands. The data do indicate an increase within those bands at the more interior sta-

tions as compared with offshore and at the inlets. A more in-depth analysis of these components will occur in the section entitled "Harmonic Analysis of the Intertidal and Intratidal Frequency Bands".

Spectral Analysis of Current Data

Spectral analysis of the currents presents more difficulty as they are vector quantities and contain direction as well as magnitude. For the purpose of the analyses, the velocity vectors were broken into their east-west and north-south components. For comparison Figure 4.13 presents the spectral density plots for the surface north-south components at each of the four UFL stations. These components contained the highest level of energy at all four stations. The remaining spectral plots are included in Appendix B.

The currents show energies in similar frequency bands as the tides with the exception of the subtidal component. All of the stations show energies in the secondary bands as well as the primary bands. As energy is a scalar quantity, it is possible to total the east-west and north-south components in order to define the total at each station. Table 4.3 lists the total energy for both the bottom and surface currents, along with the percent contained within each frequency band and the percent of the total energy captured in the five frequency bands.

Looking first at the primary bands, two of the stations exhibit higher percent energies in the sub-tidal than the other two. Stations UFL-B1 and UFL-B3 show from 2 to 8 percent sub-tidal energy, while UFL-B2 and UFL-B4 exhibit less than 1 percent sub-tidal in all of the components. These similarities between stations extend also to the distribution of the diurnal and semi-diurnal energies. Stations UFL-B1 and UFL-B3 show a more even distribution of energy between the diurnal and semi-diurnal, while UFL-B2 and UFL-B4 show a much higher percent energy within the semi-diurnal.

In Chapter 2, results from a study by Seim and Sneed (1988) were discussed
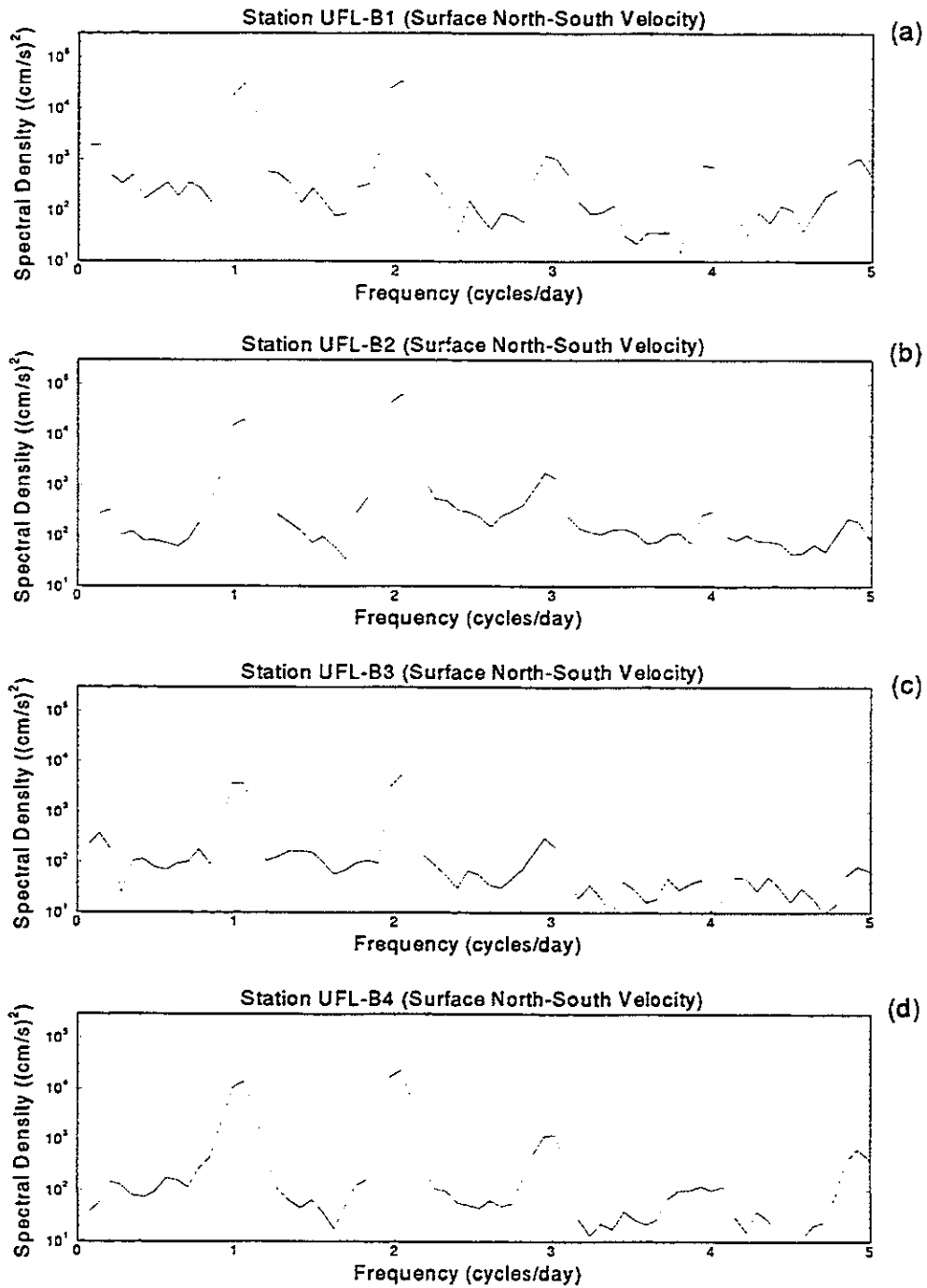
Figure 4.13: The spectral density of the measured surface north-south current components measured from Julian Day 200 to 260, 1991. a) UFL-B1; b) UFL-B2; c) UFL-B3; d) UFL-B4.

Table 4.3: The distribution of current energy ($(cm/sec)^2 - sec$) across the primary and secondary frequency bands, 1991 data (values in parenthesis represent percentage)

Station	Sensor Height	Total Energy	Sub Tidal	Diurnal	Semi Diurnal	3rd/4th Diurnal	Percent Total
UFL-B1	Bottom	6726.3	2.4	37.0	40.6	11.5	91.5
	Surface	11900.1	2.0	37.2	42.4	8.7	90.2
UFL-B2	Bottom	7042.4	.8	18.9	66.6	8.3	94.6
	Surface	13679.3	.5	23.3	65.7	4.9	94.5
UFL-B3	Bottom	750.1	6.6	25.1	25.9	13.7	71.3
	Surface	2174.5	7.7	33.1	34.5	6.4	81.8
UFL-B4	Bottom	2683.6	.8	21.5	53.6	16.8	92.8
	Surface	7254.2	.7	32.2	51.8	7.2	92.0

which showed that inlets act to increase the semi-diurnal nature of currents entering barrier island lagoons due to a transformation from a 2-D rotational flow (offshore) to a 1-D unidirectional flow (within an inlet). The two stations which show the highest percent of semi-diurnal energy (UFL-B2 and UFL-B4) share one common feature the other two do not, the forcing for these come primarily from a single direction. UFL-B2 from New Pass and Big Pass to the south and UFL-B4 from Venice Inlet to the south. Additionally, UFL-B2 and UFL-B4 are closer to the inlet forcings. The high percent energies in the semi-diurnal may be a residual influence from the passing of the flow through the inlets. Seim and Sneed also showed that traveling further into the lagoon the energy distribution begins to shift back toward the diurnal. This along with the damping may explain the energies found at UFL-B1 and UFL-B3.

UFL-B2 and UFL-B4 share one other common characteristic, their percent total energies contained within the four frequency bands are higher than UFL-B1 and UFL-B3, with UFL-B3 (the most interior station) showing the lowest total percentage.

The results for the secondary bands show that the currents experience greater influence from the non-linear interactions than seen in the tides. Percentages range from 4.9 to 16.8 in contrast to 0.1 to 1.3 for the tides. Examination of the vertical distribution of the energy shows that for all of the stations the percent energy in the
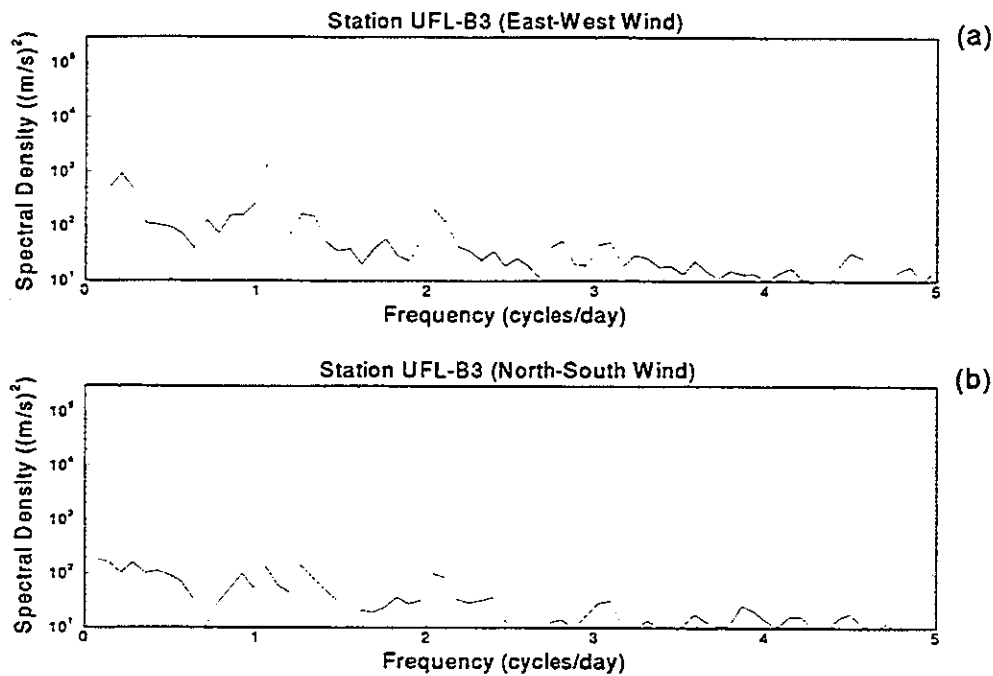
Figure 4.14: Spectral density of the measured wind speed components from Julian Day 200 to 260, 1991 at UFL-B3. a) East-west component; b) north-south component.

secondary bands is highest for the currents nearer to the bottom. Studies presented in Chapter 2 described the primary mechanism driving non-linear interaction as bottom friction (Speer and Aubrey, 1985, Aubrey and Friedrichs, 1988, Freidrichs and Aubrey, 1988, Speer, Aubrey and Friedrichs, 1991). The higher percentages in the bottom measurements support this assertion.

Spectral Analysis of Wind Data

Figure 4.14 presents the spectral density functions for the measured wind components at Station UFL-B3. The data from all four of the UFL Stations showed similar spectrums with only minor differences. The east-west winds reflect the sea-breeze with a peak in the spectral density at 1 cycle per day. The sub-tidal portion exhibits a peak similar to that found in the tidal data and indicates some possible correlations. The wind energy and its correlation to the currents and tides will be examined further

in the section 4.2.4 entitled "Analysis of Sub-Tidal Tides and Currents".

4.2.3 Harmonic Analysis of Tides and Currents

In the proceeding section the distribution of energy between the sub-tidal, diurnal, semi-diurnal and the third/fourth diurnal were determined. In this section harmonic analysis will be performed upon the water surface elevation and current data to isolate the gravitational portion of the diurnal, semi-diurnal and third/fourth diurnal frequency bands.

Harmonic analysis is the process of representing the gravitational portion of a signal using a finite number of N terms of the form:

$$T_n = H_n cos(\sigma_n t - \delta_n) \qquad (4.3)$$

where, H_n is the amplitude, δ_n is the phase lag of the tide referenced to a specific time datum (usually Greenwich) and σ is the angular frequency of the harmonic. An inherent assumption in harmonic analysis is that the mechanisms (or planetary interactions) which create each component are known prior to the analysis, and the task is to isolate chosen components from the signal.

A harmonic analysis program which utilizes least squares fitting was applied to the data. The program creates a fit between the measured data and equation 4.3 with H_n, g_n and σ_n as the unknowns. The least squares fitting is adjusted so that the square of the difference between the observed and computed tide levels, when summed over all the observed values, has its minimum value. In all of the cases the data are demeaned and detrended over the period of record prior to analysis.

The number of harmonic constituents to be analyzed is dependent upon the length of the data record. In general, the longer the data record, the greater the number of constituents which may be independently determined. A criteria for determining the amount of data required to resolve two harmonic constituents states that, only constituents separated by at least a complete period from their neighboring constituents,

Table 4.4: A list of the harmonic constituents analyzed

Constituent	Period(hours)	Origin
M_2	12.42	Principal Lunar (Semi-Diurnal)
S_2	12.00	Principal Solar (Semi-Diurnal)
N_2	12.65	Larger Elliptical Lunar
K_1	23.93	Principal Solar/Lunar (Diurnal)
O_1	25.82	Principal Lunar (Diurnal)
MO_3	8.39	Non-linear Interaction (M_2, O_1)
MK_3	8.18	Non-linear Interaction (M_2, K_1)
M_4	6.21	Non-linear Interaction (M_2)

over the length of data, should be analyzed (Pugh, 1987). For example, in order to determine the M_2 and S_2 tides independently, the number of days of data required is:

$$\text{No. of days} = \frac{1.0}{\left(\frac{1}{12.42} - \frac{1}{12.00}\right)} * 24.0 = 14.7 \text{days} \qquad (4.4)$$

The list of potential harmonic constituents is lengthy and contains over 1000 possibilities. These range from the solar annual with a period of 364.96 days to the shallow water harmonic constituents which are generated by the non-linear interaction of the primary harmonics. Applying Equation 4.4, a list of six primary constituents and three secondary constituents was determined (Table 4.4). The list is relatively short due to the length of the data record (60 days). Tidal data were available to allow a greater number to be analyzed, but the current data were limiting and test runs indicated that the components listed in Table 4.4 contained over 98 percent of the energy.

Harmonic Analysis of the Water Surface Elevation Data

Tables 4.5 and 4.6 present the harmonic constituent amplitudes and phase lags for the 1990 and 1991 tidal data. The harmonic analyses were performed on 60 days of data starting Julian Day 255 in 1990 and Julian Day 200 in 1991. In the calculation of the phase lags for both the 1990 and 1991 data, time zero was 00:00:00 EST in 1990.

Table 4.5: The harmonic constituents calculated from the 1990 tidal data

Amp. (cm)	USGS 01	USGS 02	USGS 03	USGS 04	USGS 05	USGS 06	USGS 07
M_2	16.9	15.3	15.5	13.7	16.3	10.8	11.1
S_2	8.0	7.0	7.1	6.1	7.6	4.9	5.0
N_2	3.4	3.4	3.3	3.3	3.6	2.1	2.2
K_1	9.9	9.3	9.9	9.2	9.4	8.6	8.3
O_1	15.9	14.8	15.0	14.3	15.5	13.1	13.3
MO_3	.8	1.6	1.9	1.1	.4	1.4	.4
MK_3	.3	.8	.8	.6	.3	.7	.2
M_4	.7	.3	.6	.1	.4	.2	.4
Phase Lag (deg)							
M_2	79.4	96.5	97.7	93.9	60.6	135.6	83.5
S_2	22.2	38.1	39.6	37.2	.6	78.3	24.6
N_2	-.9	24.5	22.8	11.7	-21.6	66.3	4.8
K_1	-55.5	-45.0	-43.5	-48.0	-65.1	-22.7	-48.7
O_1	29.1	41.3	41.1	38.9	21.5	62.6	36.9
MO_3	-43.8	30.0	31.8	39.9	-73.4	90.1	-93.2
MK_3	-166.9	-96.0	-82.8	-92.5	147.9	-5.3	129.4
M_4	-13.3	102.0	90.4	112.5	-102.6	-167.5	-43.5

Examination of the tidal constituent amplitudes provides further support to the findings made in the previous section. First, the 1991 offshore data (NOAA-01, UFL-02, UFL-O3) show a reduction in the tidal amplitudes traveling north to south. There is an 8 to 12 percent reduction in the semi-diurnal amplitudes and a 3 to 5 percent reduction in the diurnal amplitudes. This offshore variation manifests itself in the interior stations. For example, the tides at Anna Maria Sound show higher amplitudes than Big Pass which should be more reflective of offshore conditions. The tides at Blackburn Bay, which is just inside Venice inlet, show nearly identical amplitudes compared to Little Sarasota Bay which is much further inside.

Secondly, the spectral analysis showed that the inlets and the lagoons act as low pass filters by damping the higher frequency primary constituents. The results of the

Table 4.6: The harmonic constituents, 1991 tidal data

Amp. (cm)	NOAA O1	UFL O1	UFL O2	USGS 04	USGS 05	USGS 06	USGS 07
M_2	19.0	18.0	16.8	13.7	16.3	10.5	11.0
S_2	8.8	8.3	7.9	5.9	6.6	5.0	4.2
N_2	4.4	4.3	4.1	3.1	3.8	2.5	2.5
K_1	16.5	16.6	15.7	13.7	15.4	12.0	12.3
O_1	15.4	15.1	14.2	14.5	14.6	13.5	12.3
MO_3	.7	.9	.9	.7	.4	1.2	.6
MK_3	.2	.3	.2	.9	.3	1.3	.1
M_4	.5	.5	.5	.3	.1	.4	.2
Phase Lag (deg)							
M_2	25.3	16.8	25.2	57.7	29.3	107.5	53.9
S_2	-8.4	-18.6	-10.5	39.0	-.9	98.7	27.3
N_2	-77.7	-86.2	-76.2	-41.5	-72.8	6.8	-48.1
K_1	-59.8	-63.8	-59.7	-39.1	-57.9	-9.5	-41.4
O_1	2.9	-1.7	1.7	23.0	4.6	54.2	25.2
MO_3	-174.4	-177.7	-169.1	-23.2	-161.8	59.2	-169.1
MK_3	175.9	-174.3	-166.9	-25.5	-37.9	34.3	105.7
M_4	-119.4	-129.8	-107.2	63 .2	-140.9	155.9	-82.3

harmonic analyses allow further quantification of that damping through comparison of the form numbers (equation 2.1). As stated in Chapter 2, the form number is the ratio of the amplitudes of the two primary diurnal constituents (K_1 and O_1) to the two primary semi-diurnal constituents (M_2 and S_2). An increase in the form number indicates a shift in the energy distribution from the semi-diurnal to the diurnal constituents.

Figure 4.15 present the form numbers plotted for each station for the 1990 and 1991 data periods. The stations are ordered on the x-axes such that they become more interior (i.e. further from an inlet) moving from left to right. For the 1990 data, the values range from 0.92 offshore up to 1.38 within Little Sarasota Bay, while for the 1991 data they range from 1.15 in the offshore up to 1.68 within Little Sarasota

Bay. The filtering of the tidal wave is clearly evident in the plots; there is a shift from 0.92 to 1.04 from the offshore to Big Pass in 1990 and from 1.15 to 1.31 in 1991.

The higher magnitudes of the form numbers in the 1991 data period reflect the long term variations in the gravitational forcing mechanisms driving the tides within the Gulf of Mexico. These variations impact the percent shift in the energy distribution between the diurnal and semi-diurnal constituents. Comparison of the change in the form numbers between Big Pass and Little Sarasota Bay shows a 26 percent shift for the 1991 data and a 34 percent shift for 1990. When the higher frequency components represent a larger portion of the signal (as in the 1990 data period) the shift in the energy distribution is greater.

Harmonic analysis provides further quantification of the overtides through the calculation of the amplitudes of the non-linear constituents. Along coastlines where the primary harmonic is the M_2 tide, a measure of the degree of non-linear interaction is the M_4/M_2 amplitude ratio. Consequently, along a coastline which has mixed tides, such as the Gulf of Mexico, a similar ratio can be defined which compares the third diurnal components with the three primary components which interact to create them. An overtide ratio can be defined as;

$$\frac{(MO_3 + MK_3)}{(M_2 + O_1 + K_1)} \tag{4.5}$$

The third diurnal components are combined in order to eliminate any errors due to leakage during the harmonic analysis. Leakage is where a portion of the energy which exists in one component is mistakenly transferred to another with nearly the same frequency.

Figure 4.15 presents plots of the overtide ratios for the 1990 and 1991 data. The calculated ratios range from 0.01 at Big Pass to 0.08 in Little Sarasota Bay. These are similar to values calculated for the M_2/M_4 ratio in other studies (Boon, 1988).

Examining the trends in the form number plots versus the trends in the overtide ratio plots provides insight into the mechanisms altering the tidal wave. The over-
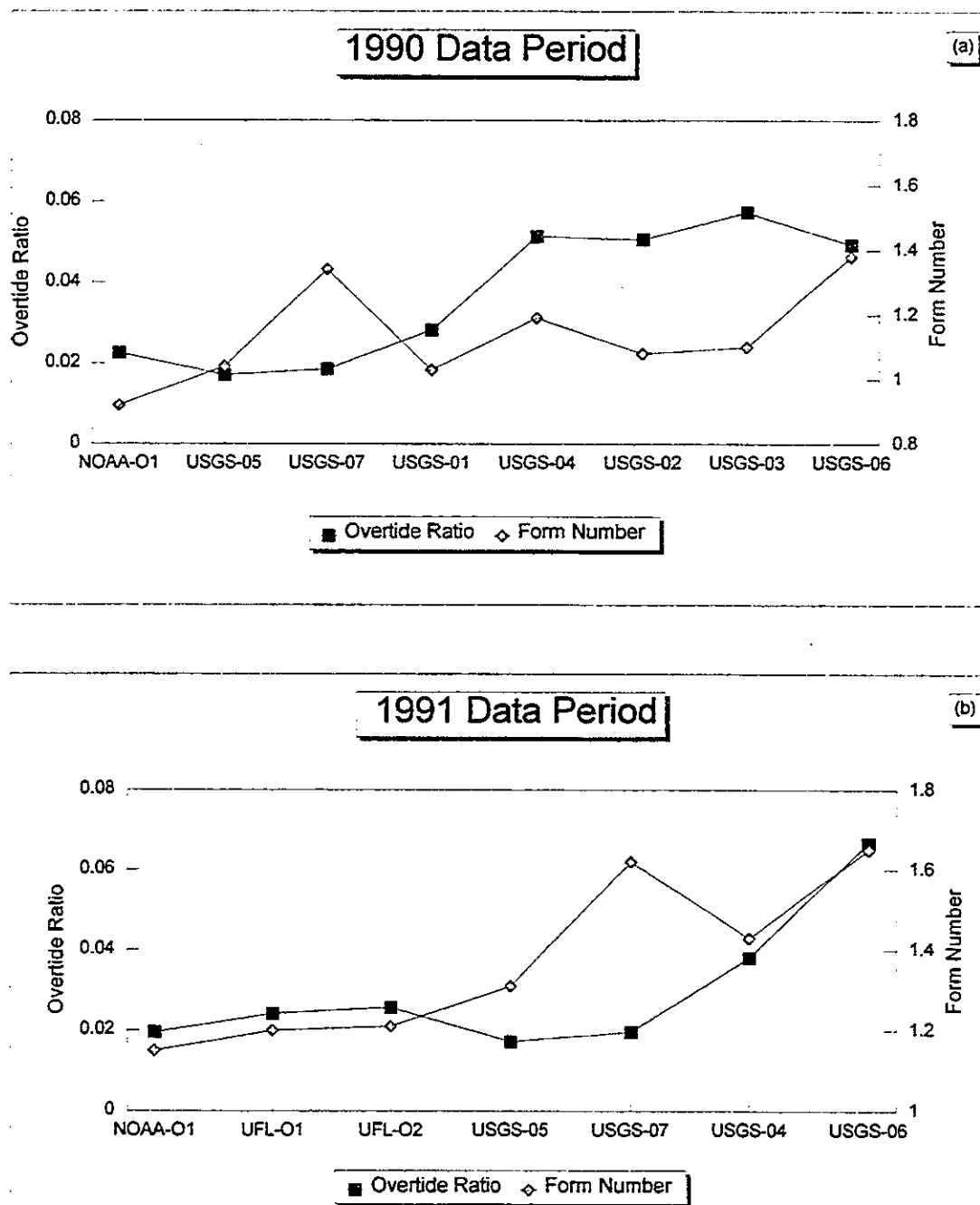
Figure 4.15: The Overtide Ratios and Form Numbers calculated from the measured water surface elevations. a) Julian Day 255 to 315; b) Julian Day 200 to 260.

tide ratios for both the 1990 and 1991 data show similar trends. The ratios decrease initially moving from the offshore through the inlets. The ratios begin to increase as the wave propagates further into the system with the maximum values at the most interior stations. The form numbers on the other hand appear to respond to restrictions within the system. Although the values increase moving further into the bay this increase appears to be due to the wave encountering additional restrictions. This phenomena is best illustrated by comparing station USGS-07 with stations USGS-02 and USGS-03. Station USGS-07 is near an opening to the Gulf of Mexico (Venice Inlet) but there are narrow restrictions leading to the station. USGS-02 and USGS-03 on the other hand are more interior but only the passes restrict the wave, the stations are in open water regions. USGS-07 has a high form number but a low overtide ratio while USGS-02 and USGS-03 have high overtide ratios but low form numbers.

The harmonic phases allow the determination of the travel time of the tidal wave. They also provide information on phase lags which may exist between the relative openings to the bay. This is important in the determination of residual flow patterns. In bodies of water with multiple inlets, a phase lag of the tidal wave arriving at one inlet relative to another can create a net flow. In Chapter 2, studies were presented which showed that within idealized multiple inlet systems a phase lag between the arrival of the tidal wave from one inlet to the other can create a net flow toward the lagging inlet (van de Kreeke and Dean, 1975, Fisher, 1979).

Comparing the phases of the two University of Florida offshore stations and the NOAA offshore station defines the progression of the tidal wave as it propagates within the Gulf of Mexico. Examination of Figure 3.1 shows that station UFL-O1 is located approximately 5 kilometers offshore between Longboat Pass and New Pass. Station UFL-O2 is located south of UFL-O1 approximately 4 kilometers offshore between Venice Inlet and Big Pass. Station NOAA-O1 is not shown on Figure 3.1 but is located approximately 10 kilometers off of the entrance to Tampa Bay north

of UFL-O1.

The data show that the tidal wave arrives first at Station UFL-O1 and nearly simultaneously at the two outer stations, UFL-O2 and NOAA-O1. This phase distribution does not support the residual flow measured at UFL-B1. Based upon the idealized studies presented in Chapter 2 (van de Kreeke and Dean, 1975) if a phase lag exists between two inlets a residual flow will develop toward the lagging inlet. Based upon the offshore phase distribution, the tides within Tampa Bay should lag behind Longboat Pass with an associated residual from Longboat toward Tampa Bay. It is difficult to directly connect this phase distribution with the residual flow because tide measurements were not taken directly north and south of UFL-B1, therefore the exact phase distribution on either side is unknown.

Harmonic Analysis of Current Data

Harmonic analysis of the currents presents more difficulty as they are vector quantities. In order to examine the tidal current harmonics it is standard practice to evaluate the harmonic ellipses. For an idealized current, taking the position of the head of the velocity vector and tracking throughout the tidal cycle with the base remaining in a constant position gives an ellipse. Harmonic analysis of the currents provides the magnitude of the principal major and minor axis lengths along with the orientation of the major axis for each harmonic constituent. From this data ellipses can be drawn which provide a visual representation of the characteristics of each current component. The following describes the results of the harmonic analysis of the currents for each station.

Station UFL-B1

Table 4.7 presents the harmonic ellipse components for Station UFL-B1. Figure 4.16 presents plots of the two primary semi-diurnal (M_2, S_2) and two primary diurnal (K_1 and O_1) harmonic ellipses for the surface and bottom currents.

Using the principal axis amplitudes for these constituents, a form number can be

Surface Velocity Harmonic Ellipses (a)

Bottom Velocity Harmonic Ellipses (b)
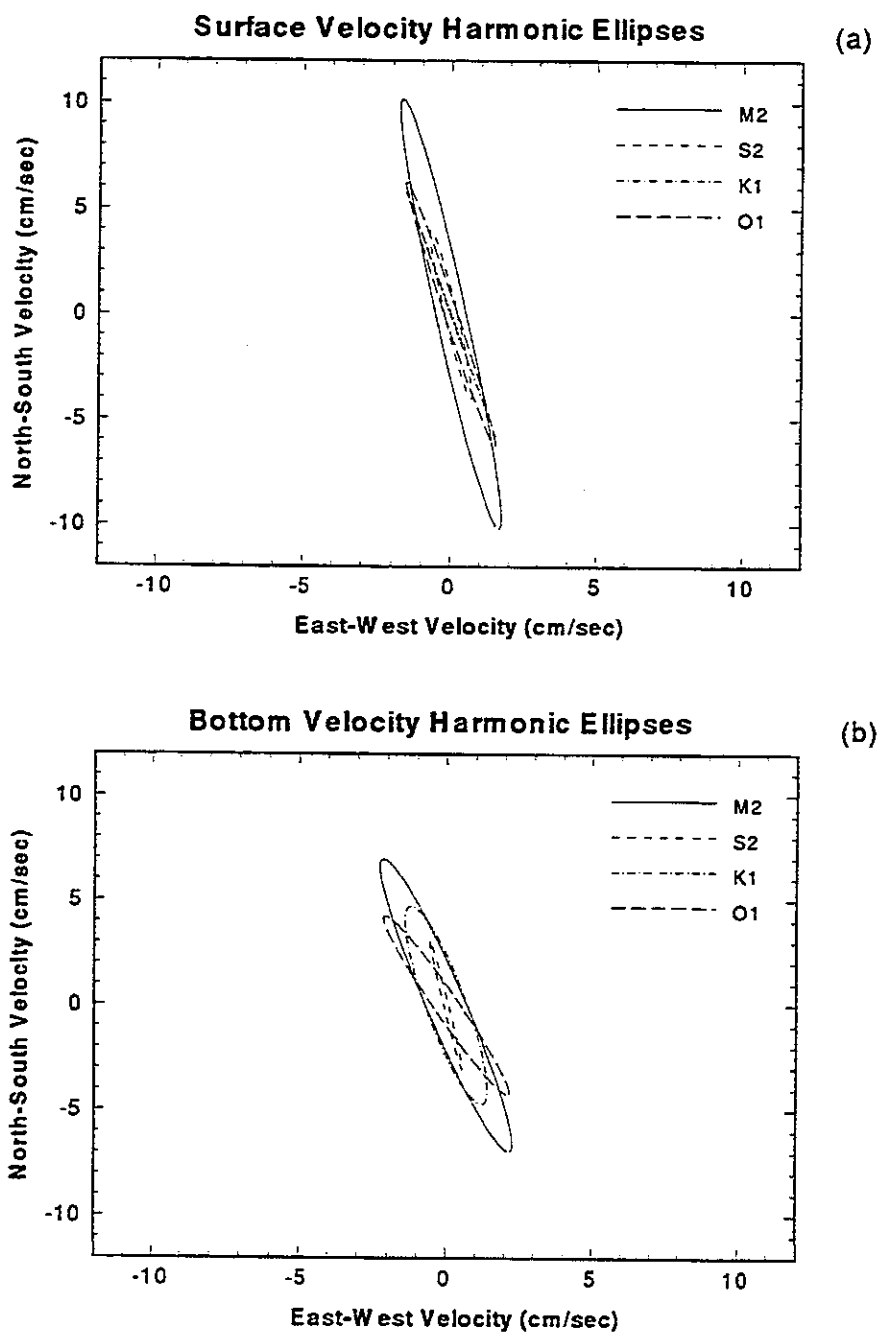
Figure 4.16: The primary harmonic ellipses at UFL-B1 for Julian Day 200 to 260, 1991. a) Surface velocities; b) bottom velocities.

Table 4.7: The principal axes harmonic constituent amplitudes, phases and axis directions for station UFL-B1, Julian Day 200 to 260

Sensor Location	Constituent	Major Axis (cm)	Minor Axis (cm)	Major Phase (hrs)	Major Angle (deg)
Bottom	M2	7.30	0.68	1.93	-72.7
	S2	3.13	0.08	-1.57	-79.5
	N2	1.59	0.16	1.14	-71.1
	K1	4.77	0.43	4.52	-73.8
	O1	4.83	0.43	0.82	-63.9
	MO3	1.43	0.20	-1.39	-62.2
	MK3	1.02	0.33	-0.27	-49.7
Surface	M2	10.34	0.52	1.77	-80.7
	S2	4.06	0.21	-1.78	-80.0
	N2	2.30	0.27	1.21	-82.8
	K1	6.35	0.02	4.80	-76.5
	O1	6.54	0.24	0.87	-76.2
	MO3	1.62	0.15	-0.92	-67.3
	MK3	1.22	0.08	-0.19	-64.3

calculated similar to those calculated for the tides. The form numbers are 0.92 and 0.90 for the bottom and surface currents. This calculation is not directly analagous to the tides because the minor axis component has been ignored. These values are lower than the lowest value calculated for the tides. This supports the assertion that the passage of the tidal wave from the offshore to the interior of the lagoons shifts the current energy from diurnal to semi-diurnal.

Overtide ratios for the currents can be similarly calculated using the data in Table 4.7. The values are 0.12 and 0.14 for the surface and bottom current components respectively. These values are higher than those calculated for the tides and agree with the findings of the spectral analysis which showed the currents to have much higher energy in the secondary frequency bands (higher harmonics). In addition, the data show a slight increase in the overtide ratios calculated for the bottom currents, this also supports the findings from the spectral analysis, and the assertion of bottom

Table 4.8: The principal axes harmonic constituent amplitudes, phases and axis directions for Station UFL-B2, Julian Day 200 to 260

Sensor Location	Constituent	Major Axis (cm)	Minor Axis (cm)	Major Phase (hrs)	Major Angle (deg)
Bottom	M2	9.48	0.74	2.05	-85.2
	S2	4.37	0.25	-1.80	-90.4
	N2	1.89	0.23	2.24	-86.3
	K1	3.68	0.48	2.43	-91.5
	O1	4.41	0.07	0.74	-91.4
	MO3	1.28	0.26	0.67	-74.3
	MK3	0.95	0.16	-1.47	-68.3
Surface	M2	13.7	0.69	2.31	-86.1
	S2	5.82	0.42	-1.66	-83.9
	N2	2.61	0.30	2.51	-84.7
	K1	5.89	0.07	3.39	-80.1
	O1	6.87	0.17	1.36	-82.6
	MO3	1.46	0.42	0.43	-76.0
	MK3	1.10	0.16	-1.59	-85.2

friction as the primary driving mechanism for the higher harmonics.

The directions of the principal axes indicate that there is a slight clockwise rotation in the current directions moving from the bottom to the surface. The surface currents align more with the overall direction of the channel, while the bottom currents flow slightly toward the deeper channel directly to the east of the platform.

The phases indicate that, for the primary harmonic constituents, the surface currents proceed the bottom currents. This is found for both the dirunal and semi-dirunal constituents. This lag is on the order of 10 to 15 minutes. For the secondary harmonics this trend is reversed, with the bottom higher harmonics leading the surface. This is as expected given that the primary mechanism creating the higher harmonic amplitudes is the bottom friction.

Station UFL-B2

Table 4.8 presents the harmonic ellipse components for Station UFL-B2. Figure

Surface Velocity Harmonic Ellipses (a)

Bottom Velocity Harmonic Ellipses (b)
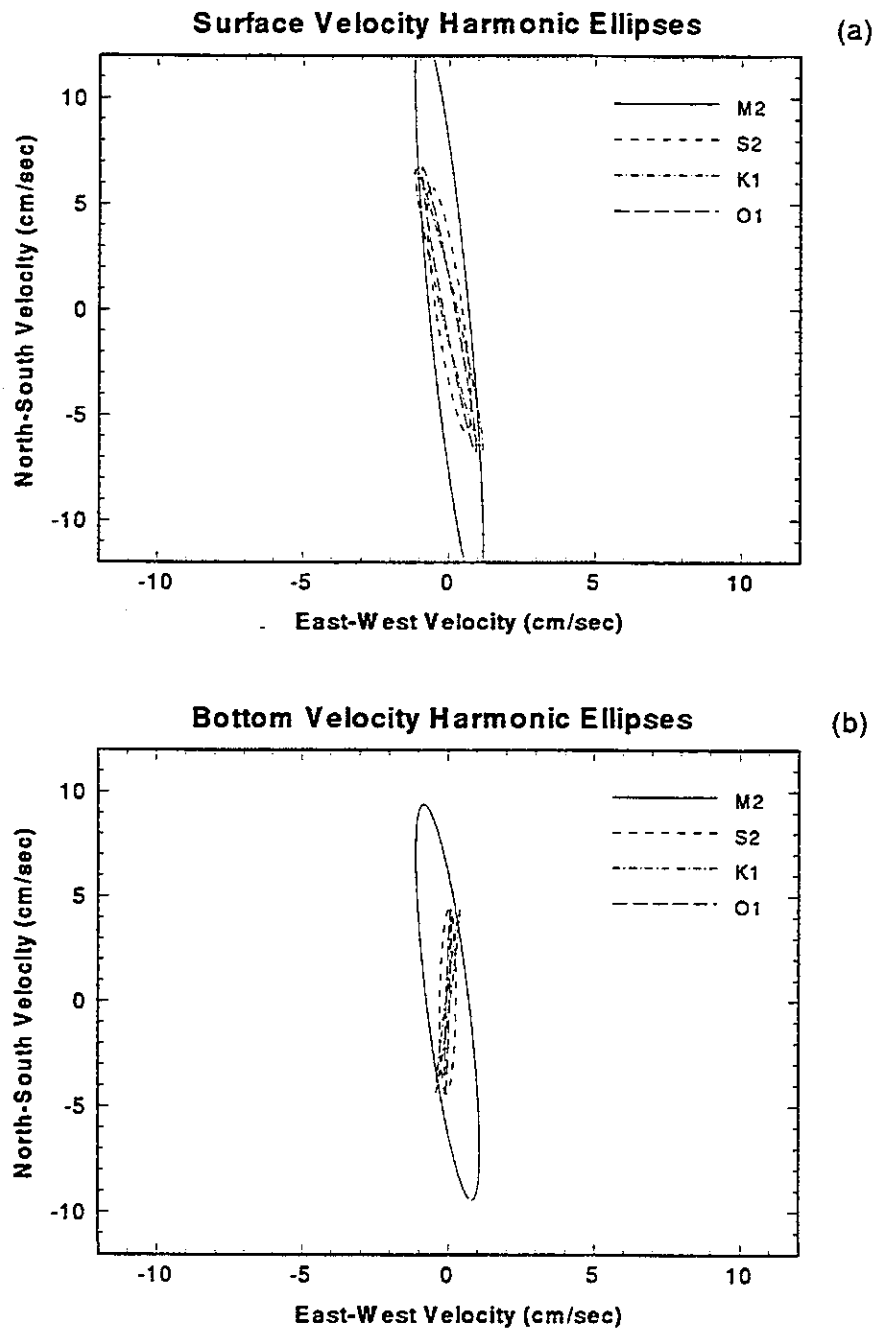
Figure 4.17: The primary harmonic ellipses at UFL-B2 for Julian Day 200 to 260, 1991. a) Surface velocities; b) bottom velocities.

4.17 presents plots of the two primary semi-diurnal (M_2, S_2) and two primary diurnal (K_1 and O_1) harmonic ellipses for the surface and bottom currents.

The form numbers calculated for this station are 0.58 and 0.65 for the bottom and surface components respectively. These values are considerably lower than those calculated for the tides and even lower than those calculated for the currents at UFL-B1.

The overtide ratios for this station are 0.13 and 0.09 for the bottom and surface components respectively. These values are of the same order of magnitude as calculated for UFL-B1. The bottom currents once again show a higher overtide ratio.

The directions of the principal axes indicate that there is a slight counterclockwise rotation in the current directions moving from the bottom to the surface. This rotation is most evident in the diurnal harmonic consituents. It appears that the bottom currents feel a greater impact from New Pass which is directly west of the station. This would create the slight rotation seen.

In contrast to station UFL-B1 the surface currents at UFL-B2 lag behind the bottom currents by 10 to 15 minutes. This adds support to the argument that the bottom currents are impacted to a greater degree by the flow through New Pass. As this inlet is closer the tidal wave propagating in would reach the station before the wave from Big Pass and therefore the bottom currents would lead the surface.

Station UFL-B3

Table 4.9 presents the harmonic ellipse components for Station UFL-B3. Figure 4.18 presents plots of the two primary semi-diurnal (M_2, S_2) and two primary diurnal (K_1 and O_1) harmonic ellipses for the surface and bottom currents.

The form numbers calculated for this station are 0.81 and 0.90 for the bottom and surface components respectively. These values are of the same order as those calculated for station UFL-B1.

The overtide ratios for this station are 0.13 and 0.13 for the bottom and surface

Surface Velocity Harmonic Ellipses   (a)
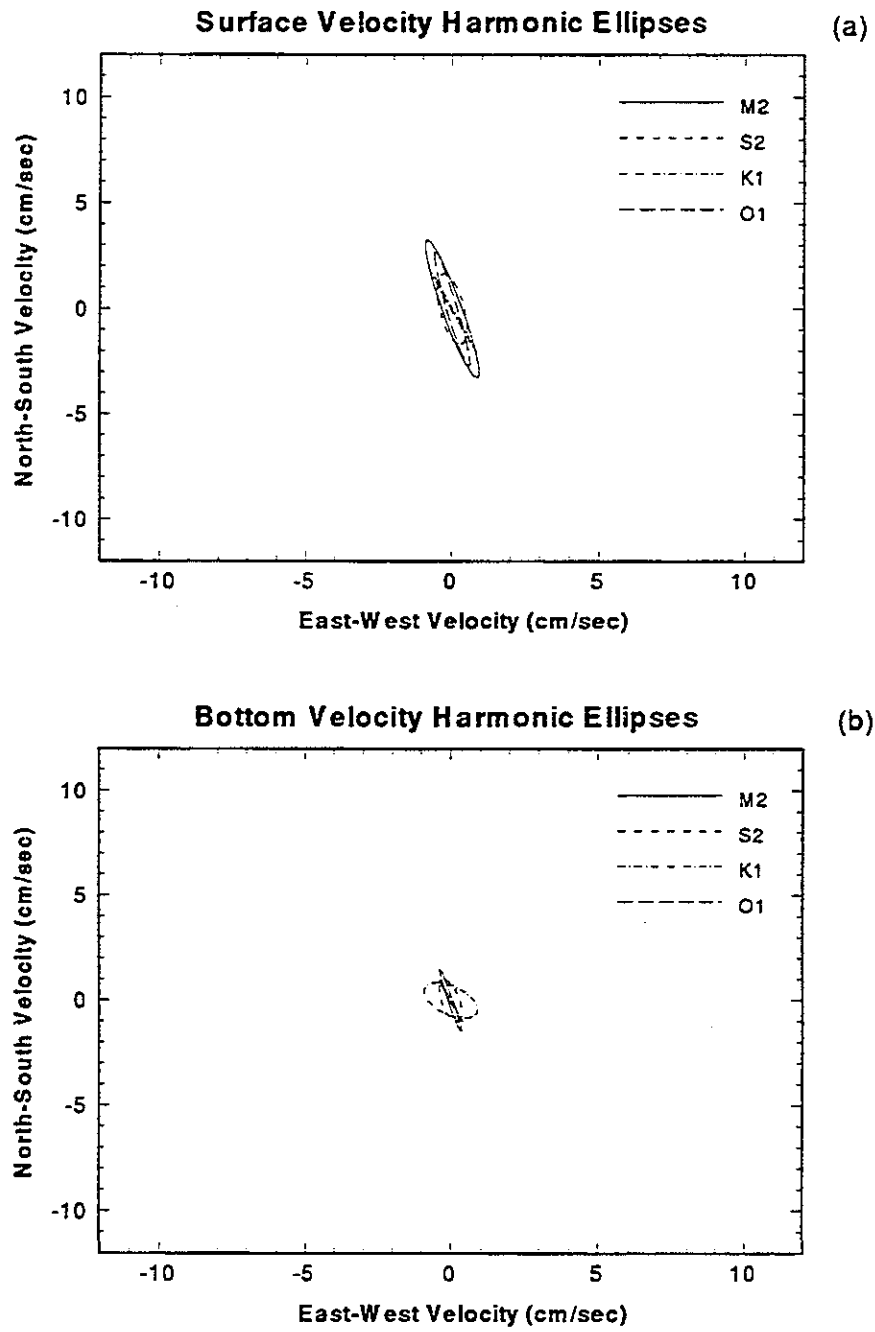
Figure 4.18: The primary harmonic ellipses at UFL-B3 for Julian Day 200 to 260, 1991. a) Surface velocities; b) bottom velocities.

Table 4.9: The principal axes harmonic constituent amplitudes, phases and axis directions for Station UFL-B3, Julian Day 200 to 260

Sensor Location	Constituent	Major Axis (cm)	Minor Axis (cm)	Major Phase (hrs)	Major Angle (deg)
Bottom	M2	1.56	0.08	-2.44	-75.4
	S2	1.04	0.31	0.01	-75.8
	N2	0.32	0.10	3.23	-96.1
	K1	1.05	0.43	-6.36	-20.9
	O1	1.06	0.02	3.40	-66.5
	MO3	0.29	0.09	-2.14	-97.2
	MK3	0.17	0.13	2.42	-46.3
Surface	M2	3.36	0.33	-1.93	-75.4
	S2	1.69	0.42	0.43	-80.0
	N2	0.38	0.05	-1.82	-62.4
	K1	1.79	0.14	-6.14	-63.7
	O1	2.78	0.22	3.52	-77.9
	MO3	0.78	0.01	-1.16	-98.7
	MK3	0.24	0.09	-1.76	-38.8

components respectively. The low overall magnitude of the components at this station makes interpretation of the results more diffucult as the magnitude of the signals is at or below the error associated with the sensors and the analyses.

The phases indicate that the bottom currents lag behind the surface currents by 10 to 20 minutes. This is also consistant with the findings for station UFL-B1.

Station UFL-B4

Table 4.10 presents the harmonic ellipse components for Station UFL-B4. Figure 4.19 presents plots of the two primary semi-diurnal (M_2, S_2) and two primary diurnal (K_1 and O_1) harmonic ellipses for the surface and bottom currents.

Station UFL-B4 shows the greatest difference between the bottom and surface harmonic plots. While the surface currents are highly uni-directional the bottom currents are elliptical. There is a counterclockwise rotation of the ellipses (5 to 10 degrees) from the surface to the bottom.

Surface Velocity Harmonic Ellipses (a)

Bottom Velocity Harmonic Ellipses (b)
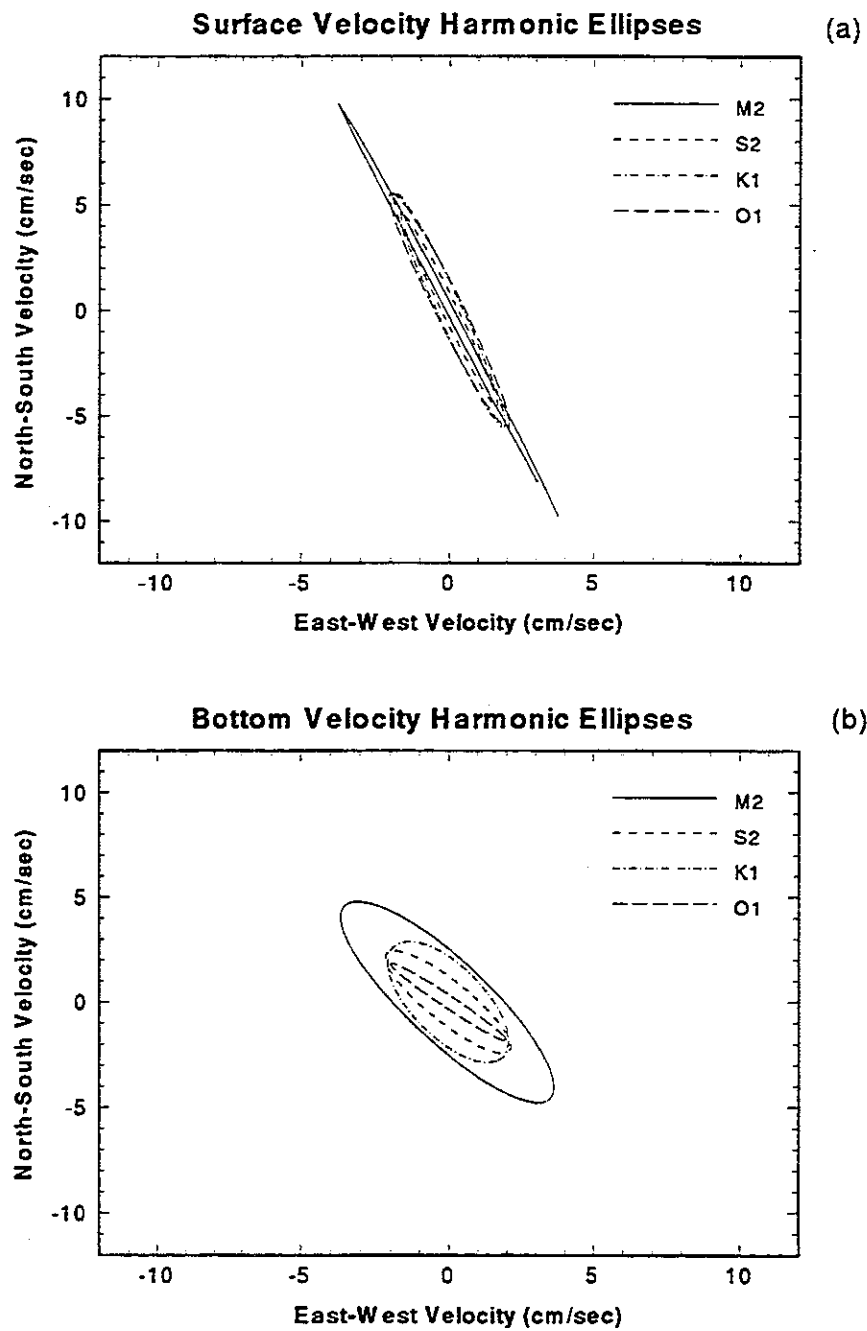
Figure 4.19: The primary harmonic ellipses at UFL-B4 for Julian Day 200 to 260, 1991. a) Surface velocities; b) bottom velocities.

Table 4.10: The principal axes harmonic constituent amplitudes, phases and axis directions for station UFL-B4, Julian Day 200 to 260

Sensor Location	Constituent	Major Axis (cm)	Minor Axis (cm)	Major Phase (hrs)	Major Angle (deg)
Bottom	M2	5.80	1.60	2.52	-54.0
	S2	3.12	0.83	-0.76	-49.0
	N2	0.99	0.03	3.09	-57.6
	K1	2.32	0.88	3.77	-52.4
	O1	2.64	0.25	1.71	-41.7
	MO3	1.32	0.00	-2.16	-54.8
	MK3	1.19	0.07	0.03	-62.2
Surface	M2	10.6	0.11	2.97	-69.1
	S2	4.89	0.25	-0.47	-70.1
	N2	1.80	0.18	2.70	-74.4
	K1	5.25	0.18	4.77	-73.7
	O1	5.62	0.47	2.41	-69.0
	MO3	1.47	0.81	-2.04	-53.5
	MK3	1.28	0.16	-0.11	-50.6

The form numbers calculated for this station are 0.59 and 0.70 for the bottom and surface components respectively. These values are of the same order as those calculated for station UFL-B2.

The overtide ratios for this station are 0.23 and 0.13 for the bottom and surface components respectively. This station has the greatest difference between the bottom and surface ratio.

The phases indicate that the surface currents lag behind the bottom currents by 10 to 20 minutes. This is also consistant with the findings for station UFL-B2.

Summary of Harmonic Analysis of the Currents

The analyses show a number of common features shared by stations UFL-B1 and UFL-B3 and by UFL-B2 and UFL-B4. The calculated form numbers for B1 and B3 are nearly 30 percent higher than those calculated for UFL-B2 and UFL-B4. The stations with the higher form numbers (UFL-B1 and UFL-B3) also have

the surface currents leading the bottom currents while the stations with the lower form numbers (UFL-B2 and UFL-B4) have the bottom currents leading the surface currents. In addition, UFL-B2 and UFL-B4 exhibit a greater difference between the overtide ratios for the surface and bottom currents.

In an attempt to explain these common characteristics, it is necessary to define physical conditions which the stations share. There does not seem to be a correlation between distance interior and the common characteristics. Although UFL-B3 is the most interior station, UFL-B1 which has the same features as UFL-B3 is no more distant from an inlet than UFL-B2, which does not share the same characteristics. In addition, it does not appear to be related to the extent of shallow water, UFL-B3 and UFL-B4 are in nearly identical bathymetric conditions. The one common feature between the stations is the way in which the tidal waves propagate toward the stations. UFL-B1 and UFL-B3 recieve tidal forcing from two sides, i.e. the stations were spaced nearly equidistant from two inlet openings. UFL-B2 and UFL-B4 on the other hand, are primarily forced from a single direction, UFL-B2 from Big Pass and New Pass to the south, and UFL-B4 from Venice Inlet. Although this does not explain the reasons for the differences, it does provide a common characteristic.

One thing which is shown by the analyses is that even in relatively shallow areas there is a distinct 3-dimensionality to the tidal currents. Any representation or model which does not account for these vertical variations will miss some of the important physics.

4.2.4 Analysis of Sub-Tidal Tides and Currents

General Methodology

The spectral analysis of the tides and currents identified a portion of the energy residing within the sub-tidal band. This region covers a frequency range from 0 to 0.5 cycles/day. The percent energy calculated for the seven USGS water surface elevation stations below 0.5 cycles per day was between 2 and 6 percent. Only two stations

(UFL-B1, UFL-B3) showed significant sub-tidal energy in the measured currents, the values ranged from 3 to 10 percent. Stations UFL-B2 and UFL-B4 had less than 1 percent of their energy below 0.5 cycles/day. Although the overall percent energies are relatively low, this portion of the signal is important in that it defines the long-term transport within the bay. The currents within the sub-tidal range are often referred to as the residual and are examined when addressing the issue of net transport.

Wong and Garvine (1984) isolated the sub-tidal energies from measured tides and currents in the Delaware estuary using spectral analysis techniques. They defined the coherence between the filtered offshore winds and the tides and currents and isolated the forcing mechanism. What they found was that the tide and current fluctuations showed the highest coherence levels when compared with the alongshore winds. They surmised that the fluctuations were driven by Ekman transport within the Gulf of Mexico creating water level fluctuations propagating along the coastline. A similar methodology will be utilized and expanded upon here to isolate the signals and evaluate the forcing mechanisms.

To isolate the sub-tidal portion of the signal, a low pass filter was applied to the data. The filter frequency response curve is presented in Figure 4.20. In designing the filter it was desired to avoid noise within the cutoff frequency band, and to have a sharp slope in the region of the cutoff frequency. The filter chosen was a Chebychev-II filter. This filter was designed to have very low noise levels within the cutoff frequency band and a sharp transition at the cutoff frequency. The filter presented in Figure 4.20 was designed through a series of iterations to produce the steepest response curve, while passing minimal noise levels.

One problem with bandpass filters is that they can introduce phase shift to the signals and this shift can be significant. In order to eliminate the phase shift the signals were filtered forwards and backwards. This process eliminates the phase shift but can introduce an artificial reduction in the signal magnitudes. To quan-
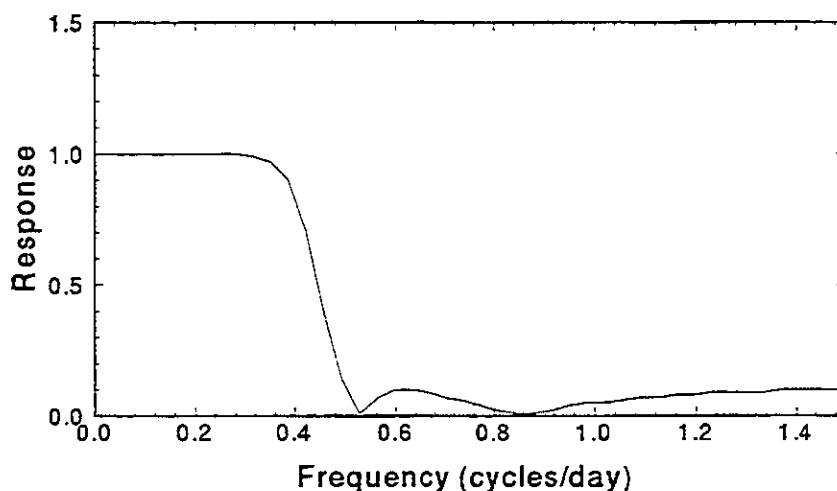
Figure 4.20: The frequency response curve for the Chebychev II, 48 hour low pass filter

tify the error produced during the filtering process, the data were filtered using the forward/backward process as well as forward. Comparison of the two signals showed that the forward/backward filtering did eliminate the phase shift but did not produce a significant magnitude reduction in the signal.

At the beginning and ends of the data records, the filtering produces some startup and ending errors. Testing of the filter indicated that the startup and ending effects for the 48 hour filter extended over 2 to 3 days. To avoid contamination of the results during spectral analysis, the beginning and ending 3 days of data (post-filtering) were removed.

Gaps exist in the current and wind data at stations UFL-B1, UFL-B2 and UFL-B4. Those gaps were filled with the mean values of the remaining data record. This correction did not effect the results unless the gaps were excessively long and close together. This only appeared to be a problem for Station UFL-B4.

Tidal Data

The tidal data from the seven USGS stations, and the wind data from the four UFL stations and Tampa Bay, were filtered using the Chebychev-II filter. The winds and tides, at different stations, showed nearly identical signals after filtering, therefore two representative tide stations and two wind were chosen for discussion. For the 1990 period, wind data from Tampa Bay and tide data from USGS-04 were compared (Figure 4.21). For the 1991 period, wind data from UFL-03 and tide data from USGS-06 were compared (Figure 4.22).

The top plots in each figure present the filtered tides along with the filtered along-shore (340 deg) and cross-shore (250 deg) winds. The residual water level fluctuations are on the order of 10 to 20 cm with the largest magnitudes occurring during the 1990 data period. The 1990 data show higher sustained winds as well as greater fluctuation in the residual wind field. This is due to the passage of frontal systems through the area. The 1991 data reflect summer conditions with lower overall wind energy and smaller water level fluctuations.

Following the methodology of Wong and Garvine, the coherence between the filtered wind vector component at a series of evenly spaced directions and the filtered water surface fluctuations were computed. The coherence is a frequency function with values between 0 and 1 which indicates the correspondence between an input X and an output Y. The coherence is calculated from the formula,

$$C_{xy} = \frac{|P_{xy}|^2}{P_{xx}P_{yy}} \tag{4.6}$$

where, P_{xx} and P_{yy} are the Power Spectral Densities of the two signals and P_{xy} is the Cross-Spectral Density of X and Y.

The bottom plots on Figures 4.21 and 4.22 present the coherence/frequency relationships for the wind vector components at 30 degree increments from 190 degrees to 340 degrees. From these figures the following observations can be made. For both the 1990 and 1991 data, the highest coherence (approximately 0.9), was obtained
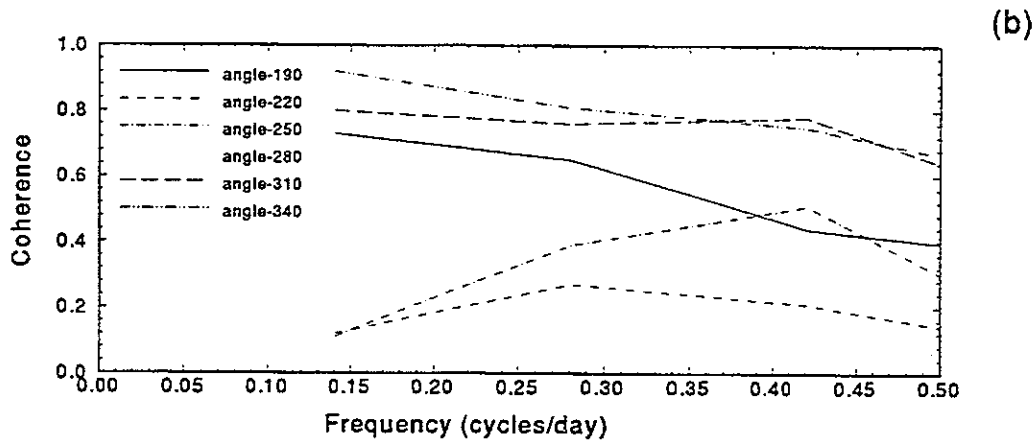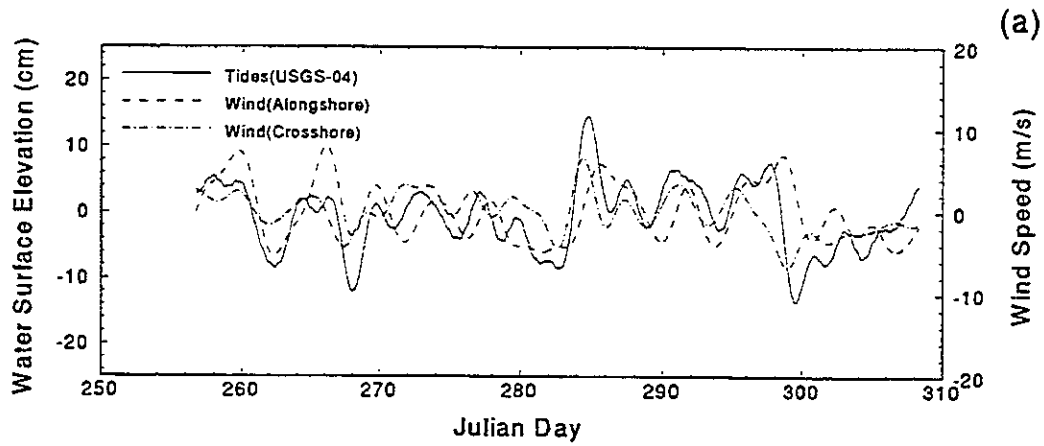
Figure 4.21: a) The filtered alongshore and cross-shore winds versus the filtered water surface elevation at USGS-04 for Julian Day 255 to 285, 1990; b) The coherence between wind vector components spaced at 30 degree increments and the filtered water surface elevation at USGS-04.

with the wind component between 310 and 340 degrees. The shoreline orientation along the barrier islands is approximately 330 degrees, therefore the highest correlation occurs with the alongshore winds. In the northern hemisphere, Ekman transport occurs at 90 degrees in a clockwise rotation from the wind. Therefore winds out of the south would create transport toward the bay and associated water level rise. The correlation between the low frequency water level fluctuations and the alongshore winds indicates a significant portion of the long term variations are driven by Ekman transport. The lowest coherences were obtained with winds oriented near 250 degrees or near the cross-shore component. The coherence values indicate that 90 percent of the energy in the long term water level fluctuations (periods near 7 days) is driven by Ekman transport within the Gulf of Mexico. At the higher frequencies (2 to 4 days) the alongshore and cross-shore coherence values converge indicating that the energy is split between Eckman transport and wind setup.

It is interesting to note that for the Delaware Estuary Wong and Garvine found the correlations between the winds and the water surface elevations to be 180 degrees out of phase. For this study, the winds and water surface elevations were 0 degrees out of phase. This is due to the nature of Eckman transport, i.e. the currents are always oriented 90 degrees to the winds in a clockwise direction in the northern hemisphere. In the Atlantic, winds out of the north (negative direction) would produce transport to the west, i.e. a rise in water level in the Delaware Estuary. In the Gulf of Mexico, winds out of the south (positive direction) would produce transport to the east, i.e. a rise in water level in Sarasota Bay.

Current Data

Figures 4.23, 4.26, 4.27, and 4.28 present the filtered current and wind vector components for the four bay stations. All of the data have been demeaned to allow comparison between the wind and current fluctuations.

Station UFL-B1 shows the highest residual velocity magnitudes of all of the sta-
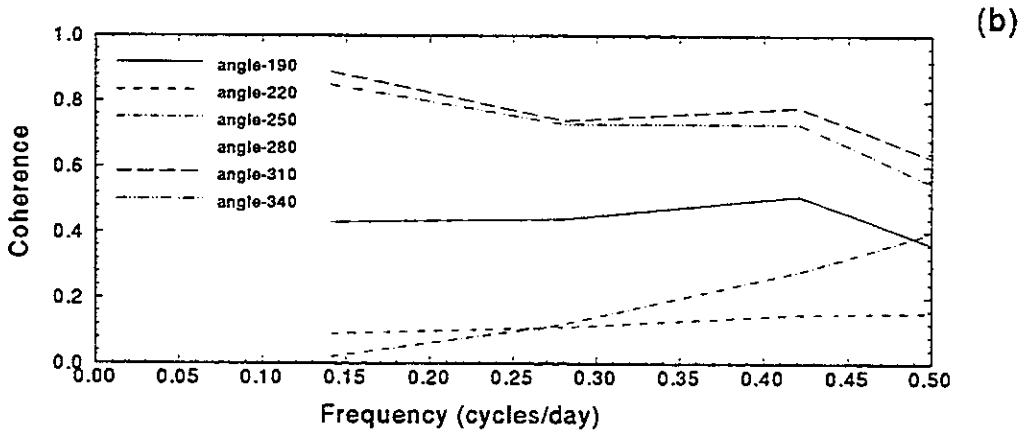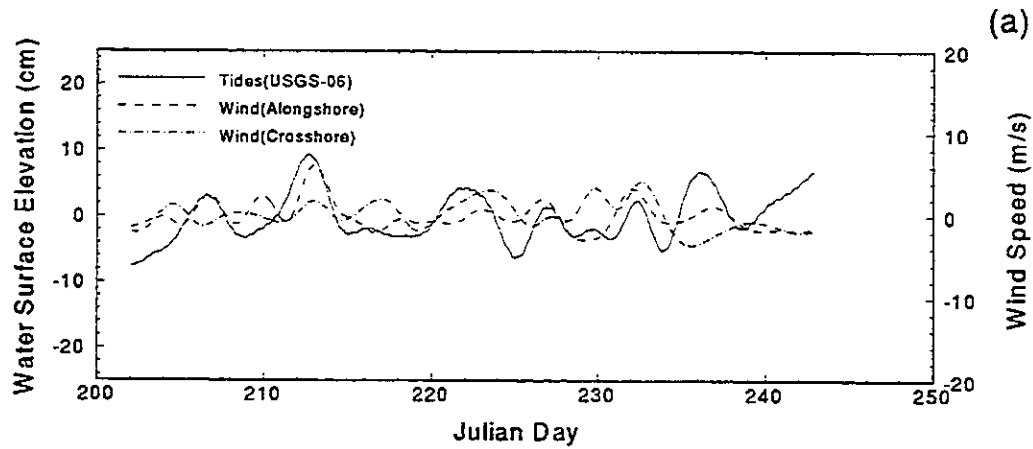
Figure 4.22: a) The filtered alongshore and cross-shore winds versus the filtered water surface elevation at USGS-06 for Julian Day 200 to 250, 1991. b) The coherence between wind vector components spaced at 30 degree increments and the filtered water surface elevation at USGS-06.
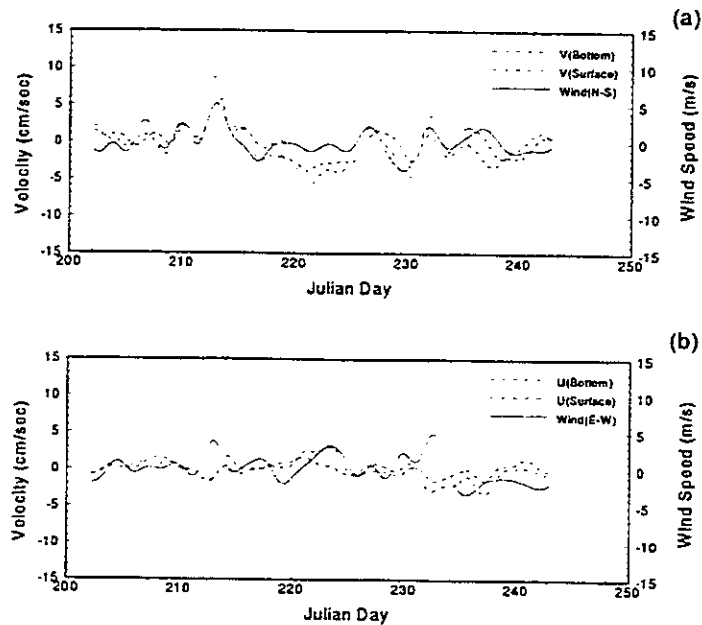
Figure 4.23: The filtered wind speed components compared to the current vector components at UFL-B1, Julian Day 200 to 260. a) North-south wind component compared to the bottom and surface north-south current component; b) east-west wind component compared to the bottom and surface east-west current component.

tions. As was discussed in Section 4.2.1, Station UFL-B1 has an additional -6 and -8.5 cm/sec residual in the north-south bottom and surface velocities respectively, and a 3 and 4 cm/sec residual in the east-west bottom and surface velocities. These residuals would be added to the plotted variations. Over the period of study the demeaned residual velocities fluctuate from -5 to 10 cm/sec in the north-south components and from -3 to 3 in the east-west components. The north-south components appear to correlate extremely well with the north-south winds. Figures 4.24 and 4.25 present plots of the coherence between the surface and bottom north-south and east-west velocity components and the wind vector components oriented at 30 degree spacings from 190 degrees to 340 degrees. These same wind vector components were compared with the filtered water surface elevation data.

In contrast to the water surface elevations, the directional nature of the currents

makes evaluation of the forcing mechanisms more difficult. In particular, it is of interest to try and define what portion of the fluctuations are the result of residual water surface elevation gradients created by Ekman waves and what portion are locally wind driven. This problem is compounded by the fact that the channel near UFL-B1, the shoreline (relative to the Ekman transport), and the north-south wind stress are all oriented within 20 degrees of each other, from 340 to 360 degrees.

Comparison of the coherence functions calculated for the surface and bottom measurements provides some insight into the forcing mechanisms. Comparison of the surface and bottom north-south current components shows the following. The bottom and surface sensors both show the highest coherence with the 190 and 340 degree wind components (near the alongshore direction), and the lowest coherence with the near cross-shore components, 250 to 280 degrees. The values for the surface component with the alongshore winds range from 0.7 at the lowest frequency (7 days) to 0.9 at the higher frequencies (1 to 2 days). The bottom component coherence is nearly constant (0.6 to 0.7) over the entire range of frequencies. Comparison of the surface and bottom east-west components shows the following. The surface east-west residuals show the highest coherence with the cross-shore or near east-west winds, and the lowest coherence with the alongshore or north-south winds. The bottom sensor, on the other hand, follows more closely with the north-south component. It shows the most significant coherence with the alongshore or near north-south winds.

From these observations the following conclusions can be made. The subtidal energy at the lower frequencies can be attributed to surface gradients created by Ekman transport within the Gulf of Mexico. At the higher frequencies, while the percent energy associated with Eckman transport appears to decline, there is an increase in the localized wind forced component. These observations are based upon comparison of the magnitudes and trends in surface and bottom coherences.

Comparison of the response time between the surface and bottom current com-

ponents shows that the bottom currents exhibit a greater lag in relation to the wind than the surface currents. This lag supports the assertion that the bottom currents are more closely linked to the Ekman transport, while the surface currents are a combination of Ekman transport and local wind forcing.

Although this explains the residual velocity fluctuations at UFL-B1, this still does not address the net velocities which at times actually oppose the wind stress. Various possible explanations have been proposed but this portion of the residual velocities remains to be explained.

The residual velocities fluctuations measured at UFL-B2 are weak in comparison with UFL-B1. The largest fluctuations range from -3 to 3 cm/sec. This agrees with the findings of the spectral analysis which showed less than 1 percent of the energy residing in the sub-tidal band. Visual inspection of the plots (Figure 4.26) indicates that some correlation exists between the north-south residual currents and the north-south winds, but the calculated coherence values were insignificant for all of the components and are not presented.

One notable observation can be made by comparing the surface and bottom residual velocities. Their fluctuations appear to mirror one another in some instances. This indicates that some form of surface wind driven flow with bottom return flow is being induced within the bay. Given the large body of open water near this station, and the uniform deeper depths, the existence of a wind induced vertical circulation gyre is reasonable.

Although station UFL-B3 showed the highest percent energy residing within the subtidal band, the measured residual flows are relatively weak. Velocity fluctuation magnitudes range from 3 to -5 cm/sec. Although this variation is small, in relation to the overall energy at this station these fluctuations are not insignificant. This was shown by the high percent energy within the sub-tidal frequency band found for this station. Examination of the variations in relation to the wind stress do not indicate

Bottom North-South Velocity versus Wind Speed Components

(a)

Bottom East-West Velocity versus Wind Speed Components

(b)
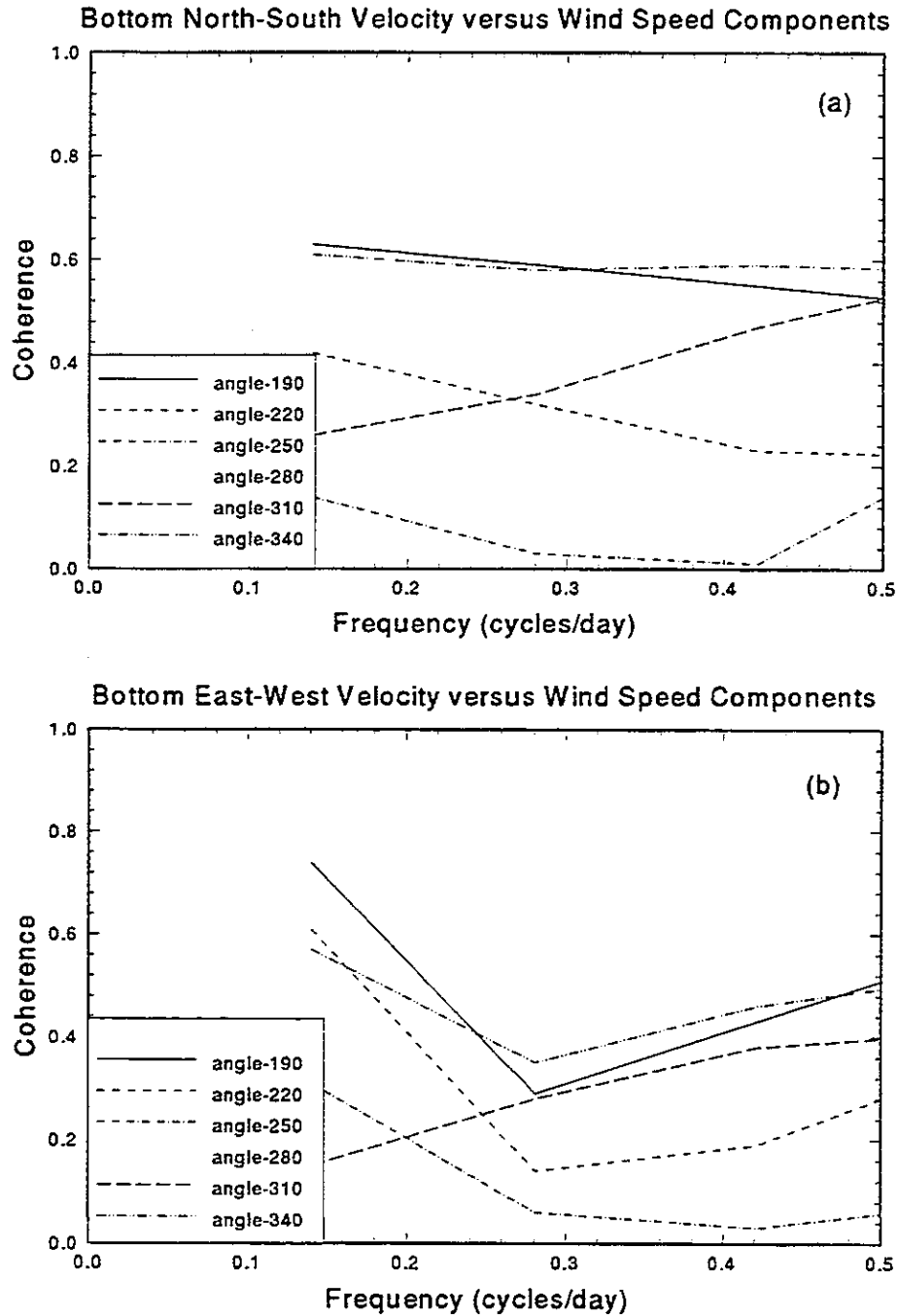
Figure 4.24: The coherence between the filtered bottom current vector components and the filtered wind vector components at 30 degree spacings from 190 to 340 degrees, UFL-B1, Julian Day 200 to 260. a) north-south currents; b) east-west currents.

Station UFL-B1
Surface North-South Velocity versus Wind Speed Components

Surface East-West Velocity versus Wind Speed Components
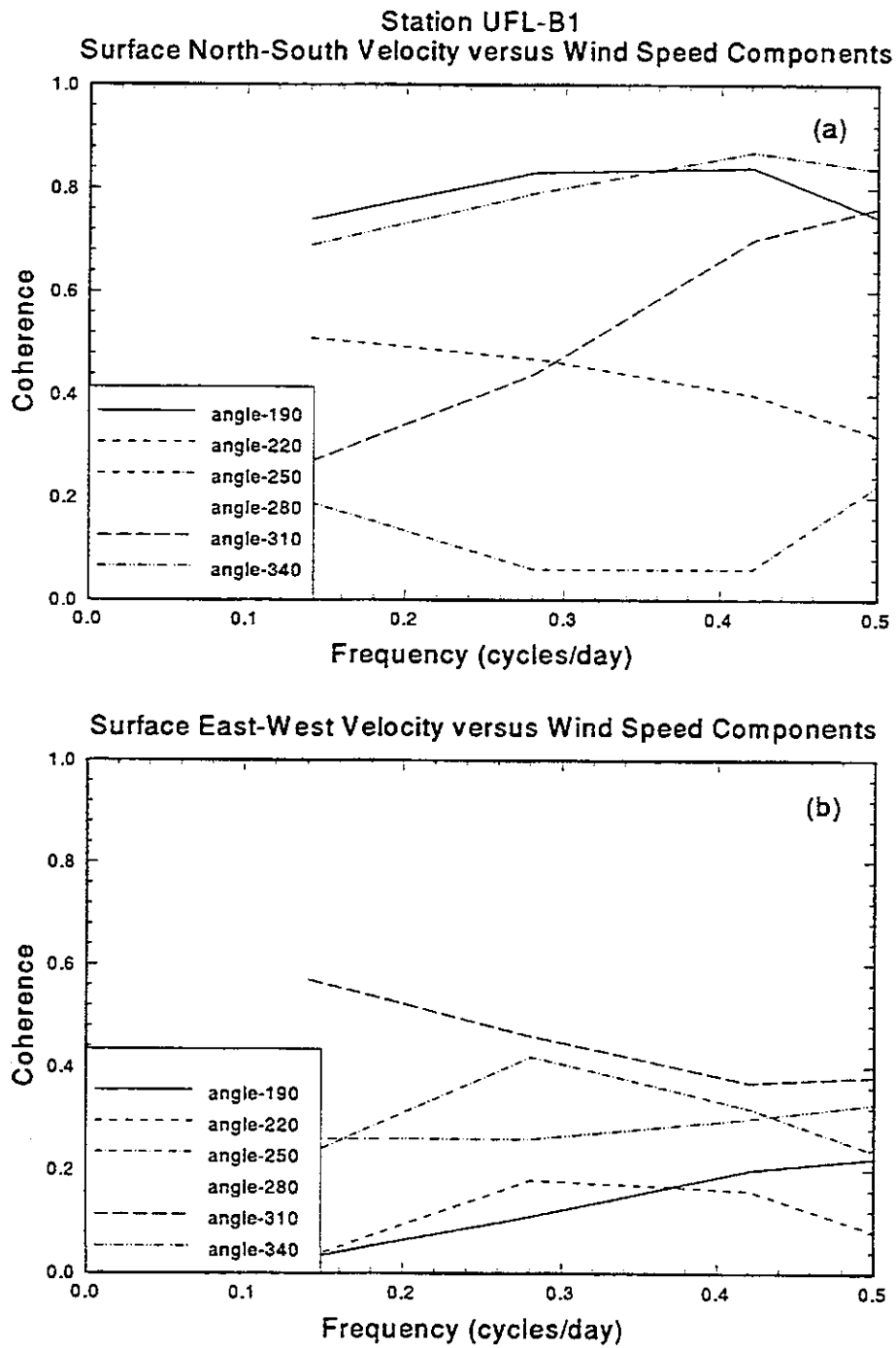
Figure 4.25: The coherence between the filtered surface current vector components and the filtered wind vector components at 30 degree spacings from 190 to 340 degrees, UFL-B1, Julian Day 200 to 260. a) north-south currents; b) east-west currents.
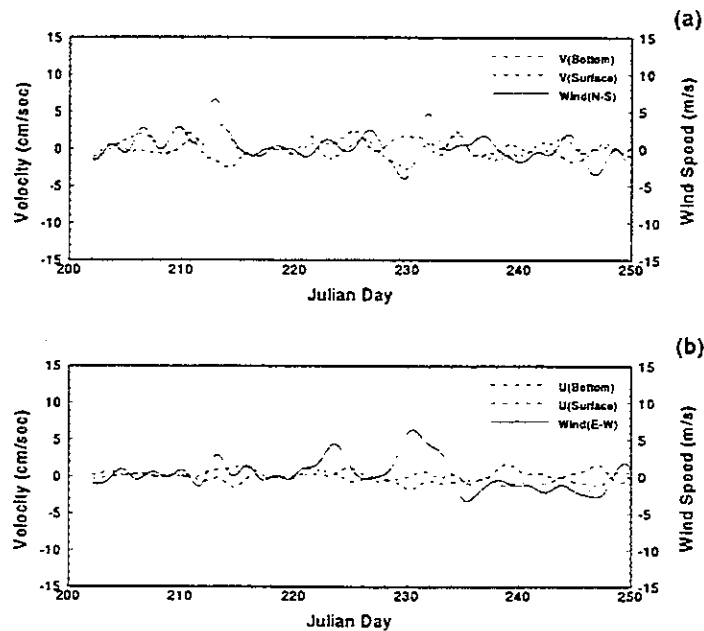
Figure 4.26: The filtered wind speed components compared to the current vector components at UFL-B2, Julian Day 200 to 260. a) North-south wind component compared to the bottom and surface north-south current component; b) east-west wind component compared to the bottom and surface east-west current component.

significant correlations and the calculation of the coherence function did not show significant correlation at any of the sub-tidal frequencies with any of the wind vector components.

UFL-B4 presented some problems due to the length of the data gaps. Examination of the plots of the filtered data show (where data are available) small residual current fluctuations. This is in agreement with the 1 percent of energy residing in the subtidal band found for this station. Coherences were unreliable due to the extent of the missing data.

4.3 Discharge Measurements

A critical parameter in the determination of the currents and tidal fluctuations within an enclosed bay or lagoon is the volume of water or tidal prism which en-
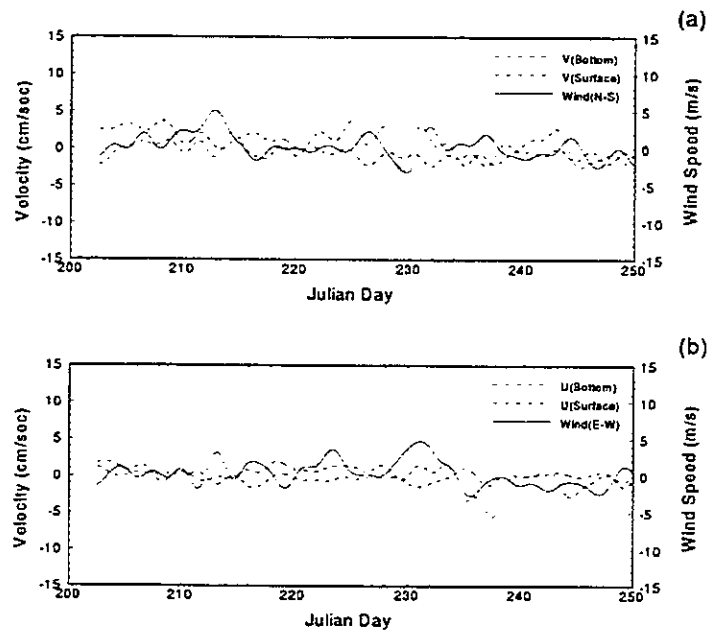
Figure 4.27: The filtered wind speed components compared to the current vector components at UFL-B3, Julian Day 200 to 260. a) North-south wind component compared to the bottom and surface north-south current component; b) east-west wind component compared to the bottom and surface east-west current component.

ters through the inlets. In multiple inlet systems, tidal prism magnitude will vary depending upon the inlet depth, width and length. These variations will determine the hydrodynamic characteristics within the interior lagoons. The following presents and discusses the data collected by the USGS during the discharge measurements described in Chapter 3, Section 3.3.3.

Roberts Bay, Little Sarasota Bay and Blackburn Bay are a series of semi-enclosed interconnected shallow lagoons (see Figures 3.1 and 3.2). Tides propagating into this sub-system enter through two openings, one located at the northern end of Roberts Bay and the other just north of Venice Inlet along the Intracoastal Waterway. As described in Chapter 3, to quantify the flows through these two openings the USGS conducted discharge measurements at the Siesta Key Bridge (north end of Roberts Bay) and the Nokomis Bridge (Blackburn Bay). The measurements were conducted
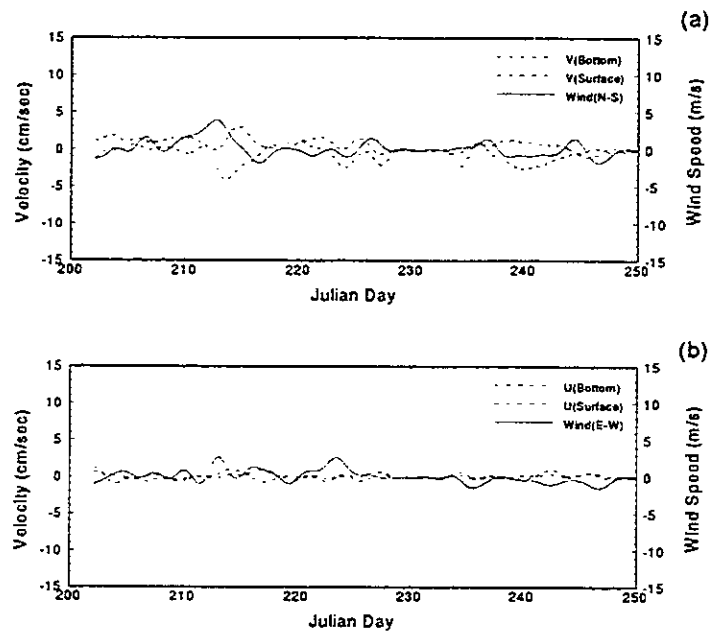
Figure 4.28: The filtered wind speed components compared to the current vector components at UFL-B4, Julian Day 200 to 260. a) North-south wind component compared to the bottom and surface north-south current component; b) east-west wind component compared to the bottom and surface east-west current component.

on Julian Days 204, 205, 224 and 225 in 1991.

Figure 4.29 presents the measured discharges at both stations along with the measured tides from Little Sarasota Bay (USGS-06). The discharge measurements could not be taken simultaneously therefore an attempt was made to collect the data over two days with similar tidal conditions. Examination of the tide data indicates that conditions were similar enough to allow some general comparisons. The tides over which the discharges were measured were predominantly diurnal from Julian Day 204 to 206 and semi-diurnal from Julian Day 224 to 226. Also the measurements on Julian Day 204 to 206 were during ebb tide and on Day 224 to 226 were during flood tide.

At the time of the measurements, the tide range (high to low or low to high) was slightly larger during the measurements at Blackburn Bay. The ranges for the first
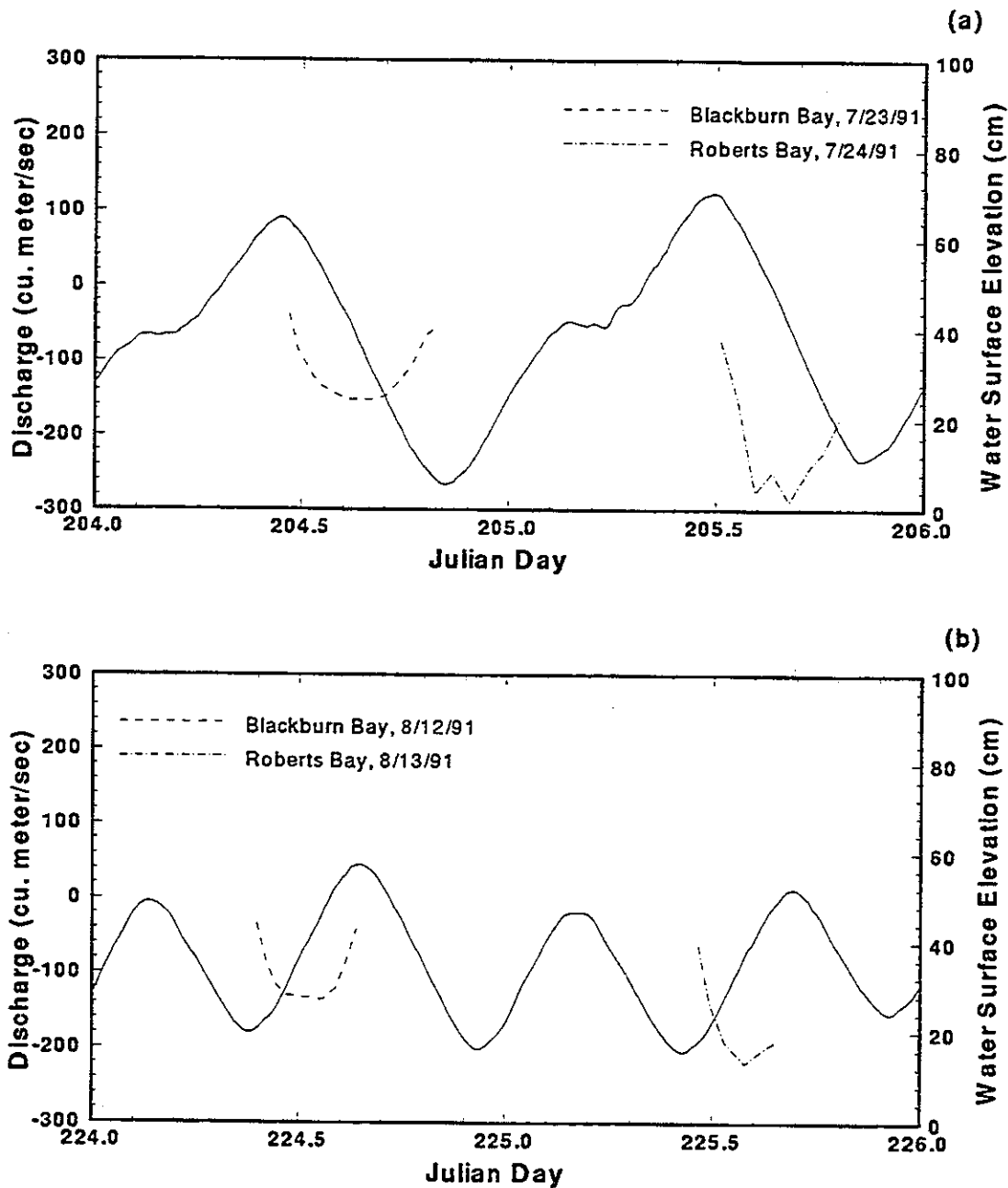
Figure 4.29: The measured discharge compared with the measured water surface elevation at Roberts Bay and Blackburn Bay (solid line is the water surface elevation, broken lines are discharge). a) Julian Day 204 to 206, 1991; b) Julian Day 224 to 226, 1991.

data collection were 60 cm and 58 cm for Julian days 204 and 205 respectively, and 38 cm and 36 cm for Julian Days 224 and 225. The data show that under ebbing tide and diurnal conditions, the maximum discharge at Roberts Bay was 280 cubic meters per second (cms), while at Blackburn Bay it was 140 cms. Under a flooding tide and semi-diurnal conditions, the maximum discharge at Roberts bay was 220 cms, while at Blackburn Bay it was 130 cms. The data indicate that the larger flow passes through Roberts Bay and it is approximately 40 percent larger.

In 1992 discharge measurements were made in Big Pass, New Pass, Longboat Pass and at the opening from Anna Maria Sound to Tampa Bay. Although this time period does not correspond to the 1990 or 1991 analyses, the data are useful in defining the relative inflows through each of the inlets. All measurements were made during ebbing tide, and therefore the conclusions are only relevant to ebb tide conditions.

Figure 4.30 shows the discharges through Longboat Pass and Anna Maria Sound versus the measured tides at Anna Maria Sound (top plot), and the discharges through New Pass and Big Pass versus the measured tides at Big Pass (bottom plot). For each inlet only a few discrete measurements were made during the tidal cycle, therefore single points are plotted as versus a continuous curve.

Examination of the water surface elevation data during each measurement period indicates that the tide range during the measurements at New Pass and Big Pass was 64 cm, while during the Longboat Pass and Anna Maria Sound measurements it was 47 cm. Table 4.11 presents maximum discharges for each pass extrapolated from the point measurements.

In order to compare the discharges through the inlets it is necessary to take measurements under the same tidal forcing conditions. As the tide range varies during the measurements, a relationship must be developed to equate the discharges. Kuelegan (1973) defined a simple formula for the maximum discharge through an inlet such
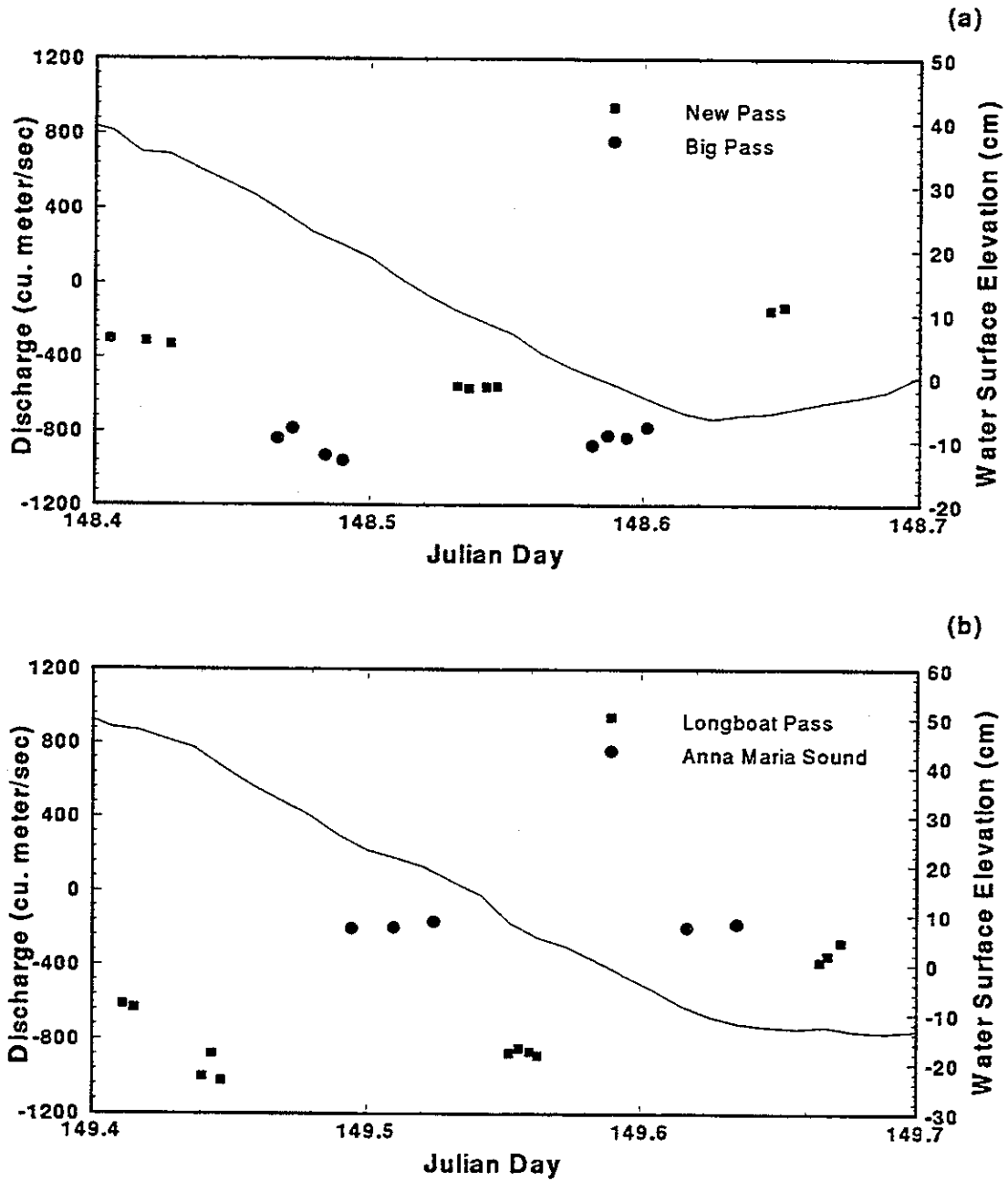
Figure 4.30: The measured discharge compared with the measured water surface elevations. a) New Pass and Big Pass, Julian Day 148, 1992; b) Longboat Pass and Anna Maria Sound, Julian Day 149, 1992.

Table 4.11: The measured maximum discharges through Anna Maria Sound, Longboat Pass, New Pass and Big Pass, Julian Days 148 to 150, 1992.

Location	Maximum Discharge (cms)
Anna Maria Sound	160
Longboat Pass	1040
New Pass	560
Big Pass	1000

that,

$$Q_{max} = \frac{\pi P C_k}{T} \tag{4.7}$$

where, Q_{max} is the maximum discharge through the inlet, P is the tidal prism, T is the tidal period and C_k is a coefficient between 0.8 and 1.0. The tidal prism P can be calculated using the formula,

$$P = RA \tag{4.8}$$

where, R is the tide range inside the bay and A is the surface area over which the inlet impacts the bay. This equation assumes a constant rise and fall over the entire bay. Assuming that the surface area over which each of the inlets influences the bay does not change, that each inlet has a constant C_k, and the tidal period is constant between the two measurements, a ratio for the maximum discharge can be developed in terms of the tide range such that,

$$\frac{Q_{max_1}}{Q_{max_2}} = \frac{R_1}{R_2} \tag{4.9}$$

Using this formula, the discharges were calculated for the tide range on day 149 in 1992. Table 4.12 presents the calculated discharges along with the percent of the total for each. The discharges shown, excluding Roberts Bay, represent all tidal inflows to the Sarasota Bay system. Roberts Bay is not included as it is inside the control volume. The percentages represent the relative contributions from each inlet to the

Table 4.12: The calculated discharges through Anna Maria Sound, Longboat Pass, New Pass, Big Pass, Roberts Bay and Blackburn Bay, Julian Day 149, 1992.

Location	Calculated Maximum Discharge (cms)	Percent
Anna Maria Sound	160	4.6
Longboat Pass	1040	29.8
New Pass	762	21.9
Big Pass	1362	39.1
Roberts Bay	307	n/a
Blackburn Bay	163	4.6

entire system. Over 90 percent of the flow out of the system goes through Big Pass, New Pass and Longboat Pass. The remaining 10 percent flows out equally through the north (Tampa Bay) and the south (Venice Inlet).

4.4 Freshwater Inflow Measurements

Freshwater inflow into the Sarasota Bay system does not originate from any one source. Inflows come through numerous small creeks and drainage canals. Figures 3.1 and 3.2 identify some of the larger creeks entering the system. These include, Bowden Creek and Whitaker Bayou into Sarasota Bay, Phillippee Creek and North Creek into Little Sarasota Bay, South Creek into Blackburn Bay, and Crane and Shackett Creek into Venice Inlet. The Manatee River, although it flows into Tampa Bay, has an impact upon the salinities within Anna Maria Sound due to its proximity to the entrance. It is the largest river entering Tampa Bay and during high rainfall events can be a significant source of freshwater.

During the period of the 1991 field measurements, the USGS was monitoring flow at a point approximately 50 kilometers upstream within the Manatee River and within Walker Creek which is a small tributary flowing into Whitaker Bayou. Whitaker Bayou in turn discharges into Sarasota Bay. Figure 4.31 shows plots of

the measured discharges from the two creeks. One significant freshwater inflow event was measured at both monitoring stations. This event occurred near Julian day 211 and produced flows as high as 120 cubic meters per second in the headwaters of the Manatee River. Based upon an average width of 800 meters and an average depth of 2 meters this equates to a velocity of 7.5 centimeters per second. An important point to note is that the measurements of flow were taken well upstream of the entrance of the Manatee River into Tampa Bay. The increased runoff produced by the additional drainage area below the measurement station is not considered. Within Walker Creek the maximum flow achieved during this event was 8 cubic meters per second. Other freshwater inflow events can be seen in the data. These events don't necessarily correlate between stations. This demonstrates the localized nature of the storm events and the varying response of the drainage basins.

The differences in the sizes of the drainage basins is evident in the magnitudes of flow and the duration of the events. The Manatee River, by virtue of its much larger drainage basin, has a higher magnitude flow, a slower time to reach peak and a longer duration of flow. Walker Creek on the other hand has a more peaked short duration response. The shorter response time and duration seen in the Walker Creek data is representative of the creeks flowing into the Sarasota Bay system.

Manatee River and Walker Creek were the only inflows monitored during the 1991 data collection period. Rainfall in Florida during the summer months occurs as localized thunderstorms and the runoff conditions may vary significantly over small distances. This is evident by examining the differences between the two monitored stations. The drainage basins for the creeks flowing into Sarasota Bay are spread over a 150 square kilometer region from the north end of Manatee County to the south end of Sarasota County. In addition, significant quantities of runoff may be due to non-point sources located all along the bay boundaries and these are difficult to quantify in total magnitude, and nearly impossible to quantify spatially.
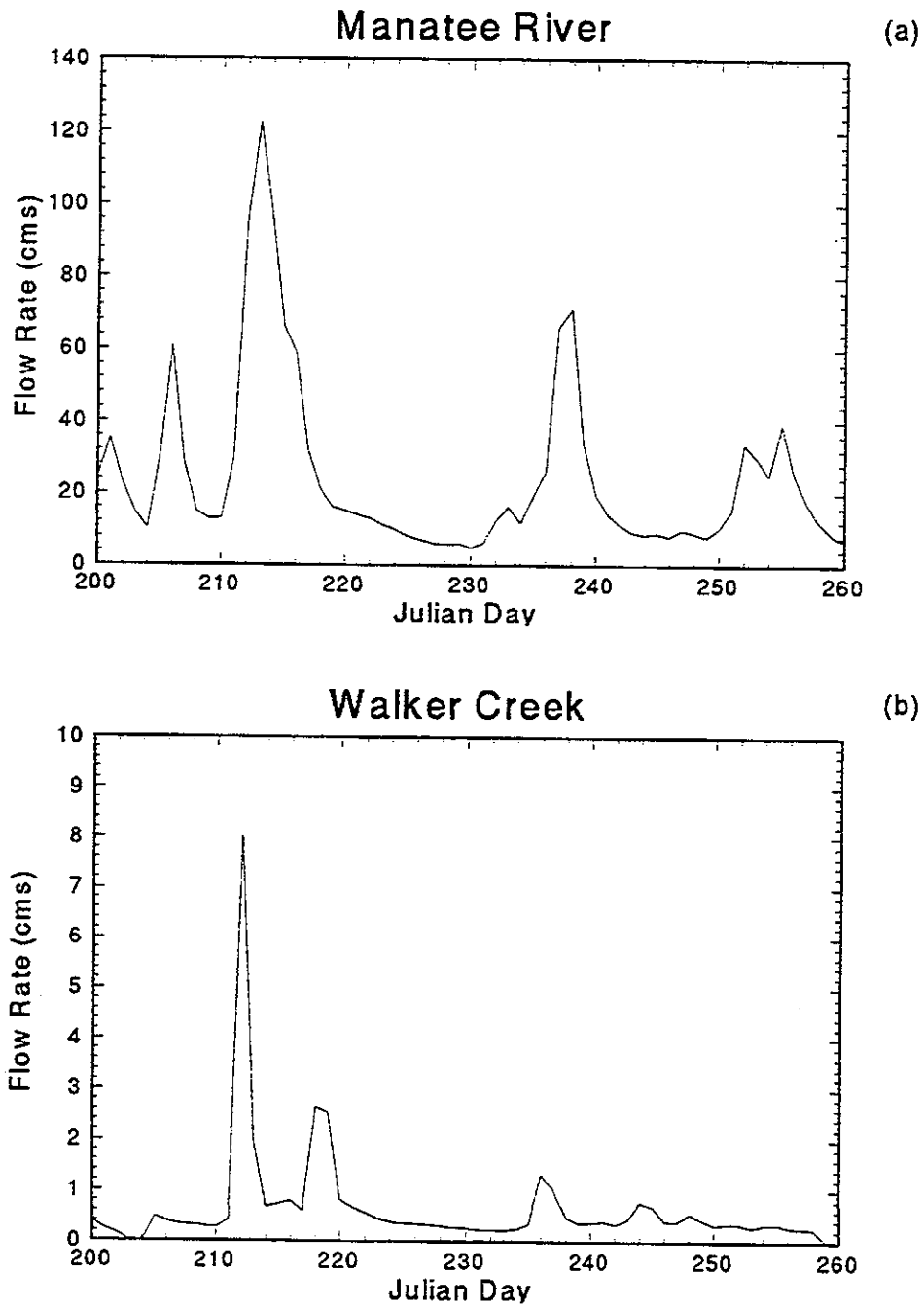
Figure 4.31: The measured freshwater inflows to the Sarasota Bay System, Julian Day 200 to 260, 1991. a) Manatee River; b) Walker Creek.

4.5 Salinities Measured at the UFL Bay Stations

This section presents salinities calculated from the measured temperature and conductivity at the four UFL bay stations. These data are discussed below in a qualitative manner in order to provide insight into the relative transport patterns and flushing characteristics of the various lagoons.

Station UFL-B1

Figure 4.32 presents the calculated near bottom and near surface salinities at UFL-B1 for Julian Days 200 to 250. From these data 3 freshwater inflow events can be isolated, Julian day 211 to 226, Julian Day 228 to 236 and Julian Day 238 to 245. The first and last events coincide with periods of high measured flow within the headwaters of the Manatee River (Figure 4.31). The middle event, which starts around Julian Day 227, does not coincide with high flow within either the headwaters of the Manatee River or Walker Creek.

Examination of the three plots identifies differences in the salinity response. The first salinity drop corresponds with the highest measured inflow from the Manatee River. The salinities drop from 34 to 31 ppt over a 6 to 8 day period. The freshwater inflow ends near Julian Day 219 at which point the salinity levels begin to recover. The recovery (or flushing) takes nearly 7 days to reach pre-storm conditions.

The second salinity change occurs over a much shorter duration. The salinities drop from 34 to 32 ppt over a 2 to 3 day period. The post-event recovery is different for this event. The salinities fluctuate from pre- to post-event levels depending upon the tidal flow direction. These fluctuations reduce in magnitude over the recovery period as the region is flushed.

The third event corresponds with a lesser flow from the Manatee River and has characteristics more in line with the first event. The overall drop in salinity is lower (less than 2 ppt) in response to the lower inflow rate. The flushing time is also shorter

for this event.

The differing responses are most likely the result of two types of inflows. The first and third are basinwide events with both Walker Creek and the Manatee River showing inflow. Due to the size of the Manatee River Basin in relation to Walker Creek the hydrograph for the Manatee River is less peaked and the duration of the flow event longer. This manifests itself in the salinity readings at UFL-B1 which drop over the inflow period and recover slowly as the inflow declines. The second event appears to be more localized, i.e. a rapid inflow of a plug of freshwater. The plug is then sloshed back and forth across the station and dispersed through the recovery period. This creates the large magnitude salinity fluctuations.

In all cases the short period drops in salinity (i.e. within a tidal cycle) correspond to ebb (or southward) flow. This defines the source of freshwater as north of the station, most likely the Manatee River.

The bottom plot on Figure 4.32 presents the difference in salinity between the bottom measurements and the surface measurements. Recalling Chapter 3, the mean depth at Station UFL-B1 is 240 cm with the bottom sensor 55 cm off of the bottom and the surface sensor 175 cm above the bottom. The data show that stratification occurs near the beginning of the recovery period for the basinwide inflow events (1 and 3) and slowly declines over the recovery period. The water column does not show stratification during the second event even though the magnitude of the salinity drop is nearly the same as the first event and greater than the third event.

Station UFL-B2

Station UFL-B2 (Figure 4.33) exhibits the smallest magnitude salinity fluctuations of the four UFL stations with values ranging from 32 to 34 ppt. During the Julian day 211 event the salinity drop is approximately 2 ppt with a slow recovery period. The time for the bay to reach pre-event conditions (the flushing time) is
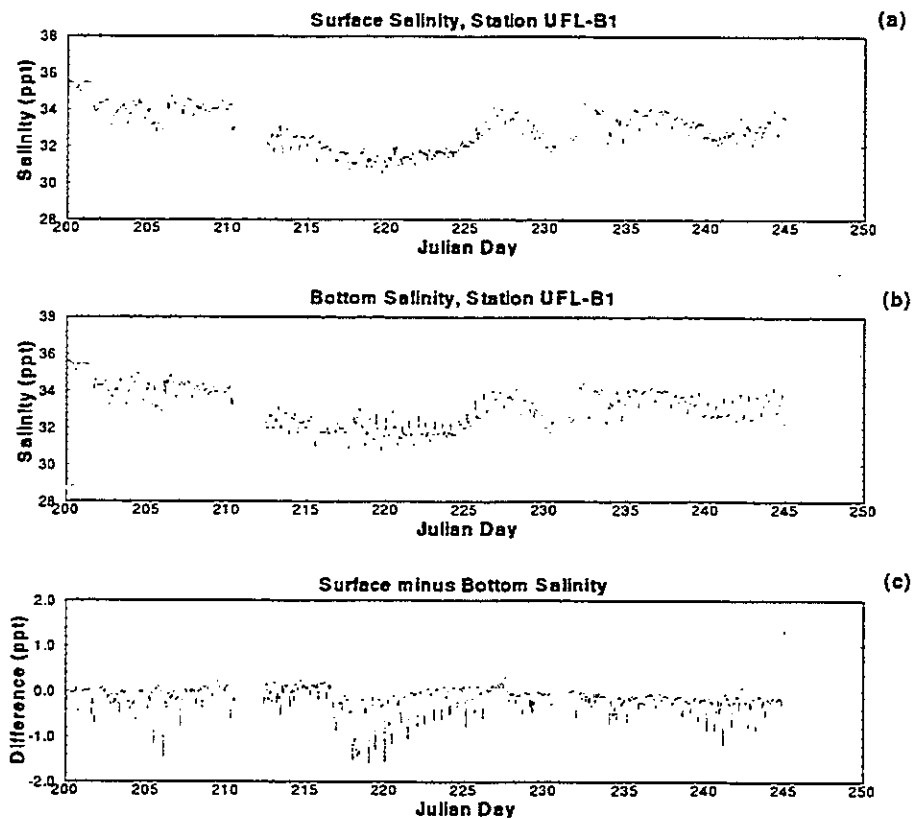
Figure 4.32: a) The surface salinity at UFL-B1 from Julian Day 200 to 250, 1991; b) The bottom salinity at UFL-B1 from Julian Day 200 to 250, 1991; c) The surface minus bottom salinity at UFL-B1 from Julian Day 200 to 250, 1991

nearly 15 days. The second event was not even measured at UFL-B2.

The plot of salinity difference indicates that stratification occurs at UFL-B2 (1 to 2 ppt) and that peaks occurred during the post-event recovery of the Julian day 211 event, this is similar to the measurements at UFL-B1. Data are missing from Julian days 217 to 220 which is a significant portion of the recovery period for this event.

From Julian day 200 to 205 stratification indicates that freshwater inflow occurred near UFL-B2. The discharge data from Walker Creek, which is a tributary inflow near UFL-B2, do not reflect an inflow during this period. Once again this may indicate a more localized event. UFL-B2 is located within Sarasota Bay which has
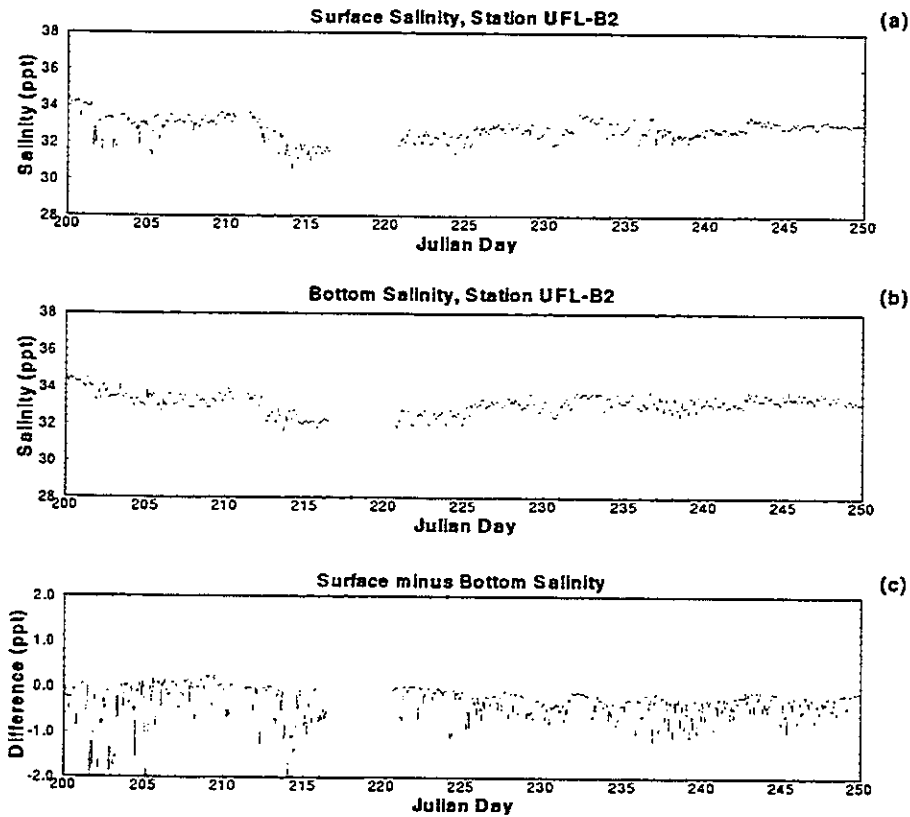
Figure 4.33: a) The surface salinity at UFL-B2 from Julian Day 200 to 250, 1991; b) The bottom salinity at UFL-B2 from Julian Day 200 to 250, 1991; c) The surface minus bottom salinity at UFL-B2 from Julian Day 200 to 250, 1991

numerous non-point discharges to it. Visual observations made during the 1991 data collection effort showed a large number of stormwater drainage pipes discharging from the mainland and from Longboat Key and Lido Key. These sources are difficult to quantify.

Station UFL-B3

Figure 4.34 presents the measured surface and bottom salinities along with the salinity differences for station UFL-B3. The data show clear responses to the Julian day 211 inflow event and the Julian day 236 event. The drop in salinity is 3 to 4 ppt during both events and occurs over a 3 to 4 day period. The post-event recovery
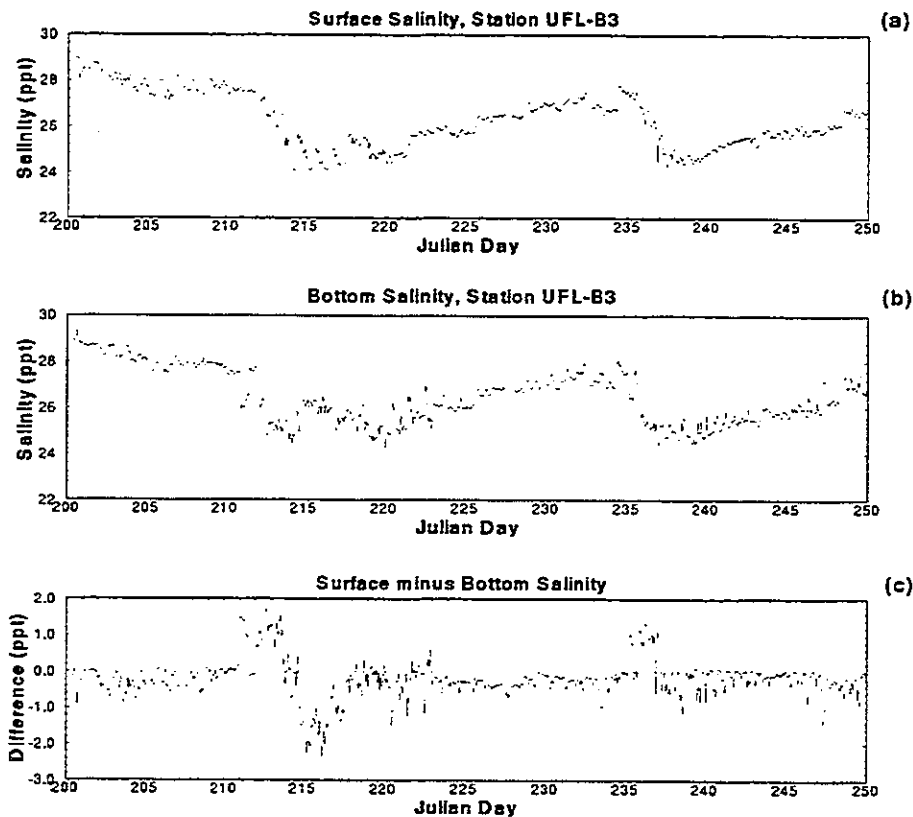
Figure 4.34: a) The surface salinity at UFL-B3 from Julian Day 200 to 250, 1991; b) The bottom salinity at UFL-B3 from Julian Day 200 to 250, 1991; c) The surface minus bottom salinity at UFL-B3 from Julian Day 200 to 250, 1991

period (flushing time) is slow, taking nearly 15 days to reach pre-event conditions. As with the other stations UFL-B3 shows stratification during the immediate post-event recovery period. The stratification is greater and more persistent at this station than was found at UFL-B1 and UFL-B2. This is most likely due to the low energy, restricted flow conditions.

An interesting phenomenon which was measured at this station during both of the freshwater inflows, was a period of stratification reversal where the salinity levels were lower near the bottom than at the surface. This is an unusual event and it only occurs immediately following freshwater inflow events. Were this the result of

colder fresher water moving beneath the surface waters there would be temperature stratification. As this was not shown by the data, the most likely explanation is that the high rainfall on the barrier islands expanded the freshwater lens within the aquifer and created groundwater seepage into the bay.

Station UFL-B4

Station UFL-B4 showed the most dynamic responses to the freshwater inflows. Figure 4.35 presents the measured surface and bottom salinities along with the salinity differences. The period of inflow is clearly seen from Julian Day 211 to 215 with a rapid decline in salinity from 32 to 27 ppt. This is the largest change measured for all of the stations. The recovery period is marked by the sloshing back and forth of the plug of freshwater with steady flushing and recovery. Although there are missing data from Julian day 227 to 234 it appears that this station never fully recovers to pre-event conditions with the associated low salinity fluctuations. Examination of the record from Julian day 200 to 211 it appears as if the bay were recovering from a previous inflow event prior to the Julian day 211 inflow.

As with the other stations the post-event recovery period is marked by periodic stratification of the water column or the passing of stratified water by the station. This stratification steadily reduces throughout the recovery period and by the time the data starts up again, even though the salinity fluctuations are still large the stratification peaks have disappeared.

4.6 Chapter Summary

This chapter presented a series of data analysis techniques performed upon 60 days of tide and wind data from 1990 and 60 days of tide, current, wind and salinity data from 1991. The analyses defined "characteristics" of the tides and currents and identified possible forcing mechanisms. In Chapter 6 the numerical model will attempt to simulate the "characteristics" defined herein, the following summarizes the findings.
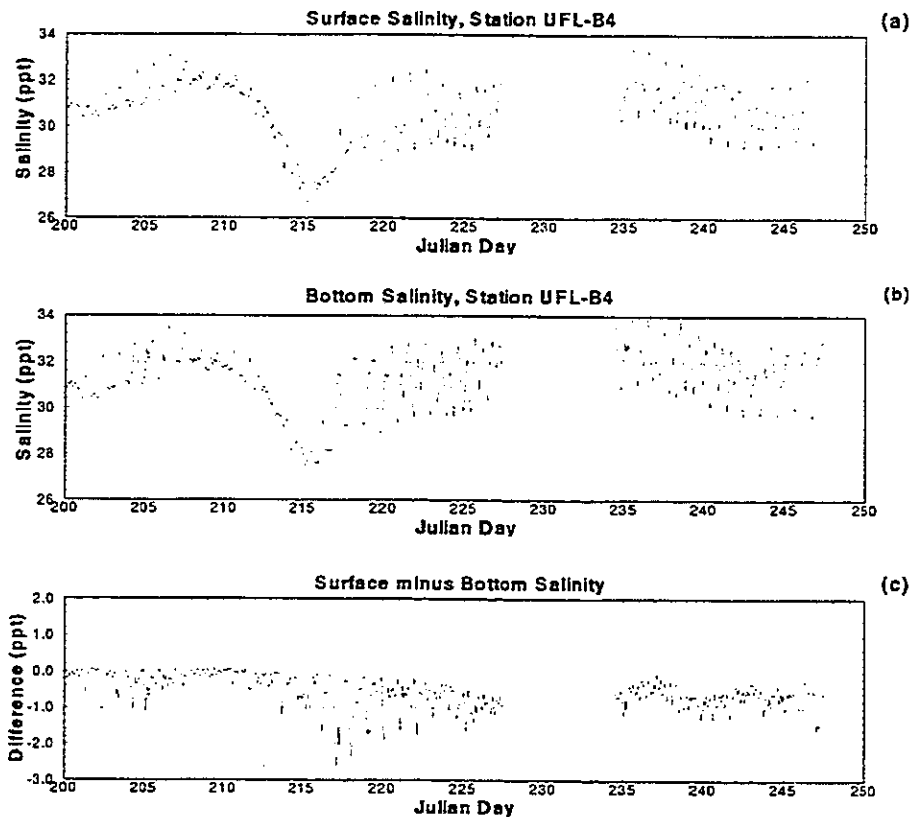
Figure 4.35: a) The surface salinity at UFL-B4 from Julian Day 200 to 250, 1991; b) The bottom salinity at UFL-B4 from Julian Day 200 to 250, 1991; c) The surface minus bottom salinity at UFL-B4 from Julian Day 200 to 250, 1991

Spectral analysis of the tides, currents and winds identified the relative energy levels within five frequency bands, the sub-tidal (greater than 2 day period), the diurnal (approximately 1 day), the semi-diurnal (approximately 12 hours), the third diurnal (approximately 8 hours), and the fourth diurnal (approximately 6 hours).

Analysis of the water surface elevations showed that between 98 and 99 percent of the total energy resides within the 5 frequency bands defined above. The inlets and constrictions within the system act as low pass filters resulting in increased diurnal and sub-tidal percent energies at the interior stations. In conjunction, the water surface elevations exhibit an increase in the third/fourth diurnal energy moving from

the offshore into the lagoons. Analysis of the offshore data shows that the energy levels decrease within the Gulf moving from north to south.

Analysis of the current data showed less of the total energy within the five frequency bands than was found for the tides, with percentages ranging from 71 to 95 percent. Stations UFL-B1 and UFL-B3 share similar characteristics as do UFL-B2 and UFL-B4. UFL-B1 and UFL-B3 show higher percentages of energy within the subtidal band while the other stations show near zero. In addition UFL-B1 and UFL-B3 exhibit a more even distribution of the diurnal to semi-diurnal energies while UFL-B2 and UFL-B4 exhibit high levels of semi-dirunal energy. One other characteristic shared by UFL-B1 and UFL-B3 is that they have less of their total energy within the five frequency bands defined above. The one common factor between UFL-B1 and UFL-B3, as versus UFL-B2 and UFL-B4, is that they receive forcing from two directions. The interaction of the two progressive waves may create the common characteristics.

All of the stations exhibit higher third/fourth diurnal energies in the bottom currents, with the shallow more interior stations showing the highest percentages. The high third/fourth dirunal energies within the bottom currents supports the assertion that bottom friction is the primary driving force in their creation.

The harmonic analysis of the water surface elevations generally supports the findings from the spectral analysis. Analysis of the form numbers and overtide rations as a function of position within the lagoons, indicates that while the higher harmonics increase moving further interior to the lagoons, the shift in energy from the semi-diurnal to the diurnal is due to constrictions within the system rather than travel distance or depth.

Calculation of the harmonic ellipses for the four bay stations shows that there is rotation of the current vectors over depth even in the very shallow stations. In addition, the bottom currents exhibit a higher degree of rotation, i.e. they are less

unidirectional. Finally, the data show that the current stations which exhibited similar characteristics (UFL-B1/B3 and UFL-B2/B4) show similar phase characteristics. At UFL-B1 and UFL-B3 the surface currents lead the bottom, at UFL-B2 and UFL-B4 the surface currents lag the bottom currents.

The tide and current data were filtered using a 48 hour low band pass filter. The tidal data exhibited residual fluctuations on the order of 10 to 20 cm. The currents showed less than 5 cm/sec fluctuations at all of the stations except UFL-B1, which had residual current fluctuations on the order of 15 to 20 cm/sec. Coherence values were calculated between the residual water level fluctuations and filtered wind vector components at 20 degree increments. The coherence was highest between the alongshore winds and the mean water level fluctuations indicating that the residual water levels are driven by Ekman Transport propagating in from the Gulf of Mexico. The coherences between the currents measured at UFL-B1 and the wind vector at incremental directions indicated that the fluctuations at UFL-B1 are the result of Ekman Transport within the Gulf of Mexico in combination with local wind forcing. The local wind forcing is felt most significantly at the surface. The other current stations (UFL-B2, UFL-B3, UFL-B4) did not exhibit significant coherences with any of the wind vector components.

Discharge measurements taken at either end of the southern portion of the Sarasota Bay System (Roberts Bay, Little Sarasota Bay and Blackburn Bay) defined the relative flow into this sub-basin. The data indicated that the flow through the northern opening was 40 percent greater than that through the southern end. Discrete discharge measurements taken within the inlets during ebb flow were analyzed to determine the relative flow through all of the openings to the Sarasota Bay System (Anna Maria Sound, Longboat Pass, New Pass, Big Pass and Venice Inlet). The results showed that 90 percent of the flow comes in through the three inlets with the remaining 10 percent through the northern (Anna Maria Sound) and southern

(Venice Inlet) openings.

Finally, salinity data from the four UFL bay stations were plotted and discussed along with freshwater inflow measurements from two locations, Manatee River and Walker Creek. The Manatee River discharges into the southwestern side of Tampa Bay near the entrance to Anna Maria Sound. Walker Creek is a small tributary which flows into Sarasota Bay, and is representative of the types of flow which impact the Sarasota Bay System. The salinity data show the most dynamic responses within the system to occur at UFL-B4 within Blackburn Bay. Rapid salinity drops of 3 to 4 ppt occur over short periods with flushing taking between 4 to 10 days depending upon the location. Based upon the salinity data from UFL-B3 Little Sarasota Bay shows the slowest flushing. UFL-B1 is also slow to return to pre-inflow conditions but this is largely due to the hydrograph of the Manatee River which is of a longer duration than that found for the small creeks.

CHAPTER 5
FORMULATION OF MODEL EQUATIONS

Although data collection provides many insights into the circulation and transport properties within barrier island lagoons, the lack of spatial resolution means that many of the gross physical properties such as flushing, spatial current patterns and residual circulation cannot be determined. In order to quantify these properties, a three-dimensional boundary-fitted circulation and transport model CH3D (Sheng, 1986) was applied to the study area. This model solves the three- dimensional continuity, momentum and advection-diffusion equations in transformed curvilinear coordinates.

The purpose of this chapter is to present the equations and boundary conditions solved for in CH3D. Although details of what is presented here can be found in other references (Sheng 1983, 1986, 1987, 1989; Sheng et al. 1989a, 1989b and 1989c), the author felt it necessary to include most of the relevant equations so that all the assumptions and simplifications can be evaluated in terms of the model results. The model has undergone many changes since its inception, the equations and relationships presented here represent the state of the model as used in this study.

The procedure will be to first present the more familiar Cartesian three-dimensional equations and boundary conditions in order to give the reader a base of reference. The vertical integration, sigma transformation and non-dimensionalization of the equations will then proceed in a stepwise manner culminating with the more general tensor invariant equations and finally the boundary fitted equations.

5.1   The Cartesian Equations of Motion and Transport

The Cartesian Reynold's averaged equations, which govern an incompressible fluid with both a gravitational and a Coriolis force acting upon it, can be written in general

118

tensor notation as:

$$\frac{\partial u_i}{\partial x_i} = 0 \tag{5.1}$$

$$\frac{\partial u_i}{\partial t} + u_j \frac{\partial u_i}{\partial x_j} = -\frac{\partial \overline{u_i' u_j'}}{\partial x_j} - \frac{1}{\rho}\frac{\partial P}{\partial x_i} + g_i - 2\epsilon_{ijk}\Omega_j u_k \tag{5.2}$$

$$\frac{\partial T}{\partial t} + u_j \frac{\partial T}{\partial x_j} = -\frac{\partial \overline{u_j' T'}}{\partial x_j} \tag{5.3}$$

$$\frac{\partial S}{\partial t} + u_j \frac{\partial S}{\partial x_j} = -\frac{\partial \overline{u_j' S'}}{\partial x_j} \tag{5.4}$$

$$\rho = \rho(T, S) \tag{5.5}$$

where equation 5.1 is the continuity equation, equation 5.2 is the momentum equation, equations 5.3 and 5.4 are the mass transport equations for salinity and temperature, and equation 5.5 is the equation of state. The terms in the equations are, u_i, the mean velocity components, x_i, the rectangular coordinates, g_i, the gravitational acceleration component, ϵ_{ijk}, the unit alternating tensor, and Ω_j, the angular velocity of the rotating earth. The primed terms are the turbulent fluctuating components, the overbarred terms in the momentum equation are the Reynold's stresses, and the overbarred terms in the salinity and temperature equation are the flux terms. To arrive at this form, the Boussinesq approximation is made. This means that the only effect the density variation has on the solution comes in through the pressure gradient terms. The temperature and salinity transport equations are shown separately as they each directly affect the solution of the momentum equations through the baroclinic forcing terms.

In order to further simplify the above equations, the turbulent Reynold's stresses are assumed to be equal to the mean flow gradient multiplied by the turbulent eddy viscosity. Another simplification which is made by most three-dimensional large scale circulation models is to assume a hydrostatic pressure distribution. This assumption is valid only when the vertical acceleration is negligible compared with the vertical pressure gradient. Introducing this assumption, along with the eddy viscosity, into

equations 5.1 through 5.4, gives the familiar form of the equations of motion and mass transport,

$$\frac{\partial u}{\partial x} + \frac{\partial v}{\partial y} + \frac{\partial w}{\partial z} = 0 \tag{5.6}$$

$$\frac{\partial u}{\partial t} + \frac{\partial uu}{\partial x} + \frac{\partial uv}{\partial y} + \frac{\partial uw}{\partial z} = fv - \frac{1}{\rho_0}\frac{\partial P}{\partial x} + \frac{\partial}{\partial x}(A_H\frac{\partial u}{\partial x}) \tag{5.7}$$
$$+ \frac{\partial}{\partial y}(A_H\frac{\partial u}{\partial y}) + \frac{\partial}{\partial z}(A_V\frac{\partial u}{\partial z})$$

$$\frac{\partial v}{\partial t} + \frac{\partial uv}{\partial x} + \frac{\partial vv}{\partial y} + \frac{\partial vw}{\partial z} = -fu - \frac{1}{\rho_0}\frac{\partial P}{\partial y} + \frac{\partial}{\partial x}(A_H\frac{\partial v}{\partial x}) \tag{5.8}$$
$$+ \frac{\partial}{\partial y}(A_H\frac{\partial v}{\partial y}) + \frac{\partial}{\partial z}(A_V\frac{\partial v}{\partial z})$$

$$\frac{\partial P}{\partial z} = -\rho g \tag{5.9}$$

$$\frac{\partial S}{\partial t} + \frac{\partial uS}{\partial x} + \frac{\partial vS}{\partial y} + \frac{\partial wS}{\partial z} = \frac{\partial}{\partial x}(D_H\frac{\partial S}{\partial x}) + \frac{\partial}{\partial y}(D_H\frac{\partial S}{\partial y}) \tag{5.10}$$
$$+ \frac{\partial}{\partial z}(D_V\frac{\partial S}{\partial z})$$

$$\frac{\partial T}{\partial t} + \frac{\partial uT}{\partial x} + \frac{\partial vT}{\partial y} + \frac{\partial wT}{\partial z} = \frac{\partial}{\partial x}(K_H\frac{\partial T}{\partial x}) + \frac{\partial}{\partial y}(K_H\frac{\partial T}{\partial y}) \tag{5.11}$$
$$+ \frac{\partial}{\partial z}(K_V\frac{\partial T}{\partial z})$$

where u, v, and w are the velocities in the x, y, and z directions, f is the corriolis parameter equal to $2\Omega sin\Phi$ (Φ is the latitude along the earth's surface), T and S are the temperature and salinity, A_H, D_H and K_H are the horizontal eddy viscosity and the horizontal diffusivities for salinity and temperature respectively, A_V, D_V and K_V are the vertical turbulent eddy viscosity and the vertical diffusivities for salinity and temperature respectively, P is the pressure, and ρ is the density.

These equations are solved within a specified domain. The solutions are dependent upon the boundary conditions applied on the surface of the domain, and the initial conditions. The following describes the general Cartesian boundary conditions used in the solution.

5.2 General Cartesian Boundary Conditions

For this study the domain in which these equations are solved is a partially enclosed water body, therefore the boundaries are the free surface, the point where land meets water, the bottom, and any prescribed surface which separates two water bodies.

5.2.1 Free Surface Boundary Conditions

At the free surface three conditions are applied. The first specifies that the horizontal component of the Reynold's stress is equal to the wind stress applied at the free surface:

$$\rho_0 A_V(\frac{\partial u}{\partial z}, \frac{\partial v}{\partial z}) = (\tau_{s_x}, \tau_{s_y}) = \rho_a C_d(u_w^2 + v_w^2)^{\frac{1}{2}}(u_w, v_w) \qquad (5.12)$$

where, τ_s is the wind stress at the free surface, ρ_a is the density of air, u_w and v_w are the components of the wind speed measured at some distance above the water surface, and C_d is the drag coefficient. The transfer of momentum across the air-water interface is a highly complex process and requires an understanding of the physics of the planetary boundary layer. It can be affected by many factors such as wave conditions, air temperature, proximity to land, etc. The drag coefficient is normally defined as a function of the wind speed at some height above the water surface through empirical relationships. For this study the results of Garratt (1967) are used to define the surface boundary condition. He gives the drag coefficient as a function of the wind speed measured at 10 meters above the water surface. The relationship states:

$$C_d = (0.75 + 0.067W_s)\,0.001 \qquad (5.13)$$

where W_s is the wind speed in m/s.

The second boundary condition is the kinematic free surface boundary condition which states:

$$w = \frac{\partial \zeta}{\partial t} + u\frac{\partial \zeta}{\partial x} + v\frac{\partial \zeta}{\partial y} \qquad (5.14)$$

where w is the vertical velocity component and ζ is the water surface elevation referenced to the mean water level.

The third is the dynamic boundary condition which states that the pressure at the free surface is equal to the atmospheric pressure (P_a). In general the pressure terms in the x and y equations of motion need to be resolved as a function of the water surface elevation and the density. Utilizing the dynamic boundary condition at the free surface, and integrating the vertical momentum equation over depth, an expression for the pressure can be defined as;

$$P(x, y, z, t) = -\int_\zeta^z \rho g \, dz + P_a \tag{5.15}$$

Substituting this term into the x and y direction pressure gradients and applying Leibnitz rule, the final forms of the pressure gradients are;

$$\frac{\partial P}{\partial x} = -g \int_\zeta^z \frac{\partial \rho}{\partial x} dz \;\; + \;\; \rho_s g \frac{\partial \zeta}{\partial x} + \frac{\partial P_a}{\partial x} \tag{5.16}$$

$$\frac{\partial P}{\partial y} = -g \int_\zeta^z \frac{\partial \rho}{\partial y} dz \;\; + \;\; \rho_s g \frac{\partial \zeta}{\partial y} + \frac{\partial P_a}{\partial y} \tag{5.17}$$

5.2.2 Bottom Boundary Conditions

In deeper water, the thickness of the bottom boundary layer is often negligibly small compared with the water depth. For this reason, the effect of the bottom friction upon the three-dimensional velocity field in deep water is negligible. However, in a shallow water body such as the one being considered for this study, the bottom boundary layer is a non-negligable fraction of the water depth. This makes the choice of the bottom boundary condition crucial in obtaining an accurate solution.

Many bottom boundary conditions have been used in the past. The most obvious one is the no slip condition. The problem with this boundary condition is that the laminar sublayer within the bottom boundary layer must be resolved, which would not be possible for our case given the varying depths in the solution domain (from 0.5 meters to 25 meters), and the use of the vertically-stretched (sigma) grid. Another

possible bottom boundary condition is the linear stress law which describes the bottom stress as a linear function of the near bottom velocity.

The bottom boundary condition used for this study is the quadratic stress law which states that the bottom shear stress is a function of the near bottom velocity such that:

$$(\tau_{b_x}, \tau b_y) = \rho C_d \sqrt{u_b^2 + v_b^2}(u_b, v_b) \qquad (5.18)$$

Brown and Trask (1980) found the drag coefficient, C_d, in a shallow estuary to be on the order of 0.035. A more reasonable formulation (Sheng, 1983) states that the drag coefficient is a function of the size of the bottom roughness elements (z_0) and the height at which the velocity u_b is measured, so long as z_1 is within the constant flux layer above the bottom (Tennekes and Lumly, 1972). The drag coefficient can be defined as:

$$C_d = \frac{\kappa^2}{ln(\frac{z_1}{z_0})^2} \qquad (5.19)$$

where κ is the Von Karman constant (0.4). For estuarine applications the range of expected roughness element heights is from 0.2 to 0.8 cm.

5.2.3 Lateral Boundary Conditions

In this section, a variety of lateral boundary conditions for the equations of motion in an estuary will be described including solid boundaries, rivers and open boundaries.

Along solid boundaries, there should be no flow across the boundary or transport of any substance across the boundary by advection or diffusion. In addition, a no slip condition is applied, i.e., the tangential velocities are zero.

Along river boundaries, the hydrodynamic variables (η, u, v, w, T, S) are prescribed. In order that this is valid, it is necessary to extend the river boundary sufficiently upstream from the entrance of the river to the estuary.

Along the open ocean boundaries, the hydrodynamic condition is defined by specifying the water surface elevation just outside the solution domain. This condition

is easier to apply than specifying the velocities along the open boundary, especially where the open boundary is fairly long (as in this study). If the large scale circulation along the open boundary can influence the solution within the system to a significant extent, specifying the water surface along the open boundary will not produce this. Therefore, it is important that the open boundaries be located sufficiently far from the domain of interest such that any inaccuracies there do not contaminate the interior solution. In this study the crucial areas of interest are inside of the lagoons, hence the open boundary is located offshore to allow the proper exchange of mass between the lagoon and the Gulf. This process is primarily driven by the water surface elevation gradients through the inlets and not the offshore currents, therefore the open boundary inaccuracies should not significantly influence the solution inside of the inlets.

Along open ocean boundaries of the model, possible boundary conditions for salinity transport include, an infinite reservior with constant value just outside the boundary and an infinite reservior during inflow but advection driven transport during outflow.

5.2.4 Initial Conditions

In order to solve partial differential equations such as the equations of motion and transport, it is necessary to define the initial conditions within the solution domain. Generally all the velocity components are specified as zero at the start of a model run. To eliminate any effects of the initial conditions on the solution, sufficient time must be allowed for the model to be spun up. Initial conditions of salinity or temperature should be based upon measured data. Whereas tidally driven circulation can be spun up within a few tidal cycles, baroclinic flows may require a number of days to "spin up".

5.3 Vertically Integrated Equations

Chapter 6 will introduce the methods used in the solution of the equations of motion and continuity. One portion of the solution uses a modified form of the vertically integrated shallow water wave equations. The following is a brief presentation of the derivation of these equations, a more complete derivation is presented in Dean and Dalrymple (1984).

The vertically integrated velocity components are defined as;

$$U = \int_{-h}^{\zeta} u\,dz$$

$$V = \int_{-h}^{\zeta} v\,dz$$

Integrating equations 5.6, 5.7 and 5.8, applying the free surface boundary condition and the Leibnitz rule gives the modified shallow water wave equations,

$$\frac{\partial \zeta}{\partial t} + \frac{\partial U}{\partial x} + \frac{\partial V}{\partial y} = 0 \tag{5.20}$$

$$\frac{\partial U}{\partial t} + \int_{-h}^{\zeta} \left(\frac{\partial uu}{\partial x} + \frac{\partial uv}{\partial y} \right) = -\ gH\frac{\partial \zeta}{\partial x} + fV + \tau_{s_x} - \tau_{b_x} \tag{5.21}$$

$$-\ \frac{g}{\rho_0} \int_{-h}^{\zeta} \int_{z}^{\zeta} \frac{\partial \rho}{\partial x} dz$$

$$+\ \int_{-h}^{\zeta} \left(\frac{\partial}{\partial x}(A_h\frac{\partial u}{\partial x}) + \frac{\partial}{\partial y}(A_h\frac{\partial u}{\partial y}) \right) dz$$

$$\frac{\partial V}{\partial t} + \int_{-h}^{\zeta} \left(\frac{\partial uv}{\partial x} + \frac{\partial vv}{\partial y} \right) = -\ gH\frac{\partial \zeta}{\partial y} - fU + \tau_{s_y} - \tau_{b_y} \tag{5.22}$$

$$-\ \frac{g}{\rho_0} \int_{-h}^{\zeta} \int_{z}^{\zeta} \frac{\partial \rho}{\partial y} dz$$

$$+\ \int_{-h}^{\zeta} \left(\frac{\partial}{\partial x}(A_h\frac{\partial v}{\partial x}) + \frac{\partial}{\partial y}(A_h\frac{\partial v}{\partial y}) \right) dz$$

where, H is the total depth, $H = h + \zeta$, τ_s is the wind stress applied at the free surface, and τ_b is the bottom friction.

The inertial terms, the horizontal diffusion terms, and the baroclinic forcing terms are shown as integrated three-dimensional values because in the model they are calculated by vertically summing the three-dimensional results rather than vertically
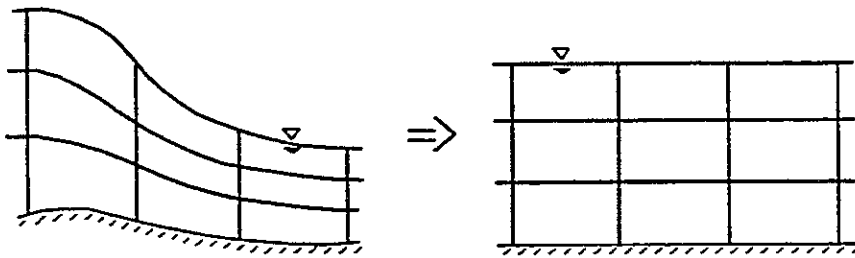
Figure 5.1: An idealized representation of the Sigma transformation integrating the terms prior to solving.

5.4   Sigma Stretching of Equations

Two types of vertical grids are generally used in three-dimensional modeling of estuaries and lakes. The first type of grid, a z-grid, defines layers of constant depth along the z-plane. This grid structure represents the physics within the flow well, and the equations are simple, but problems can arise where the depth varies a great deal over the solution domain. In order to get sufficient vertical resolution in the shallow regions, it is necessary to have a large number of grids in the deeper sections. In addition, if the grid resolution in the horizontal is insufficient, a stair step representation of what would normally be a smoothly varying bottom can occur.

The second possibility is to do a transformation on the equations by defining a

new variable, σ, such that (Phillips, 1957):

$$\sigma = \frac{z - \zeta(x,y,t)}{h(x,y) + \zeta(x,y,t)} \tag{5.23}$$

This transforms the region from $-h$ to ζ into a layer of constant width from $\sigma = 0$ to $\sigma = -1$, Figure 5.1. The advantages of this transformation are that the bottom topography is smoothly represented and the vertical grid resolution is the same in the shallow regions and the deeper regions. The disadvantages are that additional terms are introduced into the equations of motion and continuity, and in regions where the bottom topography changes abruptly, errors can be introduced(Haney, 1990).

Details of the sigma transformation for the three-dimensional equations of motion can be found in Sheng (1983). The transformed equations of motion are:

$$\frac{\partial \zeta}{\partial t} + \frac{\partial Hu}{\partial x} + \frac{\partial Hv}{\partial y} + H\frac{\partial \omega}{\partial \sigma} \tag{5.24}$$

$$\frac{1}{H}\left(\frac{\partial Hu}{\partial t} + \frac{\partial Huu}{\partial x} + \frac{\partial Huv}{\partial y}\right) + \frac{\partial u\omega}{\partial \sigma} = fv - g\frac{\partial \zeta}{\partial x} \tag{5.25}$$

$$+ g\left(H\int_\sigma^0 \frac{\partial \rho}{\partial x}d\sigma + \frac{\partial H}{\partial x}(\int_\sigma^0 \rho d\sigma + \sigma\rho)\right)$$

$$+ \frac{\partial}{\partial x}(A_h\frac{\partial u}{\partial x}) + \frac{\partial}{\partial y}(A_h\frac{\partial u}{\partial y}) + \frac{1}{H^2}\frac{\partial}{\partial \sigma}(A_v\frac{\partial u}{\partial \sigma})$$

$$\frac{1}{H}\left(\frac{\partial Hv}{\partial t} + \frac{\partial Huv}{\partial x} + \frac{\partial Hvv}{\partial y}\right) + \frac{\partial u\omega}{\partial \sigma} = -fu - g\frac{\partial \zeta}{\partial y} \tag{5.26}$$

$$+ g\left(H\int_\sigma^0 \frac{\partial \rho}{\partial y}d\sigma + \frac{\partial H}{\partial y}(\int_\sigma^0 \rho d\sigma + \sigma\rho)\right)$$

$$+ \frac{\partial}{\partial x}(A_h\frac{\partial u}{\partial y}) + \frac{\partial}{\partial y}(A_h\frac{\partial u}{\partial y}) + \frac{1}{H^2}\frac{\partial}{\partial \sigma}(A_v\frac{\partial u}{\partial \sigma})$$

The transformation of the diffusion terms produces a series of higher order terms which are considered to be negligible compared with the first order terms and are ignored in the solution (Sheng, 1986).

Applying the same transformations to the advection and diffusion equations for salinity and temperature gives;

$$\frac{1}{H}\left(\frac{\partial HS}{\partial t} + \frac{\partial HuS}{\partial x} + \frac{\partial HvS}{\partial y}\right) + \frac{\partial S\omega}{\partial \sigma} = \frac{\partial}{\partial x}(D_h\frac{\partial S}{\partial x}) \tag{5.27}$$

$$\frac{1}{H}\left(\frac{\partial HT}{\partial t} + \frac{prHuT}{\partial x} + \frac{\partial HvT}{\partial y}\right) + \frac{\partial T\omega}{\partial \sigma} = \frac{\partial}{\partial x}\left(D_h\frac{\partial T}{\partial x}\right)$$

$$+ \frac{\partial}{\partial y}\left(D_h\frac{\partial S}{\partial y}\right) + \frac{1}{H^2}\frac{\partial}{\partial \sigma}\left(D_v\frac{\partial S}{\partial \sigma}\right)$$

$$+ \frac{\partial}{\partial y}\left(D_h\frac{\partial T}{\partial y}\right) + \frac{1}{H^2}\frac{\partial}{\partial \sigma}\left(D_v\frac{\partial T}{\partial \sigma}\right) \tag{5.28}$$

Once again the higher order terms introduced by the transformation are considered negligible.

The vertical velocity in the sigma transformed computational domain can be related to the vertical velocity in the physical domain by the following equation.

$$w = H\omega + (1+\sigma)\frac{d\zeta}{dt} + \sigma\left(u\frac{\partial h}{\partial x} + v\frac{\partial h}{\partial y}\right) \tag{5.29}$$

where,

$$w = \frac{dz}{dt} \tag{5.30}$$

and,

$$\omega = \frac{d\sigma}{dt} \tag{5.31}$$

5.5 Non-Dimensionalization of Equations

Non-dimensionalization of the equations allows the evaluation of significant terms such as the Rossby Number, the Ekman Number, etc. These terms result from the non-dimensionalization and appear as multipliers to terms within the equation which have values on the order of unity. The non-dimensional variables and non-dimensional numbers are listed in Appendix C;

The non-dimensional sigma transformed Cartesian equations are;

$$\frac{\partial \zeta}{\partial t} + \beta\frac{\partial Hu}{\partial x} + \beta\frac{\partial Hv}{\partial y} + \beta\frac{\partial H\omega}{\partial \sigma} = 0 \tag{5.32}$$

$$\frac{1}{H}\frac{\partial Hu}{\partial t} + \frac{R_0}{H}\left(\frac{\partial Huu}{\partial x} + \frac{\partial Huv}{\partial y}\right) \quad + \quad \frac{R_0}{H}\left(\frac{\partial Hu\omega}{\partial \sigma}\right) = -\frac{\partial \zeta}{\partial x} + v \qquad (5.33)$$

$$+ \quad \frac{E_v}{H^2}\frac{\partial}{\partial \sigma}A_v\frac{\partial u}{\partial \sigma}$$

$$+ \quad E_h\left(\frac{\partial}{\partial x}(A_h\frac{\partial u}{\partial x}) + \frac{\partial}{\partial y}(A_h\frac{\partial u}{\partial y})\right)$$

$$- \quad \frac{R_0}{F_{r_D}^2}\left(H\int_\sigma^0 \frac{\partial \rho}{\partial x}d\sigma + \frac{\partial H}{\partial x}(\int_\sigma^0 \rho d\sigma + \sigma\rho)\right)$$

$$\frac{1}{H}\frac{\partial Hv}{\partial t} + \frac{R_0}{H}\left(\frac{\partial Huv}{\partial x} + \frac{\partial Hvv}{\partial y}\right) \quad + \quad \frac{R_0}{H}\left(\frac{\partial Hv\omega}{\partial \sigma}\right) = -\frac{\partial \zeta}{\partial y} + v \qquad (5.34)$$

$$+ \quad \frac{E_v}{H^2}\frac{\partial}{\partial \sigma}A_v\frac{\partial v}{\partial \sigma}$$

$$+ \quad E_h\left(\frac{\partial}{\partial x}(A_h\frac{\partial v}{\partial x}) + \frac{\partial}{\partial y}(A_h\frac{\partial v}{\partial y})\right)$$

$$- \quad \frac{R_0}{F_{r_D}^2}\left(H\int_\sigma^0 \frac{\partial \rho}{\partial y}d\sigma + \frac{\partial H}{\partial y}(\int_\sigma^0 \rho d\sigma + \sigma\rho)\right)$$

$$\frac{1}{H}\frac{\partial HS}{\partial t} + \frac{R_o}{H}\left(\frac{\partial HuS}{\partial x} + \frac{\partial HvS}{\partial y}\right) \quad + \quad \frac{R_0}{H}\left(\frac{\partial H\omega S}{\partial \sigma}\right) = \frac{E_v}{S_{c_v}}\frac{1}{H^2}\frac{\partial}{\partial \sigma}(D_v\frac{\partial S}{\partial \sigma}) \quad (5.35)$$

$$+ \quad \frac{E_h}{S_{c_h}}\left(\frac{\partial}{\partial x}(D_h\frac{\partial S}{\partial x}) + \frac{\partial}{\partial y}(D_h\frac{\partial S}{\partial y})\right)$$

$$\frac{1}{H}\frac{\partial HT}{\partial t} + \frac{R_o}{H}\left(\frac{\partial HuT}{\partial x} + \frac{\partial HvT}{\partial y}\right) \quad + \quad \frac{R_0}{H}\left(\frac{\partial H\omega T}{\partial \sigma}\right) = \frac{E_v}{S_{c_v}}\frac{1}{H^2}\frac{\partial}{\partial \sigma}(D_v\frac{\partial T}{\partial \sigma}) \quad (5.36)$$

$$+ \quad \frac{E_h}{S_{c_h}}\left(\frac{\partial}{\partial x}(D_h\frac{\partial T}{\partial x}) + \frac{\partial}{\partial y}(D_h\frac{\partial T}{\partial y})\right)$$

5.6 Boundary Fitted Equations

When solving the equations of motion within a body of water with complicated geometry, it is often difficult to generate a cartesian grid that adequately represents the existing shoreline without using restrictively small grids. The trade off is often a stair step representation of what is actually a smoothly varying shoreline in order to save computation time. Using a coordinate system which more closely fits the actual shorelines is a more natural solution. For example, cylindrical coordinates work best in simulations of pipe flow; spherical coordinates are most appropriate in global circulation modeling. The boundary fitted coordinate system is the natural solution for a system as complex as Sarasota Bay.

5.6.1 Grid Generation

The purpose of a boundary fitted grid is to allow the mapping of a complex non-orthogonal grid, which closely represents the desired solution domain, into a uniform rectangular grid on which finite differencing of the solution is made simple, Figure 5.2. Thompson(1983) developed a method to generate a 2-dimensional boundary fitted grid by solving the elliptic Poisson Equations. These equations define the relationship between the coordinates in the actual domain (x,y) to the coordinates in the transformed region (ξ, η), the equations are:

$$\xi_{xx} + \xi_{yy} = P$$
$$\eta_{xx} + \eta_{yy} = Q \tag{5.37}$$

with the boundary conditions,

$$\xi = \text{constant} \quad \text{On a and c}$$
$$\eta = \eta(x, y)$$

$$\eta = \text{constant} \quad \text{On b and d}$$
$$\xi = \xi(x, y)$$

where, P and Q are functions which are used to define the grid characteristics. Although these are the equations which describe the grid generation problem, in practice they are not what is solved for. It is necessary to define the interior grid coordinates in the actual domain (x,y) given the coordinates on the boundary of the domain. The solution which generates the interior points must solve the Poisson Equation. The equations which are solved are obtained by interchanging the dependent and independent variables in equations 5.37.

Grid generation for this study was performed using a program developed by Thompson (1983) termed WESCORA. The techniques used in the development of this program are only presented briefly here to introduce the concepts. Further explanation can be found in the references listed.
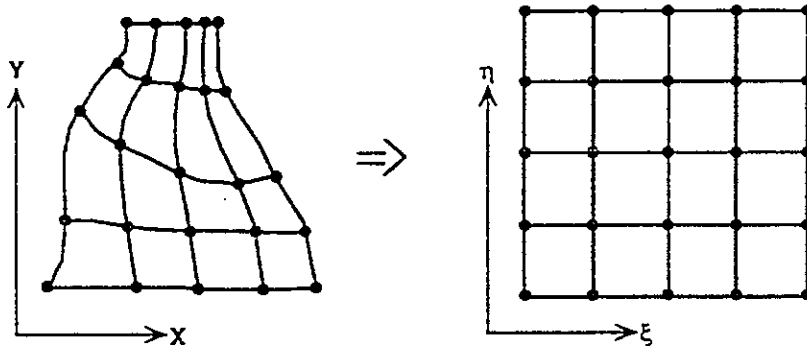
Figure 5.2: An Idealized Boundary Fitted Transformation

5.6.2   Transformation of the Equations of Motion and Transport

In order to solve the equations of motion and transport within the transformed region, it is necessary to convert the governing equations into the boundary-fitted coordinates. A variety of methods are available to accomplish this conversion. Before giving a description of the methods used in CH3D some explanation of the basic curvilinear system is warranted.

In two dimensions, the general curvilinear coordinate system consists of intersecting curves along which one of the coordinates remains constant while the other varies, Figure 5.3. Looking at the figure three types of vector components exist in the two coordinate systems, physical vector components $u(i)$, covariant vector components u_i, and contravariant vector components u^i. Relationships between the three vector components in the two coordinate systems can be established via tensor analysis. In
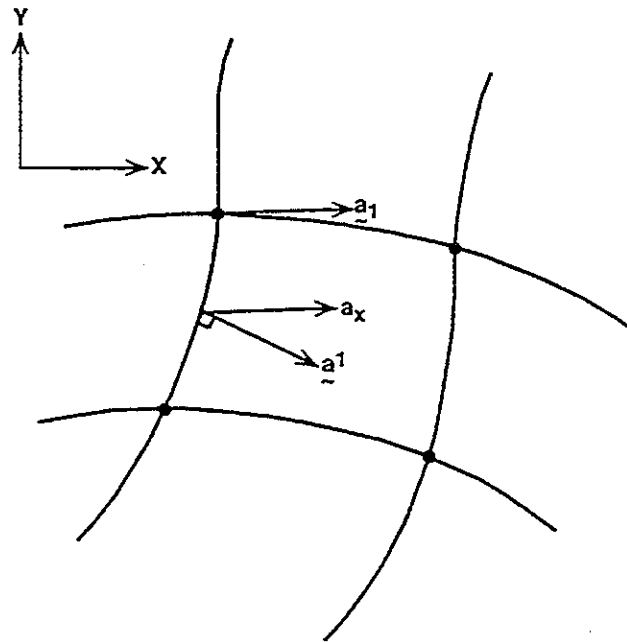
Figure 5.3: Cartesian vs. Curvilinear Coordinate Systems

the curvilinear system the contravariant vector components and the covariant components are locally orthogonal or parallel to the grid lines respectively. The physical components in the curvilinear system are neither orthogonal nor parallel to the grid lines. In the Cartesian system the three types of vectors are equal.

When transforming the equations from the Cartesian system to the curvilinear system a variety of choices on what is to be transformed are available. The transformed equations can be obtained in terms of any of the three vector components described above (Sokolnikoff, 1960). For the CH3D model, a transformation on both the dependent and independent variables is performed and the vector components are defined in terms of the contravariant base vectors. This choice makes the application of the boundary conditions easier as the components are orthogonal to the grid lines. If the physical components had been used, some problems would have resulted when trying to apply the boundary conditions within the transformed region, as the vectors

are neither parallel nor orthogonal to the local grid lines.

Appendix C presents a detailed derivation of the tensor invariant equations. Given the definitions of the different types of differentiation, and following the rules of indexing, the tensor invariant equations can be expanded to give the final form of the curvilinear, sigma-stretched, non-dimensional equations. The expansion of the equations is a difficult and tedious exercise. In the original derivation of these equations (Sheng, 1986) a symbolic manipulator was used to derive the final form used in the model CH3D. In addition, a recent rederivation of the inertial terms was performed in the momentum equations (Sheng, 1989). The final results are;

$$
\zeta_t + \frac{\beta}{\sqrt{g_o}} \left[\frac{\partial}{\partial \xi}(\sqrt{g_o} H u) + \frac{\partial}{\partial \eta}(\sqrt{g_o} H v) \right] + \beta \frac{\partial H \omega}{\partial \sigma} = 0 \qquad (5.38)
$$

the continuity equation,

$$
\begin{aligned}
\frac{1}{H} \frac{\partial H u}{\partial t} = \ & - \ \left(g^{11} \frac{\partial \zeta}{\partial \xi} + g^{12} \frac{\partial \zeta}{\partial \eta} \right) + \frac{g_{12}}{\sqrt{g_o}} u + \frac{g_{22}}{\sqrt{g_o}} v \qquad (5.39) \\
& - \ \frac{R_o}{\sqrt{g_o} H} \left\{ x_\eta \left[\frac{\partial}{\partial \xi}(y_\xi \sqrt{g_o} H u u + y_\eta \sqrt{g_o} H u v) \right. \right. \\
& \quad\quad\quad - \ \left. \frac{\partial}{\partial \eta}(y_\xi \sqrt{g_o} H u v + y_\eta \sqrt{g_o} H v v) \right] \\
& \quad - \ y_\eta \left[\frac{\partial}{\partial \xi}(x_\xi \sqrt{g_o} H u u + x_\eta \sqrt{g_o} H u v) \right. \\
& \quad\quad\quad - \ \left. \frac{\partial}{\partial \eta}(x_\xi \sqrt{g_o} H u v + x_\eta \sqrt{g_o} H v v) \right] \\
& \quad + \ \left. g_o \frac{\partial H u \omega}{\partial \sigma} \right\} + \frac{E_v}{H^2} \frac{\partial}{\partial \sigma} \left(A_v \frac{\partial u}{\partial \sigma} \right) \\
& - \ \frac{Ro}{Fr_d^2} \left[H \int_\sigma^0 \left(g^{11} \frac{\partial \rho}{\partial \xi} + g^{12} \frac{\partial \rho}{\partial \eta} \right) d\sigma \right. \\
& \quad + \ \left. \left(g^{11} \frac{\partial H}{\partial \xi} + g^{12} \frac{\partial H}{\partial \eta} \right) \left(\int_\sigma^0 \rho d\sigma + \sigma \rho \right) \right] \\
& + \ E_H A_H \cdot (\text{Horizontal Diffusion of } u)
\end{aligned}
$$

the x-direction momentum equation,

$$
\frac{1}{H} \frac{\partial H v}{\partial t} = \ - \ \left(g^{21} \frac{\partial \zeta}{\partial \xi} + g^{22} \frac{\partial \zeta}{\partial \eta} \right) - \left(\frac{g_{11}}{\sqrt{g_o}} u + \frac{g_{21}}{\sqrt{g_o}} v \right) \qquad (5.40)
$$

$$+ \frac{R_o}{\sqrt{g_o}H} \left\{ y_\xi \left[\frac{\partial}{\partial \xi} (x_\xi \sqrt{g_o} Huu + x_\eta \sqrt{g_o} Huv) \right. \right.$$

$$+ \frac{\partial}{\partial \eta} (x_\xi \sqrt{g_o} Huv + x_\eta \sqrt{g_o} Hvv) \bigg]$$

$$- x_\xi \left[\frac{\partial}{\partial \xi} (y_\xi \sqrt{g_o} Huu + y_\eta \sqrt{g_o} Huv) \right.$$

$$+ \left. \left. \frac{\partial}{\partial \eta} (y_\xi \sqrt{g_o} Huv + y_\eta \sqrt{g_o} Hvv) \right] \right\}$$

$$+ \frac{E_v}{H^2} \frac{\partial}{\partial \sigma} \left(A_v \frac{\partial v}{\partial \sigma} \right)$$

$$- \frac{Ro}{F_{r^2}} \left[H \int_\sigma^o \left(g^{21} \frac{\partial \rho}{\partial \xi} + g^{22} \frac{\partial \rho}{\partial \eta} \right) d\sigma \right.$$

$$+ \left. \left(g^{21} \frac{\partial H}{\partial \xi} + g^{22} \frac{\partial H}{\partial \eta} \right) \left(\int_\sigma^o \rho d\sigma + \sigma \rho \right) \right]$$

$$+ E_H A_H (\text{Horizontal Diffusion})$$

the y-direction momentum equation,

$$\frac{\partial HS}{\partial t} = \frac{E_v}{HS_{c_v}} \frac{\partial}{\partial \sigma} \left(D_v \frac{\partial S}{\partial \sigma} \right) - R_o \frac{\partial H\omega S}{\partial \sigma} \tag{5.41}$$

$$- \frac{R_o}{\sqrt{g_o}} \left[\frac{\partial}{\partial \xi} (\sqrt{g_o} HuS) + \frac{\partial}{\partial \eta} (\sqrt{g_o} HvS) \right]$$

$$+ \frac{E_h H}{S_{c_h}} \left[g^{11} \frac{\partial^2 S}{\partial \xi^2} + 2 g^{12} \frac{\partial^2 S}{\partial \eta \partial \xi} + g^{22} \frac{\partial^2 S}{\partial \eta^2} \right]$$

$$\frac{\partial HT}{\partial t} = \frac{E_v}{HP_{r_v}} \frac{\partial}{\partial \sigma} \left(K_v \frac{\partial T}{\partial \sigma} \right) - R_o \frac{\partial H\omega T}{\partial \sigma} \tag{5.42}$$

$$- \frac{R_o}{\sqrt{g_o}} \left[\frac{\partial}{\partial \xi} (\sqrt{g_o} HuT) + \frac{\partial}{\partial \eta} (\sqrt{g_o} HvT) \right]$$

$$+ \frac{E_h H}{S_{c_h}} \left[g^{11} \frac{\partial^2 T}{\partial \xi^2} + 2 g^{12} \frac{\partial^2 T}{\partial \eta \partial \xi} + g^{22} \frac{\partial^2 T}{\partial \eta^2} \right]$$

the advection-diffusion equations for temperature and salinity.

Likewise the 2-Dimensional boundary-fitted equations of motion and continuity can be obtained:

$$\frac{\partial \zeta}{\partial t} = \frac{\beta}{\sqrt{g_o}} \left[\frac{\partial}{\partial \xi} (\sqrt{g_o} U + \frac{\partial}{\partial \eta} \sqrt{g_o} V) \right] \tag{5.43}$$

$$\frac{\partial U}{\partial t} = - H \left(g^{11} \frac{\partial \zeta}{\partial \xi} + g^{12} \frac{\partial \zeta}{\partial \eta} \right) + \frac{g_{12}}{\sqrt{g_o}} U + \frac{g_{22}}{\sqrt{g_o}} V \tag{5.44}$$

$$- \ R_o \int_{-1}^0 [\text{x-Direction Inertia Terms}] \, d\sigma + \tau_{s_x} - \tau_{b_x}$$

$$- \ \frac{HR_o}{F_r^2} \int_{-1}^0 [\text{x-Direction Baroclinic Terms}] \, d\sigma$$

$$+ \ HE_H A_H \int_{-1}^0 [\text{x-Direction Horizontal Diffusion Terms}] \, d\sigma$$

$$\frac{\partial V}{\partial t} = \ - \ H \left(g^{21} \frac{\partial \zeta}{\partial \xi} + g^{22} \frac{\partial \zeta}{\partial \eta} \right) + \frac{g_{11}}{\sqrt{g_o}} U + \frac{g_{21}}{\sqrt{g_o}} V \qquad (5.45)$$

$$- \ R_o \int_{-1}^0 [\text{y-Direction Inertia Terms}] \, d\sigma + \tau_{s_y} - \tau_{b_y}$$

$$- \ \frac{HR_o}{F_r^2} \int_{-1}^0 [\text{y-Direction Baroclinic Terms}] \, d\sigma$$

$$+ \ HE_H A_H \int_{-1}^0 [\text{y-Direction Horizontal Diffusion Terms}] \, d\sigma$$

The integrated terms are not fully listed in these equations because they have already been presented in equations 5.39 and 5.40.

Applying the transformations to the boundary conditions presented earlier gives for the free surface,

$$A_v \left(\frac{\partial u}{\partial \sigma}, \frac{\partial v}{\partial \sigma} \right) = \frac{H}{E_v} (\tau_{s_\xi}, \tau_{s_\eta})$$
$$\frac{\partial S}{\partial \sigma} = 0$$

where, τ_{s_ξ} and τ_{s_η} are the contravariant wind stress vectors at the surface calculated using Garratt's formula. The bottom boundary conditions become,

$$A_v \left(\frac{\partial u}{\partial \sigma}, \frac{\partial v}{\partial \sigma} \right) = \frac{H}{E_v} (\tau_{b_\xi}, \tau_{b_\eta})$$
$$= \frac{U_r}{A_{v_r}} X_r Z_r C_d \left[g_{11} u^2 + 2g_{12} uv + g_{22} v^2 \right] (u, v)$$
$$\frac{\partial T}{\partial \sigma} = 0$$
$$\frac{\partial S}{\partial \sigma} = 0$$

where u and v are the contravariant bottom velocity components.

The full set of boundary-fitted equations solved for in the model have now been derived. The derivation was presented to allow a complete understanding of all as-

sumptions made in the model and give the reader a basis for evaluating the results presented later.

CHAPTER 6
THREE DIMENSIONAL NUMERICAL MODELING

The first portion of this chapter presents the boundary conditions, numerical grid, bathymetry, initial conditions and all assumptions utilized in applying the three-dimensional curvilinear grid model (CH3D) described in Chapter 5. The model is then calibrated to the data set presented in Chapter 4 and tested for sensitivity through variation in key input parameters. Once calibrated, the model is utilized to examine the relative contributions from the various forcing mechanisms on the short term and residual tides and currents through applications under varying forcing conditions and examination of the magnitudes of the non-dimensional terms within the equations of motion.

6.1   Numerical Grid and Bathymetry

Figure 6.1 presents the curvilinear grid utilized in this study. The grid covers all of Tampa Bay, Anna Maria Sound, Sarasota Bay, Roberts Bay, Little Sarasota Bay, Blackburn Bay and approximately 3-5 kilometers into the Gulf of Mexico. The grid spacing varies from 1 to 2 kilometers inside of Tampa Bay and in the Gulf of Mexico, down to 75 meters inside of Blackburn Bay and near Venice Inlet. The reduction in grid spacing reflects the changes in the scale of the waterbody from north to south.

The grid was developed under two conflicting goals; the first was to provide sufficient resolution to accurately represent the complex geometry of the entire system; the second was to minimize the computational effort of the three-dimensional model. The grid utilized within the study reflects a balance between these two goals.

The Tampa Bay portion of the grid was not originally included and the boundary

137
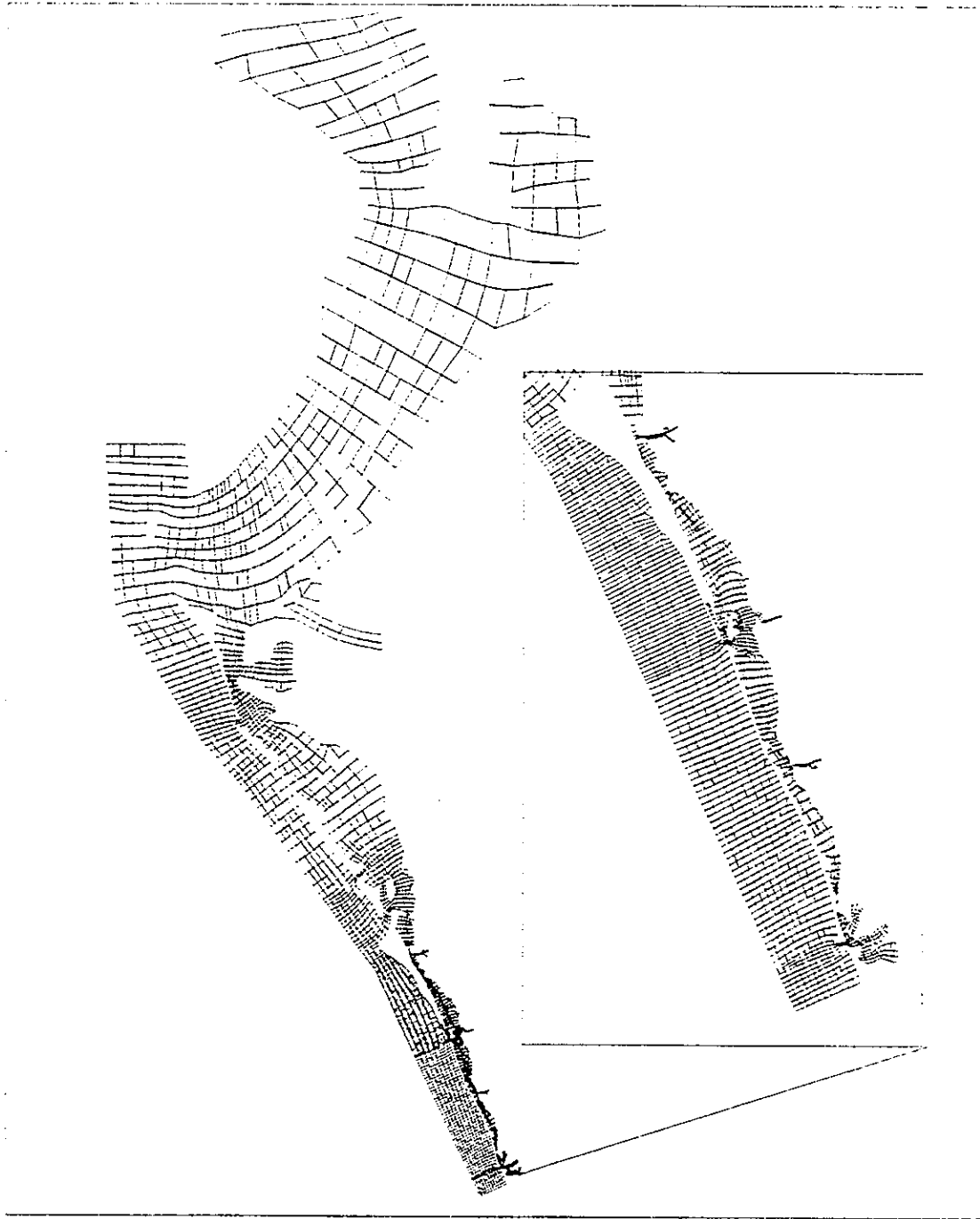
Figure 6.1: The curvilinear grid utilized with the numerical model CH3D.

only extended to the northern end of Anna Maria Sound. As Tampa Bay was not within the domain of interest this seemed to be an appropriate boundary. The decision to add Tampa Bay was based upon analysis of the current measurements taken at Station UFL-B1 and presented in Chapter 4. The residual currents indicated interactions between Tampa Bay and Sarasota Bay. The exact forcing mechanism was unknown at the time of the grid generation, and therefore it was determined that isolation of the boundary condition away from this area was necessary to allow for accurate simulation of the flow. A grid which represented only portions of Tampa Bay, would not have allowed the tidal wave to propagate in a realistic fashion, therefore the entire bay was included. The resolution within Tampa Bay was kept to the minimum required to develop accurate boundary conditions at the north end of Anna Maria Sound.

Within the study area, the curvilinear grid is designed to represent the complex geometry associated with the Intracoastal Waterway, the many tidal flats, the complex inlet bathymetry, the multiple islands, and the river and creek inflows. In regions where the Intracoastal Waterway is dredged through shallow waters, the grid resolves the narrow waterway (50 to 75 meters in width) as a series of single grids. This is most evident within Little Sarasota Bay and Blackburn Bay.

Figure 6.2 presents a contour plot of the bathymetry utilized in the numerical model for Anna Maria Sound, Sarasota Bay, Roberts Bay and offshore. The data used to generate the depths were taken from existing NOAA charts along with a bathymetric survey conducted by the University of Florida in September of 1990. The survey data were only used to verify the depths from the NOAA charts because the resolution was relatively coarse.

Figure 6.3 presents a contour plot of the bathymetry for Little Sarasota Bay and Blackburn Bay. The location of the Intracoastal Waterway is evident in the plots. Given the aerial extent of the study area, along with the variations in the lagoon
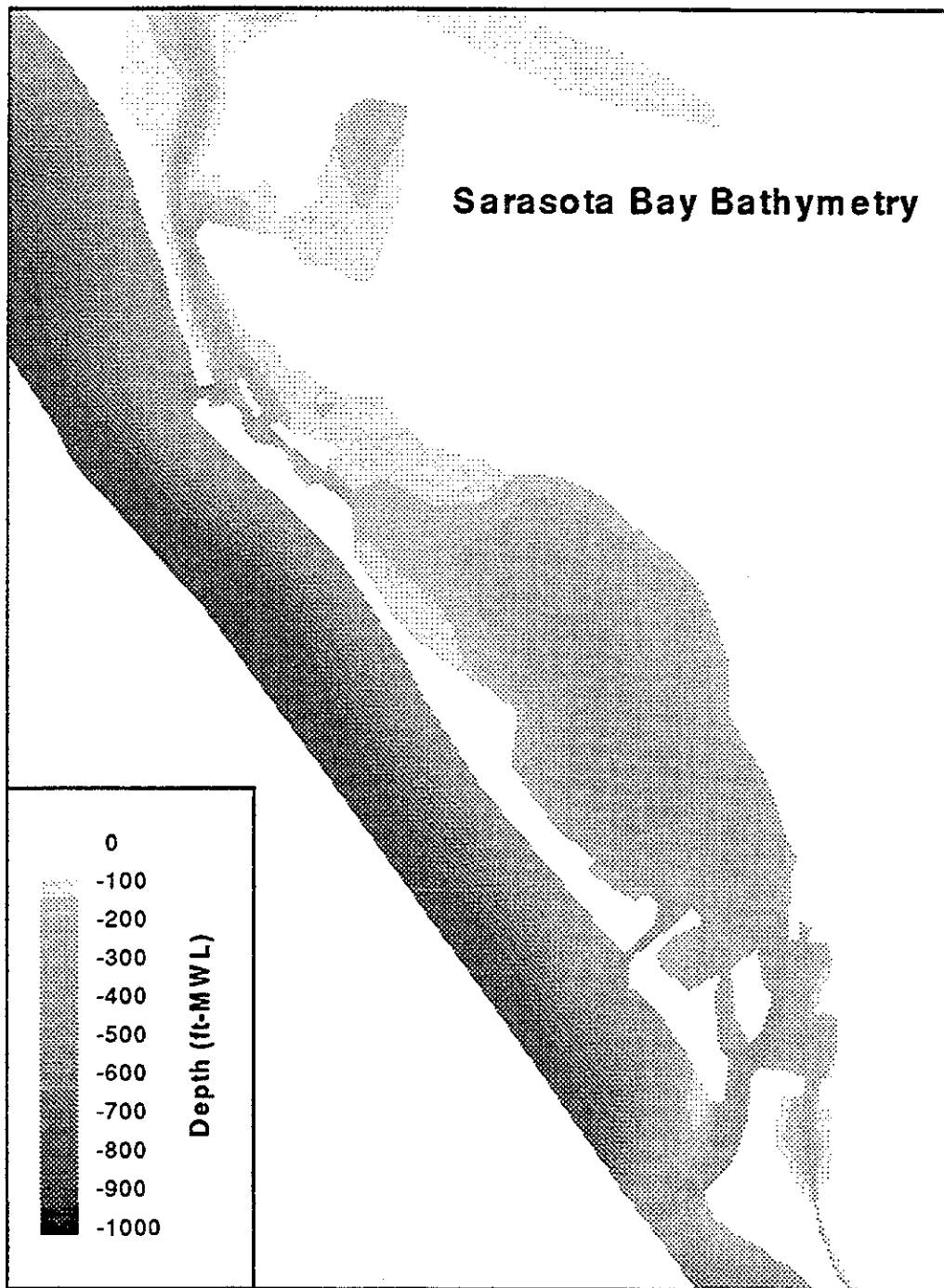
Figure 6.2: The model bathymetry within Anna Maria Sound, Sarasota Bay, Roberts Bay and the northern offshore region.
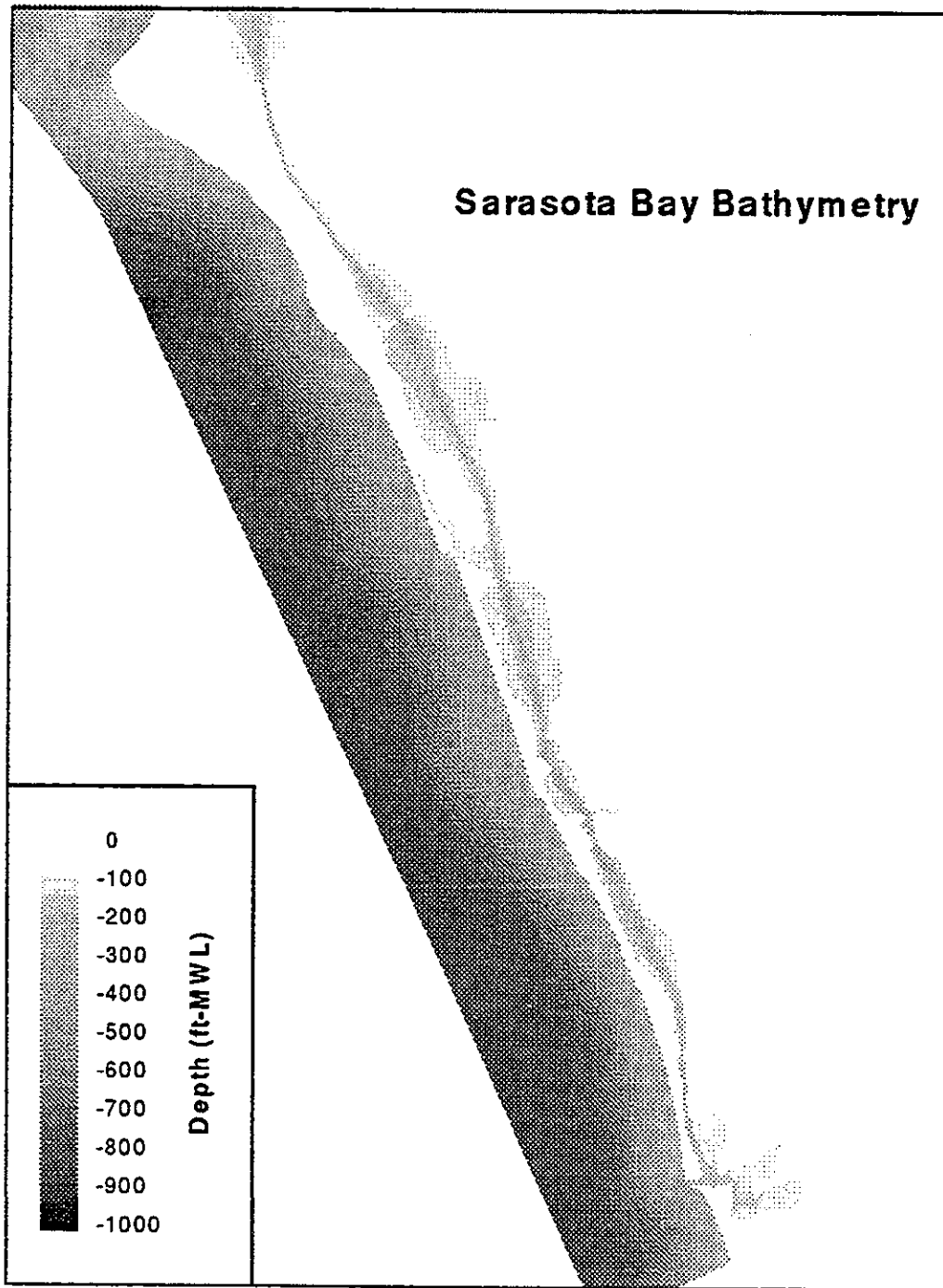
Figure 6.3: The model bathymetry within Little Sarasota Bay, Blackburn Bay and the southern offshore region.

scales, the advantages provided by the use of the curvilinear grid are apparent. The use of a Cartesian grid would have required a much finer resolution to perform accurate simulations.

6.2 Boundary Conditions

In Chapter 5 the general boundary conditions within the model were described. These include the bottom boundary, the free-surface boundary, the closed lateral boundaries, and the open lateral boundaries. The following describes the boundary conditions utilized at the free surface, and along the open boundaries to simulate the circulation in July/August of 1991.

6.2.1 Tidal Forcing

In Chapter 3, the locations of the offshore instrument platforms UFL-O1 and UFL-O2 were given (Figures 3.1 and 3.2). At these stations, the average subsurface pressure was measured at 15 minute increments, which were then converted to water surface elevation using the hydrostatic assumption. Additionally, pressure measurements were recorded by NOAA offshore of the entrance to Tampa Bay. These three data sets were utilized to develop the offshore water surface elevation boundary conditions.

As shown on Figure 6.1, the offshore boundary extends along the entire western side of the grid. It was necessary to modify the model (CH3D) to allow for calculation of a variable forcing using the measured tide data at discrete points along the boundary. Originally the model provided for a variable forcing only through the input of harmonic amplitudes and phases, and did not allow the calculation of the boundary forcings along open boundaries where multiple discrete data existed. The program modification utilizes distance weighted linear interpolation, and discrete data, to define the continuous water level along the western boundary. Where the grid boundary extended north or south of the outermost offshore stations, the data were extrapolated

to define the water surface elevation.

Table 4.2 presented a comparison of the spectral energy breakdown between the three offshore tidal stations, NOAA-O1, UFL-O1 and UFL-O2. Table 4.6 presented the amplitudes and phases of the principal harmonic constituents. Both tables indicate a reduction in the tidal energy moving from north to south, while the phases indicate that the tidal wave reaches the northern UFL offshore station (UFL-O1) prior to the NOAA station or the southern UFL offshore station (UFL-O2). The correct representation of this amplitude and phase distribution is critical to accurate simulation of the circulation inside the bay, as was demonstrated by the simple models described in Chapter 2 (van de Kreeke and Dean, 1975, van de Kreeke and Cotter, 1978, Cotter, 1974). These models defined the net transport as a function of the phase differential and amplitude differential between two inlets of a multiple inlet system. Although the bathymetry is more complex within the Sarasota Bay System, the phases and amplitudes at the inlets within the model domain defined in Figure 6.1 are directly related to the distribution of the forcing along the boundary. Therefore, minor errors in the tidal amplitudes and phases along the offshore boundary may produce significant errors in the residual circulation patterns inside the bay.

Because the gages were bottom mounted pressure sensors, the three data sets could not be leveled to provide a common datum of reference. In addition, the NOAA sensor experienced significant drift during the period of deployment. In order to provide a common datum of reference for the three sensors, each signal was demeaned and linearly detrended prior to use in the model. The assumption was made that the mean water level along the open boundary was uniform.

During the calibration of the model, the residual currents measured at station UFL-B1 could not be simulated solely through the existence of phase lags and amplitude differences along the open boundary. Although residuals did develop, their magnitude was never near the 8 to 9 cm/sec measured. The only factor which created

Table 6.1: The average wind speeds and wind stresses at the four UFL bay stations

Station	East-West Wind Speed (m/sec)	North-South Wind Speed (m/sec)	East-West Wind Stress $(dyne/cm^2)$	North-South Wind Stress $(dyne/cm^2)$
UFL-B1	2.26	2.25	0.113	0.138
UFL-B2	2.49	2.12	0.150	0.164
UFL-B3	2.34	1.59	0.107	0.076
UFL-B4	1.63	1.21	0.054	0.050

a net residual of this magnitude was a net set-up in the offshore forcing for Tampa Bay. For the calibration runs presented in the following sections, a 3.0 cm set-up was input into the offshore forcing at Tampa Bay. This set-up was based solely upon achieving the best calibration between the model and the measured data. The lack of a reference elevation datum for the offshore measurements and the interior stations prohibits verification of the existence of this offshore set-up.

6.2.2 Wind Forcing

As with the offshore boundary forcing, wind data are available at discrete points within the system, stations UFL-B1, UFL-B2, UFL-B3 and UFL-B4. Within the numerical model, wind forcing can be defined as constant over the entire domain, or temporally varying but spatially constant, or temporally and spatially varying. For the calibration, a temporally and spatially varying wind field was developed from the discrete measured data using inverse-distance weighted linear interpolation in the spatial plane and linear interpolation in the temporal plane.

In hydrodynamic studies involving the simulation of tides and currents, wind data are often not measured concurrently but are based on National Weather Service data from nearby airports or weather stations (Smith, 1990a, Wong and Garvine, 1984). In some instances these weather stations are relatively distant from the study site. The assumption is made that the spatial and temporal differences in the wind field between the station and the study site are insignificant.
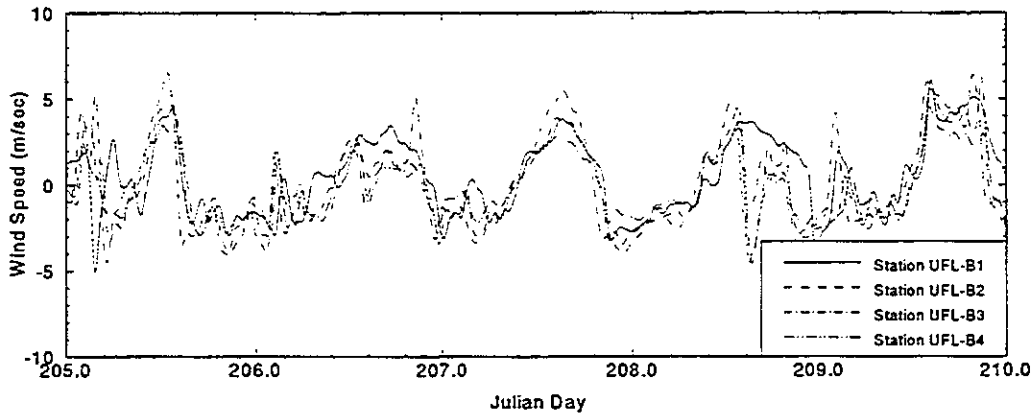
Figure 6.4: A comparison of the measured wind speed components at UFL-B1, UFL-B2, UFL-B3 and UFL-B4. a) East-west component; b) north-south component.

The instrument platforms utilized for this study were spaced between 10 and 20 kilometers apart. To examine the variations in wind speed and direction, Figure 6.4 presents the east-west and north-south components of the wind vectors over a 5 day period for the four bay stations. The data were smoothed prior to plotting to allow easier visual comparison. Examination of the plots indicates that over long time scales the data show similar trends but not similar magnitudes of variation. Table 6.1 presents the mean wind speed components and the associated mean wind stress components for each of the stations. The highest mean wind speeds and stresses occur at Station UFL-B2. This station is within the most open body of water and has the least obstruction from upland structures. The smallest wind stresses and speeds are found at Station UFL-B4. In contrast to Station UFL-B2, this station is within the smallest body of water and is the most obstructed by upland features. The variations in wind stress are more pronounced than the wind speed, this is due to the quadratic

relationship between the wind speed and stress.

The wind sensors at all of the stations were located at 4 to 5 meters above the mean water level, plus or minus 0.5 meters. Therefore, the calculated differences are not the result of variation in the elevations of the sensors. It is more likely that the differences are due to localized variations in the weather patterns as well as the proximity of the stations to upland interference. The variations between stations for the time period of measurement (July, August and September) will be larger than other seasons due to seasonal weather patterns, i.e. more localized storm events during the summer.

The data presented support the need for comprehensive wind measurements over the entire study area in order to define the spatial variations. The wind fields developed for the model calibrations (Julian Day 200 to 230) utilize all four of the bay stations as input. The error associated with this methodology is on the order of the differences between the stations.

6.3 Quantifying Model Accuracy

Calibrations of numerical circulation models often take the form of graphical or statistical comparisons between the simulated and measured currents or tides. To obtain the calibration, empirical parameters within the model are adjusted until the error between the measured and simulated signals is minimized. Once the errors have been minimized the model is considered "calibrated". The next process, "verification", involves running the model using a different data set without changing the key model parameters. If the error of the "verification" run is of the same form and overall magnitude as that found during calibration, the model is considered "validated". But what does this mean? It means that the model is simulating the circulation with consistent accuracy. Additionally, why should one expect that, in a tidally dominated environment, where the forcings are periodic, the simulations between the calibration

and verification runs would differ? Finally, the measure of whether or not a model is "calibrated" is subjective. The determination is based upon what the individual modeler deems to be sufficiently accurate.

A more appropriate presentation of model results is to attempt to quantify the accuracy of the simulations, and to determine how the model quantifies the overall physics. As was shown for the measured data in Chapter 4, the simulated currents or tides are the result of the many terms within the equations of motion and continuity. In turn, each of these terms represents an individual forcing mechanism which needs to be accurately resolved in order to simulate the overall circulation. Examination of how the model represents each of these individual mechanisms provides insight into what physical aspects of the flow are well or poorly simulated. Understanding the model's "weaknesses" allows refinement of the simulations and provides a basis on which to evaluate any results obtained. By only comparing the total signals, there is no basis established to determine where the errors are coming from.

The following sections present comparisons between the model results and measured data using the methods presented in Chapter 4. The simulation period was from Julian Day 200 to 230 in 1991. The error analyses include: calculated RMS errors, comparison of the distribution of spectral energies, comparison of the harmonic constituents, comparison of the residual current fields predicted by the model in relation to measured residual currents at the bay stations, and graphical comparisons of the discharges measured by USGS in 1991 and 1992 (1992 data are extrapolated to match 1991 conditions).

Numerical solutions can be improved in a variety of ways: improvements in grid resolution, additional data to better quantify the boundary conditions, additional bathymetric data and improved numerical solutions. The input conditions to the model, were based upon the best available shoreline and bathymetric data, a grid which resolves the entire lagoon geometry, and the most appropriate numerical so-

lutions available. The results presented herein represent the best overall agreement with the measured data. The range of values for key input parameters, variations in the boundary conditions and the geometry/bathymetry are discussed in detail in the section entitled "Model Sensitivity".

6.3.1 Calculation of the RMS Errors

Tidal Data

Figure 6.5 presents comparisons between the measured and simulated tides at USGS-04, USGS-05, USGS-06 and USGS-07. The offsets between the model results and the data are due to the errors associated with the original leveling of the gages. These errors were discussed in Chapters 3 and 4. The data show generally good agreement in both magnitude and phase. The model results for the interior stations exhibit the more peaked non-linear shape found for the data in Chapter 4. The errors at each station appear to be consistent with no station showing better or worse agreement based upon visual inspection.

In order to numerically quantify the overall accuracy, the Root Mean Squared (RMS) errors were calculated using the formula;

$$E_{RMS} = \left(\frac{1}{N} \sum_{1}^{N} (\eta_{model} - \eta_{data})^2 \right)^{\frac{1}{2}} \tag{6.1}$$

where N is the total number of discrete measurements. Table 6.2 presents the calculated RMS errors for the four tidal stations operating during the simulation period. The errors range from 2.2 cm at the Big Pass Station (USGS-05) to 4.5 cm at the Roberts Bay Station (USGS-04).

In order to compare the results between stations it is necessary to normalize the errors by the tide range. The second column in Table 6.2 presents the tide ranges calculated from the data. The percent error is then the RMS error, divided by the tide range, multiplied by 100.

The percent errors for the tides are low, all less than 5 percent. The error at the
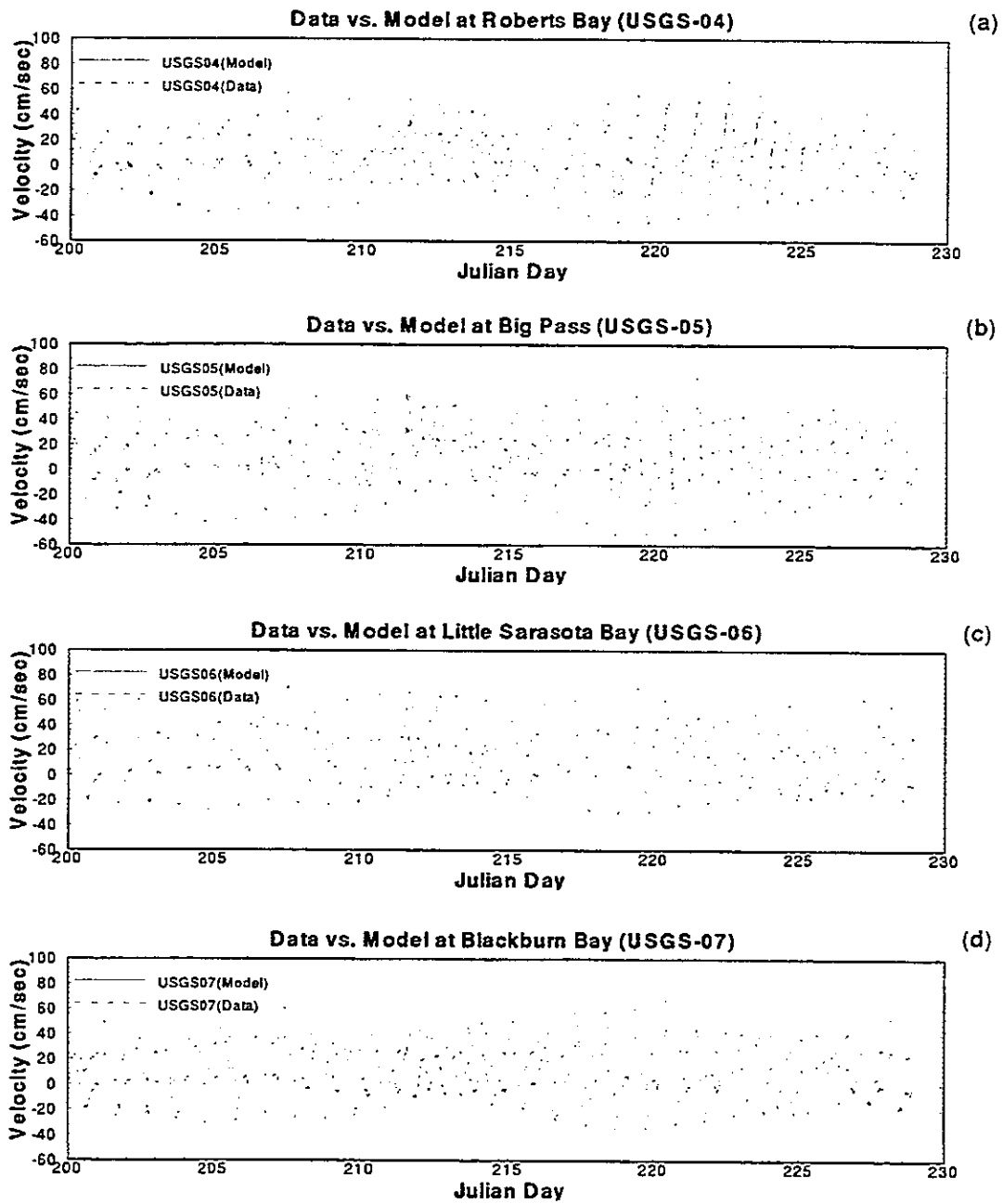
Figure 6.5: A comparison of the measured and simulated water surface elevations, Julian Day 200 to 230, 1991. a) USGS-04; b) USGS-05; c) USGS-06; d) USGS-07.

Table 6.2: The RMS errors between the measured and simulated water surface elevations, Julian Day 200 to 230, 1991

Station	RMS Error (cm)	Tide Range (cm)	Percent Error
USGS-04	4.5	97.3	4.6
USGS-05	2.2	102.5	2.2
USGS-06	3.1	77.9	4.0
USGS-07	2.7	80.0	3.4

Big Pass station is 2.2 percent. This indicates that a portion of the error for the tides within the bay may be the result of inaccuracies in the offshore forcings, or errors in the propagation of the tides from the offshore through the inlets.

Current Data

Figure 6.6 presents graphical comparisons of the measured and simulated bottom and surface velocity components at station UFL-B1. The model appears to correctly simulate the general characteristics of the east-west and north-south surface and bottom velocity components. The model overpredicts the magnitude of the currents during flood tide. The data show less than 10 cm/sec magnitude flow during flood tide (positive north-south) while the model predicts at or above 10 cm/sec. Ebb velocity magnitudes are similar between the model and measured data except during the period from Julian Day 220 to 225 when the model predictions are low.

Table 6.3 presents the RMS errors for the surface and bottom current vector components along with the current ranges and the normalized percent error (as defined for the tidal comparisons). Station UFL-B1 shows similar percent errors for all of the components, with errors between 15 and 18 percent. The lowest percentage was in the surface north-south velocity component, which has the highest overall magnitude. The primary source of error for this station appears to be the models underprediction of the residual currents and an overprediction of the magnitudes of the flood currents. The shift in the mean currents is most clearly evident near Julian Days 220 to 225.
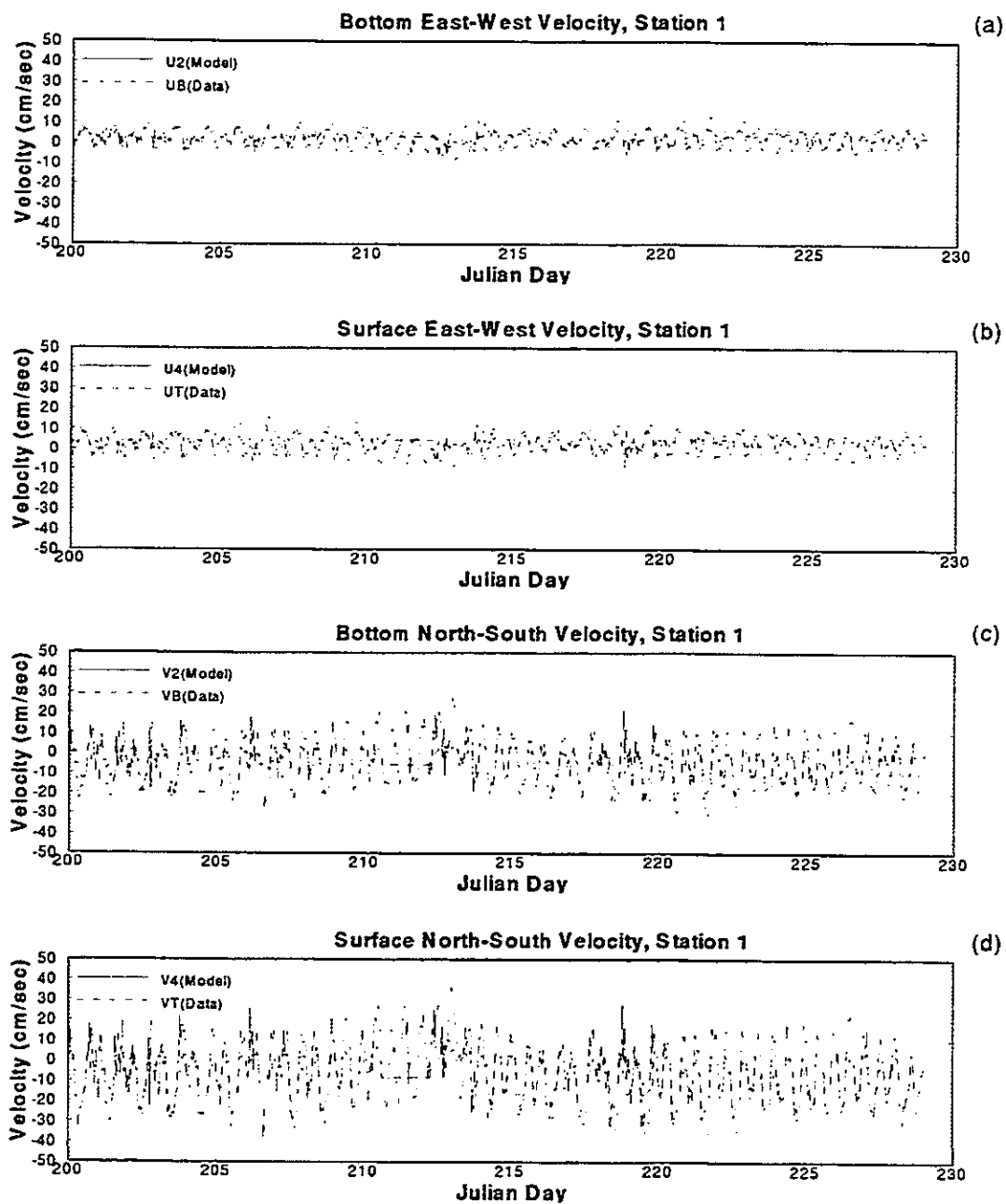
Figure 6.6: A comparison of the measured and simulated current components at station UFL-B1, Julian Day 200 to 230, 1991. a) Bottom east-west; b) surface east-west; c) bottom north-south; d) surface north-south.

Table 6.3: The RMS errors between the measured and simulated bottom and surface east-west and north-south current components, Julian Day 200 to 230, 1991

Station	Component	RMS Error (cm/s)	Range (cm/s)	Percent Error
UFL-B1	(Bot E-W)	3.6	19.4	18.5
	(Top E-W)	4.0	21.9	18.2
	(Bot N-S)	6.9	38.8	17.9
	(Top N-S)	8.7	56.4	15.4
UFL-B2	(Bot E-W)	3.4	14.3	23.9
	(Top E-W)	3.1	15.2	20.2
	(Bot N-S)	4.1	39.2	10.4
	(Top N-S)	5.2	51.9	10.1
UFL-B3	(Bot E-W)	1.9	8.0	24.0
	(Top E-W)	3.0	10.0	29.6
	(Bot N-S)	4.8	12.0	40.3
	(Top N-S)	4.4	24.0	18.1
UFL-B4	(Bot E-W)	1.9	17.4	10.8
	(Top E-W)	2.5	17.0	14.8
	(Bot N-S)	3.8	25.8	14.8
	(Top N-S)	3.7	38.0	9.8

Figure 6.7 presents graphical comparisons of the measured and simulated surface and bottom current components for station UFL-B2. The model slightly underpredicts the peak flood velocities in the north-south surface current component, while accurately predicting the ebb tide velocity magnitudes. The model appears to accurately predict the east-west surface velocity components while underpredicting the positive nature of the bottom east-west component. Comparison of the RMS errors in Table 6.3 shows the greatest percent errors in the lowest magnitude signals, the east-west components. The highest percent errors were found for the bottom east-west component, which is consistent with the results shown on Figure 6.7. The errors for the surface and bottom north-south components are approximately 10 percent with magnitudes around 4.0 to 5.0 cm/sec.

Figure 6.8 presents graphical comparisons of the velocity components for station UFL-B3. UFL-B3 is the most interior station and has the lowest overall current energy of the four UFL bay stations. The maximum measured velocity magnitudes are less than 12 cm/sec. The model appears to capture the general east-west velocity characteristics. The maximum velocity amplitudes in the east-west components and the bottom north-south component are less than 5 cm/sec, this is small in relation to the other staitons. Examination of the RMS errors for these three components shows them all to have greater than 25 percent errors. Only the surface north-south component shows an error percentage less than 20 percent. There does appear to be a phase shift, this will produce error in the RMS calculations even if the magnitudes are exactly simulated. The phase errors will be examined more closely in the section entitled "Comparison of the Measured and simulated Harmonic Constituents".

In Chapter 4, the difference between the measured surface and bottom currents was discussed. It was proposed that due to the low velocity magnitudes in this area, the bottom boundary layer may be laminar instead of turbulent. The model, in its calculation of the bottom friction, assumes a fully turbulent flow and uses the "law of
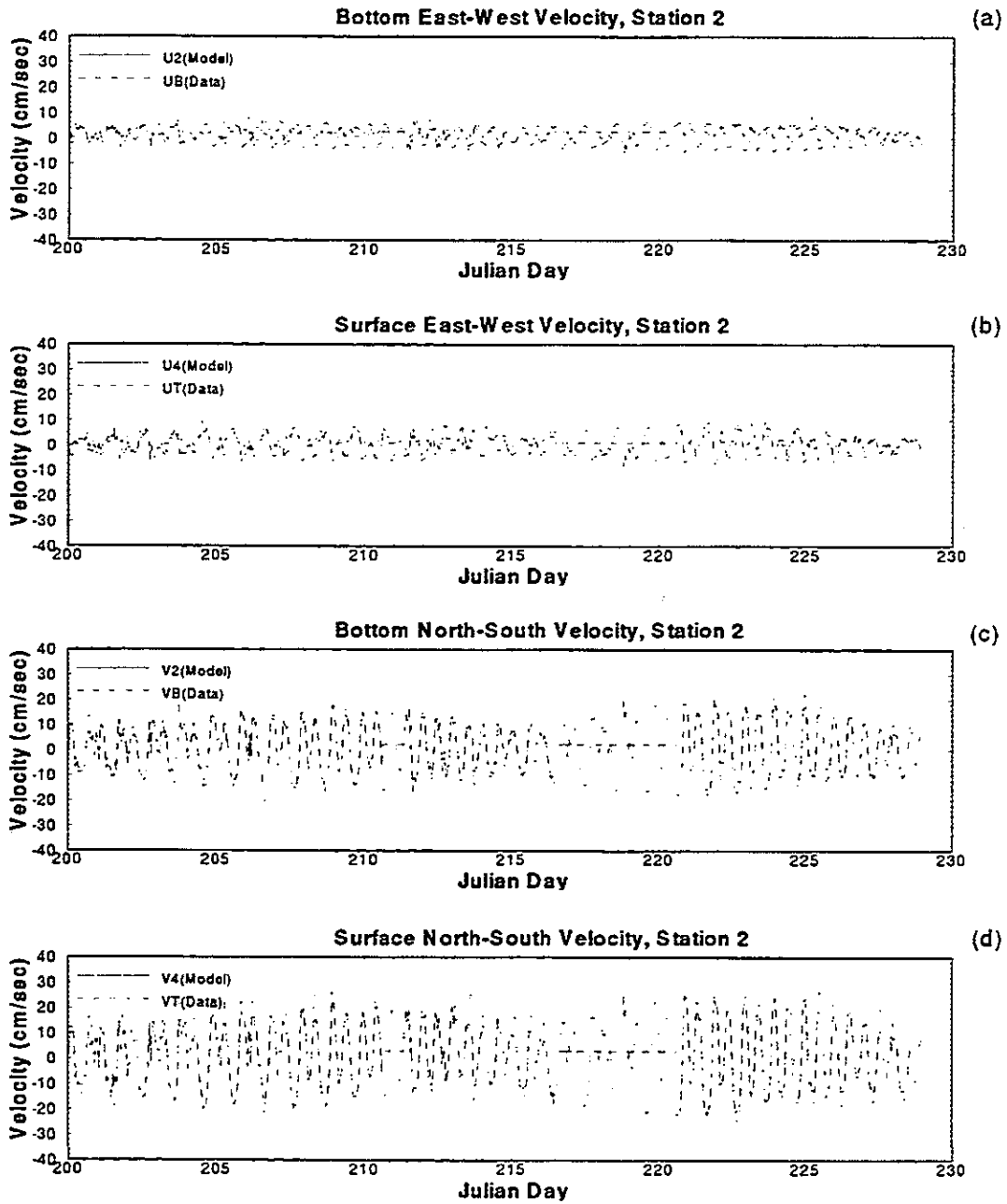
Figure 6.7: A comparison of the measured and simulated current components at station UFL-B2, Julian Day 200 to 230, 1991. a) Bottom east-west; b) surface east-west; c) bottom north-south; d) surface north-south.
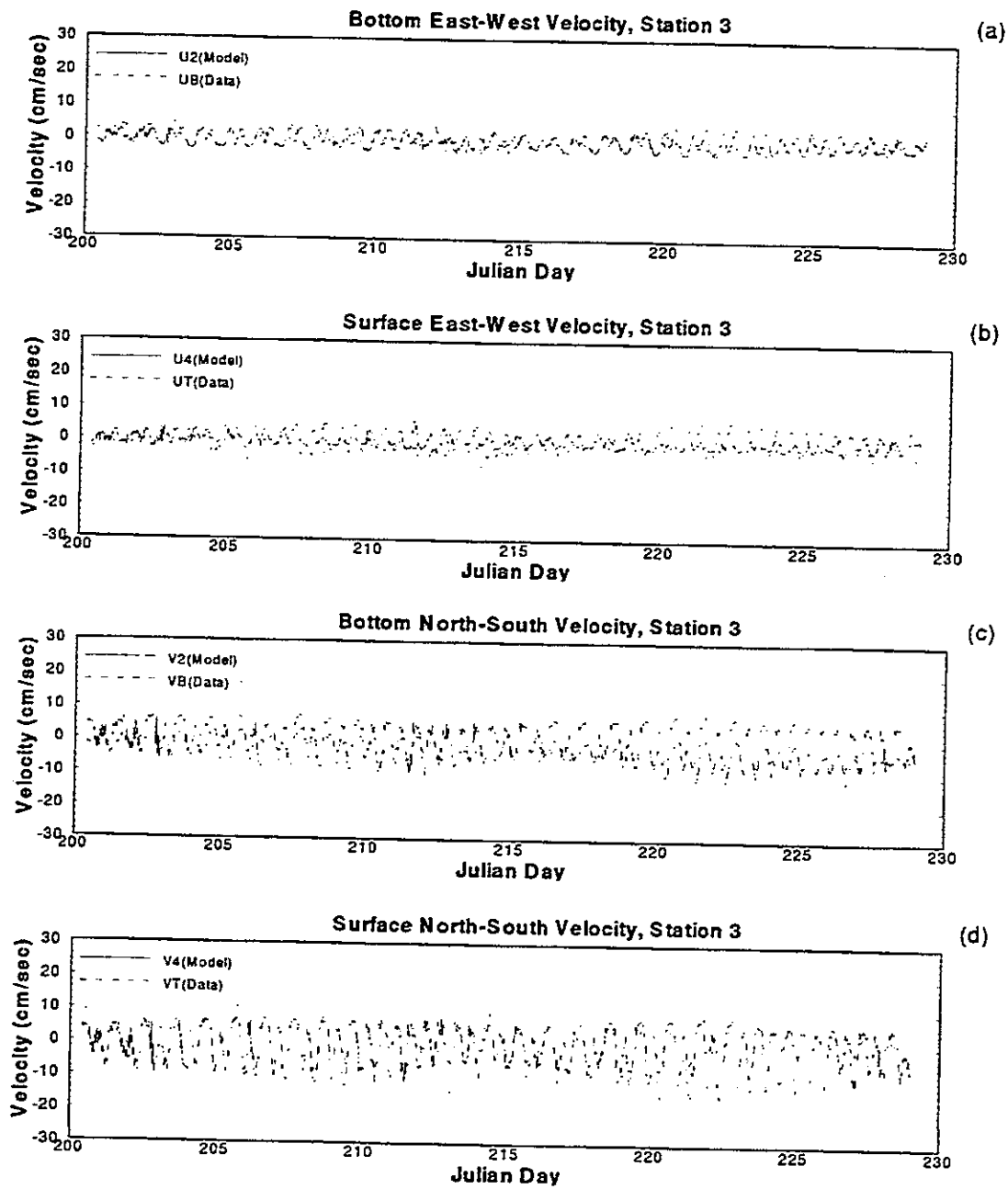
Figure 6.8: A comparison of the measured and simulated current components at station UFL-B3, Julian Day 200 to 230, 1991. a) Bottom east-west; b) surface east-west; c) bottom north-south; d) surface north-south.

the wall" to define the bottom friction coefficient. This assumption of fully turbulent flow within a region which is laminar may explain why the model overpredicts the bottom magnitudes.

Figure 6.9 presents graphical comparison of the current components for station UFL-B4. The RMS errors for all of the components are between 10 and 15 percent, these are the best overall results for any of the stations. The measured bottom north-south current component shows a strange phenomenon. During an ebbing tide, the bottom north-south component begins to flow southward with the surface current, but before the currents peak, the bottom flow drops off to near zero while the surface current remains strong. This is particularly interesting given that the meters were only 90 cm apart in 2 meters of water. The model does not capture this phenomenon. Instead, the simulated surface and bottom currents mirror one another.

6.3.2 Comparison of the Simulated and Measured Energies

Tidal Data

Table 6.4 presents comparisons of the spectral energy of the simulated and measured water surface elevations within the sub-tidal, diurnal, semi-diurnal and the third and fourth diurnal energy bands at the four USGS stations. The table presents the total energy over the entire frequency range followed by the percent of the total energy located within each band.

The total energies calculated for the model show that the water surface elevation fluctuations are consistently overpredicted by the model. The greatest overprediction occurs for the Roberts Bay (USGS-04) and the Blackburn Bay (USGS-07) stations. The magnitude of the overpredictions will be quantified by the harmonic analysis comparisons. The RMS analyses showed the overall errors to be between 2 and 4 centimeters.

A more worthwhile use of the spectral analysis is to examine how the model simulates the percent energies across the four frequency bands discussed in Chapter
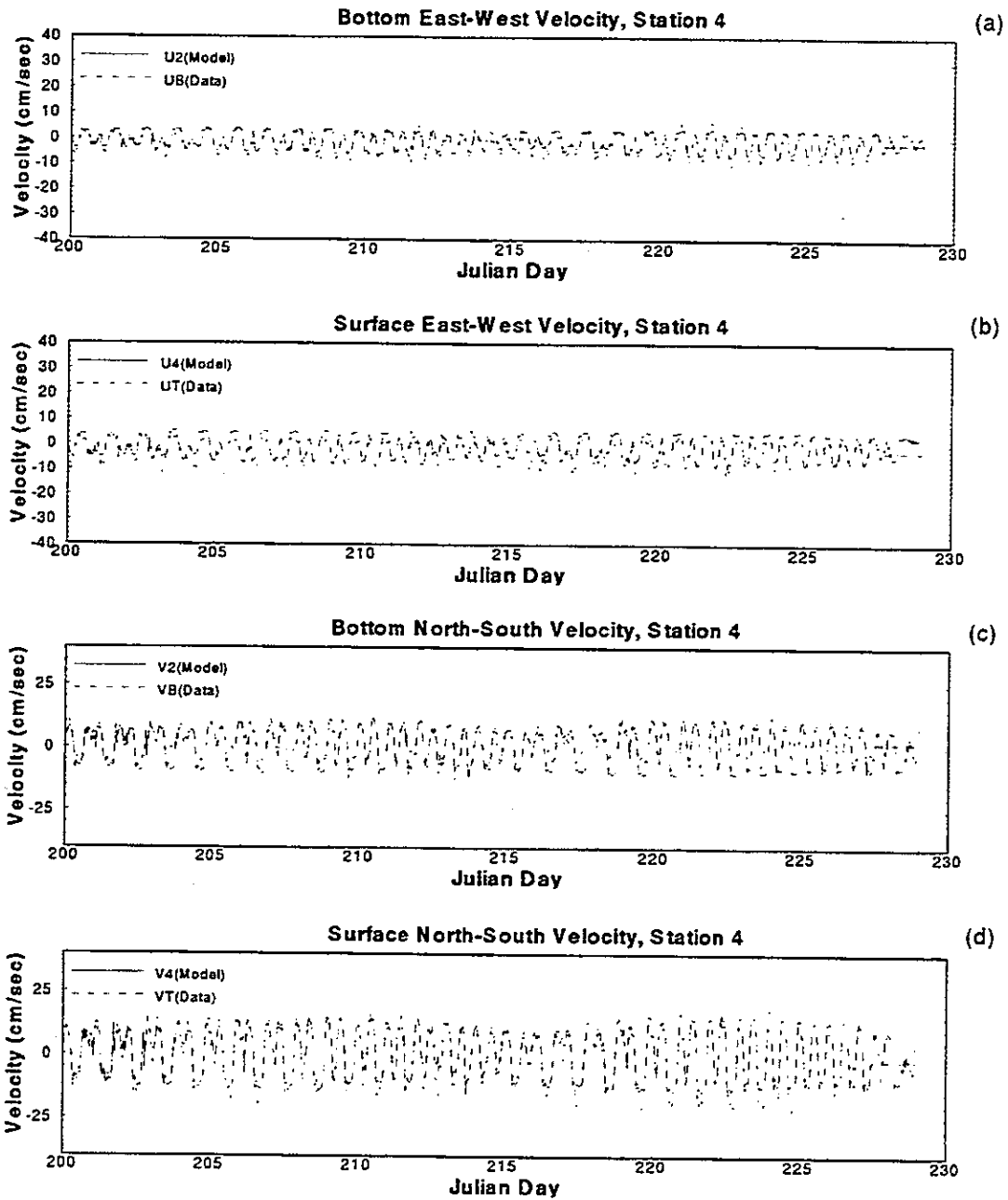
Figure 6.9: A comparison of the measured and simulated current components at station UFL-B4, Julian Day 200 to 230, 1991. a) Bottom east-west; b) surface east-west; c) bottom north-south; d) surface north-south.

4, the subtidal (0 to 0.5 cycles/day), the diurnal (0.8 to 1.2 cycles/day), the semi-diurnal (1.8 to 2.2 cycles per day), and the third diurnal and fourth diurnal (2.8 to 3.2 and 3.8 to 4.2 cycles/day). These percentages are listed in Table 6.4.

The simulated and measured sub-tidal percentages are of the same order of magnitude. The model values range from 0.9 at Big Pass (USGS-05) to 1.9 within Little Sarasota Bay (USGS-06). The data range from 1.4 to 2.8 for the same two stations respectively. The model consistently underpredicts the levels of sub-tidal energy but does capture the trend of increasing subtidal energy moving from away from the inlets.

The predicted and measured percent energies within the diurnal and semi-diurnal frequency bands are similar. The model consistently underpredicts the levels of diurnal energy by approximately 5 percent. The model simulates the filtering of the higher frequency harmonics and exhibits the shift in percent energy from the semi-diurnal to the diurnal. One point to note for these comparisons, and the comparisons of the sub-tidal energies, is that the errors at the inlet (USGS-05) are nearly equal to those at the more interior stations (USGS-06). This indicates in part that a portion of the error probably comes from the offshore boundary conditions, or from the propagation of the wave across the offshore shelf.

The higher harmonics are well simulated by the model. The magnitudes are nearly equal at all of the stations. The trend of increasing percentage moving away from the inlets is captured, with USGS-06 showing the highest percentages for both the data and the model results.

Current Data

Tables 6.5 through 6.8 present comparisons of the spectral energy calculated from the simulated and measured currents. The tables presents the total energy over the entire frequency range followed by the percent of the total energy located within each sub-band. As with the measured data, the energies are presented as the total of the north-south and east-west components.

Table 6.4: A comparison of the measured and simulated total spectral energy and the percent distribution of energy between the sub-tidal, diurnal, semi-diurnal and third-diurnal bands for the water surface elevations measured at stations USGS-04, USGS-05, USGS-06, and USGS07, Julian Day 200 to 230, 1991

Station	Source	Total Energy (cm^2)	Subtidal (percent)	Diurnal (percent)	Semi Diurnal (percent)	Third Diurnal (percent)
USGS-04	Data	31210.9	2.0	63.9	33.1	.3
	Model	36841.0	1.2	59.3	38.4	.4
USGS-05	Data	39987.3	1.4	57.5	40.1	.0
	Model	41636.5	.9	55.9	42.2	.1
USGS-06	Data	22414.7	2.8	71.0	24.4	1.0
	Model	23720.1	1.9	69.8	26.5	1.0
USGS-07	Data	21991.8	2.5	66.2	30.4	.1
	Model	25354.7	1.4	63.7	33.8	.1

Table 6.5: A comparison of the measured and simulated total spectral energy and the percent distribution of energy between the sub-tidal, diurnal, semi-diurnal and third-diurnal bands for the July/August 1991 simulations at station UFL-B1

Elevation	Source	Total Energy $(\frac{cm}{sec})^2$	Subtidal (percent)	Diurnal (percent)	Semi Diurnal (percent	Third/Fourth Diurnal (percent)
Bottom	Data	6772.5	2.4	38.9	43.9	2.1
Bottom	Model	9529.0	1.2	26.6	58.2	2.1
Surface	Data	11677.0	2.1	37.9	46.0	1.4
Surface	Model	15934.6	1.5	27.7	56.5	2.2

Table 6.6: A comparison of the measured and simulated total spectral energy and the percent distribution of energy between the sub-tidal, diurnal, semi-diurnal and third-diurnal bands for the July/August 1991 simulations at station UFL-B2

Component	Source	Total Energy $(\frac{cm}{sec})^2$	Subtidal (percent)	Diurnal (percent)	Semi Diurnal (percent	Third Diurnal (percent)
Bottom	Data	6373.7	.6	22.3	61.2	4.8
Bottom	Model	9330.8	.2	28.4	62.0	·5.1
Surface	Data	12520.6	.6	26.5	60.1	3.3
Surface	Model	13847.6	.4	29.3	61.0	4.8

At station UFL-B1 (Table 6.5) the total energy for both the bottom and surface currents is overpredicted by the model. As was found for the water surface elevations, the sub-tidal percentages are similar but the model underpredicts their magnitudes at the surface and near the bottom. The diurnal and semi-diurnal energy distributions are not simulated well by the model. The data showed a much more even distribution with values near 35 to 45 percent for both. The model is predicting a much higher percentage of semi-diurnal energy with values from 55 to 60 percent in comparison with the diurnal energies which are between 25 and 30 percent. In Chapter 4 it was found that the currents measured at UFL-B1 and UFL-B3 had a more even distribution of semi-diurnal to diurnal energy when compared with stations UFL-B2 and UFL-B4 which showed dominance in the semi-diurnal energy. This phenomena is not being captured by the model and will be examined further as the results from each station are discussed.

At UFL-B2 the total energy calculated for the simulated currents is greater than was calculated for the measured currents, with the near bottom currents exhibiting the largest discrepancy. The simulated sub-tidal energy percentages are low, which agrees with the measured data, also the simulated distribution of the semi-diurnal and diurnal energies agree. The near bottom higher harmonics are well simulated, but the near surface values are overpredicted.

Table 6.7: A comparison of the measured and simulated total spectral energy and the percent distribution of energy between the sub-tidal, diurnal, semi-diurnal and third-diurnal bands for the July/August 1991 simulations at station UFL-B3

Component	Source	Total Energy $(\frac{cm}{sec})^2$	Subtidal (percent)	Diurnal (percent)	Semi Diurnal (percent	Third Diurnal (percent)
Bottom	Data	617.4	5.5	37.5	21.7	5.1
Bottom	Model	2556.9	.5	26.9	59.4	7.9
Surface	Data	1941.6	3.3	43.9	33.3	3.5
Surface	Model	3610.8	1.0	24.7	59.0	9.6

Table 6.8: A comparison of the measured and simulated total spectral energy and the percent distribution of energy between the sub-tidal, diurnal, semi-diurnal and third-diurnal bands for the July/August 1991 simulations at station UFL-B4

Component	Source	Total Energy $(\frac{cm}{sec})^2$	Subtidal (percent)	Diurnal (percent)	Semi Diurnal (percent	Third Diurnal (percent)
Bottom	Data	3665.1	.8	25.2	53.1	9.9
Bottom	Model	5313.7	.1	35.2	52.7	6.0
Surface	Data	10100.8	.4	35.8	51.4	5.0
Surface	Model	9422.5	.2	34.6	52.9	6.4

It is difficult to compare the simulated and measured near bottom currents at UFL-B3 because of the low overall signal energy. Examination of the surface values show that the model overpredicts the total energy at this station. The percent subtidal is underpredicted while the higher harmonic energies are overpredicted. As was found for station UFL-B1 the data show a more even distribution of semi-diurnal to diurnal energy, while the model predicts a much higher percentage within the semi-diurnal band.

Station UFL-B4 follows very closely the findings for station UFL-B2. The low sub-tidal energies are captured although underpredicted. The percent distribution between the diurnal and semi-diurnal energies are well simulated. The one difference is that at UFL-B4 the higher harmonic energies are underpredicted for the bottom

currents.

6.3.3 Comparison of the Measured and Simulated Harmonics

Tidal Data

Table 6.9 presents comparisons of the measured and simulated harmonic constituent amplitudes and phases for the water surface elevation data from USGS-04, USGS-05, USGS-06, and USGS-07. The results show the errors in the tidal amplitudes to be all less than 10 percent and the phases for the primary harmonic constituents to be less than 40 minutes. The phases are presented as hours not degrees in order to allow intercomparison between the different period harmonic constituents.

The tidal amplitudes are consistently overpredicted by the model, this agrees with the findings of the spectral comparisons. Within Big Pass (USGS-05) the predictions are 0.5 to 1.0 cm high. This indicates possible inaccuracies in the tidal forcing, or insufficient damping of the wave as it propagates from the offshore through this inlet. At the Roberts Bay station (USGS-04) , which receives tidal forcing through Big Pass, the predictions are 1.0 to 1.5 cm high indicating insufficient damping of the tidal wave in the region between these stations. The phase errors support this conclusion because, on average, they increase from less than 10 minutes at Big Pass to 20 to 30 minutes at Roberts Bay.

The tides at the Blackburn Bay station are overpredicted by 1.0 to 1.5 cm but the phase errors show that the simulated tides lag the measured tides by approximately 10 minutes. This indicates two possible sources of error. The first is insufficient damping of the tidal wave as it passes through the inlet. The second is errors in the phase and possibly the amplitude of the offshore forcing of the tidal wave near Venice Inlet. As described in the section entitled "Boundary Conditions", under the tidal forcing, the southernmost offshore data collection station was north of Venice Inlet. In order to define the tidal conditions near Venice Inlet the tidal characteristics (amplitude reduction and phase lag) were extrapolated from the known stations. This may have

Table 6.9: A comparison between the measured and simulated harmonic tidal constituents for the July/August 1991 data

Station	Constituent	Amplitude Data (cm)	Amplitude Model (cm)	Error (cm)	Phase Data (hours)	Phase Model (hours)	Error (hours)
USGS-04	M2	13.60	15.25	-1.65	-1.51	-1.97	.47
	S2	5.90	7.21	-1.31	1.28	.56	.73
	N2	3.04	3.46	-.42	-1.89	-2.43	.53
	K1	13.72	14.71	-.99	-2.60	-3.06	.46
	O1	14.45	14.65	-.20	-5.58	-6.09	.51
	MO3	.62	.87	-.25	3.19	2.08	1.11
	MK3	.95	.94	.01	-2.82	-3.78	.95
USGS-05	M2	16.29	16.54	-.25	-2.47	-2.55	.09
	S2	6.64	7.68	-1.04	-.03	-.21	.19
	N2	3.75	3.87	-.12	-2.99	-3.06	.07
	K1	15.40	15.65	-.25	-3.85	-3.84	-.01
	O1	14.70	14.47	.23	-6.90	-6.97	.07
	MO3	.40	.65	-.24	-.20	.07	-.27
	MK3	.33	.24	.09	-2.98	3.89	-6.87
USGS-06	M2	10.28	10.75	-.46	.22	-.21	.43
	S2	4.89	5.21	-.32	3.30	2.74	.56
	N2	2.41	2.38	.03	-.16	-.58	.42
	K1	11.99	12.51	-.52	-.62	-.98	.36
	O1	13.45	13.46	-.01	-3.34	-3.77	.43
	MO3	1.09	.97	.12	-3.28	-3.39	.11
	MK3	1.26	1.39	-.13	-1.48	-1.50	.02
USGS-07	M2	10.95	12.22	-1.27	-1.63	-1.49	-.15
	S2	4.20	5.30	-1.10	.90	1.10	-.20
	N2	2.40	2.74	-.34	-2.13	-1.99	-.13
	K1	12.31	12.93	-.61	-2.75	-2.57	-.18
	O1	12.32	12.79	-.47	-5.43	-5.39	-.04
	MO3	.57	.19	.38	-.29	-1.08	.79
	MK3	.11	.60	-.49	-.18	-1.97	1.79

introduced the errors described above.

The tides at the Little Sarasota Bay station show better agreement in amplitude than stations to either side of it. This indicates that the errors to either side of it cancel out to some extent. The predicted phases at Roberts Bay were such that the tidal wave arrived there too soon. The predicted phases at Blackburn Bay were such that the tidal wave arrived there too late. The phase errors at Little Sarasota Bay are a combination of these two errors as the wave propagates from both ends.

Examination of the relative errors between the diurnal and semi-diurnal constituents indicates that, overall, the simulation errors are greater for the semi-diurnal constituents than the diurnal. The model does not appear to damp (or filter) out the semi-diurnal constituents to the degree found in the data. This is consistent with the findings for the spectral analyses. In Chapter 4, the form numbers and the overtide ratios were plotted as a function of increasing distance from the inlets. Figure 6.10 presents comparisons of the model and measured harmonic constituents in a similar manner. Looking first at the plots for the Form Numbers, the model appears to simulate the overall characteristics but it consistently underpredicts the Form Numbers. This underprediction exists at the inlets (Big Pass, USGS-05) and increases at the two stations just inside the inlets (Roberts Bay, USGS-04 and Blackburn Bay, USGS-07). By the time the waves reach the most interior station (Little Sarasota Bay, USGS-06) the simulated and measured Form Numbers are nearly equal. It appears that the model does not filter the semi-diurnal tidal constituents at the inlets to the degree measured. The filtering of the tidal wave as it propagates into Little Sarasota Bay (a region with multiple constrictions) is actually overpredicted by the model, this is based upon the relative changes in the simulated and measured Form Numbers moving toward Little Sarasota Bay.

Figure 6.10 also presents the measured and simulated Overtide Ratios. Once again the model predicts the general characteristics. The values at the inlet (Big Pass) and

1991 Data Period
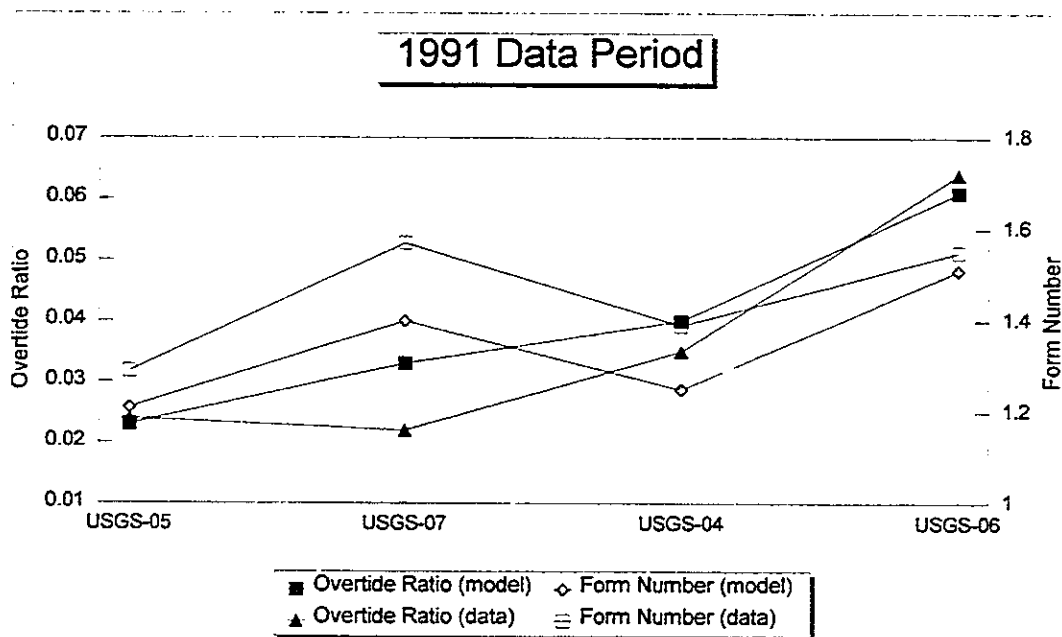
Figure 6.10: A comparison of the measured and simulated form numbers and overtide ratios for the tides at USGS-04, USGS-05, USGS-06 and USGS-07, Julian Day 200 to 230, 1991

the most interior station (Little Sarasota Bay) are nearly equal. The model slightly overpredicts the ratio at Roberts Bay with the greatest error at the Blackburn Bay station where the model overpredicts the ratio by 30 percent. Results from the data analysis showed that the growth of the non-linear energy was small in the region of Venice Inlet, this phenomena was not simulated by the model.

Current Data

Tables 6.10 through 6.13 present comparisons between the measured and simulated principal major and minor axis harmonic constituent amplitudes along with the phases and the orientation of the principal axis constituents. The following summarizes the results from those comparisons.

At station UFL-B1 the model overpredicts the amplitudes of the major axis semi-diurnal constituents by as much as 40 percent while predicting the diurnal and the higher harmonic amplitudes to within 10 percent. This result is consistent in both the surface and bottom amplitudes. This overprediction of the semi-diurnal component manifested itself in distorted spectral energy distributions.

The model underpredicts the minor axis amplitudes for the diurnal, semi-diurnal and the higher harmonics. This indicates that the model produces a more unidirectional current pattern than was actually measured. This may be due to the inability of the grid to resolve the rotational component. The calculated values for the minor axis components for both the model results and the data are less than 1 cm/sec. Therefore this error is not overly significant.

In contrast to the errors in amplitude, the phase errors are large (1 to 2 hours) for the diurnal constituents, and small (15 to 30 minutes) for the semi-diurnal constituents. This combination of large amplitude errors in the semi-diurnal constituents and large phase errors in the diurnal constituent, suggests some error in the phase or amplitude distribution of the offshore forcing, although the graphical results appear reasonable. It appears that some portion of the interaction between the two

Table 6.10: A comparison between the measured and simulated harmonic current constituents for the July/August 1991 data at UFL-B1

Sensor Location	Constituent	Data Major (cm/s)	Model Major (cm/s)	Error (cm/s)	Data Minor (cm/s)	Model Minor (cm/s)	Error (cm/s)
Bottom	M2	6.61	11.02	4.42	.66	.04	-.62
	S2	2.62	4.30	1.69	.21	.02	-.19
	N2	1.73	1.90	.17	.29	.04	-.25
	K1	4.96	4.61	-.35	.34	.14	-.20
	O1	4.79	5.51	.72	.36	.09	-.27
	MO3	1.28	1.02	-.26	.11	.01	-.10
	MK3	1.04	1.27	.23	.29	.05	-.24
Surface	M2	9.37	13.97	4.59	.51	.03	-.48
	S2	3.00	5.44	2.43	.28	.09	-.19
	N2	2.21	2.41	.20	.30	.01	-.29
	K1	6.25	6.01	-.24	.04	.46	.43
	O1	6.46	7.14	.69	.24	.01	-.23
	MO3	1.48	1.19	-.29	.22	.02	-.20
	MK3	1.18	1.66	.48	.03	.05	.02

Sensor Location	Constituent	Data Phase (hrs)	Model Phase (hrs)	Error (hrs)	Data Angle (deg)	Model Angle (deg)	Error (deg)
Bottom	M2	2.03	1.41	-.62	-71.36	-72.89	-1.53
	S2	-1.69	-1.56	.13	98.22	106.46	8.24
	N2	.74	.72	-.02	-74.08	-72.78	1.30
	K1	4.31	1.86	-2.46	-74.39	-73.83	.56
	O1	1.24	-.29	-1.53	-64.05	-71.83	-7.78
	MO3	-.96	-2.04	-1.08	-57.78	-77.93	-20.15
	MK3	-.35	-1.43	-1.08	-49.30	-78.65	-29.35
Surface	M2	1.87	1.45	-.42	-80.53	-73.93	6.59
	S2	-2.05	-1.53	.52	100.09	106.33	6.24
	N2	.82	.56	-.26	-80.33	-73.48	6.85
	K1	4.48	2.12	-2.37	-75.92	-70.42	5.50
	O1	1.30	-.18	-1.48	-75.68	-73.91	1.76
	MO3	-.36	-1.73	-1.37	-68.68	-79.92	-11.24
	MK3	-.06	-1.25	-1.19	-62.56	-77.18	-14.62

propagating waves is not being simulated.

The errors in the orientation of the principal current vectors are within 5 to 10 percent overall. This is considered reasonable agreement given the complex nature of the bathymetry within this region.

For station UFL-B2, the errors between the simulated and measured results are similar for both the semi-diurnal and the diurnal components, with magnitudes on the order of 1 to 2 cm/sec. The overall errors for the bottom currents are greater than those for the surface currents. This agrees with the findings from the spectral analysis which showed good agreement in the percent distribution of energy while showing overprediction of the total energy by the model. The rotational nature of the currents are better represented for this station than for UFL-B1, with reduced errors between the measured and simulated minor amplitude magnitudes. The model still underpredicts the overall rotation of the current vectors.

The phase errors are on the average between 30 and 40 minutes with the surface currents showing slightly greater error than the bottom. The model does not consistently overpredict or underpredict the phases but the errors vary from positive to negative depending upon the constituent.

The orientations calculated from the model results are consistently rotated 10 to 20 degrees clockwise from those calculated from the measured data. The surface current orientations are more closely simulated than the bottom currents.

At station UFL-B3 the model consistently overpredicts the major amplitudes with the largest errors found for the semi-diurnal constituents. This agrees with the findings of the spectral analyses. Error magnitudes range from 0 to 4 cm/sec and average near 1.0 to 1.5 cm/sec. Given the low magnitude velocities in this area, these errors are considered significant. Once again the model underpredicts the rotational nature of the currents.

The phase errors are between 30 minutes and 1 hour on the average, with the

Table 6.11: A comparison between the measured and simulated harmonic current constituents for the July/August 1991 data at UFL-B2

Sensor Location	Constituent	Data Major (cm/s)	Model Major (cm/s)	Error (cm/s)	Data Minor (cm/s)	Model Minor (cm/s)	Error (cm/s)
Bottom	M2	7.57	9.75	2.18	.65	.05	-.60
	S2	4.00	5.12	1.11	.02	.08	.06
	N2	1.03	2.05	1.01	.10	.01	-.09
	K1	2.98	5.20	2.22	.60	.25	-.35
	O1	3.58	4.94	1.36	.18	.04	-.14
	MO3	1.12	1.75	.64	.19	.08	-.11
	MK3	1.22	1.58	.36	.09	.08	-.01
Surface	M2	11.09	11.57	.47	.52	.18	-.34
	S2	4.97	6.23	1.26	.40	.35	-.04
	N2	1.76	2.57	.80	.24	.06	-.19
	K1	5.13	6.41	1.28	.05	.37	.32
	O1	5.33	6.06	.73	.24	.13	-.11
	MO3	1.66	2.04	.37	.36	.15	-.20
	MK3	1.36	1.92	.55	.28	.01	-.26
Sensor Location	Constituent	Data Phase (hrs)	Model Phase (hrs)	Error (hrs)	Data Angle (deg)	Model Angle (deg)	Error (deg)
Bottom	M2	1.84	1.78	-.06	-83.12	-72.79	10.33
	S2	-.99	-1.70	-.71	90.80	105.90	15.10
	N2	1.02	1.54	.52	-92.09	-73.92	18.17
	K1	2.58	3.31	.72	-97.92	-75.50	22.42
	O1	.46	.36	-.10	-93.18	-71.87	21.31
	MO3	.43	.69	.26	104.93	108.30	3.37
	MK3	-1.79	-1.55	.24	-71.83	-73.01	-1.18
Surface	M2	2.11	1.88	-.23	-87.05	-74.28	12.78
	S2	-.79	-1.66	-.87	96.00	108.47	12.47
	N2	1.27	1.55	.27	-80.63	-73.13	7.51
	K1	3.29	3.55	.26	-75.69	-65.63	10.07
	O1	1.57	.53	-1.04	-80.36	-74.46	5.89
	MO3	.28	.58	.29	100.25	105.89	5.64
	MK3	-1.45	-1.65	-.20	-84.91	-75.74	9.17

Table 6.12: A comparison between the measured and simulated harmonic current constituents for the July/August 1991 data at UFL-B3

Sensor Location	Constituent	Data Major (cm/s)	Model Major (cm/s)	Error (cm/s)	Data Minor (cm/s)	Model Minor (cm/s)	Error (cm/s)
Bottom	M2	1.13	4.79	3.66	.11	.03	-.08
	S2	.98	2.71	1.73	.33	.16	-.17
	N2	.39	1.09	.70	.09	.01	-.08
	K1	1.48	2.60	1.12	.70	.01	-.69
	O1	1.24	2.63	1.39	.06	.01	-.06
	MO3	.53	1.07	.55	.04	.01	-.02
	MK3	.26	1.23	.97	.16	.05	-.11
Surface	M2	3.20	5.68	2.48	.37	.05	-.32
	S2	1.72	3.05	1.33	.31	.22	-.09
	N2	.57	1.24	.68	.01	.02	.01
	K1	2.63	2.80	.18	.08	.00	-.07
	O1	3.16	3.06	-.11	.02	.03	.02
	MO3	.59	1.34	.75	.00	.02	.01
	MK3	.66	1.65	.99	.09	.07	-.02

Sensor Location	Constituent	Data Phase (hrs)	Model Phase (hrs)	Error (hrs)	Data Angle (deg)	Model Angle (deg)	Error (deg)
Bottom	M2	-2.47	-3.25	-.78	-68.58	-68.89	-.31
	S2	.54	-.42	-.96	-88.02	-68.41	19.61
	N2	-2.71	-3.83	-1.12	-96.54	-68.49	28.06
	K1	-6.88	-6.41	.47	-18.64	-60.79	-42.15
	O1	2.78	2.88	.10	117.62	110.37	-7.25
	MO3	1.29	-1.41	-2.70	-82.84	-69.58	13.26
	MK3	-1.38	.15	1.52	110.28	109.72	-.56
Surface	M2	-2.07	-3.22	-1.14	-76.02	-70.68	5.33
	S2	.98	-.42	-1.40	-81.74	-69.80	11.94
	N2	-2.64	2.44	5.08	-68.03	-70.42	-2.39
	K1	-6.51	-6.87	-.36	-71.00	-82.56	-11.56
	O1	3.24	3.00	-.24	98.24	111.12	12.88
	MO3	-.87	-1.34	-.47	85.11	108.63	23.52
	MK3	-2.13	.25	2.38	-57.99	-70.49	-12.5

exception of the N_2 constituent. The model underpredicts the phases for the semi-diurnal constituents (i.e. the predicted wave arrives too early), while overpredicting the diurnal constituent phases.

The model predicts the orientations of the major axis components to within 10 to 20 degrees, with the bottom orientations showing higher variability than the surface.

The best overall agreement between the simulated and measured currents from the spectral analysis was at station UFL-B4. The harmonic analysis supports this finding, with the largest major axis amplitude error less than 2.0 cm/sec. The errors are consistent for the semi-diurnal and the diurnal constituents. The model either overpredicts or underpredicts depending upon the constituent, with errors less than 1.0 cm/sec.

The phase errors are all 30 minutes or less. The bottom currents do not show an overall pattern while the surface currents show that the model underpredicts the phases (i.e. the wave arrives too soon). This is in contrast to the error found for the simulated waterlevel data.

The major axis orientations calculated from the simulations are rotated 10 to 15 degrees clockwise from the actual orientation. For the surface sensors, the orientations calculated from the simulation are rotated 5 to 10 degrees counterclockwise. Whereas the data show the surface and bottom current vectors rotated 10 to 20 degrees in relation to each other the model predicts the surface and bottom vectors along the same alignment.

The one area where the simulations are significantly in error are the predictions of the rotational nature of the bottom currents. In the data analysis of Chapter 4 it was found that the surface currents were primarily unidirectional while the bottom currents were rotational. This was a curious result given that the two sensors were only 1.5 meters apart in 2 meters of water. Figure 4.19 presented the comparison of the surface and bottom harmonic ellipses for the measured currents. The model

Table 6.13: A comparison between the measured and simulated harmonic current constituents for the July/August 1991 data at UFL-B4

Sensor Location	Constituent	Data Major (cm/s)	Model Major (cm/s)	Error (cm/s)	Data Minor (cm/s)	Model Minor (cm/s)	Error (cm/s)
Bottom	M2	5.61	7.03	1.42	1.49	.03	-1.46
	S2	3.04	3.97	.93	.69	.07	-.62
	N2	1.18	1.55	.37	.05	.02	-.03
	K1	2.96	4.67	1.71	1.05	.02	-1.03
	O1	2.80	4.30	1.50	.16	.02	-.14
	MO3	1.27	1.15	-.12	.06	.07	.01
	MK3	1.82	1.53	-.30	.13	.04	-.08
Surface	M2	9.61	9.07	-.54	.23	.01	-.22
	S2	4.53	5.37	.84	.23	.14	-.09
	N2	2.56	1.99	-.57	.13	.02	-.11
	K1	5.93	6.29	.35	.20	.04	-.15
	O1	5.69	5.46	-.22	.68	.06	-.62
	MO3	1.39	1.50	.11	.66	.03	-.63
	MK3	1.99	2.13	.14	.25	.09	-.16

Sensor Location	Constituent	Data Phase (hrs)	Model Phase (hrs)	Error (hrs)	Data Angle (deg)	Model Angle (deg)	Error (deg)
	M2	2.56	2.88	.31	-57.57	-65.28	-7.71
	S2	-.50	-.30	.21	129.91	116.38	-13.53
	N2	2.86	2.43	-.42	-58.20	-65.20	-7.00
	K1	4.48	4.61	.14	-54.64	-68.82	-14.18
	O1	2.14	2.37	.24	-46.17	-66.26	-20.09
	MO3	-1.86	-2.05	-.19	-60.01	-59.53	.48
	MK3	.02	.13	.12	-62.59	-59.54	3.05
Surface	M2	2.92	2.91	-.01	-68.79	-66.30	2.49
	S2	-.33	-.34	-.02	110.27	114.87	4.60
	N2	2.81	2.24	-.57	-69.65	-65.67	3.98
	K1	5.29	4.78	-.52	-74.43	-64.22	10.22
	O1	2.52	2.34	-.18	-70.02	-68.65	1.37
	MO3	-1.74	-2.01	-.27	-60.28	-59.53	.75
	MK3	.07	.17	.10	-58.43	-60.81	-2.38

Table 6.14: The mean water surface elevation predicted by the model for Julian Day 200 to 230, 1991

Station	Water Surface Elevation (cm)
USGS-01	3.6
USGS-02	1.8
USGS-03	2.0
USGS-04	1.5
USGS-05	0.2
USGS-06	4.0
USGS-07	2.6

predicts unidirectional currents for both the surface and bottom.

6.3.4 Comparison of the Measured and Simulated Residuals

The previous section examined the accuracy of the model in predicting the short term periodic tides and currents. This section compares the simulated residual water surface elevations and currents with the measured residual water surface elevations and currents. These current components, although only a small portion of the total energy, are the primary mechanisms for the net movement of dissolved and particulate material within the lagoons.

Residual Water Surface Elevations

As discussed in Chapter 3 the original surveys conducted by the USGS to define the elevations of the tide gages were in error. Therefore the gage elevations are not available to determine the relative set-up and set-down within the lagoons. The existence of superelevations within enclosed basins has been shown through simplified models (Mann, 1987). Although no data are available to verify them, it is worthwhile to present the results of the simulations. Table 6.14 presents the model elevations at the seven USGS stations within the bay.

These results are based upon a zero mean water level elevation along the open boundary, except for offshore of Tampa Bay where the mean elevation is set to 3.0 cm.

The high residual water level at Anna Maria Sound is the result of the offshore setup needed to generate the net flow through Cortez. The greatest superelevation was simulated within Little Sarasota Bay with a net elevation 4.0 cm above the offshore mean water level. This net setup decreases in areas closer to the Gulf and the inlets. Within Big Pass there is a net set-up of 0.2 cm.

In addition to the net set-up, long term residual water surface fluctuations were identified in Chapter 4 by filtering the data. These fluctuations were attributed to Ekman Transport within the Gulf of Mexico. Figure 6.11 presents plots of the residual water surface elevations predicted by the model in comparison with the measured tides. The data have been demeaned to allow examination only of the magnitudes of the fluctuations. The model captures the general trends of the long term changes but underpredicts the magnitude of the fluctuations measured between Julian Days 210 to 215. This underprediction exists at all of the stations but is greatest at the Roberts Bay Station (USGS-04). The difference also exists within Big Pass. This indicates that either there is an error in the mean water level within the offshore or there was a net set-up against the coastline which is not simulated, i.e. a wind set-up not simulated within the offshore portion of the grid.

Residual Currents

As with the water surface elevations, the residual currents can be examined in two ways. First, by looking at the net mean current over the entire 30 day simulation in comparison with the measured mean. Secondly, the temporal variations in the residual over the thirty day period can be examined for each of the individual stations.

Table 6.15 presents comparisons of the measured and simulated mean current vector components over the 30 day simulation. To better compare the model results with the measured data, plots of the residual vector fields in the immediate vicinity of each of the UFL stations are presented in Figures 6.12 through 6.16. The plots present the residual field at each of the four vertical layers within the model.
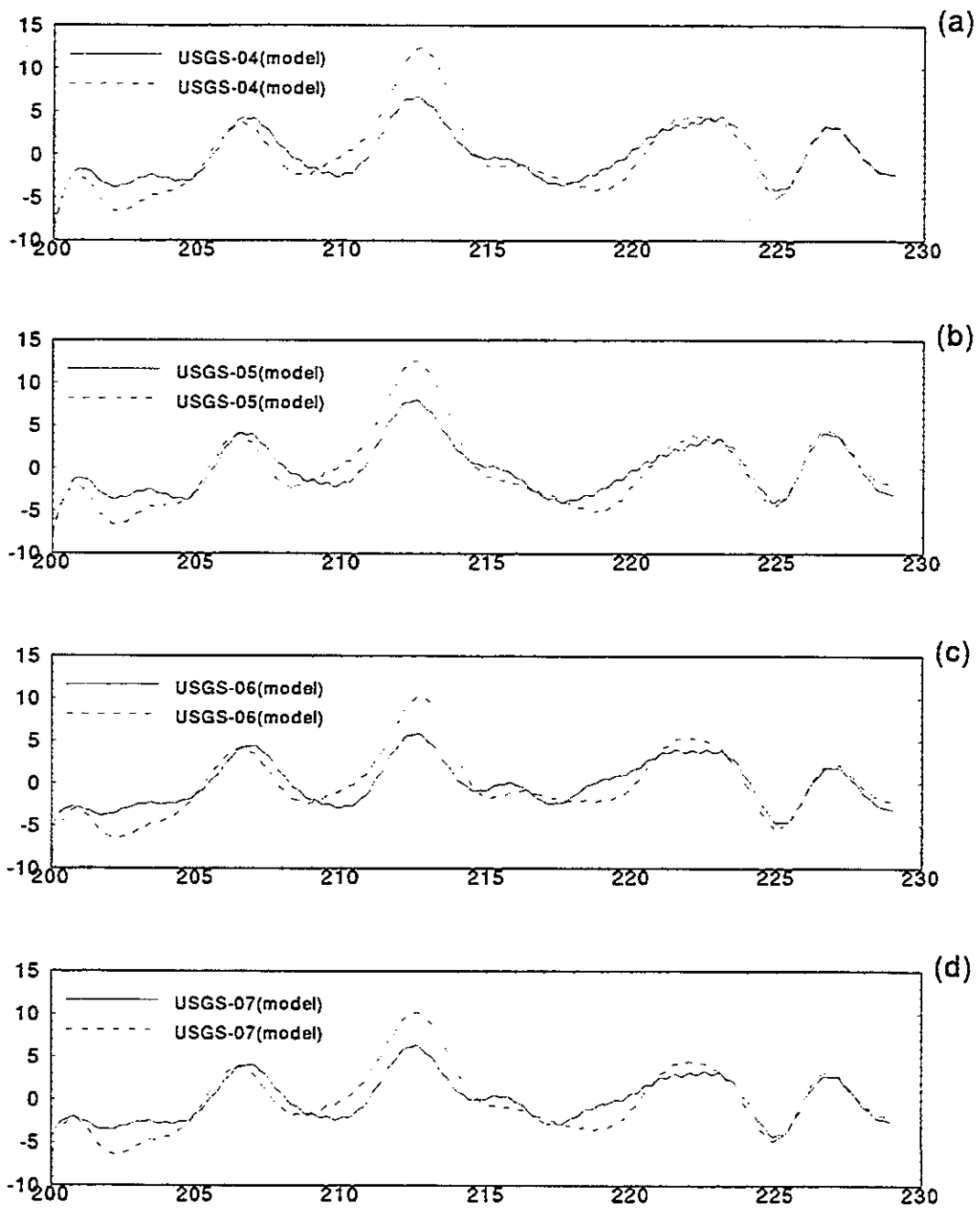
Figure 6.11: A comparison between the simulated and measured water surface elevations, Julian Day 200 to 230, 1991. a) USGS-04; b) USGS-05; c) USGS-06; d) USGS-07.

Table 6.15: A comparison of the measured and simulated mean currents for Julian Day 200 to 230, 1991

Station	Component	Simulated Residual (cm/sec)	Measured Residual (cm/sec)
UFL-B1	Bottom (E-W)	1.59	3.55
	Bottom (N-S)	-3.85	-5.79
	Surface (E-W)	2.04	4.46
	Surface (N-S)	-4.72	-8.46
UFL-B2	Bottom (E-W)	0.90	2.68
	Bottom (N-S)	-0.02	2.27
	Surface (E-W)	0.11	1.33
	Surface (N-S)	0.69	3.15
UFL-B3	Bottom (E-W)	-0.23	-0.34
	Bottom (N-S)	-0.02	-2.57
	Surface (E-W)	0.71	-1.26
	Surface (N-S)	-0.79	-0.80
UFL-B4	Bottom (E-W)	-1.02	-1.77
	Bottom (N-S)	0.68	1.94
	Surface (E-W)	-1.03	n/a
	Surface (N-S)	1.09	n/a

At UFL-B1 the model accurately simulates the residual current direction and distribution over the vertical. The magnitude of the residual is underpredicted by 50 percent. Examining the results on Figure 6.12 the residual velocity extends across the entire cross-section with the highest magnitudes within the deeper portions of the channel (east side). The residual is directly a function of the net set-up created within Tampa Bay through the superelevation of the offshore boundary condition.

Figure 6.13 presents the temporal variations in the measured and simulated current vector components at UFL-B1. The results show that the model simulates the overall characteristics of the fluctuations but overpredicts the fluctuation magnitude during the period from Julian Day 210 to 215. This was a period with high winds which created a residual reversal in both the model and the data, i.e. the net currents flowed north. It appears from the results that the model overestimates the influence of the wind stress in driving the residual flow. This is manifested most severely in the surface currents but can also be seen in the bottom currents. In addition, there is a lag between the measured bottom currents, i.e. the peak bottom currents occur later than that for the measured surface currents. This phenomenon is not seen in the model results.

At UFL-B2 the model significantly underpredicts the magnitude of the residual velocity. Examination of the vector field plotted in Figure 6.14 does indicate the model is simulating some of the characteristics of the data. The data show that the bottom residual current vector is oriented at 51 degrees from north while the surface residual is rotated in a counterclockwise direction and oriented at 21 degrees. Examination of the residual current fields plotted in Figure 6.14 show that the residual current vectors rotate in a counterclockwise direction from the bottom to the surface. Also the residual current vectors near UFL-B2 are oriented in a manner similar to that found for the measured data.

In Chapter 4 the measured residual velocity fluctuations at stations UFL-B2,
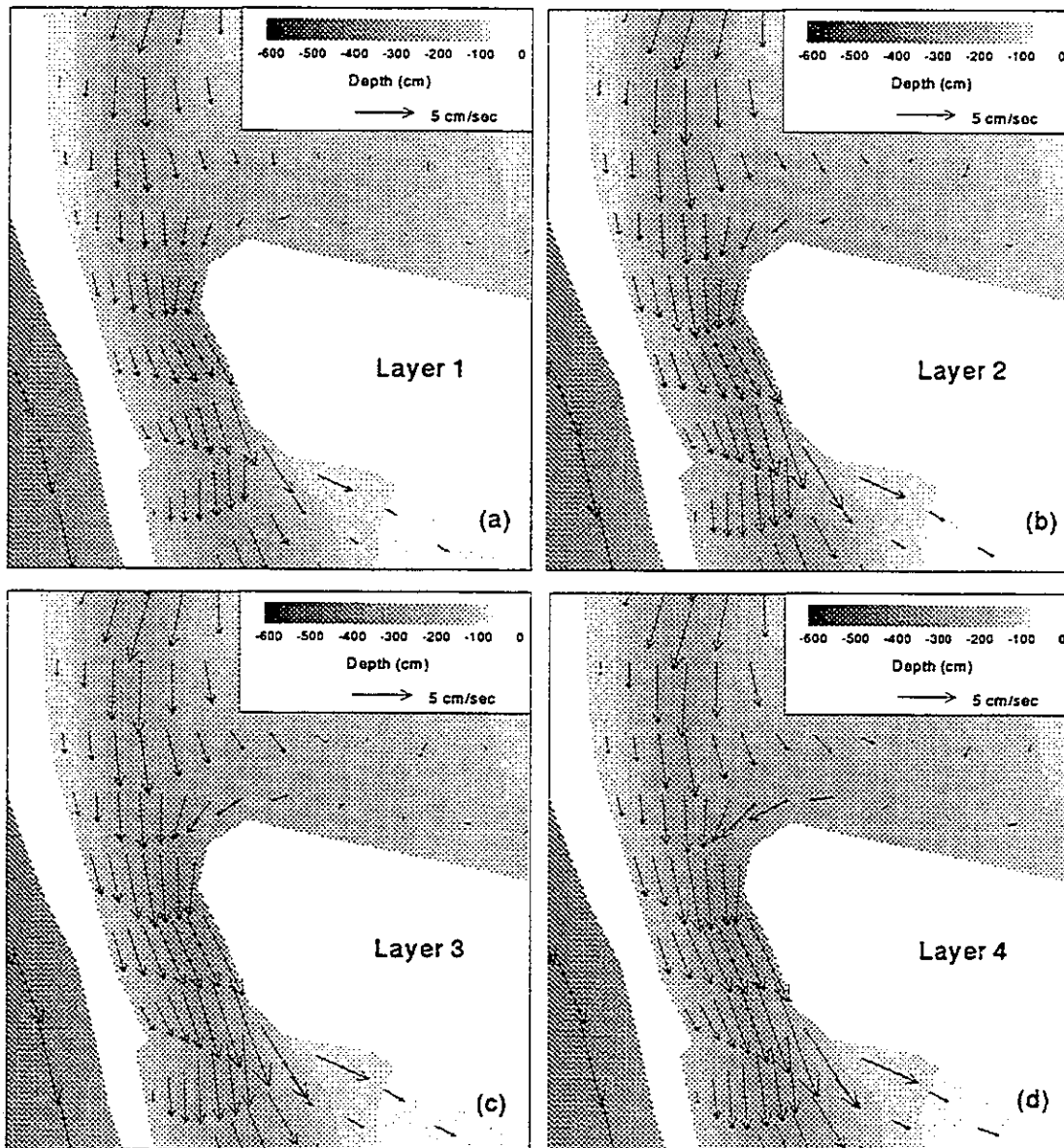
Figure 6.12: The residual velocity vectors near UFL-B1 predicted by the model, Julian Day 200 to 230, 1991. a) Layer 1; b) layer 2; c) layer 3; d) layer 4.
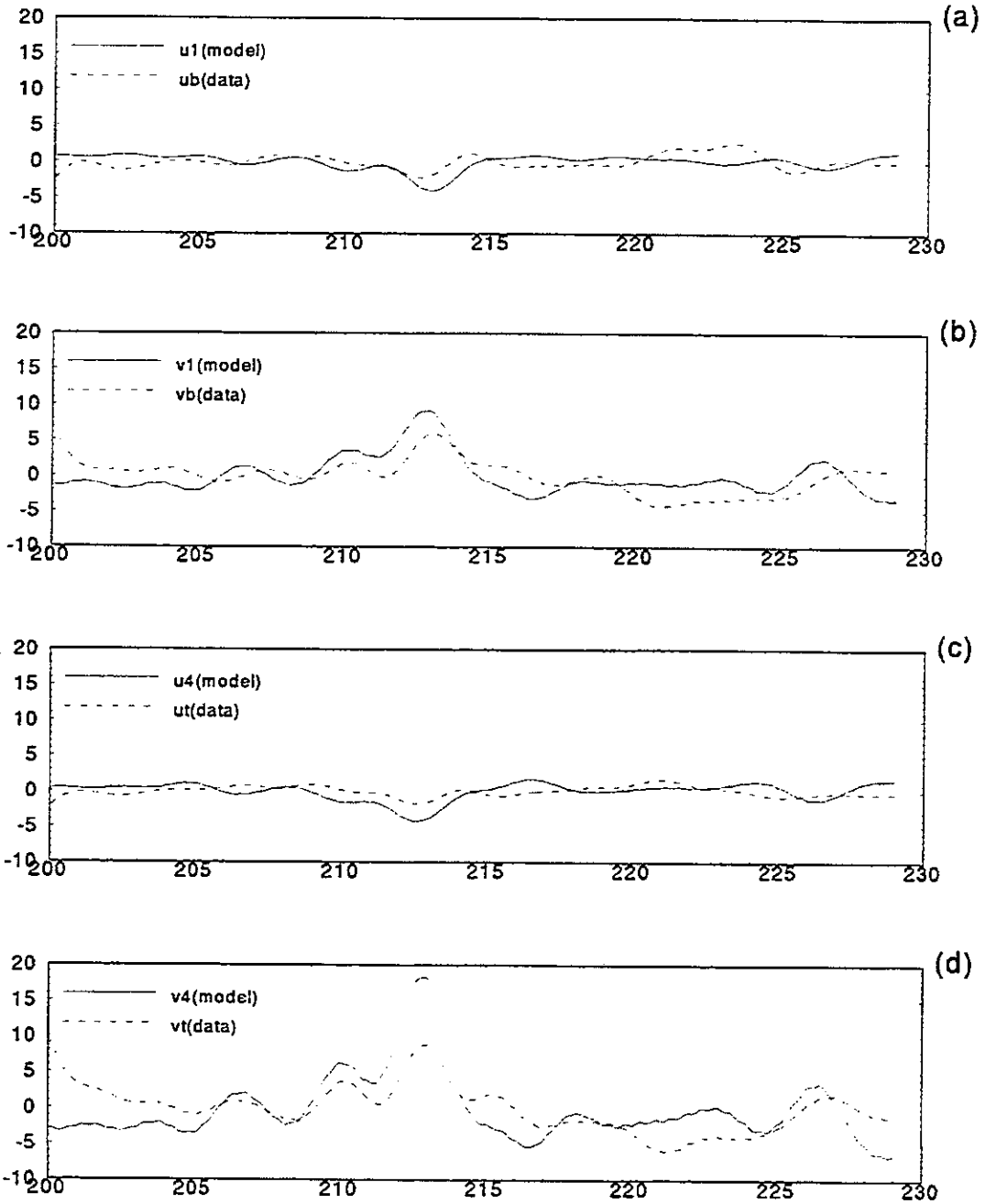
Figure 6.13: The Long Frequency Variations in the simulated and Measured Residual Current Vectors at UFL-B1, Julian Days 200 to 230, 1991. a) Bottom east-west component; b) bottom north-south component; c) surface east-west component; d) surface north-south component.

UFL-B3 and UFL-B4 were presented. The results showed negligible fluctuations at these stations and therefore only the 30 day mean currents are compared with the model results.

At station UFL-B3 the data show that the residual current vector has a magnitude of approximately 3 cm/sec and is oriented at approximately 188 degrees on the bottom and 237 degrees at the surface (Table 6.15). Although the simulated mean currents do not appear to agree, the vector field plots in Figure 6.15 exhibit similar characteristics to the data. The vectors rotate in a clockwise manner from surface to bottom and in the vicinity of UFL-B3 have similar magnitude and orientations. Given the complex nature of this region and the relatively coarse resolution of the grid this prediction is reasonable.

The measured and simulated residual currents at UFL-B4 show better agreement. The surface current sensor at UFL-B4 had calibration problems therefore the residual currents for this sensor are not reliable. Comparison of the simulated and measured mean bottom current shows the vectors to be of the same order of magnitude and general direction but once again the simulations underpredict the residual magnitude.

The residual vector fields near UFL-B3 and UFL-B4 show similar trends due to their proximity to constrictions directly to the north. The characteristic flood and ebb current patterns near a constriction create residual eddies which flow with the jet along the channel with return flow along the boundaries. The measured data support the existence of these patterns and they can be seen in the residual vector field plots (Figures 6.15 and 6.16). The same flow pattern may create the counterclockwise gyre seen near UFL-B2 (Figure 6.14).

6.3.5 Comparison of the Measured and Simulated Discharges

The discharge measurements conducted by USGS for this project were described in detail in Chapter 3, and the results were presented in Chapter 4. The data included measurements taken at the constriction to the north of Roberts Bay and across the
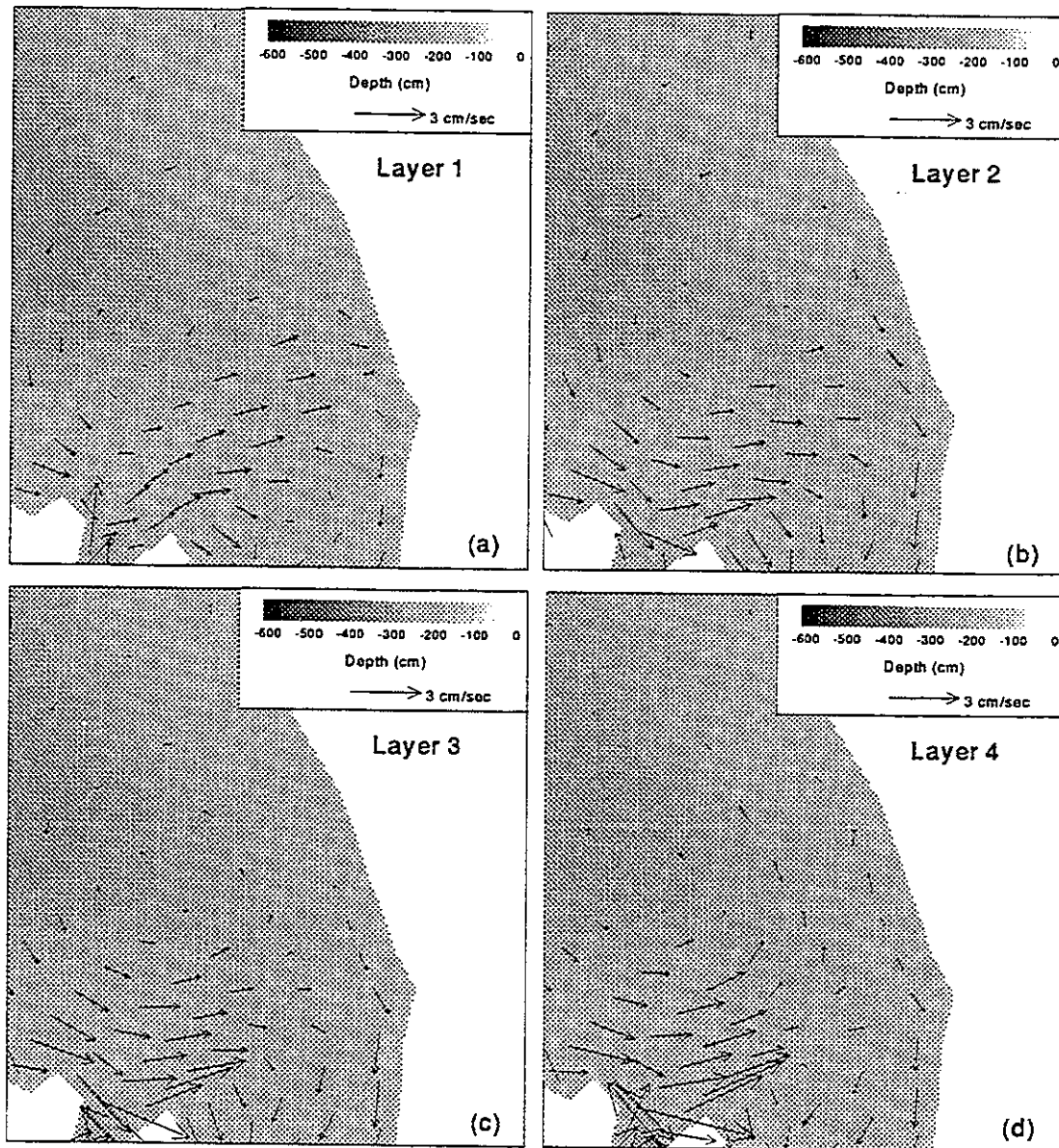
Figure 6.14: The residual velocity vectors near UFL-B2 predicted by the model, Julian Day 200 to 230, 1991. a) Layer 1; b) layer 2; c) layer 3; d) layer 4.
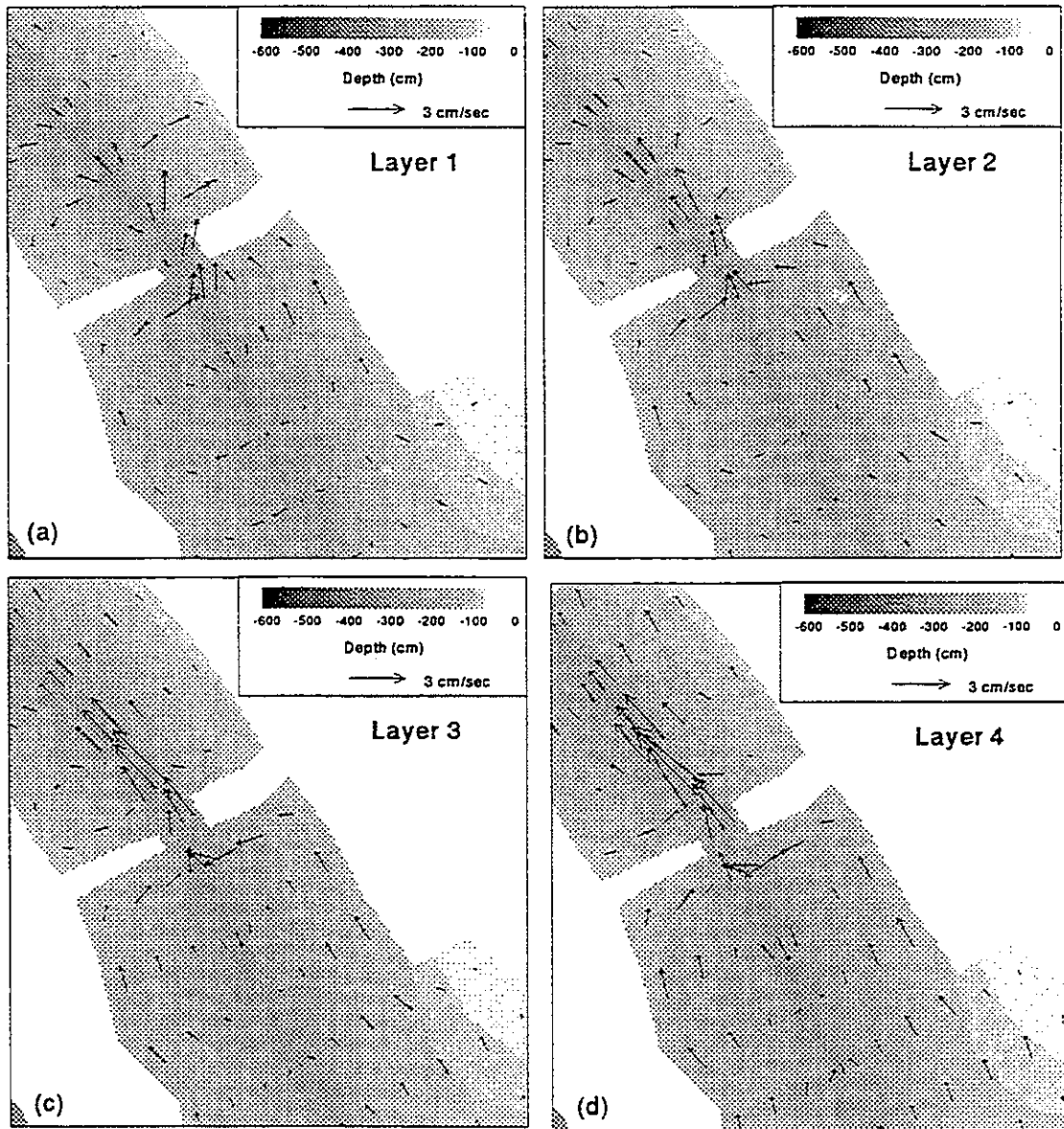
Figure 6.15: The residual velocity vectors near UFL-B3 predicted by the model, Julian Day 200 to 230, 1991. a) Layer 1; b) layer 2; c) layer 3; d) layer 4.
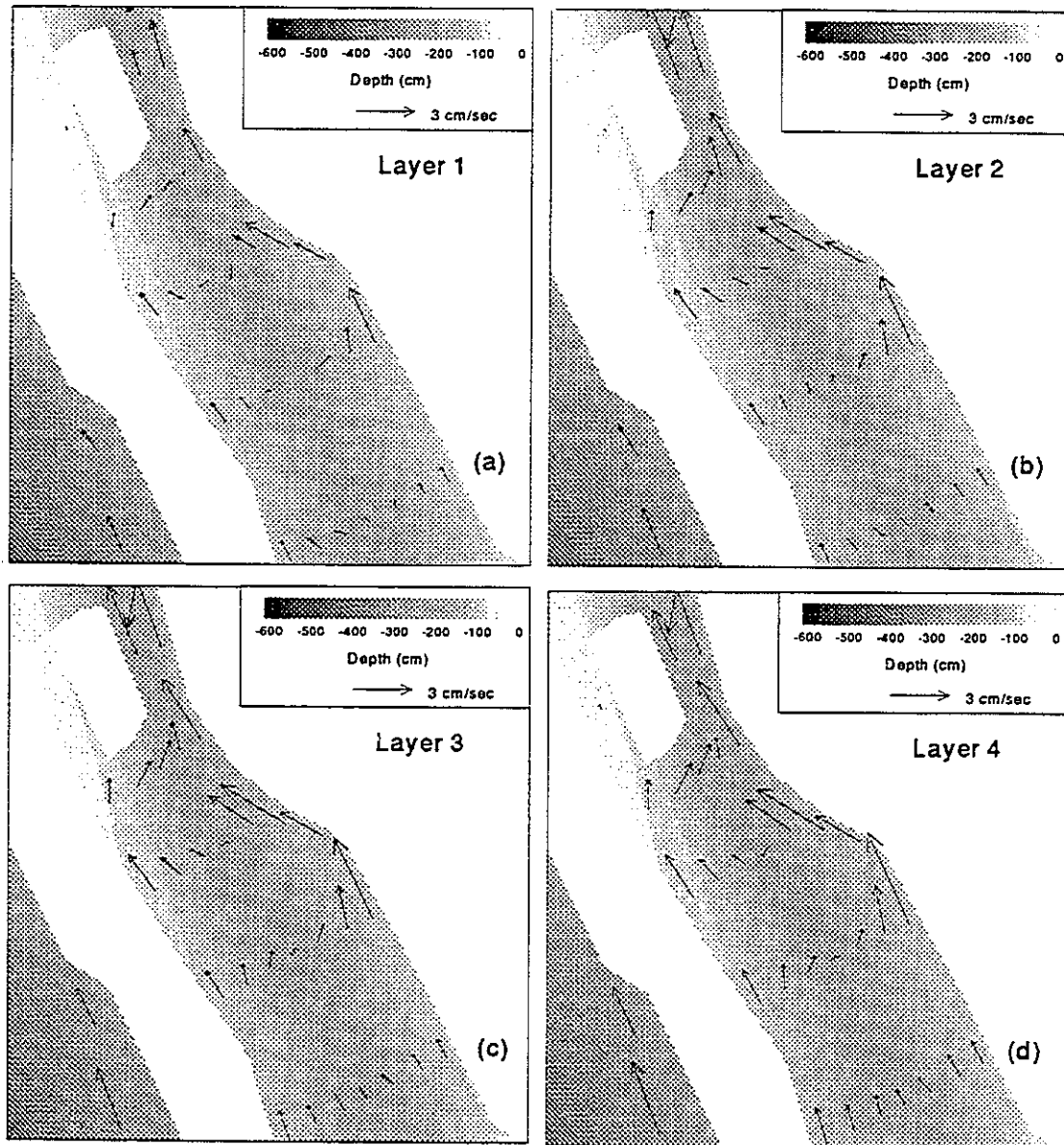
Figure 6.16: The residual velocity vectors near UFL-B4 predicted by the model, Julian Day 200 to 230, 1991. a) Layer 1; b) layer 2; c) layer 3; d) layer 4.

Intracoastal Waterway south of Blackburn Bay. Measurements were conducted over four days in 1991 during the deployment of the UFL instruments. In 1992 discrete discharge measurements were taken at each of the inlets entering the system except Venice Inlet, this includes Anna Maria Sound which opens onto Tampa Bay. Whereas the 1991 data are compared directly with the model results, the 1992 data are only used in a relative manner to check how well the model is simulating the distribution of flow through all five openings.

Figure 6.17 presents comparisons between the measured and simulated discharges into Roberts Bay and Blackburn Bay. The results show very good agreement for both flood and ebb tide. The distribution of flow into the lower bay system appears to be simulated well.

The USGS measurements of discharge through the passes were taken during the spring of 1992. In Chapter 4 an analysis was performed which equated the discharges measured under varying tidal forcing. From this analysis the percent of the total flow passing through each inlet was determined. If the assumption is made that the relative flow through each inlet does not change significantly over a tidal cycle then the percent contributions (during ebbing tide) can be utilized as a way of determining the accuracy of the 1991 discharge simulations. Table 6.16 presents the percent total flow through each inlet as calculated for the 1992 case in comparison with the percent total calculated from the model results.

The comparison shows that the model predicts the percentages within 5 percent at all of the inlets. It must be noted that numerous assumptions were utilized to calculate the 1992 percent contributions and these were based upon a small number of discrete measurements. The comparisons must be examined in light of these assumptions.
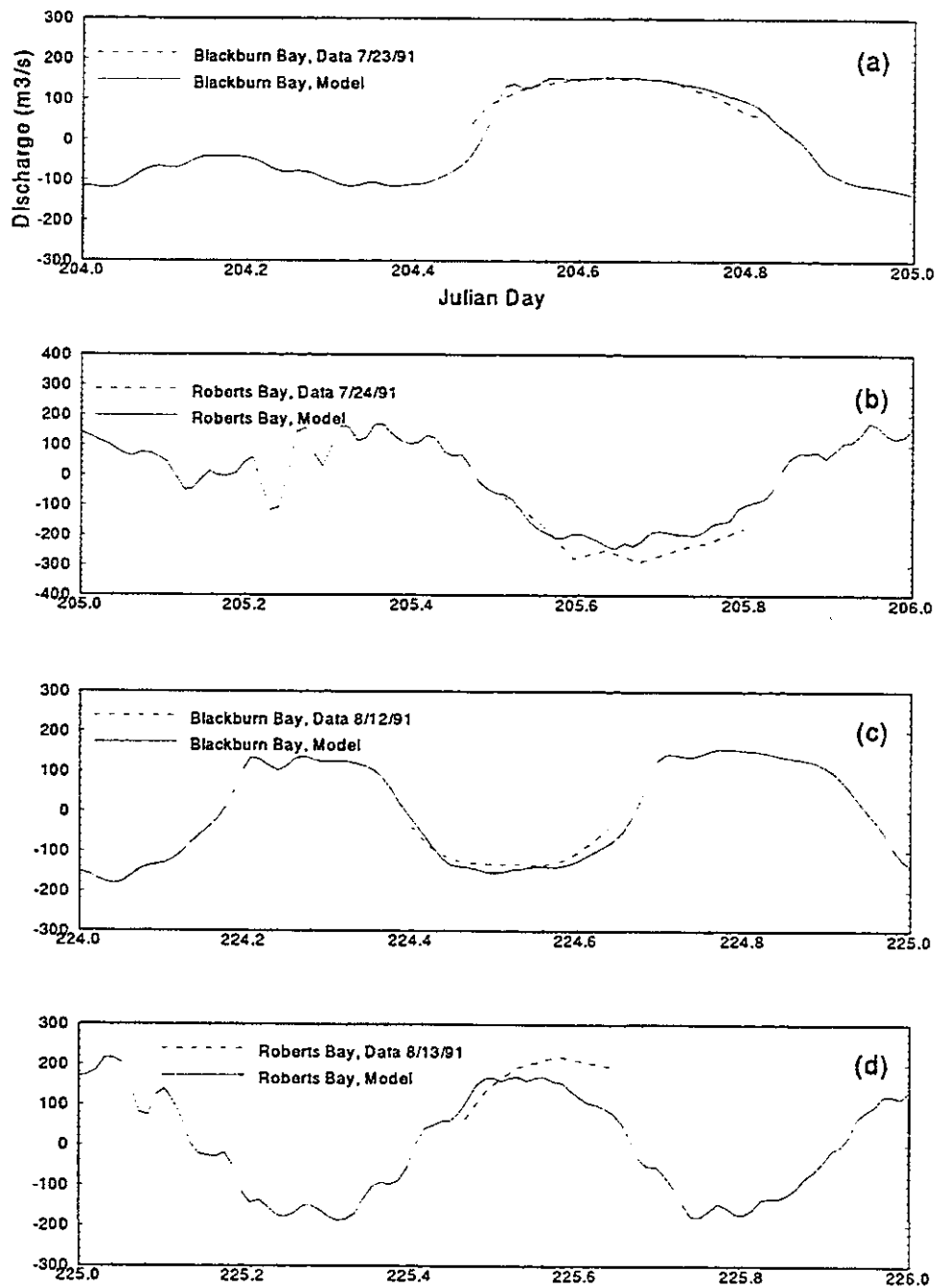
Figure 6.17: Comparisons of the Measured and simulated Discharges. a) Blackburn Bay, Julian Day 204 to 205, 1991; b) Roberts Bay, Julian Day 205 to 206, 1991; c) Blackburn Bay, Julian Day 224 to 225, 1991; d) Roberts Bay, Julian Day 225 to 226, 1991.

Table 6.16: A comparison of the percent of the total discharge through the inlets to Sarasota Bay and Anna Maria Sound between the calculated discharges for 1992 and the simulated discharges for Julian Days 200 to 230, 1991

Inlet	Percent Total 1992	Percent Total 1991
Anna Maria Sound	4.8	9.3
Longboat Pass	31.3	33.6
New Pass	22.9	18.2
Big Pass	41.0	38.9

6.3.6 Comparison of the Measured and Simulated Salinities

Section 4.4 presented the freshwater inflow measurements from the Manatee River and Walker Creek. In order to define the freshwater inflow from all other creeks within the system the time series of discharge for Walker Creek was divided by the drainage basin area, this defined a flow per unit acreage time series. This flow per unit acreage was then multiplied by the drainage area for each of the creeks to define the discharge condition. Figures 6.18 and 6.19 show plots of the freshwater inflow for each of the inflows to the model. The discharge from Walker Creek was used as the baseline because it is more representative of the small creeks which discharge to the Sarasota Bay System. Although the Manatee River will impact the system, its large drainage basin and longer response time are not compatible with the creeks which flow into the lagoons.

Although the data and methodology utilized to define the freshwater inflow boundary conditions was the best available, there are very definite limitations to it's accuracy. The assumptions which are being made are; the rainfall is the same within each of the drainage basins; the overland flow characteristics are the same within each basin; and the soil types and retention capacities are the same within each basin. These assumptions may not be realistic and all model results must be examined keeping in mind the inaccuracies of the boundary conditions.
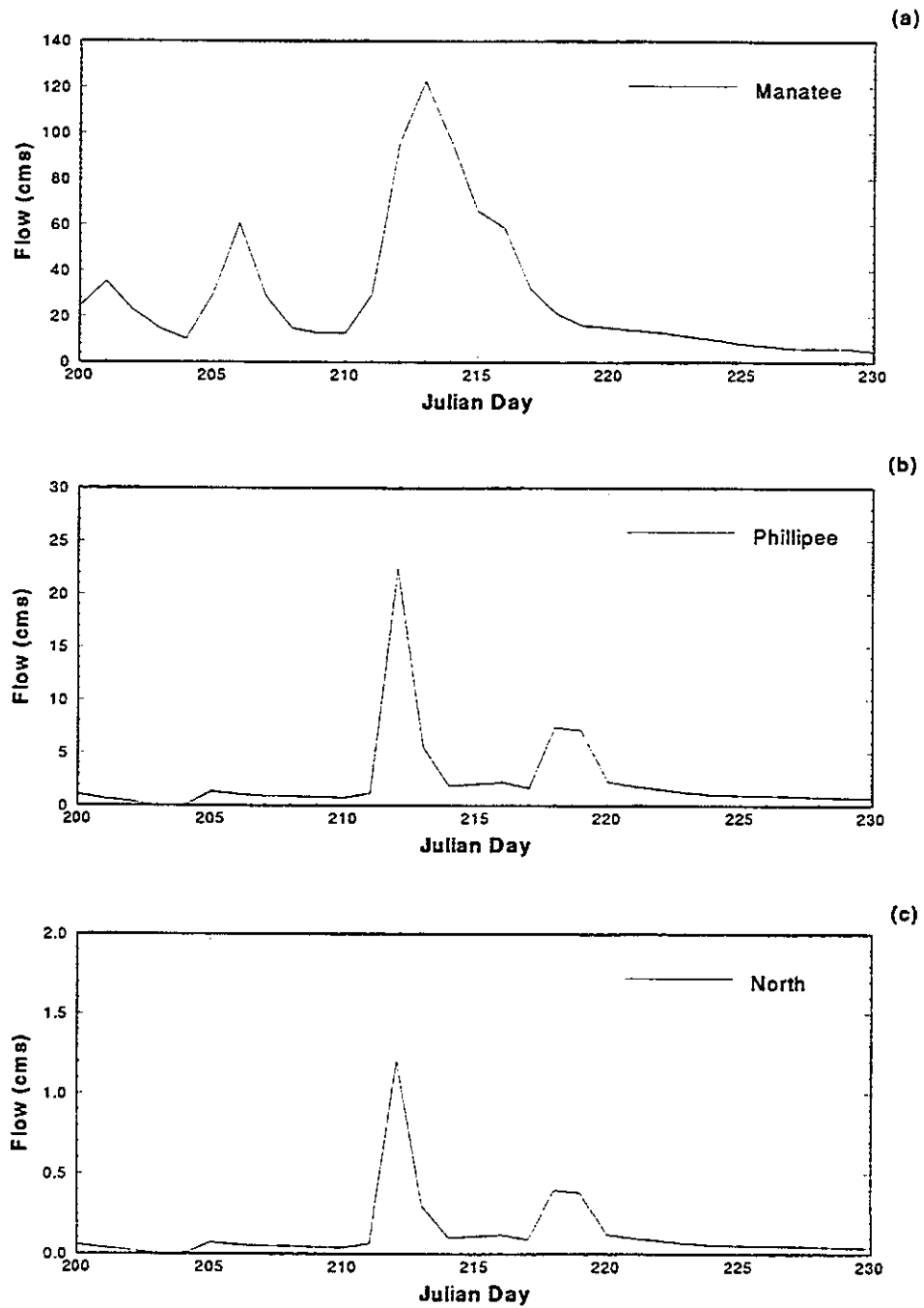
Figure 6.18: The Freshwater Inflow Boundary Conditions Utilized in the Model; a). Manatee River; b). Phillipee Creek; c). North Creek
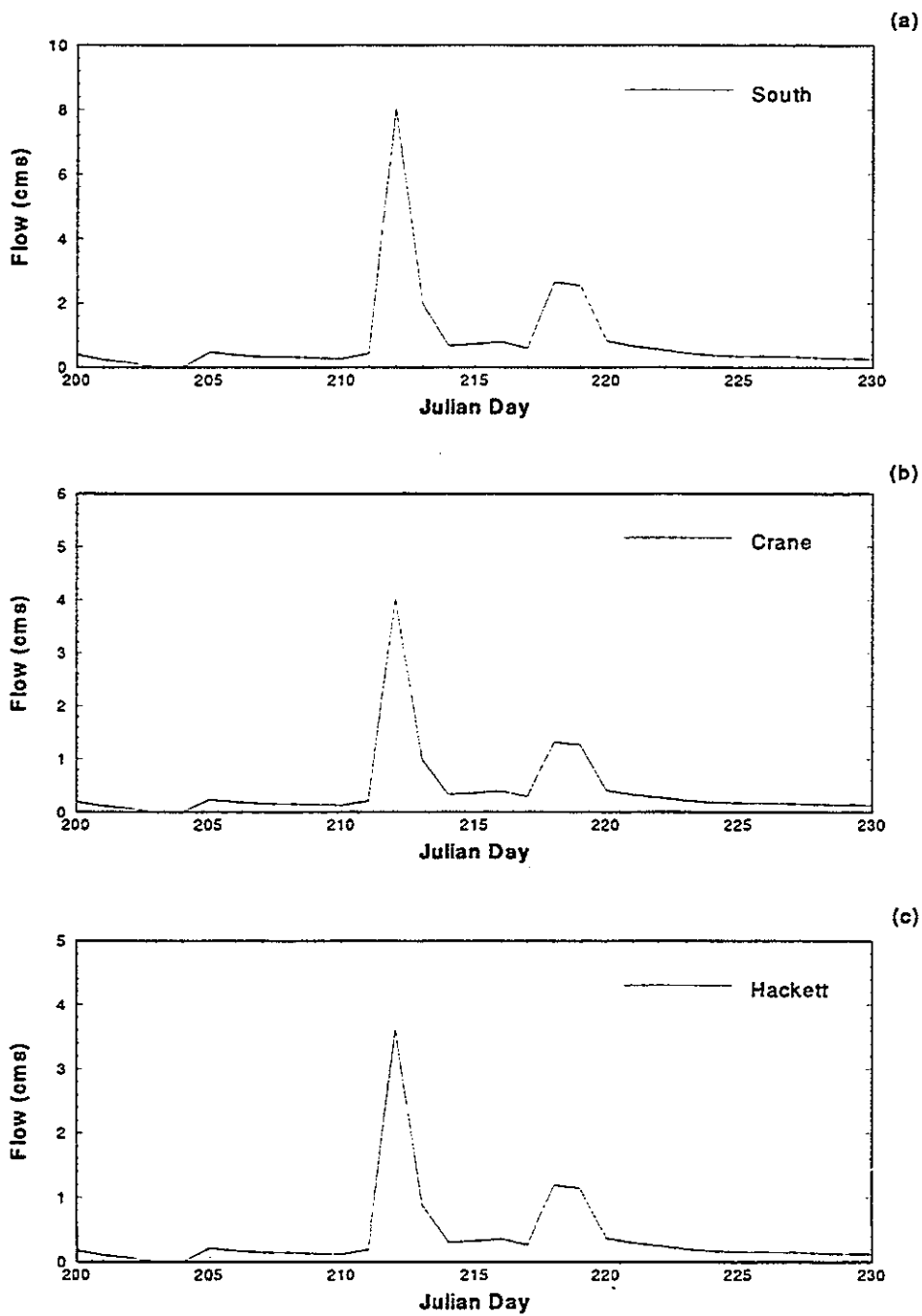
Figure 6.19: The Freshwater Inflow Boundary Conditions Utilized in the Model; a). South Creek; b). Crane Creek; c). Hackett Creek

Figures 6.20 and 6.21 present comparisons between the measured and simulated salinities at the four UFL stations. The plots present both the bottom and surface measurements and simulations.

At UFL-B1 the model simulates the general downward trend of the salinities but near the period of the high freshwater inflows, Julian Days 205 to 220, the model exhibits a much more dynamic response. At the time of the wind reversal the model predicts a rise in the salinity whereas the data show a steady fall. In the determination of the model accuracy it was shown that the model overpredicts the residual flow to the north during the high wind event near Julian Day 215. This may account for the rise in salinity seen in the model but not in the data. This overprediction of the wind residual may also be the cause of the rapid drop seen in the model results after day 215. It is noteworthy that the model simulates the net change in salinity over the 26 day period.

At UFL-B2 the model consistently overpredicts the salinity levels within the bay. There is a net difference of between 2 and 3 ppt between the model and the data. The model appears to capture the general trends in the salinity, i.e. it shows a similar drop in salinity during the high inflow period. The difference also appears to be greater in the surface predictions than in the bottom.

At UFL-B3 the model shows a net downward trend as seen with the data but the magnitude of the drop (7 to 8 ppt) is greater than that seen in the data (3 to 4 ppt). In addition the model predicts periods of rise and fall whereas the data show a nearly constant decrease.

UFL-B4 exhibited the most dynamic response to the freshwater inflow of all of the stations. This dynamic response appears to have been captured by the model although there is an immediate drop in salinity shown in the model which is not seen in the data. Upon completion of this drop the model then appears to mirror the measured data predicting similar drops and recoveries with a net -5 ppt difference.
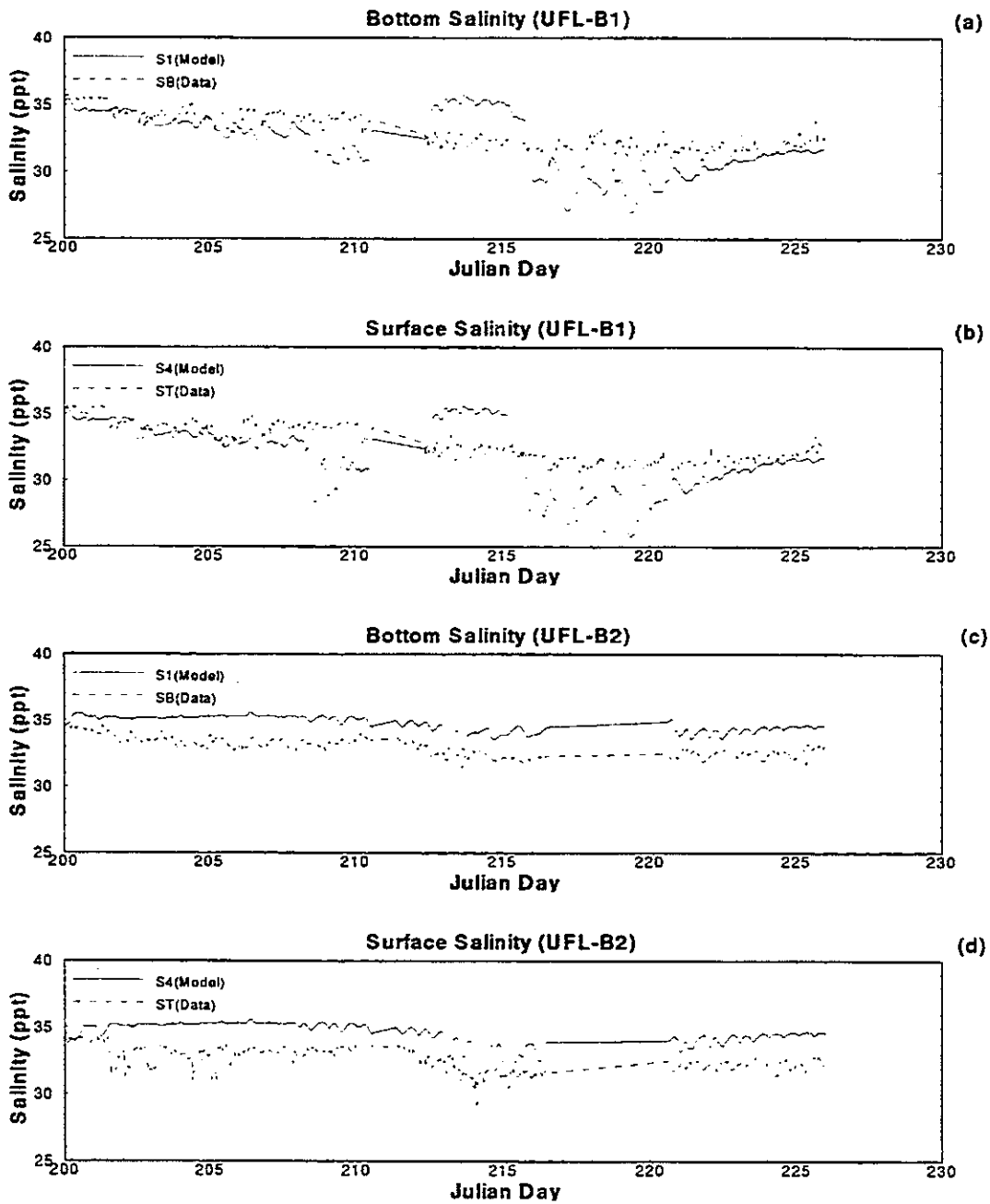
Figure 6.20: A Comparison Between the Measured and Simulated Salinities at Stations UFL-B1 and UFL-B2; a) Bottom Salinity UFL-B1; b). Surface Salinity UFL-B1; c). Bottom Salinity UFL-B2; d). Surface Salinity UFL-B2
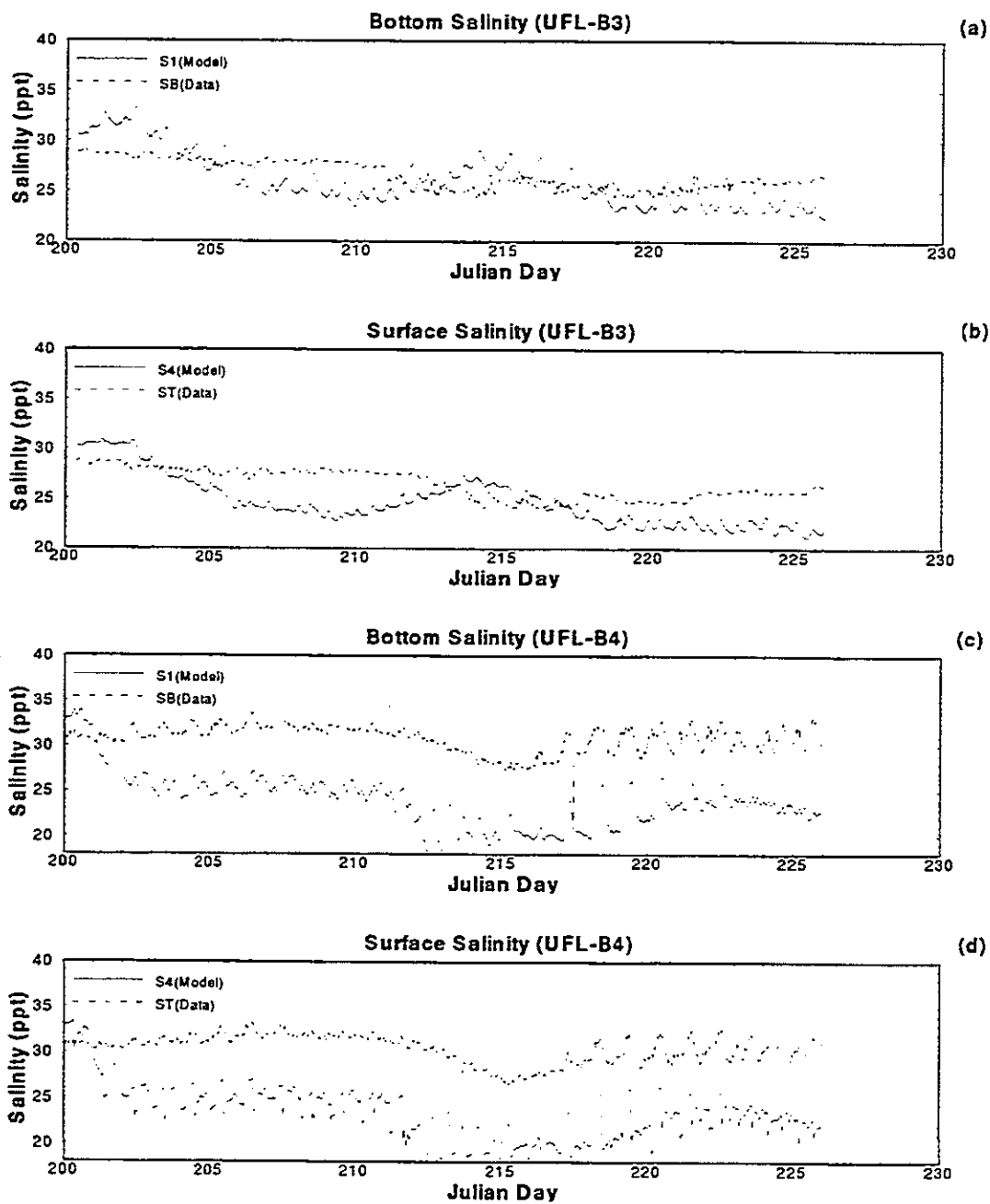
Figure 6.21: A Comparison Between the Measured and Simulated Salinities at Stations UFL-B3 and UFL-B4; a) Bottom Salinity UFL-B3; b). Surface Salinity UFL-B3; c). Bottom Salinity UFL-B4; d). Surface Salinity UFL-B4

This net error may be the result of inaccurate initial or boundary conditions.

Although the model does not simulate the overall magnitudes of the salinity well it does appear to capture much of the dynamic response. With more accurate initial and boundary conditions the model may be able to simulate the general trends in the salinity more accurately.

<p style="text-align: center;">6.4   <u>Model Sensitivity</u></p>

The numerical model, as described in Chapter 5 and Appendix C, contains various empirical parameters which are generally unknown prior to running the simulations. These empirical parameters are varied within the model in order to achieve the best fit between the model results and data. The model calibration presented in the previous section was obtained through iterative simulations in which these empirical parameters and other geometric and boundary conditions were varied. The final results represent the best overall comparison between the available data and the model.

The "sensitivity" of a numerical model is defined as the percent variation in the solution given a range of possible values for an unknown empirical constant. The following sections present results from sensitivity tests performed upon the three-dimensional numerical model as applied to the Sarasota Bay system. Tests are presented for variations to the bottom friction, the horizontal diffusion, the vertical turbulence and the bathymetry. Also the convergence of the model is tested by increasing the vertical resolution.

Table 6.17 presents a listing of the various runs performed and the values of critical input parameters. The table presents a description of the run, which forcing mechanisms are on or off, the horizontal eddy viscosity, the vertical eddy viscosity, and the bottom roughness coefficient. For the vertical eddy viscosity the values are either listed as "calc." or a number. The "calc." indicates that the second order closure model (Sheng, 1989) was utilized to calculate the vertical eddy viscosity within the

193

Table 6.17: A Listing of the Critical Model Input Values used within the Sensitivity Tests

Run Description	Salinity	Wind Forcing	Non-Linear Interaction	Horz. Eddy (A_h)	Vert. Eddy (A_v)	Bottom Roughness (z_1)
Base Run	no	yes	yes	50000	calc.	0.8
Low z_1	no	yes	yes	50000	calc.	0.02
Base z_1	no	yes	yes	50000	calc.	0.8
High z_1	no	yes	yes	50000	calc.	2.0
Low A_h	no	yes	yes	5000	calc.	0.8
Base A_h	no	yes	yes	50000	calc.	0.8
High A_h	no	yes	yes	100000	calc.	0.8
Const. A_v	no	yes	yes	50000	10.0	0.8

model. The following subsections discuss the results of the "sensitivity" testing for each of the runs listed.

6.4.1 Bottom Friction

As described in Chapter 5 the model defines the bottom friction through a quadratic solution of the form:

$$\tau_{b_x} = \rho C_d \sqrt{u_b^2 + v_b^2}(u_b) \tag{6.2}$$

where u_b and v_b are defined as the velocity components within the bottom cell. Given the nature of the sigma stretched solution the elevation of these bottom currents will vary depending upon the local depth. The drag coefficient is therefore defined as a function of a pre-defined bottom "roughness" z_1 and the elevation of the bottom velocity z_0 through the law of the wall for fully turbulent flow (Tennekes and Lumly, 1972). The equation states;

$$C_d = \frac{\kappa^2}{ln(\frac{z_1}{z_0})^2} \tag{6.3}$$

where κ is Von Karman's constant (0.4).

Within equation 6.3 the bottom roughness, z_1, represents a height, in centimeters, of elements along the bottom. This value is one of the empirical parameters which

may be used in model calibration. For the sensitivity tests the model was run with values of 0.02, 0.8 and 2.0 centimeters. The latter value (2.0) is unreasonable to assume as a roughness height to actually utilize within the model, but is only input for test purposes. The actual value used in the model calibrations was 0.8.

The calibration presented comparisons of the spectral energy, the harmonic constituents, the overall RMS errors, the spatial and temporal variations in the residual currents, and the discharges through the inlets and interior openings. Presenting all of these comparative analyses for each value of the test parameter is not necessary to establish the model sensitivity. Therefore a representative set of locations and parameters were defined to do the sensitivity tests. The tidal and current harmonic amplitudes and phases are compared to examine the impacts to the higher frequency components (i.e. less than a tidal cycle), while the net residual currents and water surface elevation at specific stations are utilized to compare the impacts to the low frequency components.

Table 6.18 presents comparisons of the tidal harmonic amplitudes calculated from the model results for the three roughness element heights. The simulated tides are not sensitive to the specification of the bottom roughness. The results show that over the range of expected roughness heights there is at most a 0.1 centimeter difference in the water surface elevation simulations. Based upon these results, an accurate specification of the bottom roughness is not critical to the simulation of the short term tides.

Table 6.19 presents comparisons of the current harmonic amplitudes for stations UFL-B2 and UFL-B3, calculated from the model results for the three roughness element heights. As with the tides, the currents do not exhibit a high level of sensitivity. The results show that a 10 fold variation in the bottom roughness element height creates at the greatest a 1 cm/sec difference in the current harmonic amplitudes.

Tables 6.20 and 6.21 present the sensitivity results for the residual water surface

Table 6.18: A Comparison of Tidal Harmonic Constituents Under Varying Bottom Roughness Height, Base Value = 0.8 cm, Low Value = 0.02 cm, High Value = 2.0 cm (USGS-04, USGS-05, USGS-06)

Station	Const.	Base (0.8) (cm)	Low (0.02) (cm)	High (2.0) (cm)
USGS-04	M2	15.5	15.5	15.6
	S2	6.2	6.2	6.3
	N2	3.2	3.2	3.2
	K1	16.2	16.2	16.3
	O1	11.9	11.8	11.9
	MO3	0.5	0.5	0.5
	MK3	1.8	1.8	1.8
USGS-05	M2	16.4	16.3	16.4
	S2	6.8	6.8	6.8
	N2	3.2	3.2	3.2
	K1	17.1	17.1	17.2
	O1	11.4	11.4	11.4
	MO3	0.7	0.7	0.7
	MK3	0.9	0.9	0.9
USGS-06	M2	12.1	11.9	12.4
	S2	4.2	4.2	4.3
	N2	3.2	3.2	3.3
	K1	13.6	13.5	13.7
	O1	11.7	11.7	11.9
	MO3	0.3	.3	0.3
	MK3	2.1	2.1	2.1

196

Table 6.19: A Comparison of the Principal Axis Current Harmonic Amplitudes Under Varying Bottom Roughness Height, Base Value = 0.8 cm, Low Value = 0.02 cm, High Value = 2.0 cm (UFL-B2, UFL-B3)

Station(Level)	Const.	Base (0.8) (cm/sec)	Low (0.02) (cm/sec)	High (2.0) (cm/sec)
UFL-B2(Bottom)	M2	10.3	10.2	10.4
	S2	4.0	4.0	4.1
	N2	2.4	2.5	2.4
	K1	5.5	5.5	5.6
	O1	4.5	4.4	4.5
	MO3	0.7	0.7	0.7
	MK3	2.5	2.5	2.5
UFL-B2(Surface)	M2	12.2	12.2	12.2
	S2	4.8	4.8	4.8
	N2	2.9	2.9	2.9
	K1	6.6	6.6	6.6
	O1	5.4	5.4	5.5
	MO3	0.9	0.9	1.0
	MK3	3.0	3.0	3.0
UFL-B3(Bottom)	M2	5.7	5.6	5.8
	S2	1.9	1.9	2.0
	N2	1.7	1.7	1.8
	K1	2.7	2.7	2.7
	O1	2.2	2.2	2.2
	MO3	0.4	0.4	0.4
	MK3	2.1	2.0	2.1
UFL-B3(Surface)	M2	6.8	6.7	6.9
	S2	2.7	2.6	2.7
	N2	2.1	2.1	2.2
	K1	2.9	3.0	2.9
	O1	2.5	2.5	2.5
	MO3	0.5	0.5	0.5
	MK3	2.7	2.7	2.7

Table 6.20: A Comparison of Mean Water Surface Elevation Under Varying Bottom Roughness Height, Base Value = 0.8 cm, Low Value = 0.02 cm, High Value = 2.0 cm (USGS-04, USGS-05, USGS-06)

Station	Base(0.8) (cm)	Low(0.02) (cm)	High(2.0) (cm)
USGS-04	0.5	0.5	0.4
USGS-05	-0.9	-0.9	-0.9
USGS-06	3.1	3.2	3.1

Table 6.21: A Comparison of Residual Velocity Components Under Varying Bottom Roughness Height, Base Value = 0.8 cm, Low Value = 0.02 cm, High Value = 2.0 cm (UFL-B2, UFL-B3)

Station	Component	Base(0.8) (cm/sec)	Low(0.02) (cm/sec)	High(2.0) (cm/sec)
UFL-B2	Bottom East-West	1.1	1.0	1.1
	Surface East-West	-0.1	-0.1	-0.1
	Bottom North-South	-0.3	-0.2	- 0.3
	Surface North-South	0.3	0.3	0.3
UFL-B3	Bottom East-West	-0.2	-0.2	-0.2
	Surface East-West	0.5	0.5	0.5
	Bottom North-South	0.3	0.3	0.3
	Surface North-South	-0.8	-0.8	-0.8

elevations and the residual currents. The results show that over the range of expected roughness heights the variation in the simulated mean water level is less than 0.1 cm. Similarly the residual velocities show less than a 0.1 variation.

6.4.2 Horizontal Diffusion

Within the numerical model the horizontal diffusion is defined based upon the spatial gradient within the velocity field and the horizontal turbulent eddy coefficient (A_h). The horizontal eddy coefficient is an empirical constant within the model, which is adjusted in order to produce the best fit between the simulations and the measured data. The value which produced the best fit between the model and data was 50000 $cm^2 - sec$. The following presents a series of sensitivity tests similar to those shown

Table 6.22: A Comparison of Tidal Harmonic Constituents Under Varying Horizontal Eddy Coefficient , Base Value = 50000 $cm^2 - sec$cm, Low Value = 5000 $cm^2 - sec$, High Value = 100000 $cm^2 - sec$ (USGS-04, USGS-05, USGS-06)

Station	Const.	Base (50000) (cm)	Low (5000) (cm)	High (100000) (cm)
USGS-04	M2	15.5	15.3	15.6
	S2	6.2	6.2	6.3
	N2	3.2	3.1	3.2
	K1	16.2	16.1	16.3
	O1	11.9	11.8	11.9
	MO3	0.5	0.5	0.5
	MK3	1.8	1.7	1.9
USGS-05	M2	16.4	16.3	16.4
	S2	6.8	6.8	6.8
	N2	3.2	3.2	3.2
	K1	17.1	17.1	17.1
	O1	11.4	11.3	11.4
	MO3	0.7	0.7	0.7
	MK3	0.9	0.9	0.9
USGS-06	M2	12.1	11.9	12.3
	S2	4.2	4.4	4.2
	N2	3.2	2.8	3.3
	K1	13.6	13.5	13.6
	O1	11.7	11.6	11.9
	MO3	0.3	0.4	0.3
	MK3	2.1	2.3	2.1

for bottom friction in which the horizontal diffusion is varied from 100000 $cm^2 - sec$ down to 5000 $cm^2 - sec$. The higher value is limited based upon time step criteria and the smallest grid spacing within the solution domain.

Table 6.22 presents comparisons of the tidal harmonic amplitudes calculated from the model results for the three eddy diffusivities. The results show a maximum 0.4 cm variation over the expected range of coefficients.

Table 6.23 presents comparisons of the current harmonic amplitudes for stations UFL-B2 and UFL-B3 calculated from the model results for the three eddy coefficients.

Table 6.23: A Comparison of the Principal Axis Current Harmonic Amplitudes Under Varying Horizontal Eddy Coefficient, Base Value = 50000 $cm^2 - sec$, Low Value = 5000 $cm^2 - sec$, High Value = 100000 $cm^2 - sec$ (UFL-B2, UFL-B3)

Station(Level)	Const.	Base (50000) (cm/sec)	Low (5000) (cm/sec)	High (100000) (cm/sec)
UFL-B2(Bottom)	M2	10.3	10.1	10.4
	S2	4.0	4.0	4.1
	N2	2.4	2.4	2.5
	K1	5.5	5.5	5.6
	O1	4.5	4.4	4.5
	MO3	0.7	0.6	0.7
	MK3	2.5	2.4	2.5
UFL-B2(Surface)	M2	12.2	12.0	12.3
	S2	4.8	4.8	4.9
	N2	2.9	2.9	3.0
	K1	6.6	6.6	6.7
	O1	5.4	5.4	5.5
	MO3	0.9	0.9	1.0
	MK3	3.0	2.9	3.0
UFL-B3(Bottom)	M2	5.7	8.9	4.8
	S2	1.9	2.7	1.6
	N2	1.7	2.5	1.6
	K1	2.7	4.9	2.0
	O1	2.2	3.5	1.7
	MO3	0.4	0.6	0.4
	MK3	2.1	3.2	1.8
UFL-B3(Surface)	M2	6.8	11.0	5.7
	S2	2.7	3.7	2.2
	N2	2.1	3.0	2.1
	K1	2.9	6.0	2.1
	O1	2.5	3.9	1.8
	MO3	0.5	0.8	0.4
	MK3	2.7	4.7	2.2

Table 6.24: A Comparison of Mean Water Surface Elevation Under Varying Bottom Roughness Height, Base Value $= 50000$ $cm^2 - sec$, Low Value $= 5000$ $cm^2 - sec$, High Value $= 100000$ $cm^2 - sec$ (USGS-04, USGS-05, USGS-06)

Station	Base(50000) (cm)	Low(5000) (cm)	High(100000) (cm)
USGS-04	0.5	0.4	0.5
USGS-05	-0.9	-0.9	-0.9
USGS-06	3.1	1.5	4.7

The results show a much higher level of sensitivity to the horizontal eddy coefficient at Station UFL-B3 than UFL-B2. Over the range of coefficients the model shows a maximum 0.4 cm/sec variation at UFL-B2 while at UFL-B3 the maximum variation is 5.3 cm/sec or approximately a 100 percent change in the magnitude.

Tables 6.24 and 6.25 present the sensitivity results for the residual water surface elevations and the residual currents. The results show that over the range of eddy coefficients there is a significant variation in the mean water level at the most interior station UFL-B3 while at the other stations there is less than a 0.1 cm change. Similar results are found for the residual currents with variations of 5 cm/sec at the surface, this is nearly a five fold variation in comparison to the residual currents.

6.4.3 Vertical Turbulence

The vertical eddy viscosity (A_v) within the model can be determined using various methods. The model allows for input of a constant value throughout the solution domain, it allows for calculation of A_v using first order closure schemes and it allows for calculation of A_v through the solution of a simplified second order closure model (Sheng, 1989). For the calibration run presented earlier, the second order closure model was utilized to calculate the vertical eddy coefficient. To test the sensitivity of the solution to the definition of the vertical turbulence, the following presents a comparison between a model run with a constant A_v and a run which utilizes the second order closure model.

Table 6.25: A Comparison of Residual Velocity Components at Under Varying Horizontal Eddy Coefficient. Base Value = 50000 cm^2-sec, Low Value = 5000 cm^2-sec, High Value = 100000 cm^2-sec (UFL-B2, UFL-B3)

Station	Component	Base(50000) (cm/sec)	Low(5000) (cm/sec)	High(2.0) (cm/sec)
UFL-B2	Bottom East-West	1.1	1.0	1.1
	Surface East-West	-0.1	-0.2	-0.1
	Bottom North-South	-0.3	-0.3	- 0.2
	Surface North-South	0.3	0.3	0.3
UFL-B3	Bottom East-West	-0.2	0.9	-0.6
	Surface East-West	0.5	2.6	-0.1
	Bottom North-South	0.3	-2.7	1.3
	Surface North-South	-0.8	-4.7	0.6

Table 6.26 presents comparisons of the tidal harmonic amplitudes calculated from the model results under the two input conditions. Once again the short term tides do not exhibit a high degree of sensitivity to this input parameter. The greatest differences are seen at the most interior station (USGS-06) with maximum constituent amplitude variations of 0.7 cm.

Table 6.27 presents comparisons of the current harmonic amplitudes for stations UFL-B2 and UFL-B3 calculated from the model results under the two input conditions. There does not appear to be a high level of sensitivity within the tidal currents and unlike the tides there is no increase in sensitivity at the interior station (UFL-B3). The maximum fluctuation in the current harmonics is 0.8 cm/sec and this occurs at UFL-B2.

Tables 6.28 and 6.29 present the results for the residual water surface elevations and the residual currents under the two input conditions. The results show that the residual water level is not impacted to a significant degree by the definition of the vertical turbulence. The residual velocities on the other hand show significant sensitivity to the vertical turbulence with order of magnitude variations between the two method.

Table 6.26: A Comparison of Tidal Harmonic Constituents using Constant Vertical Eddy Viscosity (10 $cm^2 - sec$) versus a Second Order Closure Model (USGS-04, USGS-05, USGS-06)

Station	Const.	Second Order Closure Model	Constant A_v
USGS-04	M2	15.5	15.2
	S2	6.2	6.1
	N2	3.2	3.1
	K1	16.2	16.0
	O1	11.9	11.9
	MO3	0.5	0.5
	MK3	1.8	1.8
USGS-05	M2	16.4	16.3
	S2	6.8	6.8
	N2	3.2	3.1
	K1	17.1	17.1
	O1	11.4	11.4
	MO3	0.7	0.7
	MK3	0.9	0.9
USGS-06	M2	12.1	11.4
	S2	4.2	3.9
	N2	3.2	3.1
	K1	13.6	13.3
	O1	11.7	11.5
	MO3	0.3	0.2
	MK3	2.1	1.9

Table 6.27: A Comparison of the Principal Axis Current Harmonic Amplitudes Using Constant Vertical Eddy Viscosity (10 cm^2-sec) Versus a Second Order Closure Model (UFL-B2, UFL-B3)

Station(Level)	Const.	Second Order Closure Model	Constant A_v
UFL-B2(Bottom)	M2	10.3	10.0
	S2	4.0	3.8
	N2	2.4	2.4
	K1	5.5	5.2
	O1	4.5	4.2
	MO3	0.7	0.8
	MK3	2.5	2.6
UFL-B2(Surface)	M2	12.2	13.0
	S2	4.8	5.0
	N2	2.9	3.2
	K1	6.6	7.1
	O1	5.4	5.8
	MO3	0.9	1.1
	MK3	3.0	3.3
UFL-B3(Bottom)	M2	5.7	5.3
	S2	1.9	1.7
	N2	1.7	1.6
	K1	2.7	2.8
	O1	2.2	2.1
	MO3	0.4	0.4
	MK3	2.1	1.8
UFL-B3(Surface)	M2	6.8	6.4
	S2	2.7	2.7
	N2	2.1	2.0
	K1	2.9	3.1
	O1	2.5	2.2
	MO3	0.5	0.3
	MK3	2.7	2.7

Table 6.28: A Comparison of Mean Water Surface Elevation Under Constant Vertical Eddy Viscosity ($10 \frac{cm^2}{sec}$) versus a Second Order Closure Model (USGS-04, USGS-05, USGS-06)

Station	Second Order Closure Model	Constant A_v
USGS-04	0.5	0.5
USGS-05	-0.9	-0.9
USGS-06	3.1	3.3

Table 6.29: A Comparison of Residual Velocity Components using Constant Vertical Eddy Viscosity versus a Second Order Closure Model (UFL-B2, UFL-B3)

Station	Component	Second Order Closure Model	Constant A_v
UFL-B2	Bottom East-West	1.1	0.7
	Surface East-West	-0.1	0.8
	Bottom North-South	-0.3	-0.1
	Surface North-South	0.3	0.4
UFL-B3	Bottom East-West	-0.2	0.0
	Surface East-West	0.5	2.6
	Bottom North-South	0.3	-0.2
	Surface North-South	-0.8	0.1

6.4.4 Bathymetric Conditions

The bathymetry is not considered a variable parameter within the model, i.e. it is not an empirical constant which is unknown and needs to be calibrated. In general the most accurate data available are input to the model and the runs calibrated based upon those values. For this study the complexity of the bathymetry within the study area warrant some general discussion as it was one of the most varied parameters during the calibration of the model.

The variation in scale of the Sarasota Bay system from Tampa Bay down to Venice Inlet created problems in the generation of a numerical grid which resolved the complexities but which did not contain such a large number of cells that the computational time would be restrictive. The grid presented in Figure 6.1 represents the end product of multiple iterations and tests. Upon creation of the initial grid tests runs of the model indicated that modifications needed to be made to resolve some of the more fine scale geometries. For instance, in the area of Longboat Pass the channel splits into a Y and goes north and south. The grid generation program created interior grids which did not align with the Intracoastal Waterway. Hand modification of the grid was required to create the desired alignment. This same problem was found within Little Sarasota Bay and Blackburn Bay. The grid generation program was unable to align the grids to the width and location of the Intracoastal Waterway. The tendency of the program was to smear the grid spacings evenly across the long narrow lagoons and align with the boundary elements. The Intracoastal Waterway does not always align with the center of the lagoon and once again hand modifications were required to achieve the desired alignment.

The bathymetry was input to the grid generation program as a file of random coordinates with depths. The depths were then interpolated onto the grid using distance weighted linear averaging. Where bathymetric data were too coarse to resolve complex bathymetry, hand modifications were required. Each iterative change to the

grid and bathymetry created improvements in the overall accuracy of the simulations. The magnitude of the improvements were significant in relation to the sensitivity runs shown above.

6.4.5   Vertical Resolution

The error in a numerical solution is directly proportional to the size of the grid spacing. Therefore as the resolution of the grid is increased, the accuracy of the solution should improve, this is termed convergence. In order to test the convergence of the solution, the vertical grid resolution was increased and a short term simulation was conducted and compared with a similar run of lesser resolution. In the calibration runs the vertical grid resolution was set to four, this was deemed sufficient to represent the relatively shallow system and avoided excessive computation time. To test the convergence two 10 day runs were performed one with a grid resolution of four and one with a grid resolution of eight. If the solution is truly convergent, then the overall accuracy should be greater for the higher resolution runs. To evaluate this, the RMS errors between the measured data and the simulations were calculated for the ten day runs. Table 6.30 presents comparisons of the RMS errors for the two simulations.

The results show that overall the increased resolution in the vertical grid improves the solution. Various points show identical or worse RMS errors between the two model runs but the large percentage of the stations show improvement on the order of 5 to 10 percent. This indicates that the solution is convergent.

6.4.6   Summary of Model Accuracy and Sensitivity

The next step in utilizing the numerical model will be to examine the relative influence of the forcing mechanisms of wind, tides, salinity and non-linear interaction upon the short term and long term circulation within the system. Prior to doing this it is worthwhile to summarize the relative accuracy and sensitivity of the model in order to define how useful it will be as a predictive or analytic tool. The following summarizes the findings in relation to the model accuracy and sensitivity.

Table 6.30: A Comparison of the RMS Errors Between the Measured Tides and Currents and Simulated Tides and Currents Using Four Vertical Layers and Eight Vertical Layers.

Data Type	Station	RMS Error 4 Layers	RMS Error 8 Layers
Tides (cm)	USGS-04	3.8	3.4
	USGS-05	2.0	1.9
	USGS-06	2.9	2.3
	USGS-07	2.7	2.5
Currents (cm/s)	UFL-B1 (Bottom E-W)	3.6	3.6
	UFL-B1 (Surface E-W)	4.4	4.5
	UFL-B1 (Bottom N-S)	7.2	6.6
	UFL-B1 (Surface N-S)	9.2	8.9
	UFL-B2 (Bottom E-W)	3.4	3.5
	UFL-B2 (Surface E-W)	3.1	3.0
	UFL-B2 (Bottom N-S)	4.2	4.2
	UFL-B2 (Surface N-S)	5.1	5.0
	UFL-B3 (Bottom E-W)	1.9	1.7
	UFL-B3 (Surface E-W)	2.7	2.4
	UFL-B3 (Bottom N-S)	4.2	3.9
	UFL-B3 (Surface N-S)	4.1	3.9
	UFL-B4 (Bottom E-W)	2.1	2.0
	UFL-B4 (Surface E-W)	2.9	2.8
	UFL-B4 (Bottom N-S)	3.8	3.6
	UFL-B4 (Surface N-S)	3.5	3.7

The model simulates the short term water level fluctuations to within 5 percent error at all of the stations. Although the model overpredicts the energy in the water surface fluctuations slightly, the distribution of energy across the sub-tidal, diurnal, semi-diurnal and higher harmonic energy bands is well represented. One consistent error seen for the simulations is that the model does not damp the higher frequency (semi-diurnal) tidal fluctuations to the degree found in the measured data. The phases of the tidal fluctuations are predicted within 30 to 40 minutes at all of the stations. The characteristics of the residual water level fluctuations are simulated well in both phase and magnitude although the model slightly underpredicts the level of surge during the one high wind event.

The accuracy of the simulations of the currents is not as good as that for the tides. The percent errors in the short term tidal fluctuations ranges from less than 10 percent to as high as 30 percent. The greatest errors are seen for the most interior stations with the lowest total energy. The distribution of the energies was simulated well for two of the four stations. The model predicts high semi-diurnal percentages in comparison with the diurnal at all of the stations, whereas the data show specific stations (UFL-B1 and UFL-B3) to have a more even distribution of energy between the dirunal and semi-diurnal bands. The common physical characteristic found for the two stations which exhibit a more even distribution of energy is that they receive forcing from two sources in opposite directions. In this situation the model appears to have reduced accuracy. The residual current simulations indicate that the model is able to produce the general characteristics measured, but the simulations of the magnitude are not highly accurate. The model overpredicts the impact of the wind forcing upon the residual circulation and underpredicts the overall net residuals.

The magnitude of the discharges into the southern lagoons (Little Sarasota Bay and Blackburn Bay) are well simulated. Comparison of the distribution of the discharges between the inlets show the model is simulating the distribution of the total

flow to within 5 percent. Overall the simulations appear to be exchanging the proper volume of water through each of the inlets.

The simulations of salinity indicate that while the model does not predict accurate salinity magnitudes, the general characteristics and fluctuations over the simulation period are somewhat captured. In examining the influence of the salinity upon the circulation (through baroclinic forcing) the magnitudes of the salinity gradients will not be accurate but the relative fluctuations in the magnitude may be realistic.

The model does not exhibit significant sensitivity in its simulation of the short term water levels and currents for any of the parameters tested. Therefore inaccuracies in the input parameters should not signifcantly impact the results. The residual water levels and currents on the other hand exhibit high levels of sensitivity to the definition of the horizontal diffusion and the vertical turbulence. For this reason, results which utilize the model to determine the relative influence of the forcing mechanisms upon the residual water levels and currents should be examined critically.

6.5 The Relative Influence of the Model Forcing Mechanisms

Sections 6.3 and 6.4 presented a comprehensive analysis of the accuracy and sensitivity of the numerical model in simulating the short term and residual water levels and currents. With this understanding, it is now possible to utilize the model in defining how the various forcing mechanisms interact to create the water level fluctuations and currents within the bay, keeping in mind the "weaknesses" of the model identified in the previous sections.

Within the numerical model, various individual forcing terms are calculated, these include the surface slope, the non-linear terms, the bottom friction, the wind stress and the Coriolis. These terms can be isolated and output as a time series just as the tides and currents were. This was done for the simulations presented under the model calibration and the following examines the results.

6.5.1 Periodic/Short Term Forcings

The model calibration showed that for the higher frequency fluctuations the model simulates the magnitudes and characteristics of both the tides and currents well. In addition, the model did not exhibit significant sensitivity to any of the empirical input parameters tested, therefore the model should be reasonably accurate in its representation of the magnitude and characteristics of the forcing terms.

To examine the short period fluctuations, only a portion of the 30 day simulation is presented. An important point to keep in mind in reading the plots is that the terms are relative to the numerical grid presented in Figure 6.1 and not to east-west or north-south. The alongchannel (or x) direction is along lines of constant ψ or moving longitudinally through the lagoons, positive being southerly. The crosschannel (or y) direction is along lines of constant η or moving across the lagoons, positive being easterly. This convention holds true for all results presented.

Figures 6.22 through 6.25 present plots of the non-dimensional terms for the surface slope, non-linear interaction, bottom friction and Coriolis. The time period chosen (Julian Day 200 to 210) was one which had relatively low wind stress. During periods of high wind stress the short term influence of the winds appeared to be primarily in the crosschannel results driving rapid changes in the surface slope. The results presented for the short period fluctuations do not include the wind forcing in order to examine the relative influence of the other terms within the equations of motion.

The alongchannel currents showed the highest magnitudes at all of the stations. The alongchannel terms show a force balance between the surface slope term and bottom friction, with the friction opposing the currents driven by the surface slope. At the shallower stations (UFL-B3 and UFL-B4) there is an additional influence from the non-linear terms which is significant in relation to the slope and friction terms. UFL-B1 and UFL-B2 also show some influence from the non-linear terms but their

Figure 6.22: The Non-Dimensional Forcing Terms Within the Equations of Motion for the 30 Day No Wind Simulation in 1991 at UFL-B1; a). Alongchannel Component, b). Crosschannel Component

Figure 6.23: The Non-Dimensional Forcing Terms Within the Equations of Motion for the 30 Day No Wind Simulation in 1991 at UFL-B2; a). Alongchannel Component, b). Crosschannel Component

Figure 6.24: The Non-Dimensional Forcing Terms Within the Equations of Motion for the 30 Day No Wind Simulation in 1991 at UFL-B3; a). Alongchannel Component, b). Crosschannel Component
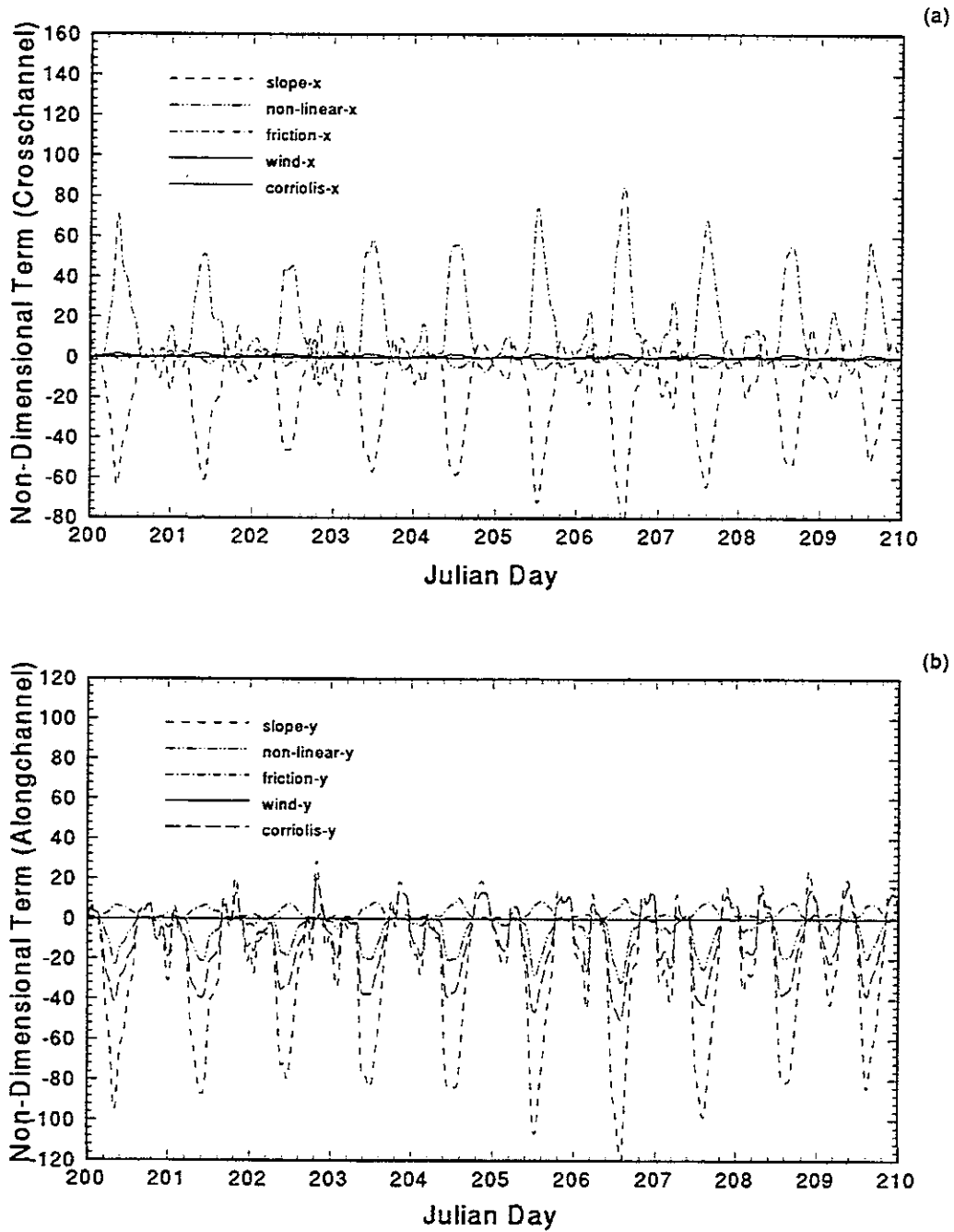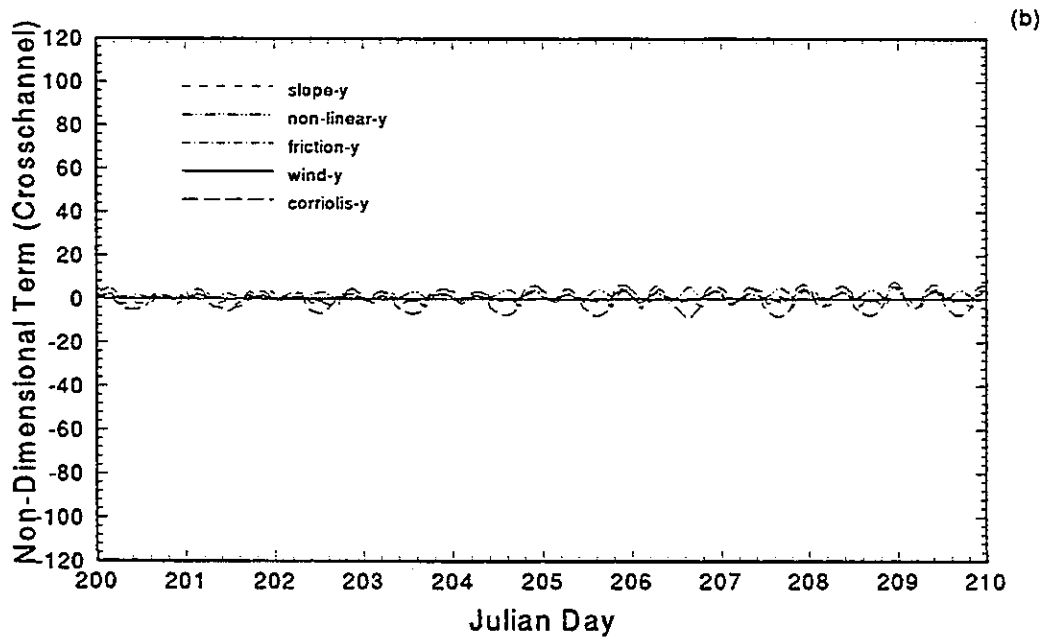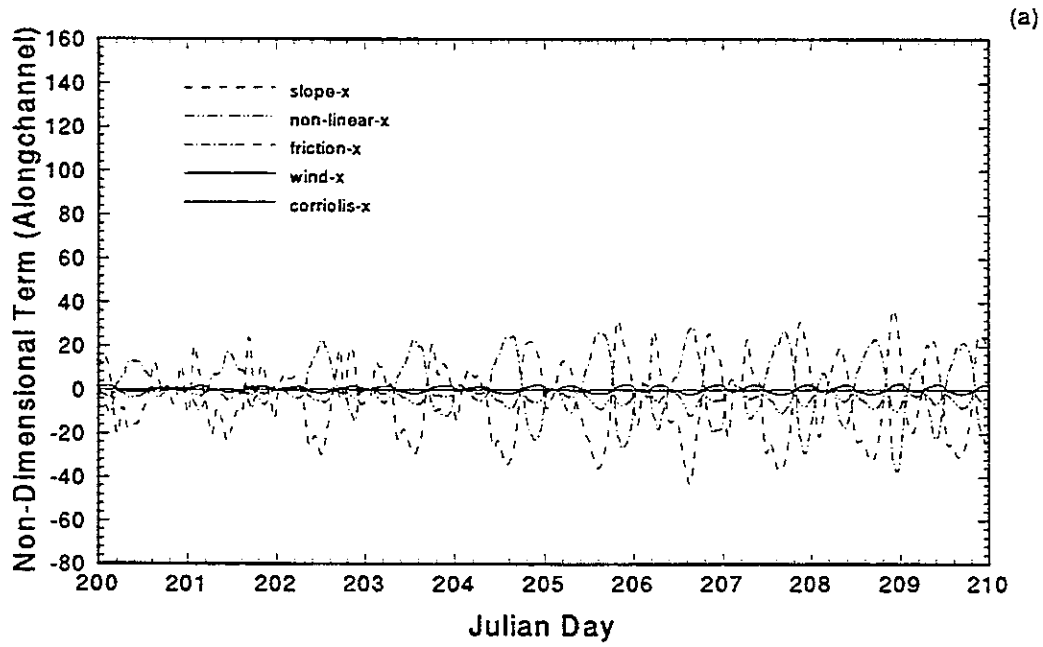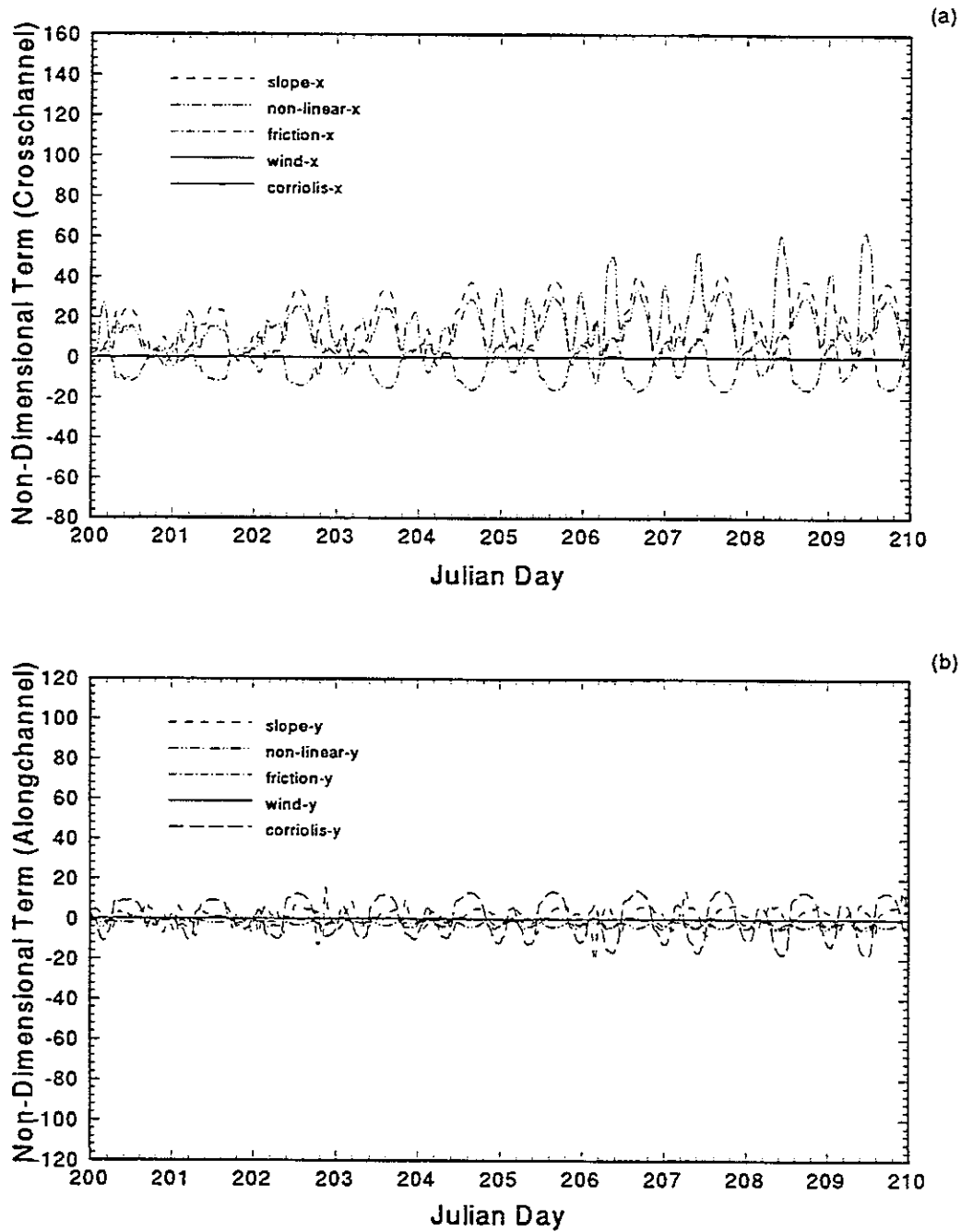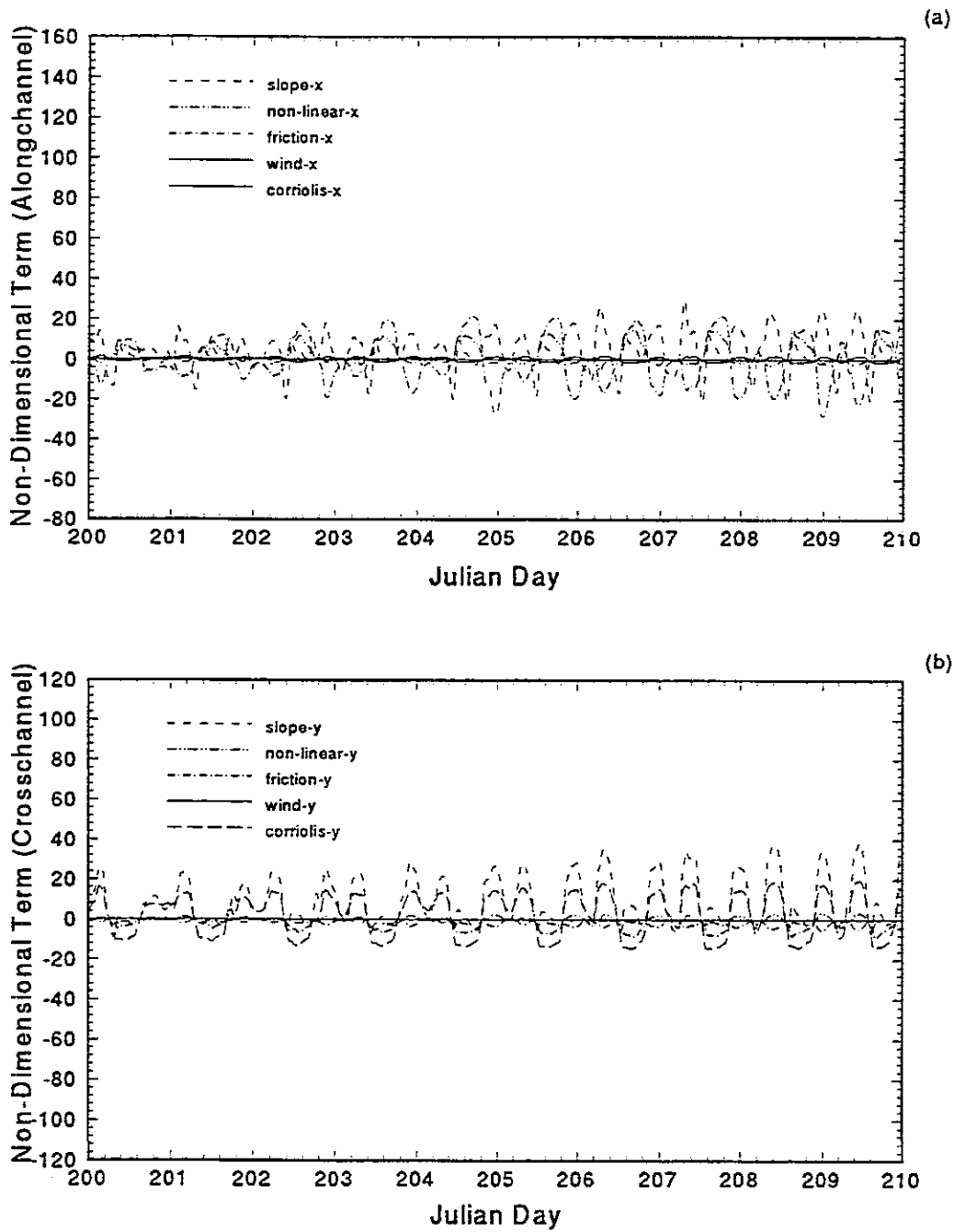
Figure 6.25: The Non-Dimensional Forcing Terms Within the Equations of Motion for the 30 Day No Wind Simulation in 1991 at UFL-B4: a). Alongchannel Component, b). Crosschannel Component

magnitude is smaller in relation to the surface slope and the bottom friction.

The crosschannel terms also show a significant surface slope but whereas the alongchannel slope was balanced by bottom friction (due to the velocities) the crosschannel slope appears to be balanced by the Coriolis term. Once again the non-linear terms show some impact, but these are lower than the surface slope and Coriolis.

6.5.2 Residual Forcings

The tests of the model accuracy showed that although the model simulated the overall trends in the residual water levels and currents, the magnitudes were generally not well simulated. In addition, the sensitivity testing showed that the residual water levels and currents are highly sensitive to the values of the empirical input parameters, especially the horizontal and vertical eddy diffusivities. Therefore the relative influence of the forcing terms defined by the model herein should be examined as indicative of the general characteristics and not the absolute magnitudes.

As was done for the water levels and currents, the time series of forcing terms was filtered using a 48 hour low band pass filter. The following presents discussion of the results from each of the four stations.

UFL-B1

Figure 6.26 presents the alongchannel and crosschannel residual forcing terms at UFL-B1. The results show the net slope which drives the residual current at this station. This net slope is the result of the 3.0 centimeter set-up input at the northern offshore boundary condition. In the alongchannel direction this net slope is balanced by the bottom friction. This net slope also appears in the cross-channel terms, but given the restrictive nature of the cross-section, a significant flow does not develop. The effect of the wind is to modulate the surface slope both in the alongchannel and crosschannel direction. During the high wind event near Julian Day 213, there is a reduction in the surface slope in the alongchannel direction, this reduction is in opposition to the wind stress whereas in the crosschannel, there is a wind setup across
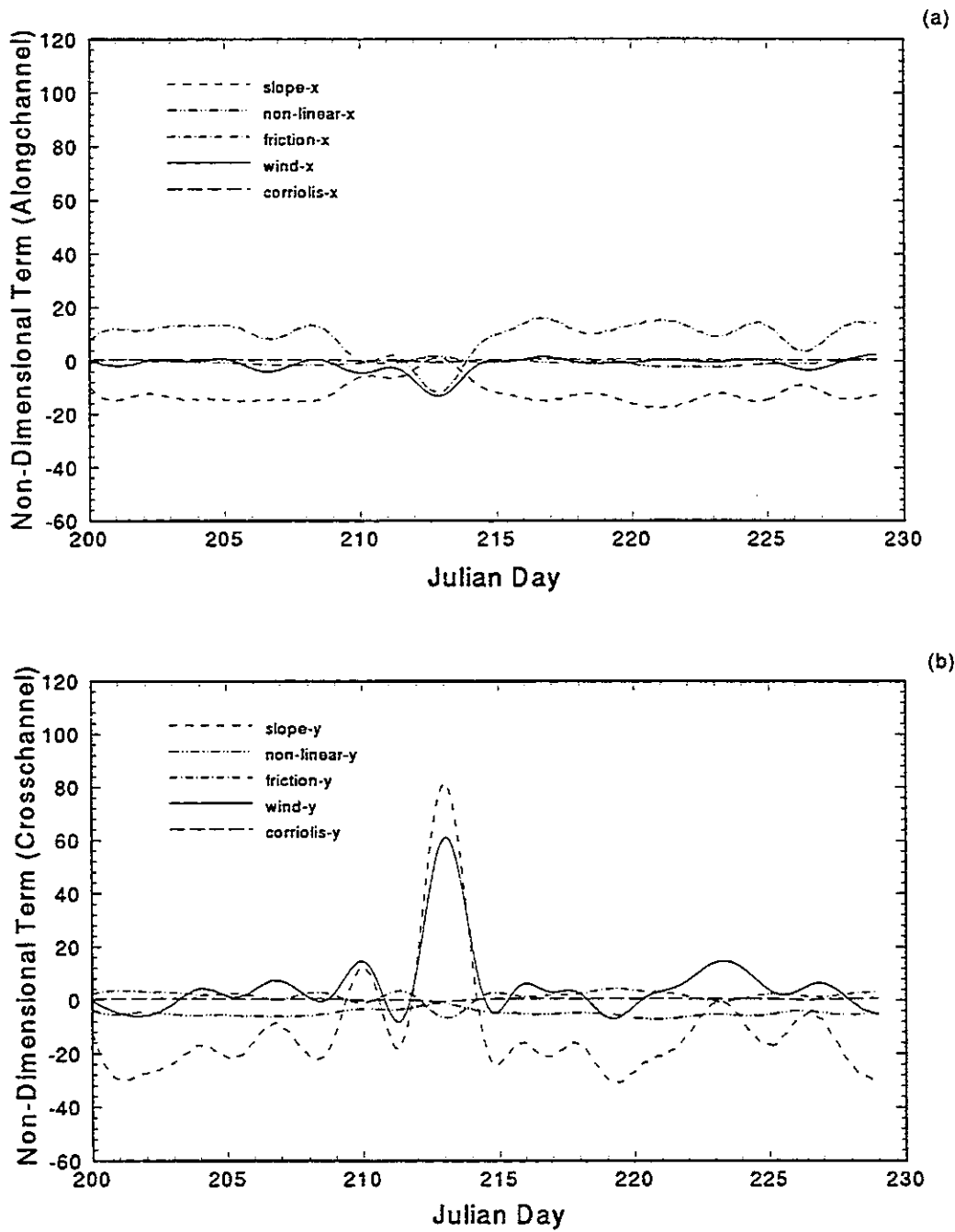
Figure 6.26: The Filtered Non-Dimensional Forcing Terms Within the Equations of Motion for the 30 Day Simulation in 1991 at UFL-B1; a). Alongchannel Component, b). Crosschannel Component

the channel.

To explain what is physically occurring at this station it is necessary to describe the wind conditions. Between Julian day 210 to 215 sustained winds blew out of the southwest at up to 10 m/s. Given the geometry of Sarasota Bay in relation to Tampa Bay a net setup was created from south to north which was sufficient to oppose the 3.0 centimeter setup in the offshore forcing. This differential setup, along with local wind stress, generated residual currents to the north.

Remembering Chapter 4, the forcing mechanisms for the residual currents were defined as a combination of local winds and Ekman transport. The model now allows us to examine more closely the actual impacts of the Ekman transport upon the residual currents at this station. To do this the model was run without wind forcing. Figure 6.27 presents the residual force balance at UFL-B1 without wind. The Ekman transport effects will remain in the simulations even without the wind forcing as they are included in the offshore boundary conditions. The net setup still remains, but much of the residual fluctuations have dissappeared. Some fluctuations are still present although small in relation to the wind driven changes. Figure 6.28 presents a comparison between the alongchannel and crosschannel surface slope terms and the mean water level fluctuations within the bay. The water surface slopes show a direct correlation with the mean water level fluctuations and therefore these small residual fluctuations appear to be driven by the Ekman transport.

Given these results, along with the analyses from Chapter 4, the forcing mechanisms driving the residual fluctuations at UFL-B1 can now be qualitatively identified. A small portion is driven by surface gradients within the lagoons created by the offshore water level fluctuations due to Ekman transport within the Gulf of Mexico. The remainder of the fluctuations are driven by local wind forcing with the largest portion due to surface gradients created by differential setup and setdown within Tampa Bay and Sarasota Bay. A smaller portion of the residual flow (nearer the surface) is due

Figure 6.27: The Filtered Non-Dimensional Forcing Terms Within the Equations of Motion for the 30 Day No Wind Simulation in 1991 at UFL-B1; a). Alongchannel Component, b). Crosschannel Component
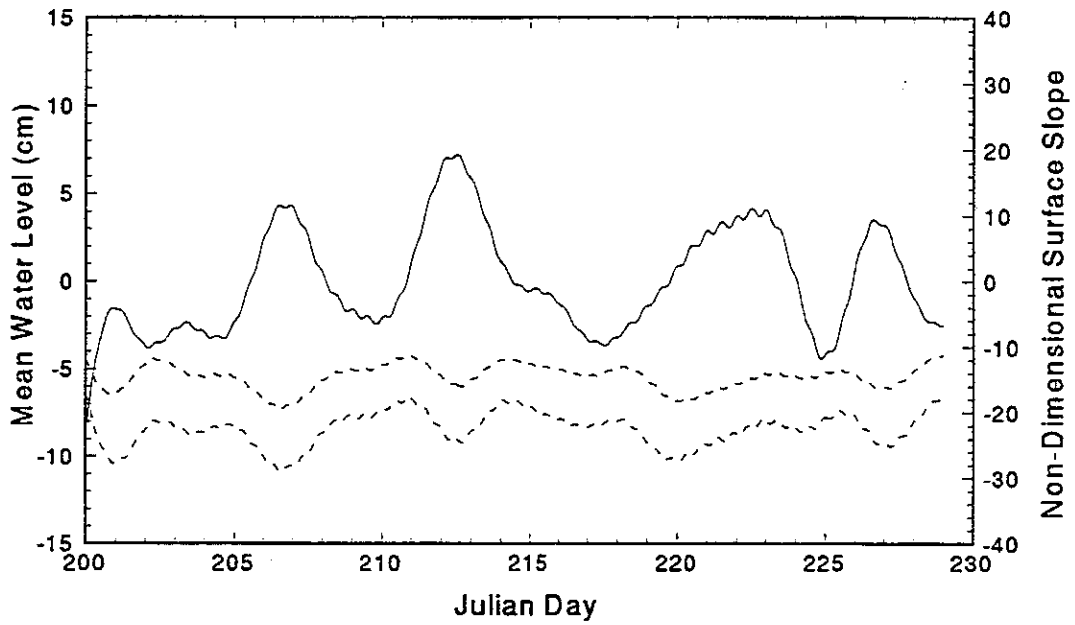
Figure 6.28: A Comparison Between the Simulated Residual Water Level Fluctuations and the Simulated Alongchannel and Crosschannel Surface Slope Terms for the 30 Day No Wind Run 1991 (dashed lines are surface slope, solid line is water level)

to local wind stress.

UFL-B2

Figure 6.29 presents the residual forcing terms for UFL-B2. In Chapter 4 the analyses identified very little residual current at this station and the filtering of the forcing terms supports this finding. The results indicate some fluctuations in the surface slope terms but these are small in relation to the other stations.

UFL-B3

In Chapter 4 it was determined that this station had a high level of subtidal energy, but coherence calculations indicated that there was not a significant correlation between the winds and the residual fluctuations. Figure 6.30 presents the residual forcing terms. The results indicate that while there does appear to be a crosschannel setup induced by the wind this setup does not drive a significant residual. The alongchannel results indicate that, although the wind does modulate the signals, non-linear interaction and surface slope are the driving mechanisms, with a small opposing bottom friction. The residual current patterns identified at this station in Section 6.3.4 indicated that the residual currents are driven by the flood and ebb patterns associated with the constriction located immediately north of this station. The residual forcing terms support this assertion.

UFL-B4

The analyses in Chapter 4 identified very little subtidal energy at this station, this is supported by the residual forcing terms (Figure 6.31). As was found for UFL-B3 this station exhibits a crosschannel setup due to the wind forcing with some return flow. The alongchannel residual forcings are small with a small positive net non-linear and surface slope and opposing bottom friction. The earlier results indicate that the residual flow at this station is primarily driven by the ebb and flood patterns associated with the constriction immediately to the north. This is somewhat supported by the residual forcing terms.
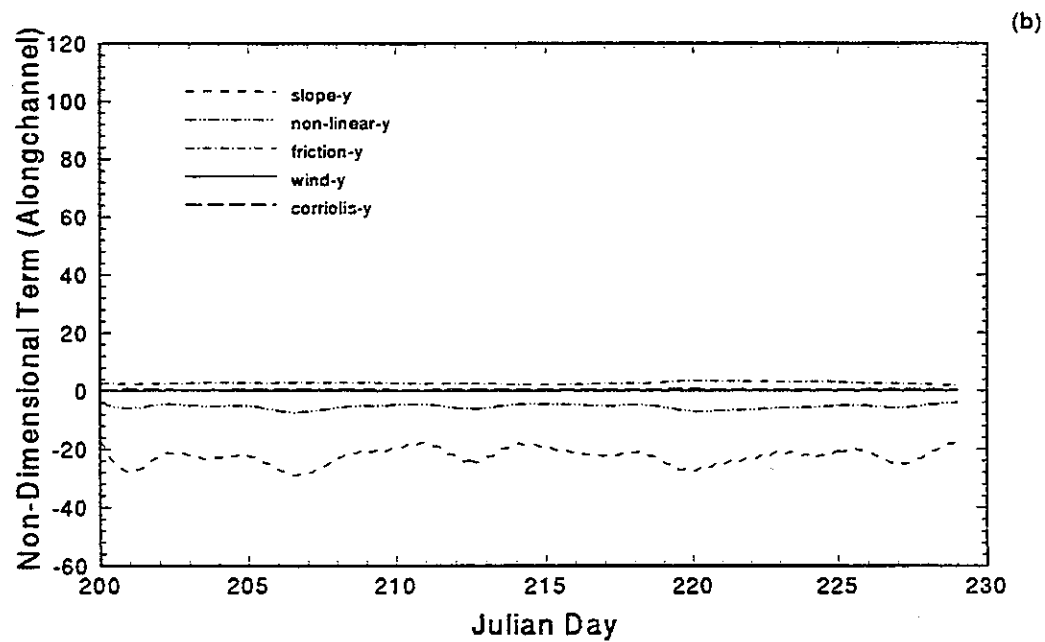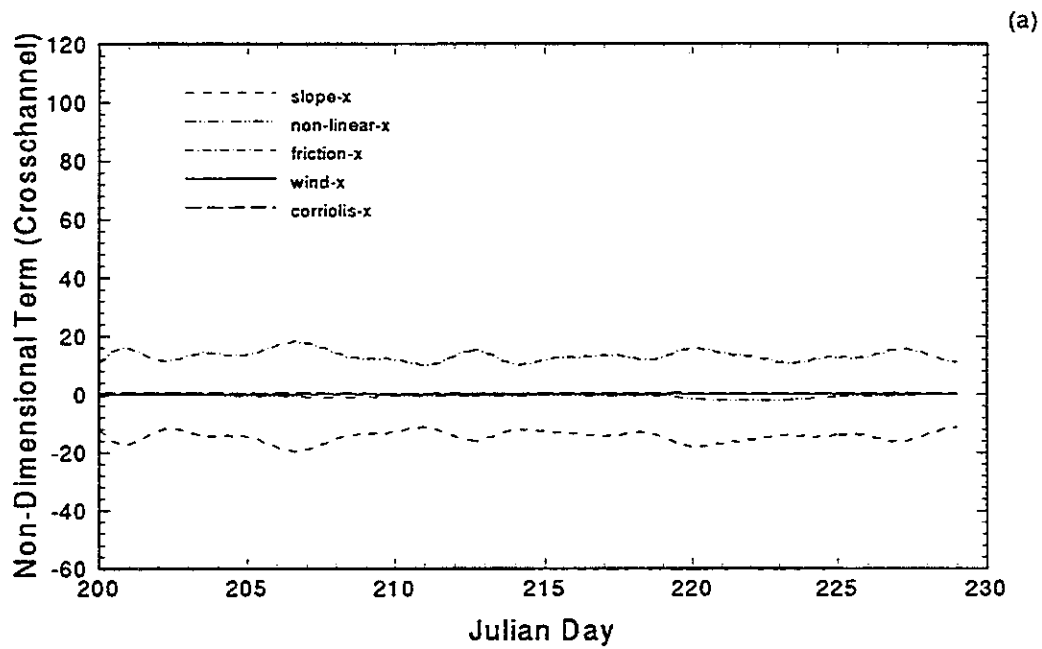
Figure 6.29: The Filtered Non-Dimensional Forcing Terms Within the Equations of Motion for the 30 Day Simulation in 1991 at UFL-B2; a). Alongchannel Component, b). Crosschannel Component
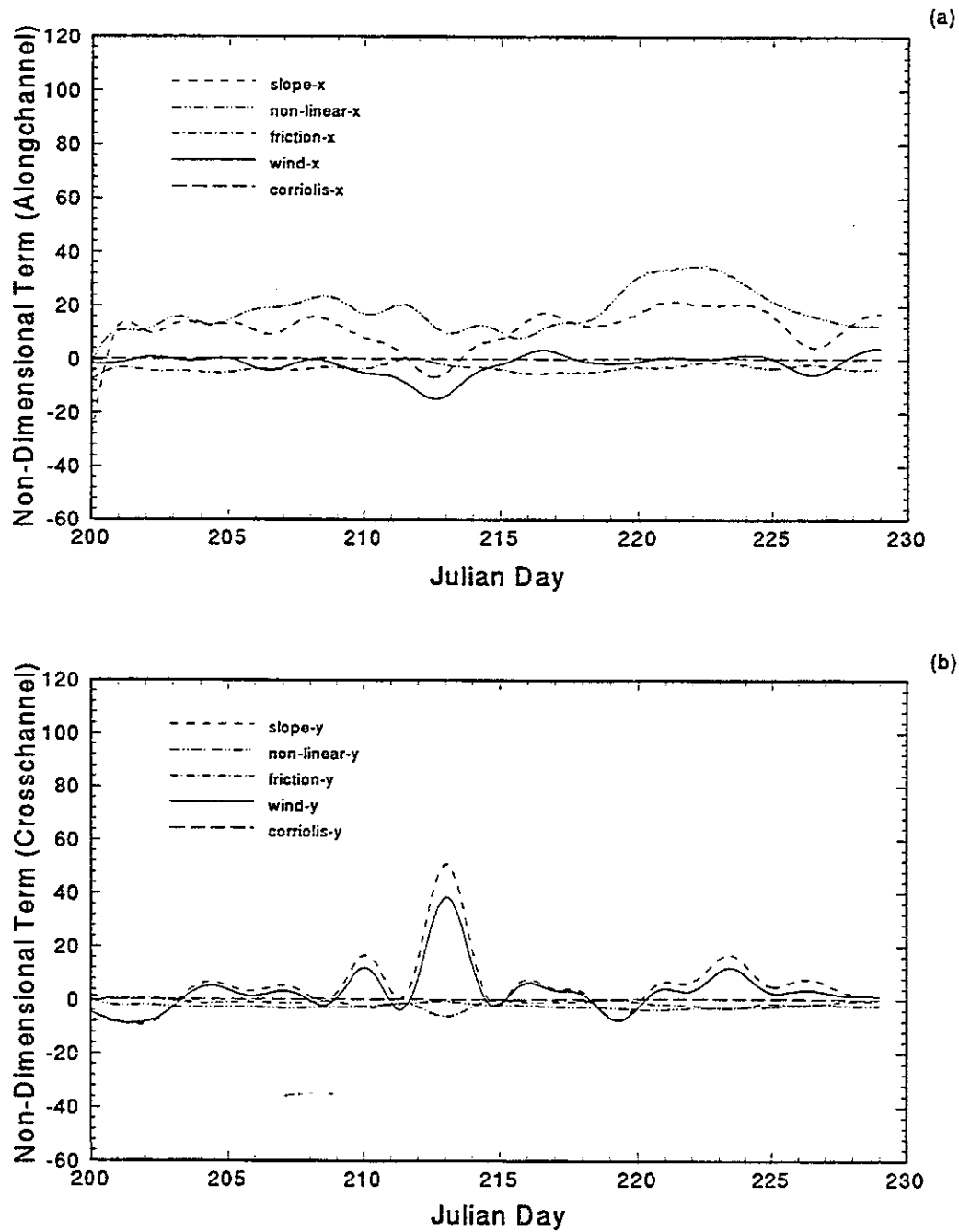
Figure 6.30: The Filtered Non-Dimensional Forcing Terms Within the Equations of Motion for the 30 Day Simulation in 1991 at UFL-B3; a). Alongchannel Component, b). Crosschannel Component

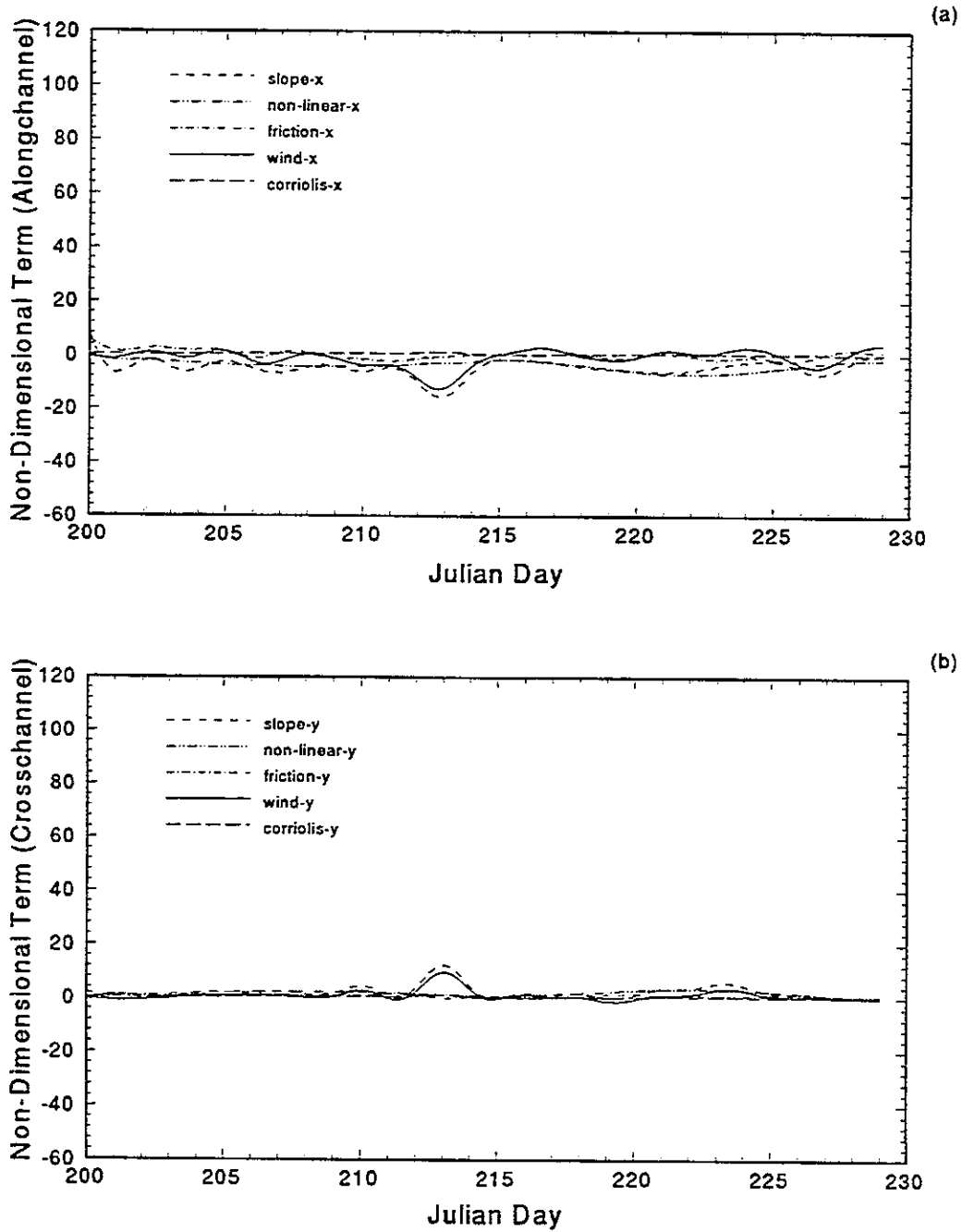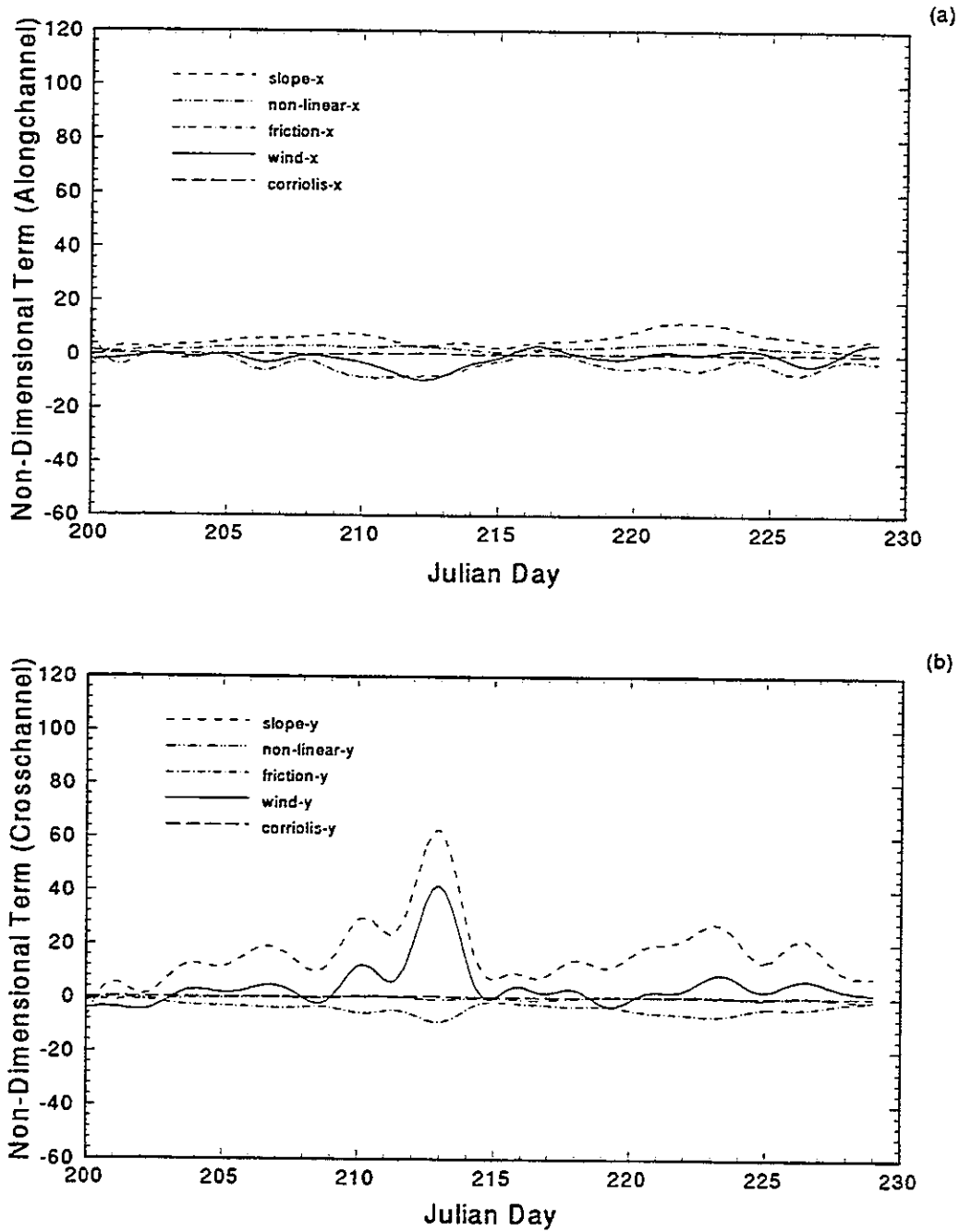Figure 6.31: The Filtered Non-Dimensional Forcing Terms Within the Equations of Motion for the 30 Day Simulation in 1991 at UFL-B4: a). Alongchannel Component, b). Crosschannel Component

CHAPTER 7
SUMMARY AND CONCLUSIONS

The primary goal of this study was to develop a more complete understanding of the circulation and transport within a multi-inlet, shallow, barrier island lagoon system, through investigation of the forcing mechanisms which drive the water levels and currents. Toward this goal two tools were utilized. The first was analysis of an extensive data set collected between 1990 and 1992 by the University of Florida in cooperation with the United States Geologic Survey. The second was calibration and application of a three-dimensional curvilinear grid hydrodynamic and transport model.

The investigation was conducted on a series of shallow interconnected barrier island lagoons located along the west coast of Florida. The boundaries of the study extended from Tampa Bay in the north, down to Venice Inlet in the south and 5 kilometers offshore. The overall length of the project area was approximately 80 kilometers.

The data collected by the University of Florida consisted of pressure measurements at two stations located along the offshore boundary of the study area. Also, four instrument platforms were installed at even spacing along the interior lagoons. The platforms, which were designed and built for this study, proved to be easy to install and maintain, and as they were surface piercing, allowed wind measurements to be made coincident with currents, temperature and conductivity. The University of Florida platforms and offshore stations collected data over a 60 day period from Julian Day 200 to 260 in 1991. The data collected by the United States Geologic Survey consisted of water surface elevations at 7 stations spaced evenly along the

interior lagoons. These stations were maintained on and off from September of 1990 to August of 1992.

The data analyses focused upon two 60 day periods, Julian Days 200 to 260, 1991 (the time of the University of Florida deployments) and Julian Days 255 to 315, 1990. As the 1991 period reflected summer conditions the second period was chosen to reflect fall or winter conditions.

Spectral and harmonic analysis of the water surface elevation data identified the distribution of energy across five frequency bands, the sub-tidal band (period greater than 48 hours), the diurnal band (period around 24 hours), the semi-diurnal band (period around 12 hours), the third diurnal band (period around 8 hours) and the fourth diurnal (period around 6 hours). The energy within the first three bands, termed the "primary" bands, are remotely forced and propagate into the system through the multiple inlets connecting the lagoons with the Gulf of Mexico. The latter bands, termed the "secondary" bands are created through the non-linear interaction of the primary harmonics and are locally driven. Between 98 and 99 percent of the total water surface energies were found to reside within these five bands at all measurement stations within the lagoon system, with greater than 90 percent found within the diurnal and semi-diurnal bands.

Although the total energies accounted for remained relatively constant, the distribution of energy varied as a function of position. The inlets connecting the lagoons to the Gulf of Mexico, as well as the many constrictions found within the interior, were found to act as low pass filters reducing the levels of the higher frequency "primary" bands and creating a shift in the energy distribution toward the lower frequencies. In conjunction with this shift in energy distribution among the "primary" bands, the "secondary" bands experienced increased percentages as the tidal wave propagated into the system. It is surmised that these higher harmonics grow as a function of travel distance as the tidal waves move over the shallow bottom, with the primary

forcing function for these higher harmonics being the bottom friction.

Filtering of the water surface elevation and wind data for the 1990 and 1991 data periods with a 48 hour low band pass filter isolated the residual water levels and winds. Significant mean water level fluctuations, on the order of 10 to 20 centimeters, were found for the fall 1990 data, while lesser magnitudes, on the order of 5 to 10 centimeters were found for the summer 1991 data. The higher magnitude fluctuations coincide with periods of higher sustained winds. Coherence calculations between the residual winds and water levels identified the greatest correlation with the alongshore wind component. Based upon, (i) the coherence values, (ii) the uniformity of the mean water level fluctuations throughout the lagoons, and (iii) the phases between the winds and water levels, the driving force is determined to be Ekman Transport within the Gulf of Mexico. Convergence of the coherence functions at the higher frequency end of the sub-tidal band identified that a portion of the mean water level variations may also be driven by set-up and set-down of the water level against the coastline.

As was done for the water surface elevation data, the current data were decomposed into the five frequency bands defined above. In contrast to the water surface elevation data, the range of total energy captured within the five bands varied significantly with position in the lagoon system. Between 70 and 95 percent of the total energies resided within the five frequency bands for the four current measurement stations, with the lowest total percentages found for the most interior/lowest energy station.

The decomposition of the current signals through spectral and harmonic analysis identified "characteristics" of the currents which two of the locations (UFL-B1, UFL-B3) shared while the remaining two stations (UFL-B2, UFL-B4) exhibited contrasting "characteristics". The "characteristics" included the distribution of diurnal/semi-diurnal energies, the percent of energy within the subtidal frequency band, the phas-

ing between the bottom and surface currents and the total energy captured within the subtidal, diurnal, semi-diurnal and third/fourth diurnal energy bands. The similarities are attributed to the location within the lagoon system and whether or not tidal forcing occurs from multiple directions or is unidirectional. The currents within regions which receive unidirectional forcing exhibit similar characteristics such as, high semi-diurnal energy levels, low subtidal energy and a phase lag of the surface currents relative to the bottom. The currents within regions which receive forcing from opposing directions exhibit, more even distribution of diurnal to semi-diurnal energy, higher subtidal energy and a phase lag of the bottom currents relative to the surface. Harmonic analysis of the currents also showed that the higher harmonic energy is greater in the bottom currents indicating that bottom friction is the primary driving mechanism in the generation of the overtides.

Coherence calculations between the residual currents and the winds identified that surface gradients, created by the long term rise and fall of the nearshore water levels due to Ekman transport within the Gulf of Mexico, along with local wind forcing, are the primary driving mechanisms for the residual flow in the northern end of Sarasota Bay. Similar calculations within other regions of the bay did not produce significant correlation's between the winds and the residual flows. The data also showed that throughout the lagoons, the currents exhibit considerable vertical variation in both magnitude and direction. This was found for both the short period and residual currents. Numerical simulations which do not account for this three-dimensionality will not produce useful simulations especially in terms of the residual flow patterns which showed the largest vertical variations.

A comprehensive test of the accuracy and sensitivity of the numerical simulations was accomplished using the decomposition techniques performed upon the measured data. In contrast to methods utilized in past model studies, this method allowed the determination of the physical aspects of the circulation which were well or poorly

simulated, and helped to identify ways of improving the simulation accuracy. The use of this methodology in future studies will provide greater confidence in the ability of numerical models to simulate the physics of circulation within shallow lagoons.

The analyses showed that the model accurately simulated the short term water level and current fluctuations under the forcing of tides and wind, and although the overall magnitudes were not captured, the model was able to simulate the general trends in the long term residual water levels and currents. The model was also able to somewhat capture the characteristics of the transport of salinity within the system using limited freshwater inflow boundary data. The measured residual current magnitudes were near the accuracy level of the current meters. Therefore, the differences between the model results and the measured data may be a combination of instrument and simulation errors.

Comparison of the measured winds throughout the system indicated the need for comprehensive multiple wind measurements in order to define accurate wind forcing. The errors associated with wind measurements taken from distant weather stations may be of the same order of magnitude as the measured wind conditions.

The numerical simulations of the short term water level and current fluctuations did not exhibit significant sensitivity to the empirical model constants of bottom friction, horizontal diffusion and vertical turbulence. The residual water surface elevations and currents, in contrast, exhibited significant sensitivity to the horizontal and vertical eddy viscosity. This sensitivity of the model allowed only qualitative analysis of the residual forcing mechanisms utilizing the numerical model. Coupled with the data analyses though this still proved to be a powerful tool.

Comparison of the model forcing terms identified that the short term fluctuations are driven primarily by a balance between the surface slope terms and the bottom friction. The non-linear terms were significant within the model simulations at the shallower stations and were present at all locations in lesser amounts. The determi-

nation of the driving mechanisms for the residual fluctuations varied upon position within the system. At the northern end of Sarasota Bay near the entrance to Tampa Bay the residual currents were found to be driven by a combination of local wind stress, water surface gradients generated by differential wind setup in Tampa Bay and Sarasota Bay, surface gradients generated by the rise and fall of the offshore water surface due to Ekman transport within the Gulf of Mexico, and possibly by a constant net set up of the water surface offshore of Tampa Bay. The determination of the latter forcing mechanism was based solely upon matching of the model results and data and does not represent any physically measured quantity.

The remaining regions within the lagoon system, where data were collected, exhibited some degree of wind driven residual currents but the most significant forcing mechanism in the creation of the residual flow patterns was the interaction of the tidal waves with the local geometry. The flow patterns associated with the ebb and flood through the many constrictions within the system created circulation gyres with flow in the direction of the jet and return flow along the outer regions.

The simulations of the water levels and currents within the bay, especially within the northern lagoons near Tampa Bay, are highly sensitive to the offshore boundary forcings as well as the interior lagoon geometry. A 3.0 centimeter setup within a portion of the offshore boundary created a significant residual flow within the lagoons. Because the offshore measurements were taken with subsurface pressure gages, the existence or non-existence of variations in the mean water surface elevations along offshore boundaries is unknown. In the interior lagoons, errors associated with the leveling of the tide gages did not allow the determination of a common datum of reference to verify the existence of superelevations within the lagoon. The model calculated set ups of as much as 4.0 centimeters within the interior lagoons but these values could not be verified. In future studies, improved data collection techniques which would allow for the establishment of a common datum of reference over the

entire study area would increase the level of confidence in the simulations.

Additional data which would improve the accuracy of the simulations include: better measurements of freshwater inflow; measurements of the currents at additional locations, especially within the navigation channel in the southern lagoons; long term measurements of currents within the inlets correlated to flow conditions; additional offshore tidal measurements; and more comprehensive bathymetric measurements throughout the system. In conjunction with the latter data the model grid resolution could be improved in order to better quantify the complex geometries, especially in the narrow southern lagoons and near Anna Maria Sound and Longboat Pass.

This study has presented an in depth analysis and discussion of the physical processes which drive the tides and currents within a system of shallow barrier island lagoons. In relation to previous studies, the level of detail presented herein is unprecedented, and represents a significant contribution to the general understanding of circulation and transport phenomena in barrier island lagoons, as well as the specific patterns within the Sarasota Bay System.

APPENDIX A
INSTRUMENT CALIBRATION

As described in Chapter 4, five different types of instruments were deployed by the University of Florida within Sarasota Bay for this study. These were Marsh-Mcbirney Electromagnetic Current Meters, Sea-Bird conductivity and temperature sensors, R.M. Young wind sensors and Transmetrics pressure sensors. The following describes the calibration procedures used for all the instruments and lists the calibration coefficients used.

The calibration of the current sensors was conducted at the Stennis Space Center in Louisiana by the United States Geological Survey. The meters were calibrated in their flow tank and the data processed and sent to the University of Florida. The range of currents over which calibration was conducted was 0 - 1.2 fps. The directionality was calibrated over the full 360 degree range. Table A and A gives the results from the calibraton runs for the Marsh-Mcbirney current sensors and Table A gives the final calibration constants along with the sensor error.

Serial No.	Run No.	Flow Velocity (ft/sec)	X-Meter Output (volts)	Calc. X Velocity (ft/sec)	Percent Diff.	Y-Meter Output (volts)	Calc. X Velocity (ft/sec)	Percent Diff.
S931	1	0.000	2.4966	-0.004		2.5221	-0.007	
	2	0.244	2.5416	0.247	1.08	2.5672	0.254	0.38
	2	-0.244	2.4524	-0.250	2.47	2.4812	-0.243	-0.38
	3	0.323	2.5557	0.325	0.66	2.5798	0.326	1.04
	3	-0.323	2.4382	-0.329	1.89	2.4670	-0.325	0.64
	4	0.553	2.5984	0.563	1.79	2.6207	0.563	1.73
	4	-0.553	2.3971	-0.558	0.89	2.4268	-0.557	0.76
	5	1.114	2.6967	1.110	-0.34	2.7149	1.107	-0.67
	5	-1.114	2.2987	-1.106	-0.73	2.3309	-1.111	-0.26
S926	1	0.000	2.4930	-0.005		2.4570	0.000	
	2	0.244	2.5401	0.245	0.22	2.5061	0.252	3.17
	2	-0.244	2.4453	-0.258	5.70	2.4097	-0.242	-0.92
	3	0.322	2.5555	0.326	1.29	2.5211	0.329	2.02
	3	-0.322	2.4314	-0.332	2.98	2.3925	-0.330	2.42
	4	0.553	2.6001	0.563	1.72	2.5680	0.569	2.82
	4	-0.553	2.3884	-0.559	1.17	2.3460	-0.568	2.68
	5	1.114	2.7038	1.112	-0.17	2.6719	1.100	-1.22
	5	-1.114	2.2864	-1.100	-1.25	2.2408	-1.106	-0.69
S929	1	0.000	2.4999	-0.002		2.5091	-0.001	
	2	0.244	2.5514	0.256	4.78	2.5604	0.261	6.82
	2	-0.244	2.4509	-0.247	1.29	2.4605	-0.250	2.40
	3	0.322	2.5668	0.333	3.32	2.5735	0.328	1.73
	3	-0.322	2.4348	-0.328	1.77	2.4457	-0.325	1.08
	4	0.554	2.6128	0.563	1.60	2.6195	0.563	1.56
	4	-0.554	2.3870	-0.567	2.32	2.3982	-0.568	2.56
	5	1.114	2.7209	1.104	-0.93	2.7252	1.103	-1.01
	5	-1.114	2.2794	-1.105	-0.79	2.2930	-1.106	-0.74
S930	1	0.000	2.4335	-0.008		2.4157	-0.013	
	2	0.244	2.4819	0.250	2.65	2.4649	0.243	-0.25
	2	-0.244	2.3873	-0.254	4.16	2.3686	-0.259	6.15
	3	0.322	2.4958	0.325	0.81	2.4795	0.320	-0.76
	3	-0.322	2.3728	-0.331	2.95	2.3554	-0.328	1.83
	4	0.554	2.5420	0.571	3.07	2.5271	0.568	2.51
	4	-0.554	2.3303	-0.558	0.75	2.3117	-0.556	0.34
	5	1.113	2.6437	1.113	0.04	2.6316	1.113	0.01
	5	-1.113	2.2298	-1.094	-1.68	2.6316	1.113	0.01

Table A.1: Calibration runs for the Marsh-Mcbirney current sensors

Serial No.	Run No.	Flow Velocity (ft/sec)	X-Meter Output (volts)	Calc. X Velocity (ft/sec)	Percent Diff.	Y-Meter Output (volts)	Calc. X Velocity (ft/sec)	Percent Diff.
S939	1	0.000	2.5057	0.012		2.5227	0.011	
	2	0.244	2.5521	0.251	2.87	2.5697	0.248	1.81
	2	-0.244	2.4545	-0.251	2.89	2.4715	-0.247	1.39
	3	0.322	2.5672	0.329	2.07	2.5875	0.338	5.06
	3	-0.322	2.4395	-0.328	1.93	2.4570	-0.321	-0.43
	4	0.552	2.6128	0.563	2.04	2.6304	0.555	0.52
	4	-0.552	2.3930	-0.567	2.79	2.4073	-0.572	3.54
	5	1.114	2.7173	1.101	-1.19	2.7379	1.098	-1.47
	5	-1.114	2.2882	-1.106	-0.67	2.3002	-1.112	-0.15
S943	1	0.000	2.4867	-0.004		2.5144	-0.001	
	2	0.244	2.5375	0.249	1.89	2.5626	0.249	1.88
	2	-0.244	2.4378	-0.246	0.90	2.4676	-0.243	-0.31
	3	0.323	2.5532	0.327	1.09	2.5761	0.318	-1.40
	3	-0.323	2.4233	-0.318	-1.50	2.4517	-0.326	0.79
	4	0.552	2.6003	0.560	1.50	2.6702	0.549	-0.48
	4	-0.552	2.3753	-0.556	0.79	2.4063	-0.561	1.56
	5	1.113	2.7088	1.099	-1.28	2.7305	1.118	0.43
	5	-1.113	2.2619	-1.119	0.56	2.3012	-1.105	-0.75
S925	1	0.000	2.4922	-0.023		2.4793	0.014	
	2	0.244	2.5447	0.241	-1.40	2.5269	0.250	2.54
	2	-0.244	2.4456	-0.256	5.00	2.4252	-0.253	3.86
	3	0.323	2.5615	0.325	0.56	2.5421	0.325	0.77
	3	-0.323	2.4303	-0.333	3.07	2.4107	-0.325	0.69
	4	0.552	2.6101	0.568	2.98	2.5898	0.562	1.76
	4	-0.552	2.3846	-0.562	1.81	2.3574	-0.589	6.73
	5	1.114	2.7199	1.119	0.44	2.6989	1.102	-1.08
	5	-1.114	2.2795	-1.089	-2.26	2.2551	-1.096	-1.64
S942	1	0.000	2.5406	-0.130		2.5474	-0.194	
	2	0.244	2.6191	0.264	8.34	2.5506	0.036	-85.25
	2	-0.244	2.5218	-0.224	-8.00	2.5488	-0.093	-61.83
	3	0.322	2.6328	0.333	3.47	2.5508	0.050	-84.37
	3	-0.322	2.5026	-0.321	0.33	2.5487	-0.100	-68.85
	4	0.553	2.6810	0.575	4.04	2.5515	0.101	-81.82
	4	-0.553	2.4582	-0.544	-1.63	2.5498	-0.021	-96.13
	5	1.114	2.7896	1.121	0.62	2.5675	1.248	12.05
	5	-1.114	2.3516	-1.080	-3.09	2.5358	-1.026	-7.94

Table A.2: Calibration runs for the Marsh-Mcbirney current sensors

Serial No.	X-Slope	X-Intercept	R Squared	Y-Slope	Y-Intercept	R Squared
926	5.3002	-13.217527	0.9998099	5.11897	-12.577375	0.9997453
931	5.5680	-13.904828	0.9999113	5.77463	-14.571711	0.9999050
929	5.0026	-12.508719	0.9997894	5.10968	-12.822535	0.9997587
930	5.3335	-12.988366	0.9997253	5.21743	-12.615688	0.9997683
943	4.9635	-12.345106	0.9998848	5.17717	-13.018346	0.9999349
939	5.1437	-12.876761	0.9997286	5.04892	-12.725629	0.9996834
925	5.0134	-12.515936	0.9994773	4.95241	-12.262932	0.9993301
942	5.0242	-12.893943	0.9942574	Bad	Bad	Bad

Table A.3: Calibration coefficients for Marsh-Mcbirney current sensors

The calibration of the conductivity and temperature sensors was performed by the manufacturer prior to shipment of the instruments. The sensors were deployed for the first time as part of this study, therefore recalibration was not necessary. Copies of the calibration sheets for the sensors are shown in Figures A.1 through A.16.

The conductivity and temperature calibrations are presented as the difference between the measured conductivity and the actual conductivity based upon the calibration parameters provided. The temperature data are presented in degrees C and the conductivity in siemens per meter.

The wind sensors were calibrated at the University of Florida in the Aerospace Engineering wind tunnel. Figures A.17 through A.20 show the calibration curves for the sensors along with the RMS error and the correlation coefficient. Each of the calibrations showed two distict slopes which were used in the data conversion. The break in slope occurred at almost the exact same wind speed for all of the sensors.
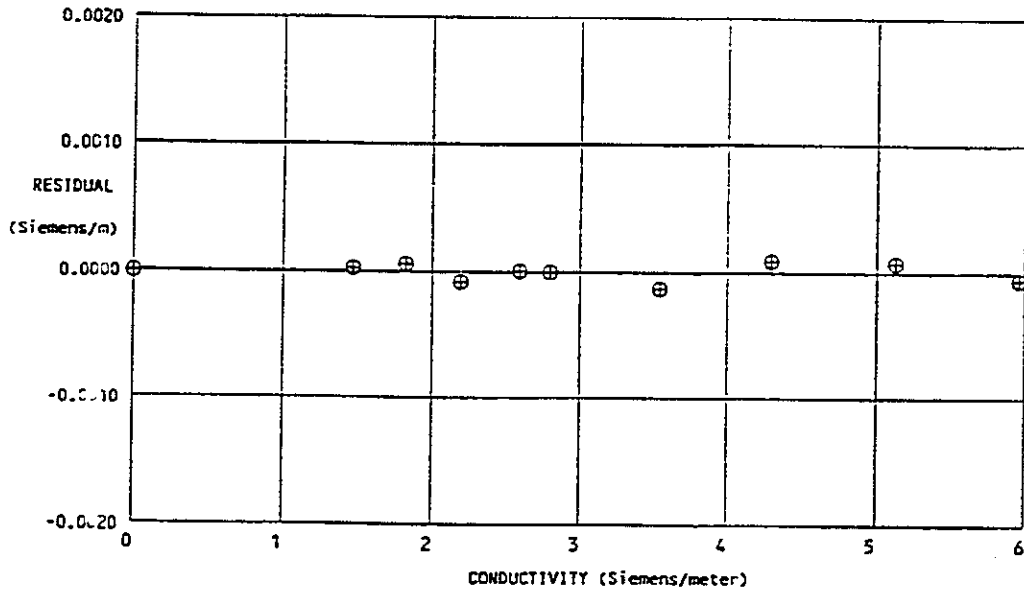
Figure A.1: The Residual Conductivity for Sensor 825 (Residual=Instrument Conductivity - Bath Conductivity), Bottom Sensor UFL-B1
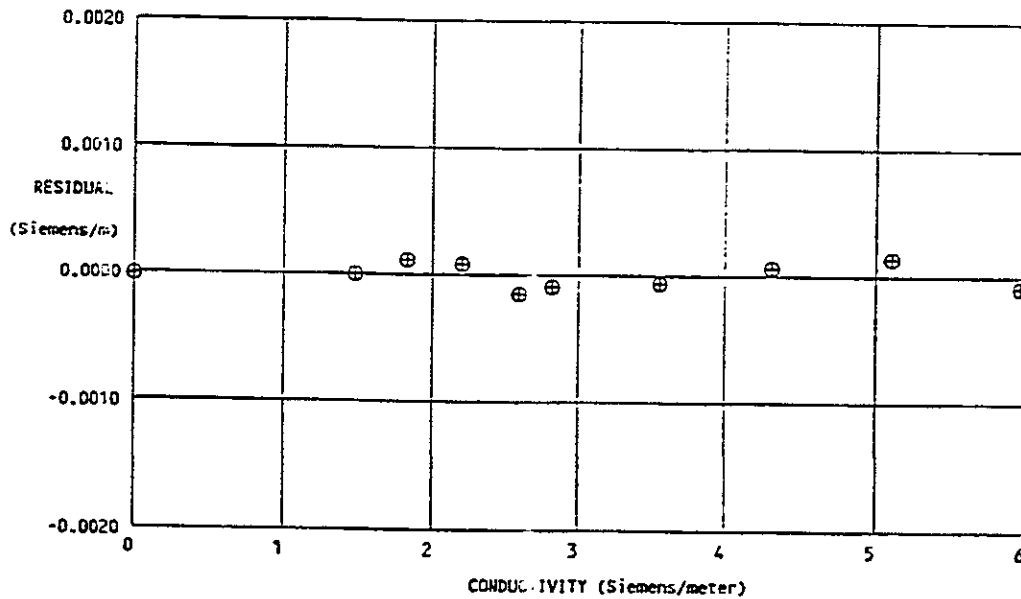

Figure A.2: The Residual Conductivity for Sensor 829 (Residual=Instrument Conductivity - Bath Conductivity), Top Sensor UFL-B1
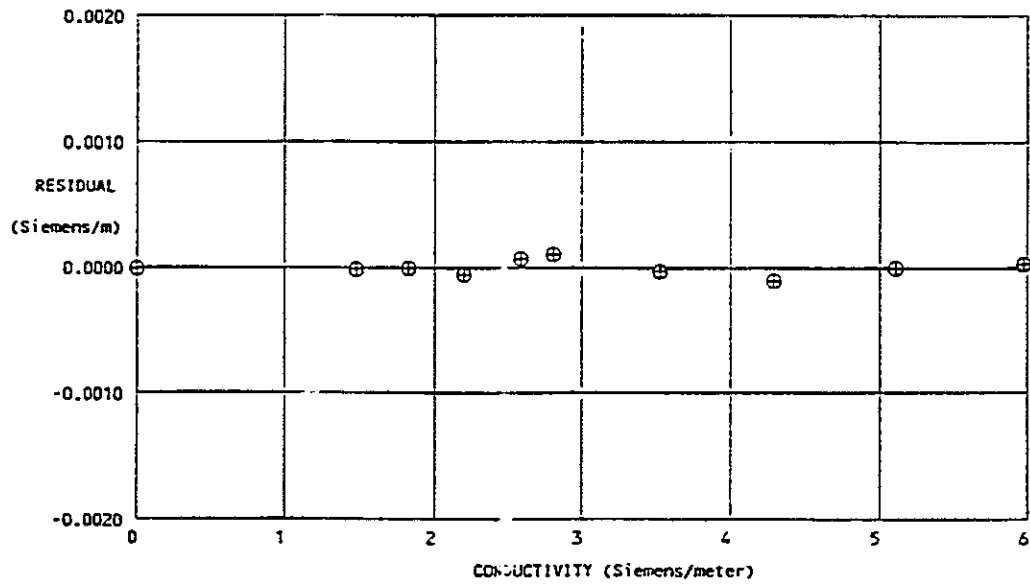
Figure A.3: The Residual Conductivity for Sensor 823 (Residual=Instrument Conductivity - Bath Conductivity), Bottom Sensor UFL-B2
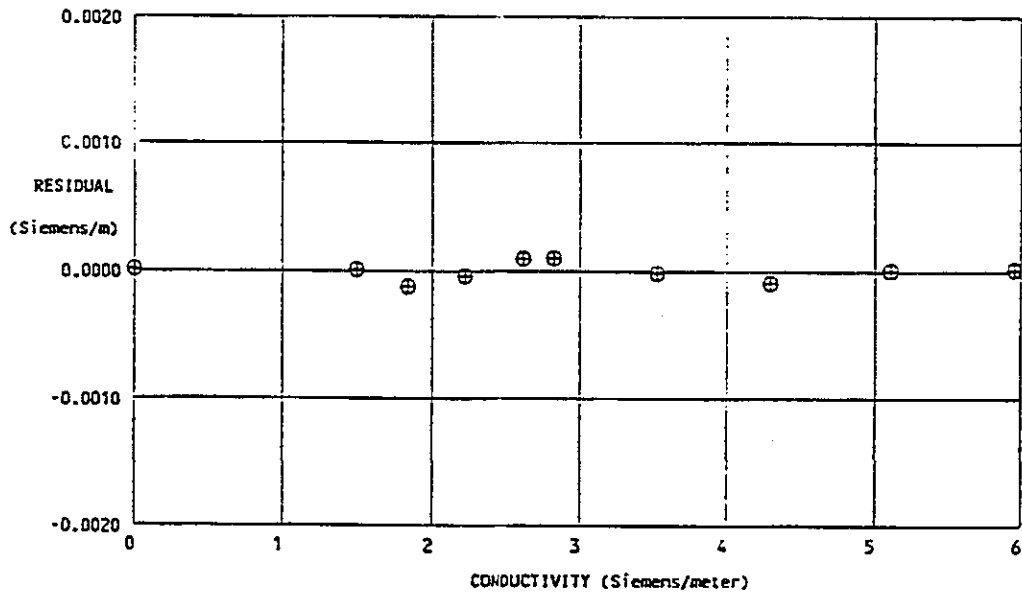

Figure A.4: The Residual Conductivity for Sensor 816 (Residual=Instrument Conductivity - Bath Conductivity), Top Sensor UFL-B2
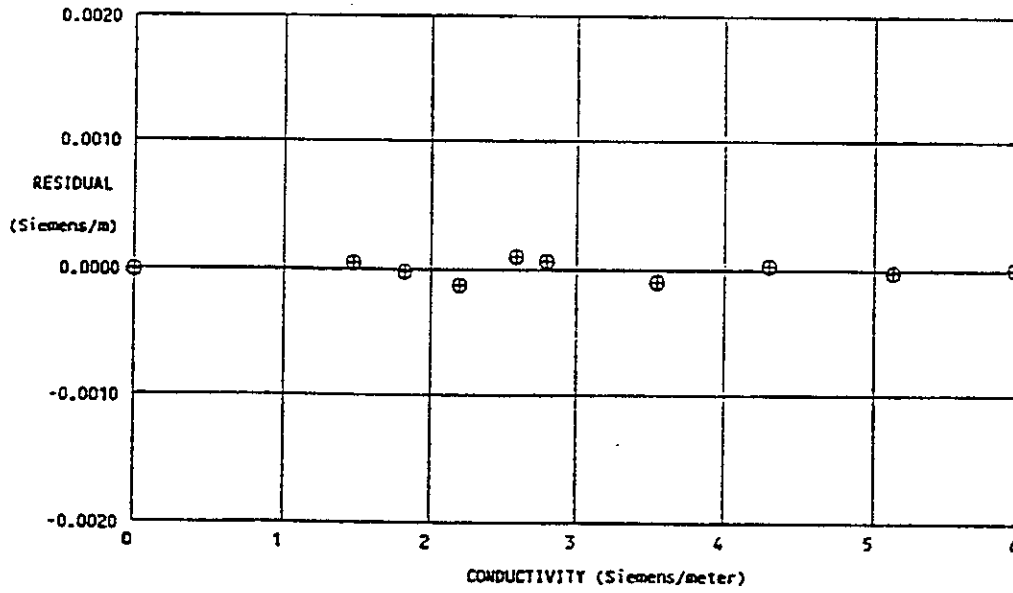
Figure A.5: The Residual Conductivity for Sensor 824 (Residual=Instrument Conductivity - Bath Conductivity), Bottom Sensor UFL-B3
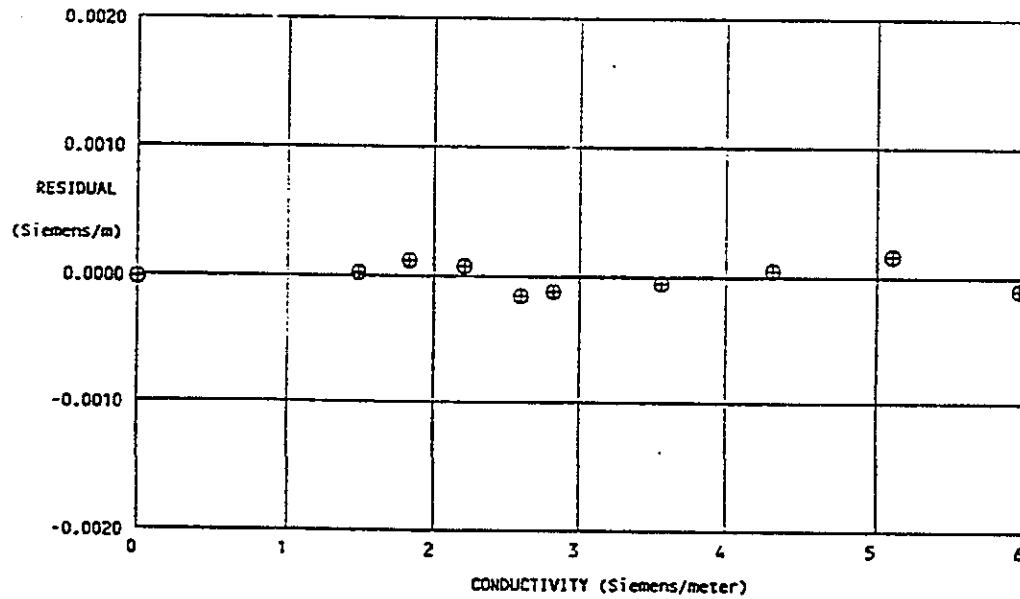

Figure A.6: The Residual Conductivity for Sensor 828 (Residual=Instrument Conductivity - Bath Conductivity), Top Sensor UFL-B3
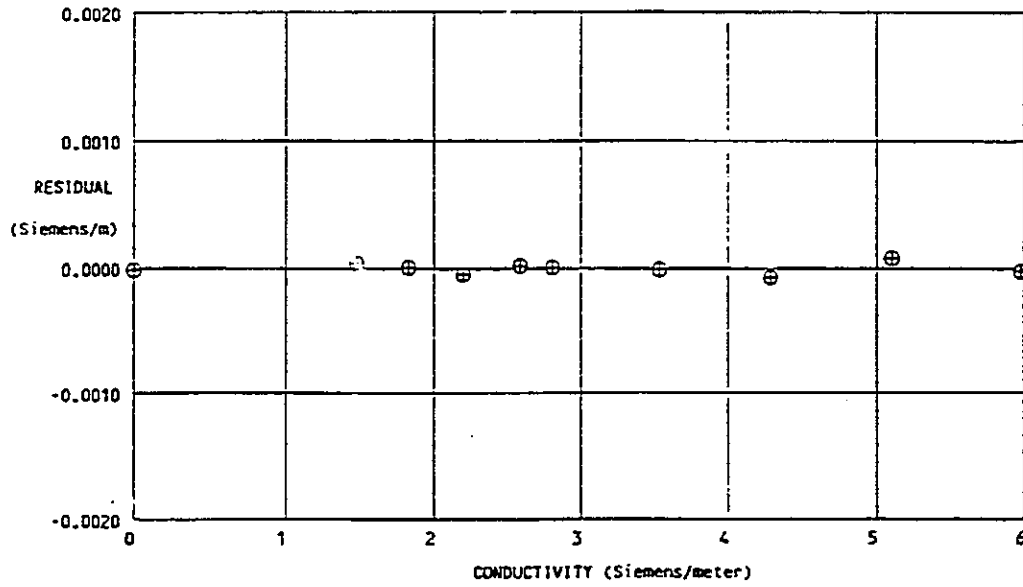
Figure A.7: The Residual Conductivity for Sensor 822 (Residual=Instrument Conductivity - Bath Conductivity), Bottom Sensor UFL-B4
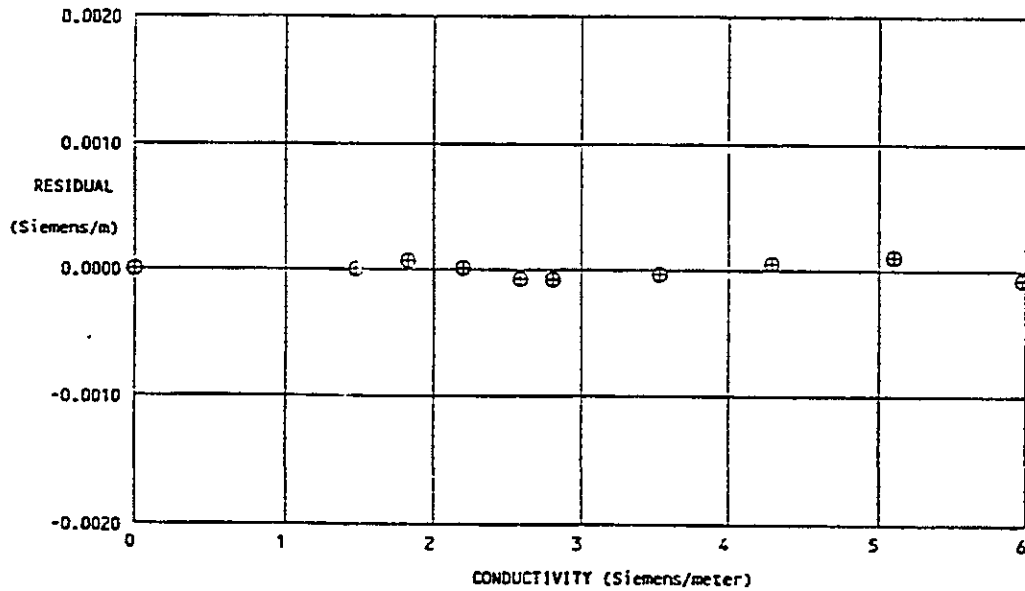

Figure A.8: The Residual Conductivity for Sensor 821 (Residual=Instrument Conductivity - Bath Conductivity), Top Sensor UFL-B4

Figure A.9: The Residual Temperature for Sensor 1125 (Residual=Instrument Temperature - Bath Temperature), Bottom Sensor UFL-B1

Figure A.10: The Residual Temperature for Sensor 1126 (Residual=Instrument Temperature - Bath Temperature), Top Sensor UFL-B1
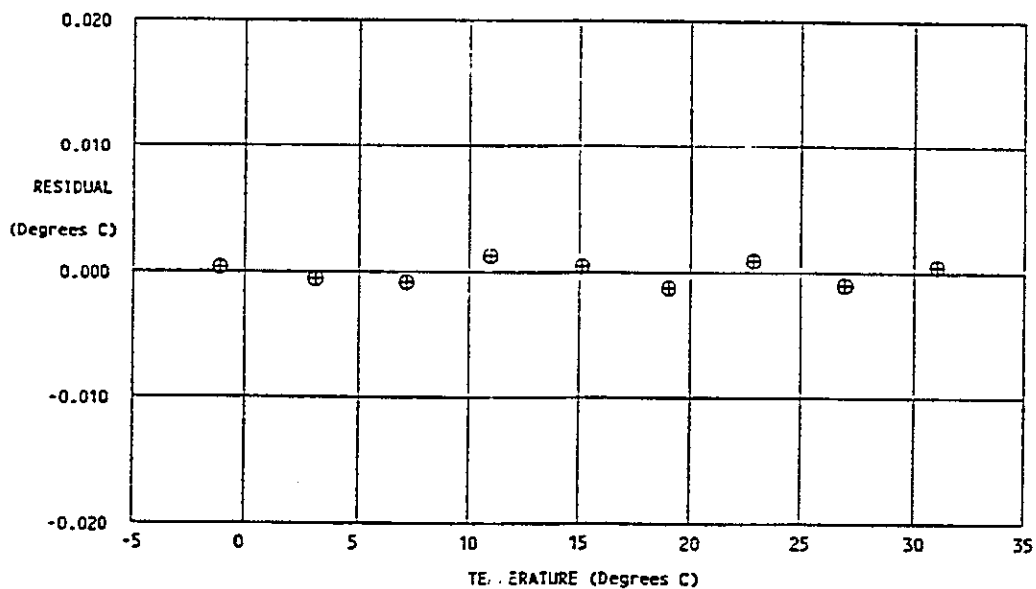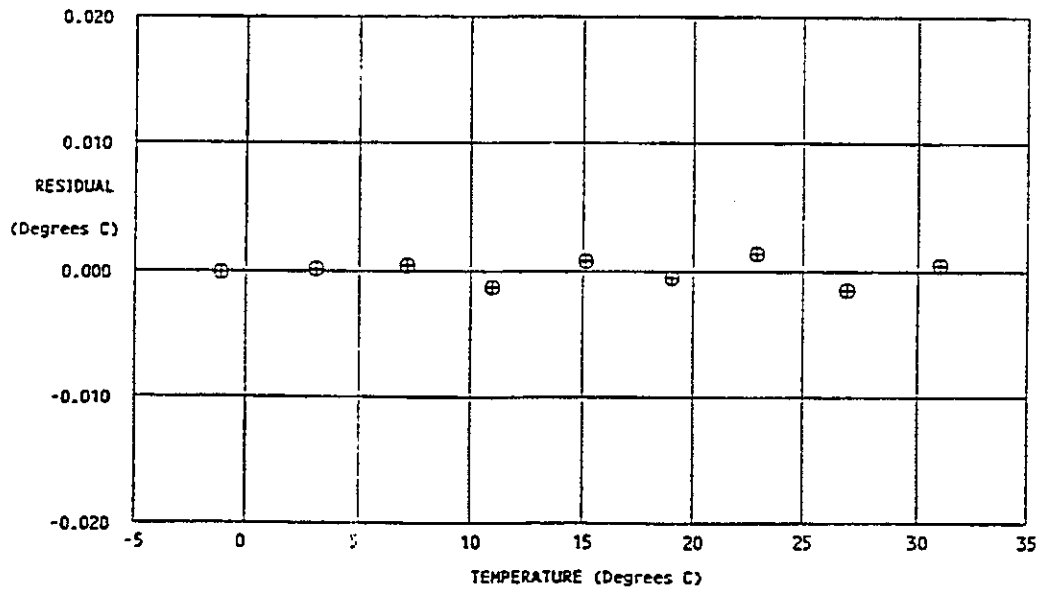
Figure A.11: The Residual Temperature for Sensor 1127 (Residual=Instrument Temperature - Bath Temperature), Bottom Sensor UFL-B2

Figure A.12: The Residual Temperature for Sensor 1132 (Residual=Instrument Temperature - Bath Temperature), Top Sensor UFL-B2

Figure A.13: The Residual Temperature for Sensor 1131 (Residual=Instrument Temperature - Bath Temperature), Bottom Sensor UFL-B3
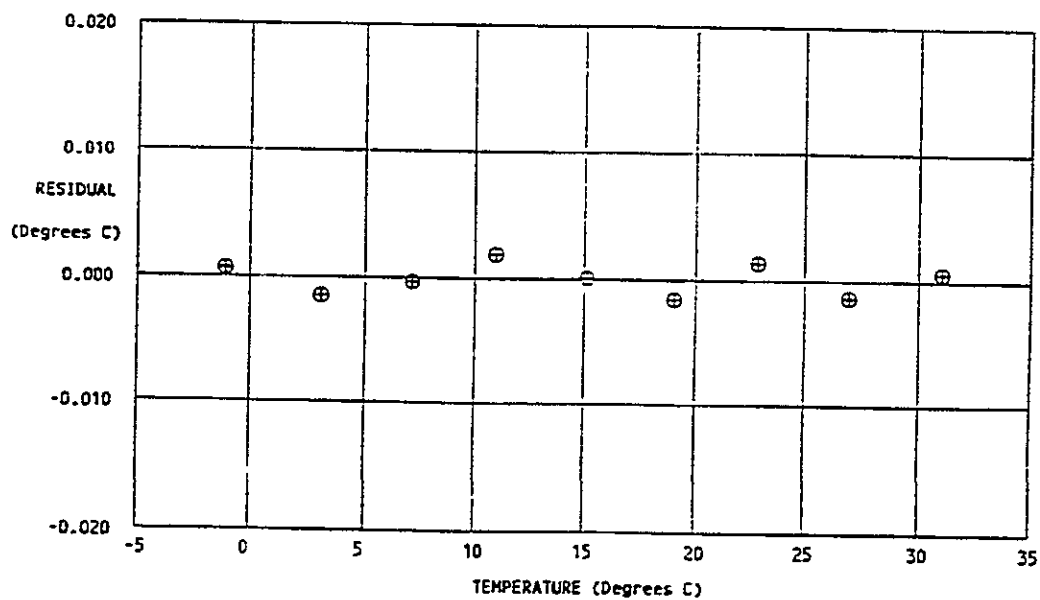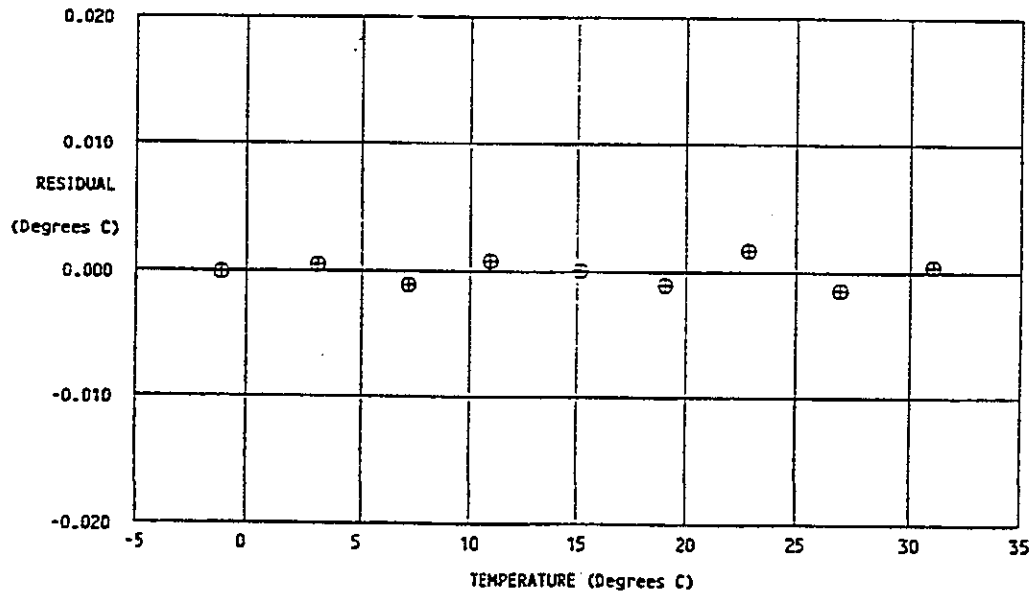

Figure A.14: The Residual Temperature for Sensor 1130 (Residual=Instrument Temperature - Bath Temperature), Top Sensor UFL-B3
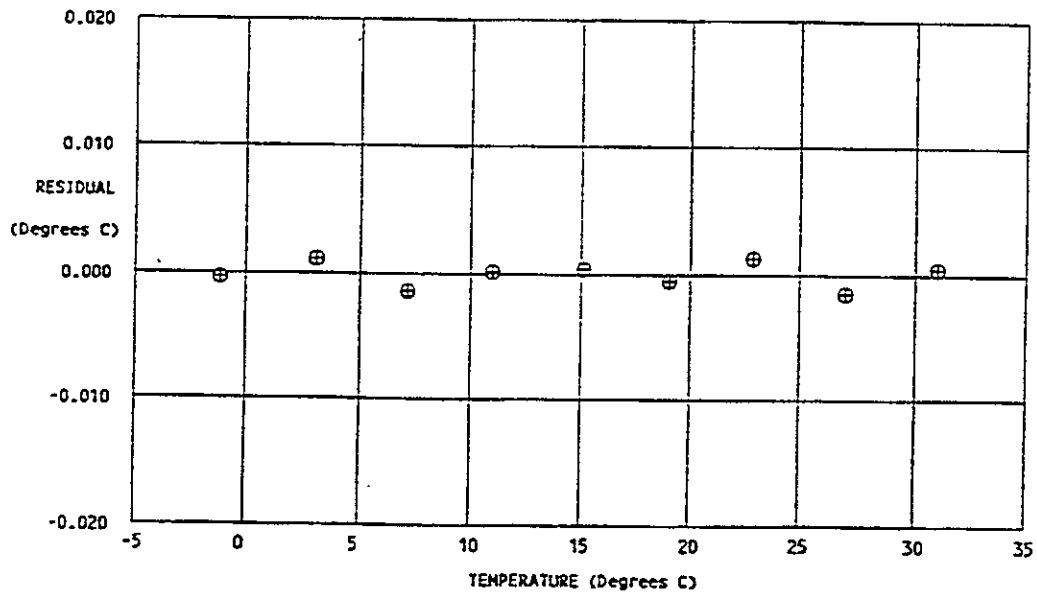
Figure A.15: The Residual Temperature for Sensor 1129 (Residual=Instrument Temperature - Bath Temperature), Bottom Sensor UFL-B4
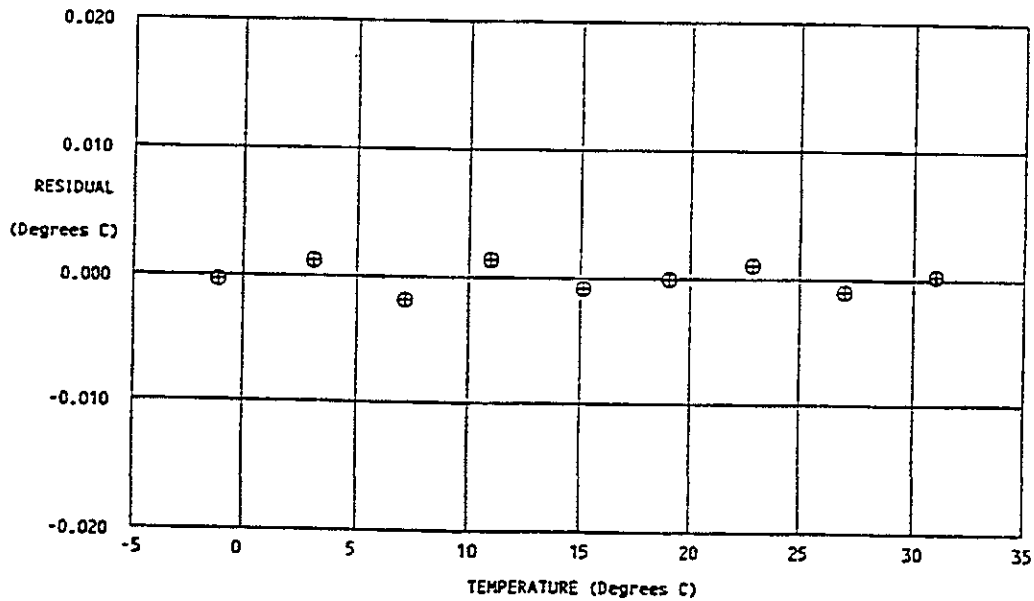
Figure A.16: The Residual Temperature for Sensor 1128 (Residual=Instrument Temperature - Bath Temperature), Top Sensor UFL-B4
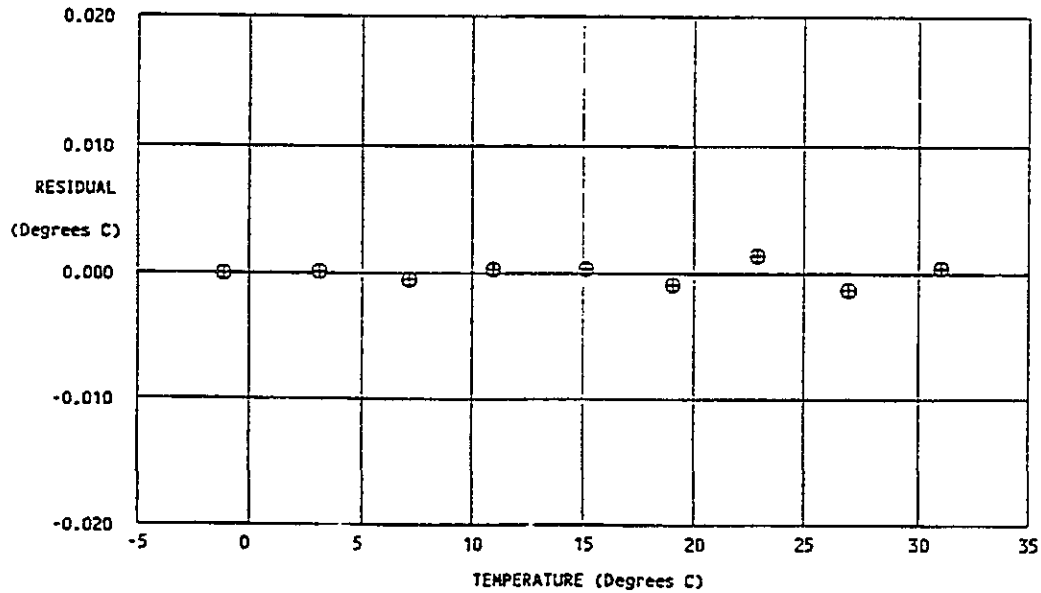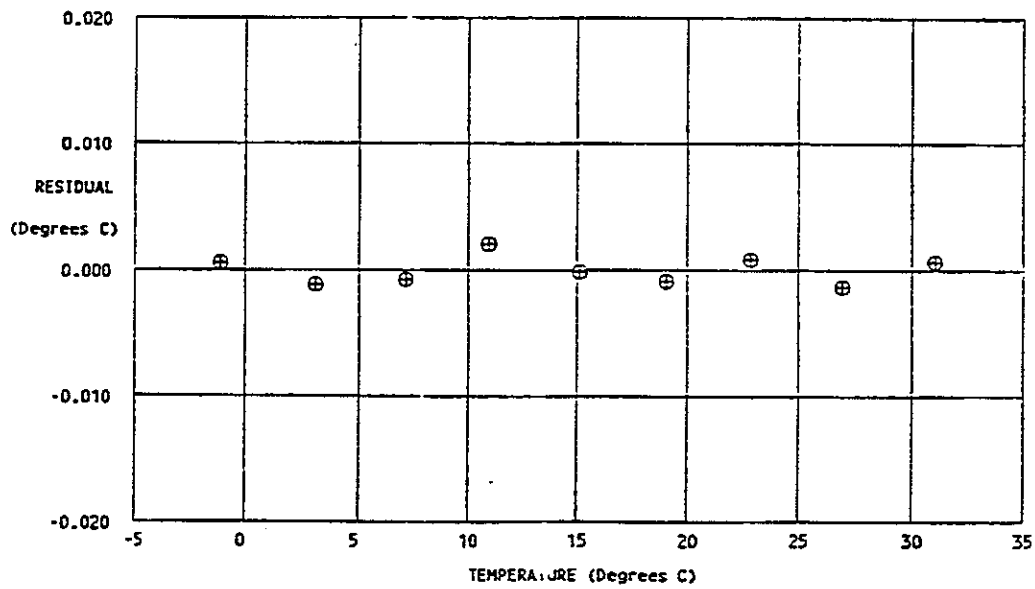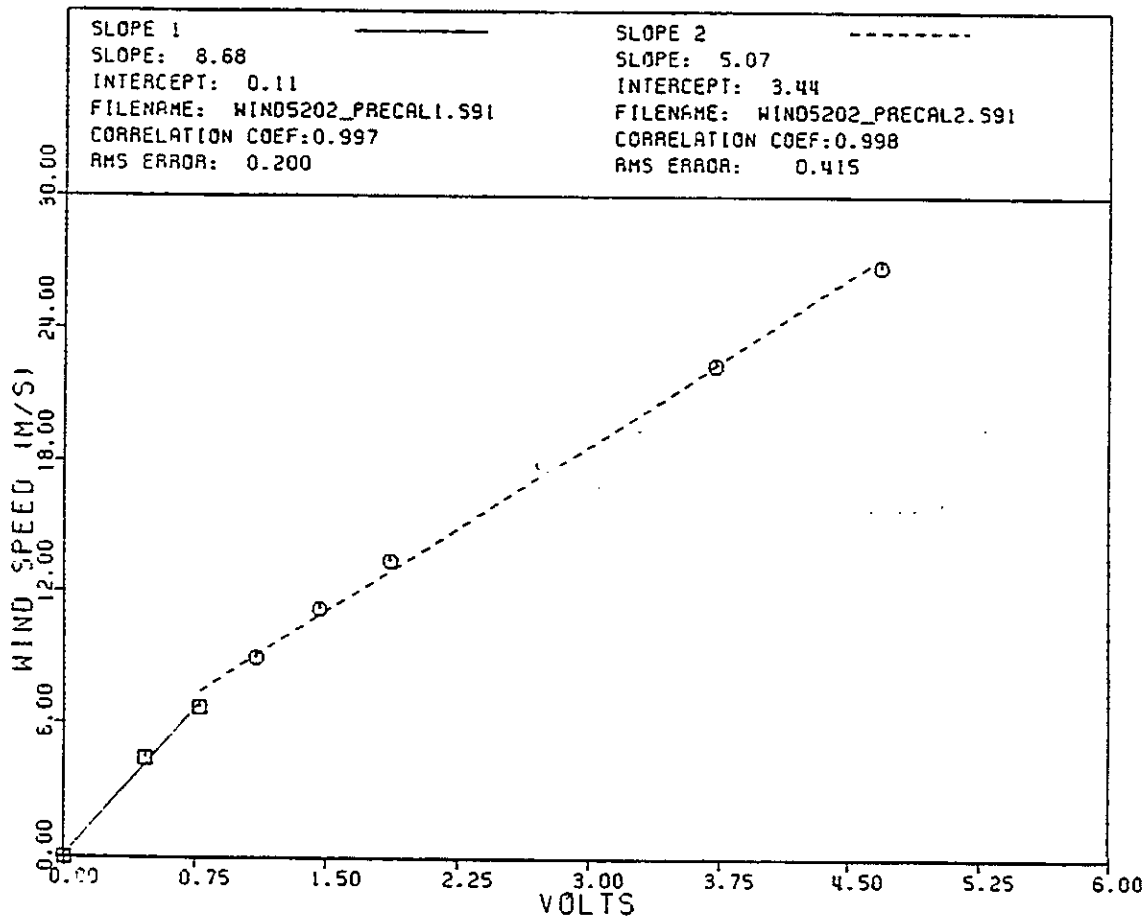
Figure A.17: The Calibration Curve for Wind Sensor 5202, Station UFL-B1
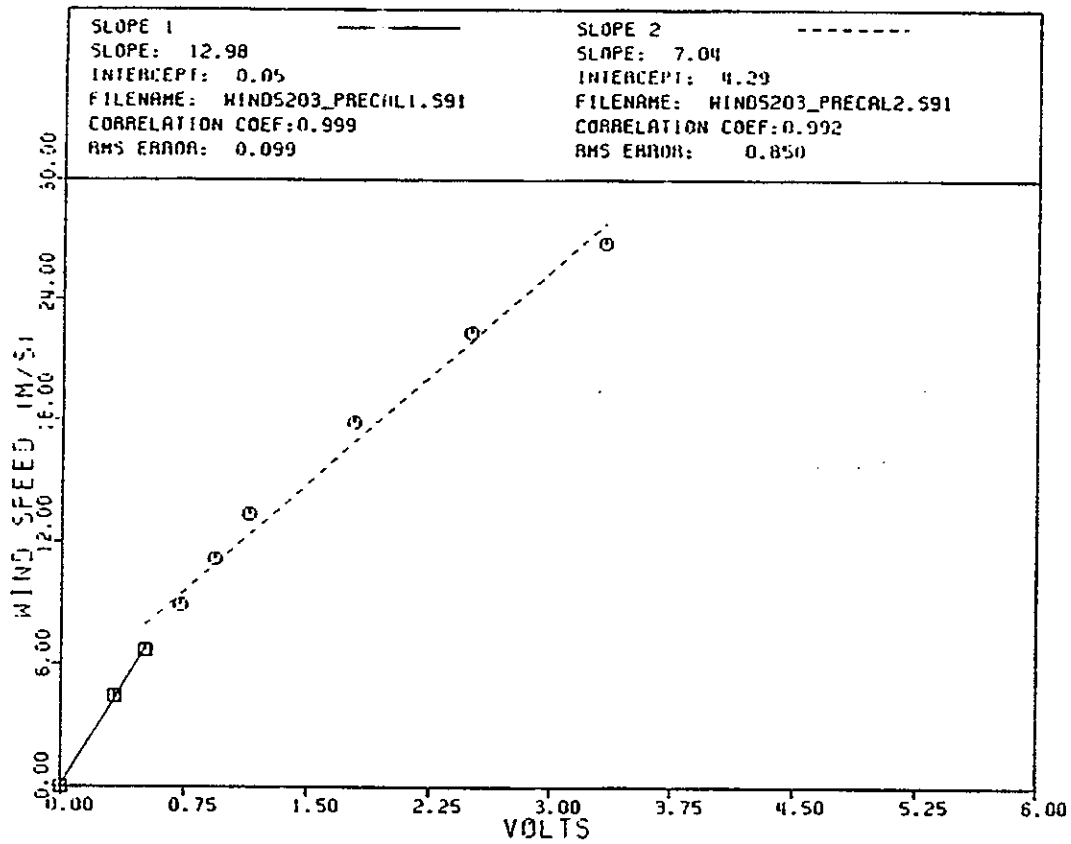
Figure A.18: The Calibration Curve for Wind Sensor 5203, Station UFL-B2
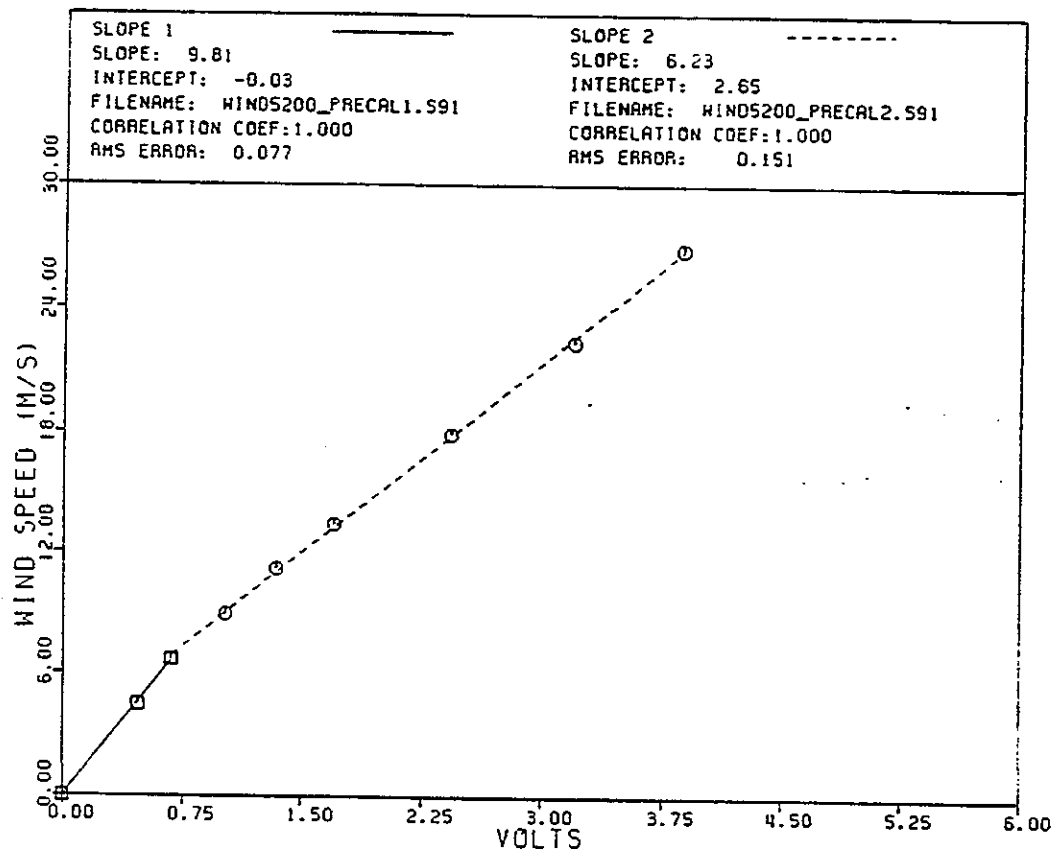
Figure A.19: The Calibration Curve for Wind Sensor 5200, Station UFL-B3
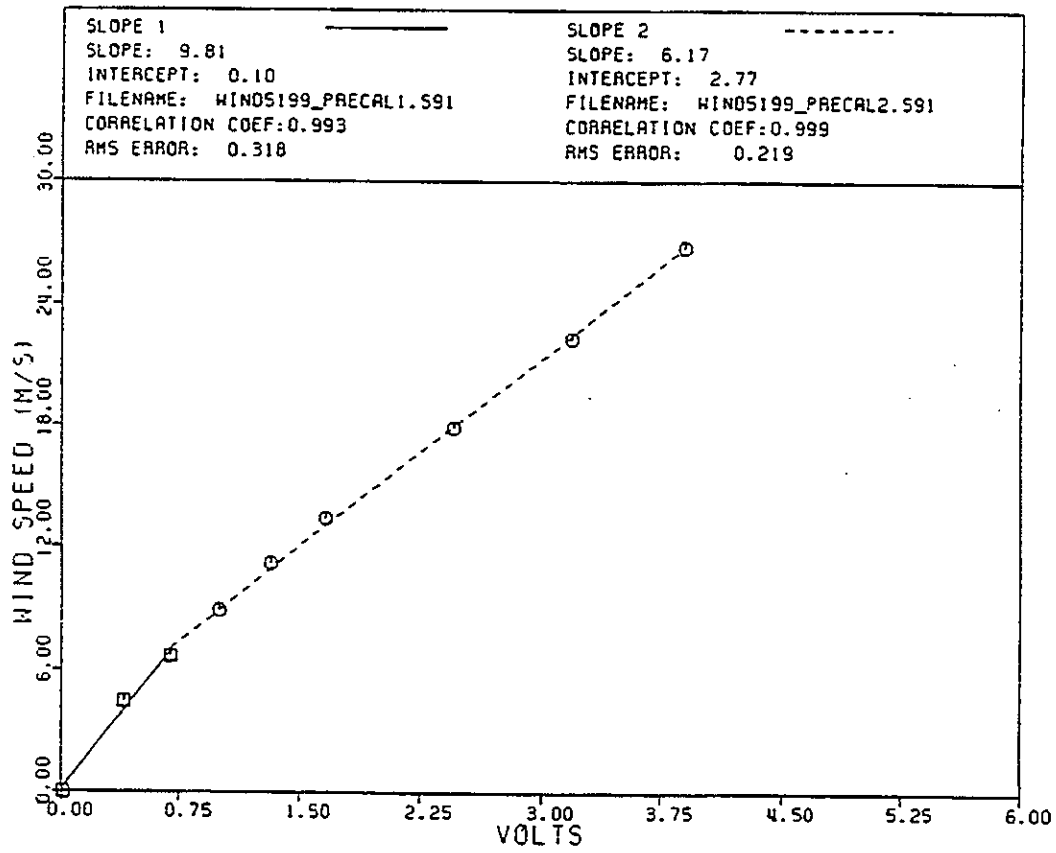
Figure A.20: The Calibration Curve for Wind Sensor 5199, Station UFL-B4

APPENDIX B
DATA PLOTS

Appendix B presents the remaining data collected and analyzed by the United States Geologic Survey and the University of Florida Coastal and Oceanographic Engineering Department as part of the Sarasota Bay Study. The complete data set although not utilized in all of the analyses presented earlier is included within this report for completeness and reference.

Figure B.1: The Water Surface Elevation Measured at the Anna Maria Station (USGS-01) from Julian Day 255, 1990 to Julian Day 50, 1991 and Julian Day 250, 1991 to Julian Day 300, 1991

Figure B.2: The Water Surface Elevation Measured at the Anna Maria Station (USGS-01) from Julian Day 300, 1991 to Julian Day 100, 1992

Figure B.3: The Water Surface Elevation Measured at the Anna Maria Station (USGS-01) from Julian Day 100, 1992 to Julian Day 300, 1992

251
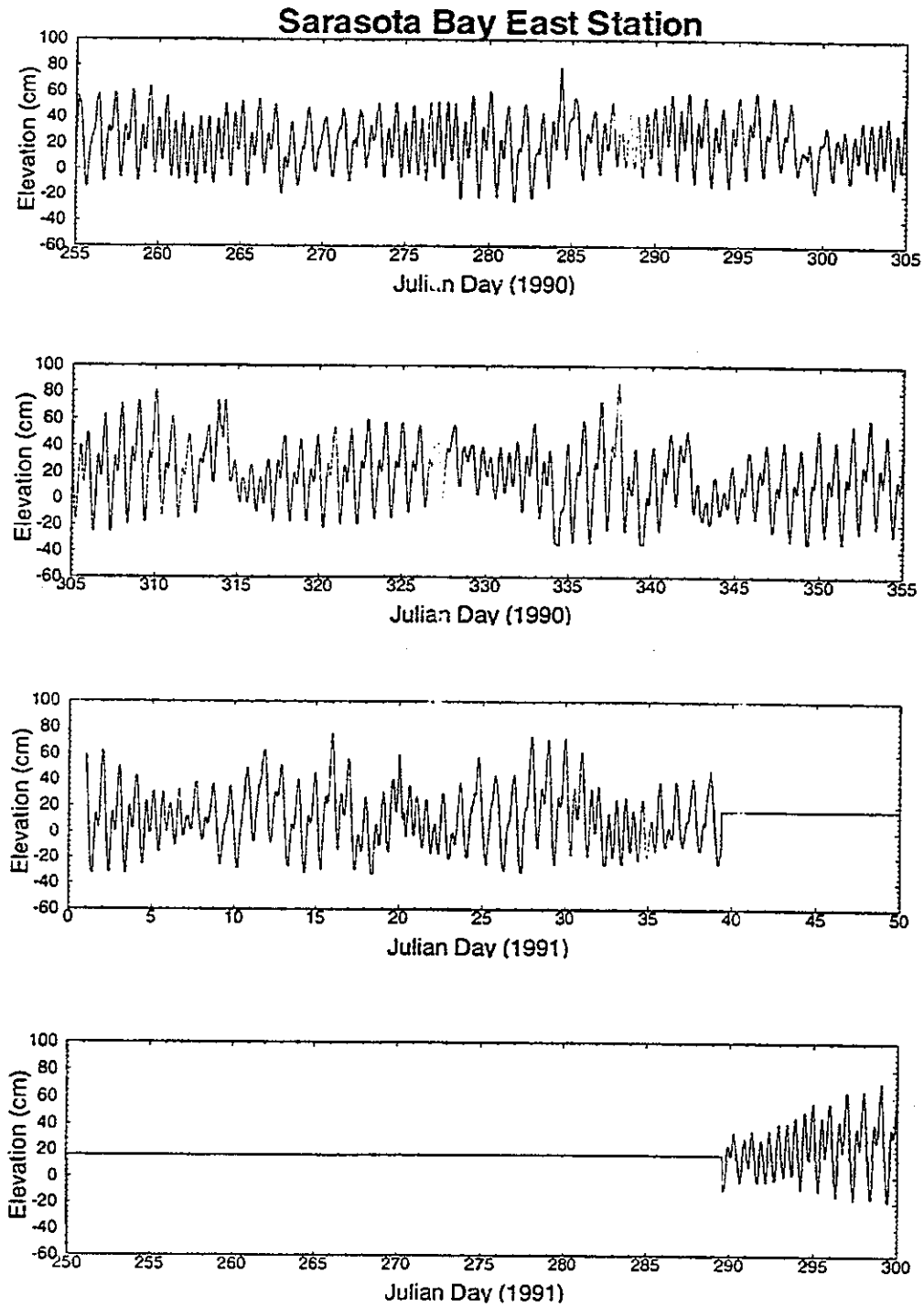
Figure B.4: The Water Surface Elevation Measured at the Sarasota Bay East Station (USGS-02) from Julian Day 255, 1990 to Julian Day 50, 1991 and Julian Day 250, 1991 to Julian Day 300, 1991
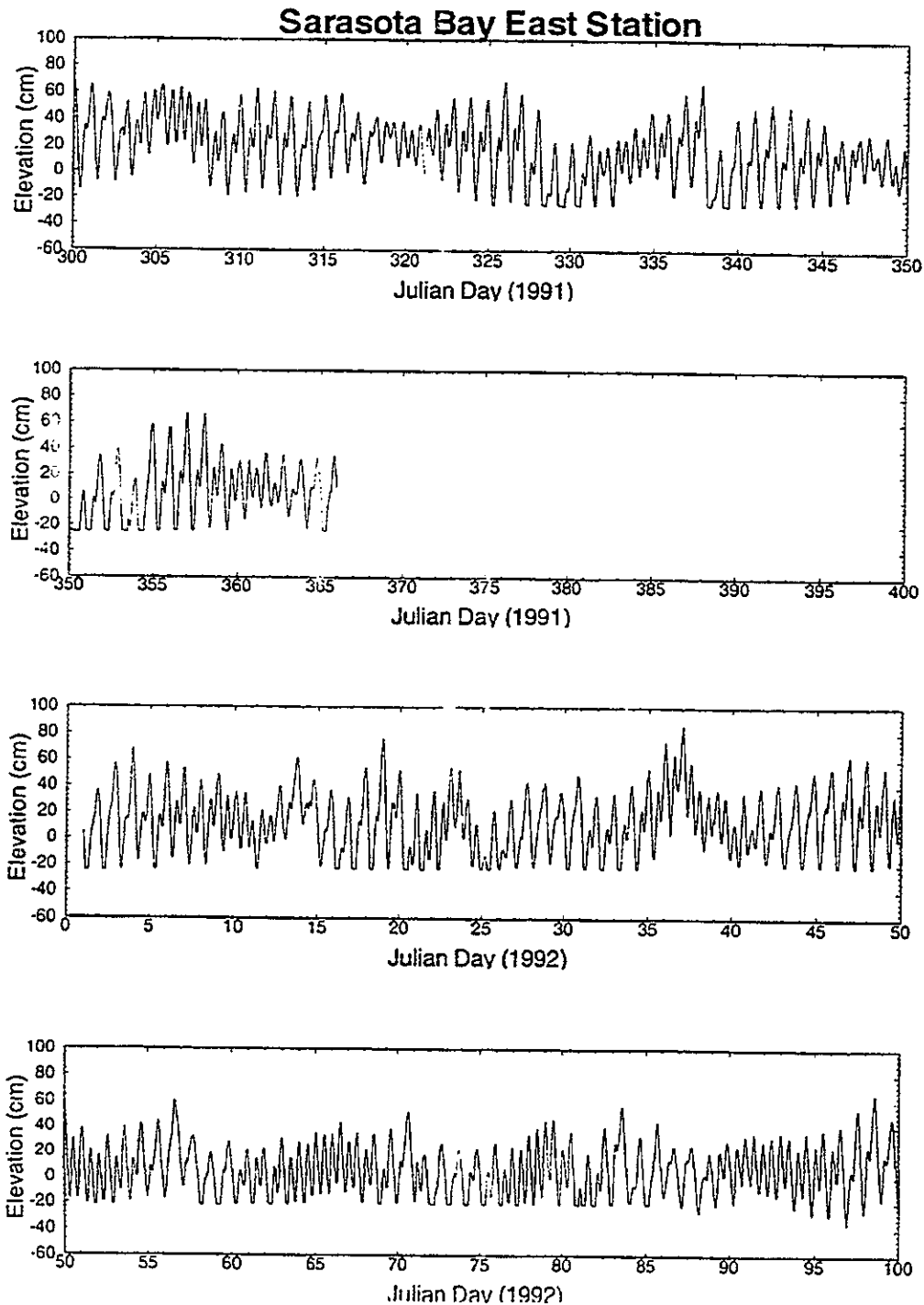
Figure B.5: The Water Surface Elevation Measured at the Sarasota Bay East Station (USGS-02) from Julian Day 300, 1991 to Julian Day 100, 1992
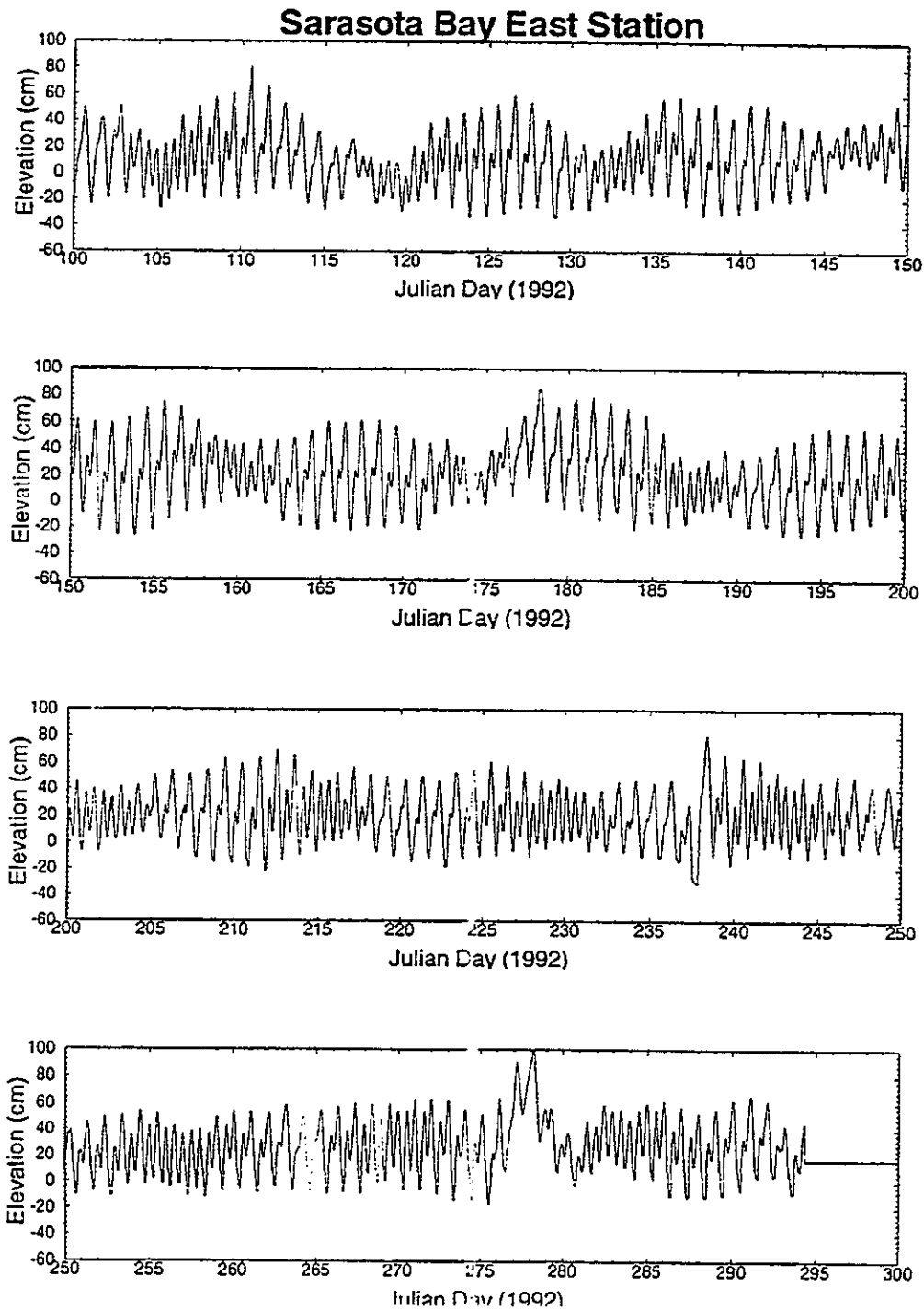
Figure B.6: The Water Surface Elevation Measured at the Sarasota Bay East Station (USGS-02) from Julian Day 100, 1992 to Julian Day 300, 1992
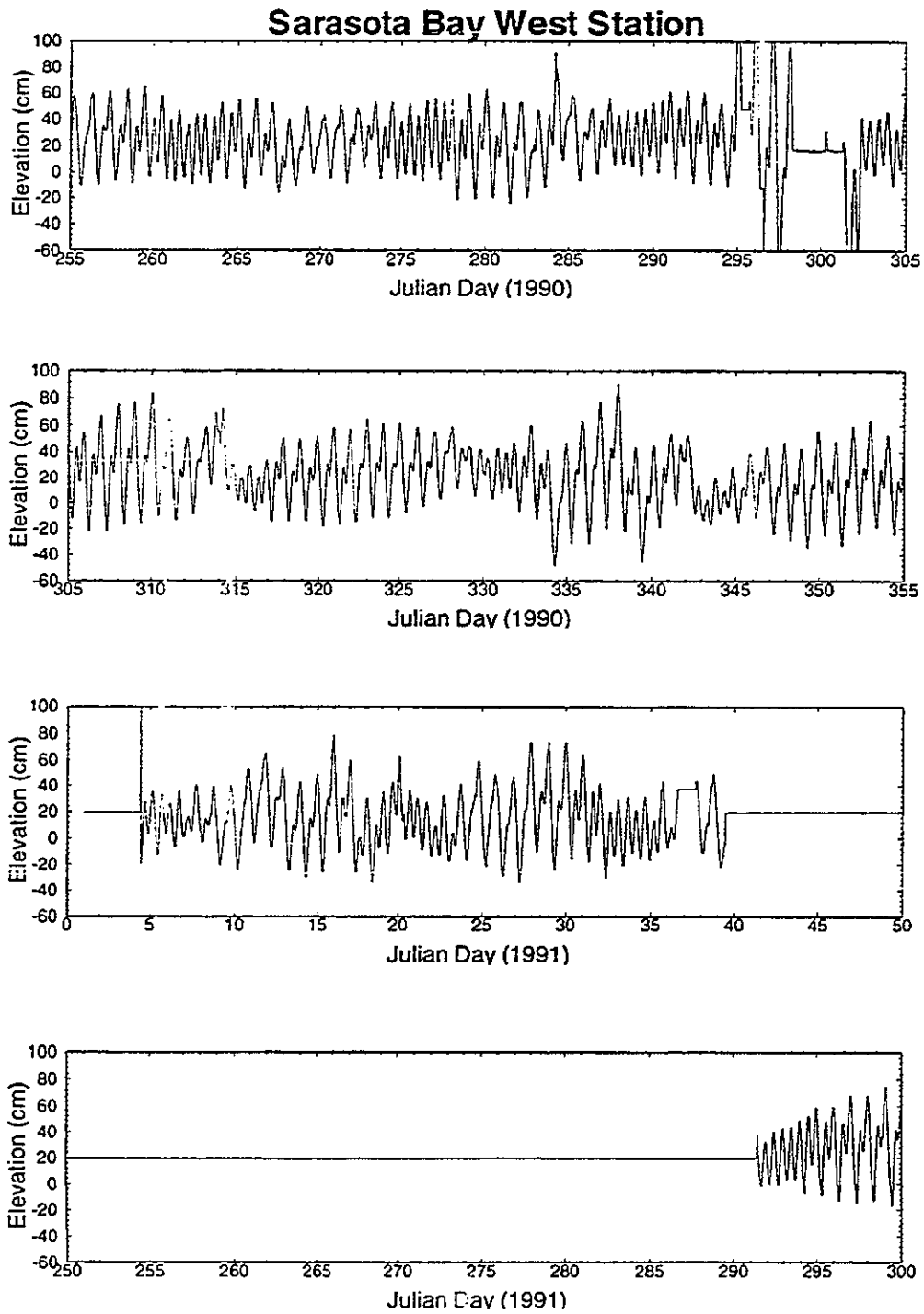
Figure B.7: The Water Surface Elevation Measured at the Sarasota Bay West Station (USGS-03) from Julian Day 255, 1990 to Julian Day 50, 1991 and Julian Day 250, 1991 to Julian Day 300, 1991
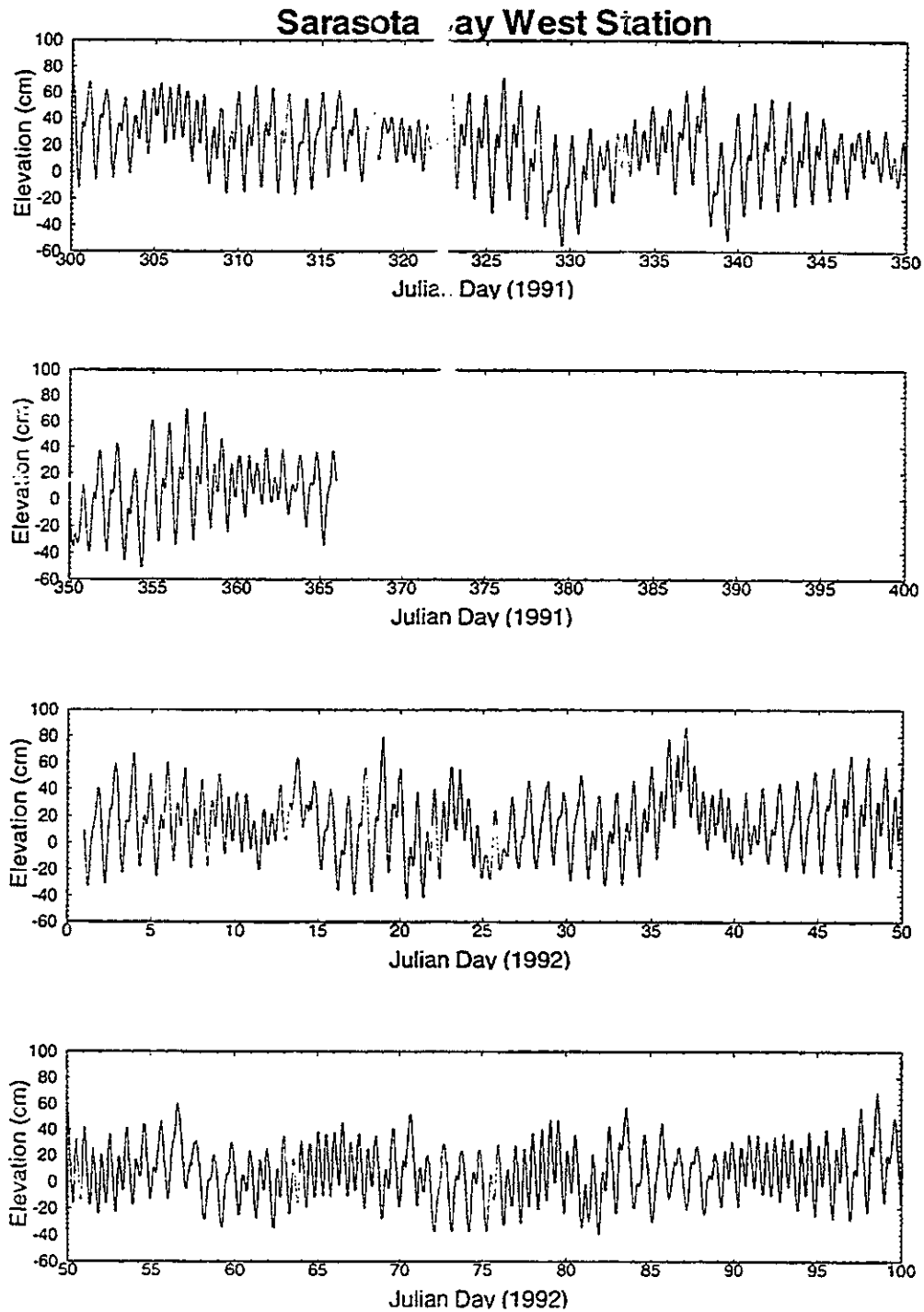
Figure B.8: The Water Surface Elevation Measured at the Sarasota Bay West Station (USGS-03) from Julian Day 300, 1991 to Julian Day 100, 1992
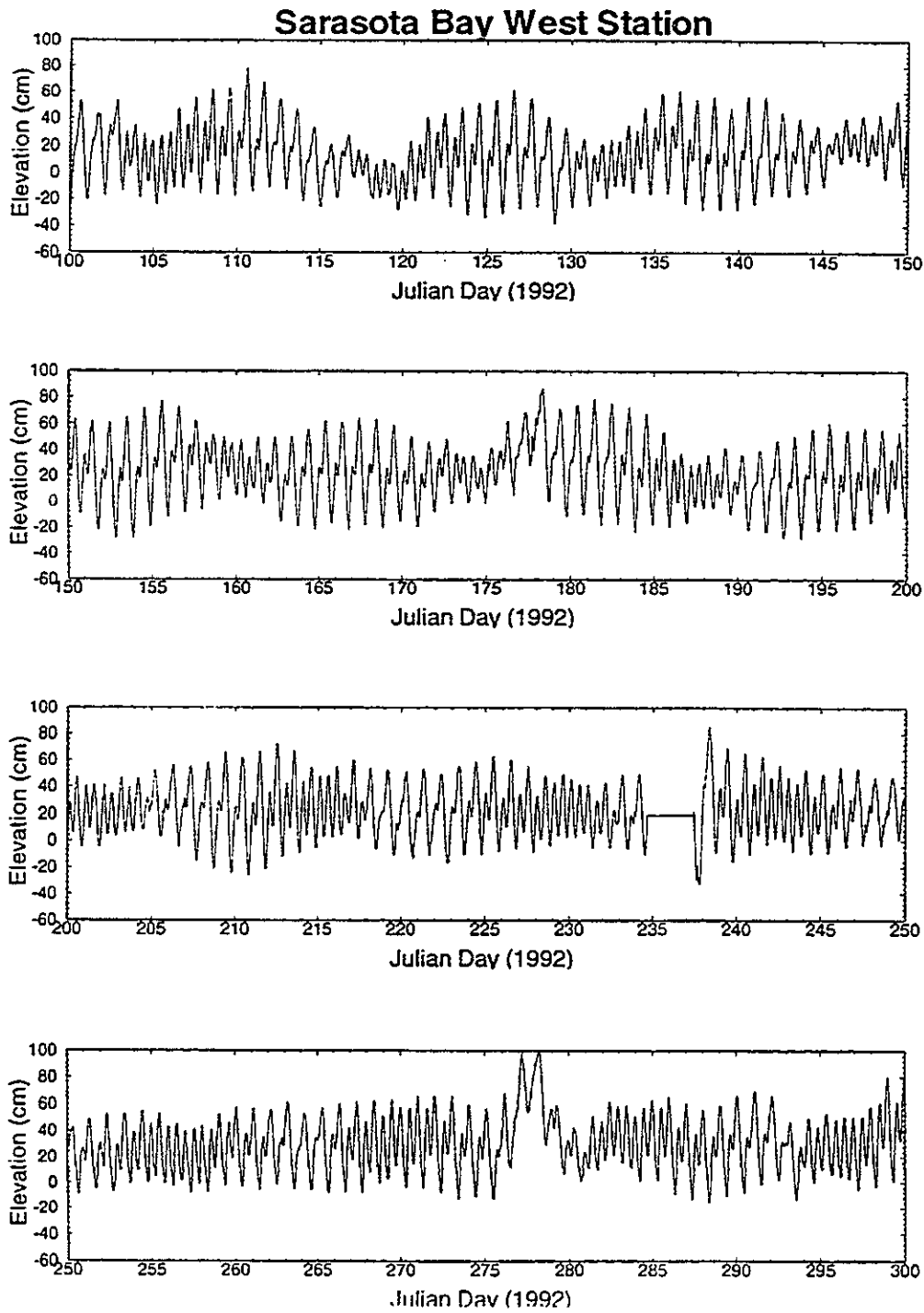
Figure B.9: The Water Surface Elevation Measured at the Sarasota Bay West Station (USGS-03) from Julian Day 100, 1992 to Julian Day 300, 1992
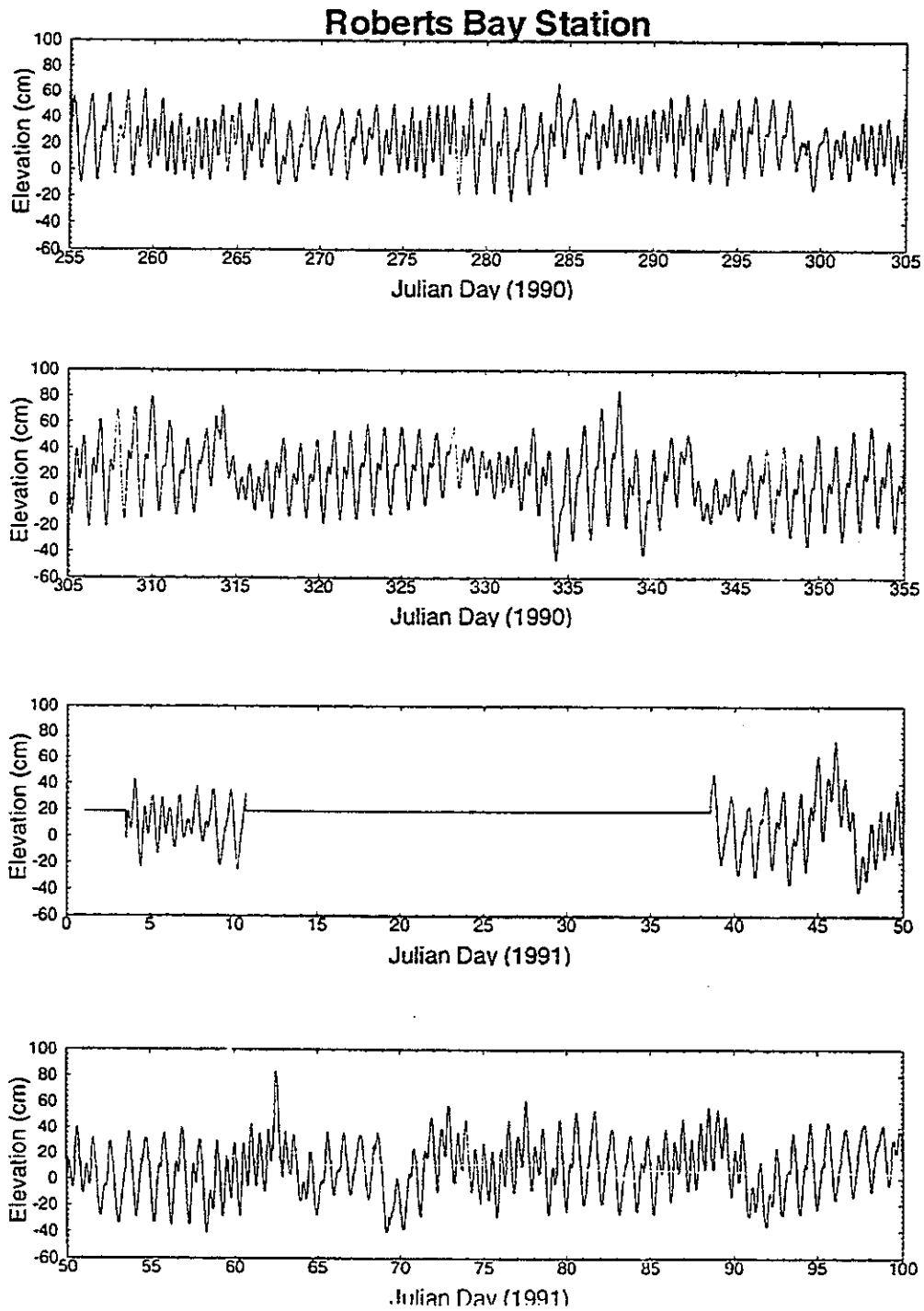
Figure B.10: The Water Surface Elevation Measured at the Roberts Bay Station (USGS-04) from Julian Day 255, 1990 to Julian Day 100, 1991
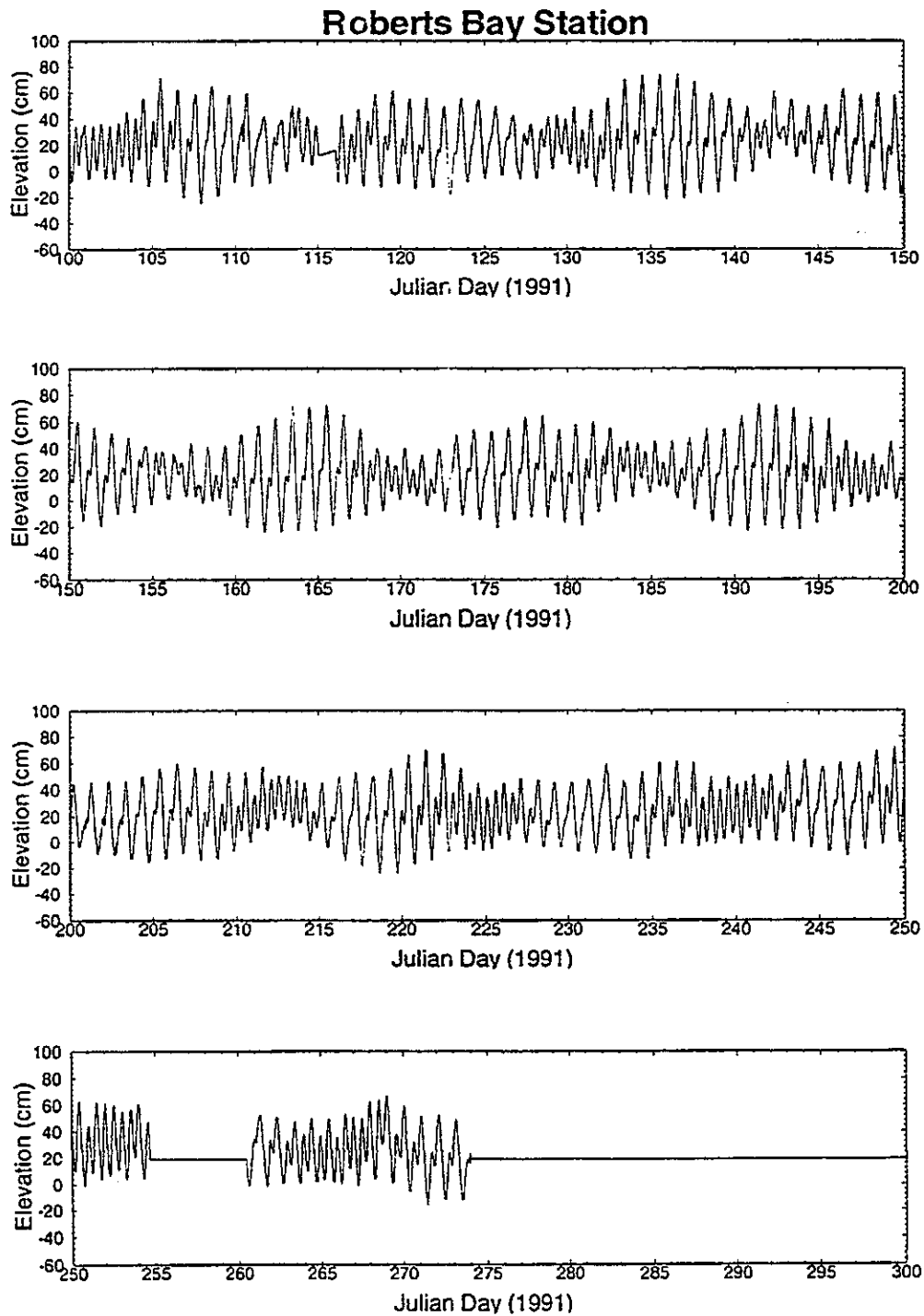
Figure B.11: The Water Surface Elevation Measured at the Roberts Bay Station (USGS-04) from Julian Day 100, 1991 to Julian Day 300, 1991
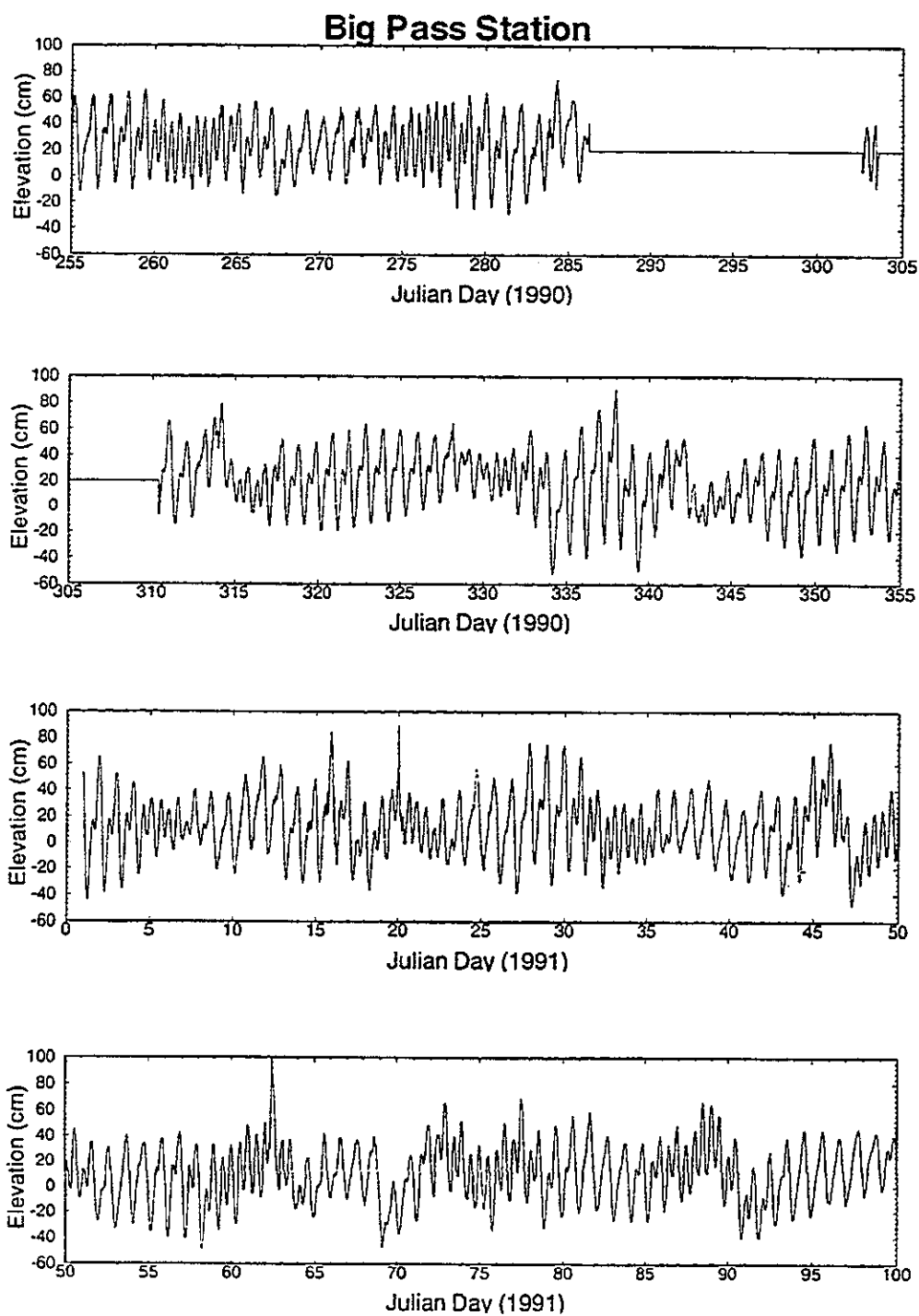
Figure B.12: The Water Surface Elevation Measured at the Big Pass Station (USGS-05) from Julian Day 255, 1990 to Julian Day 100, 1991
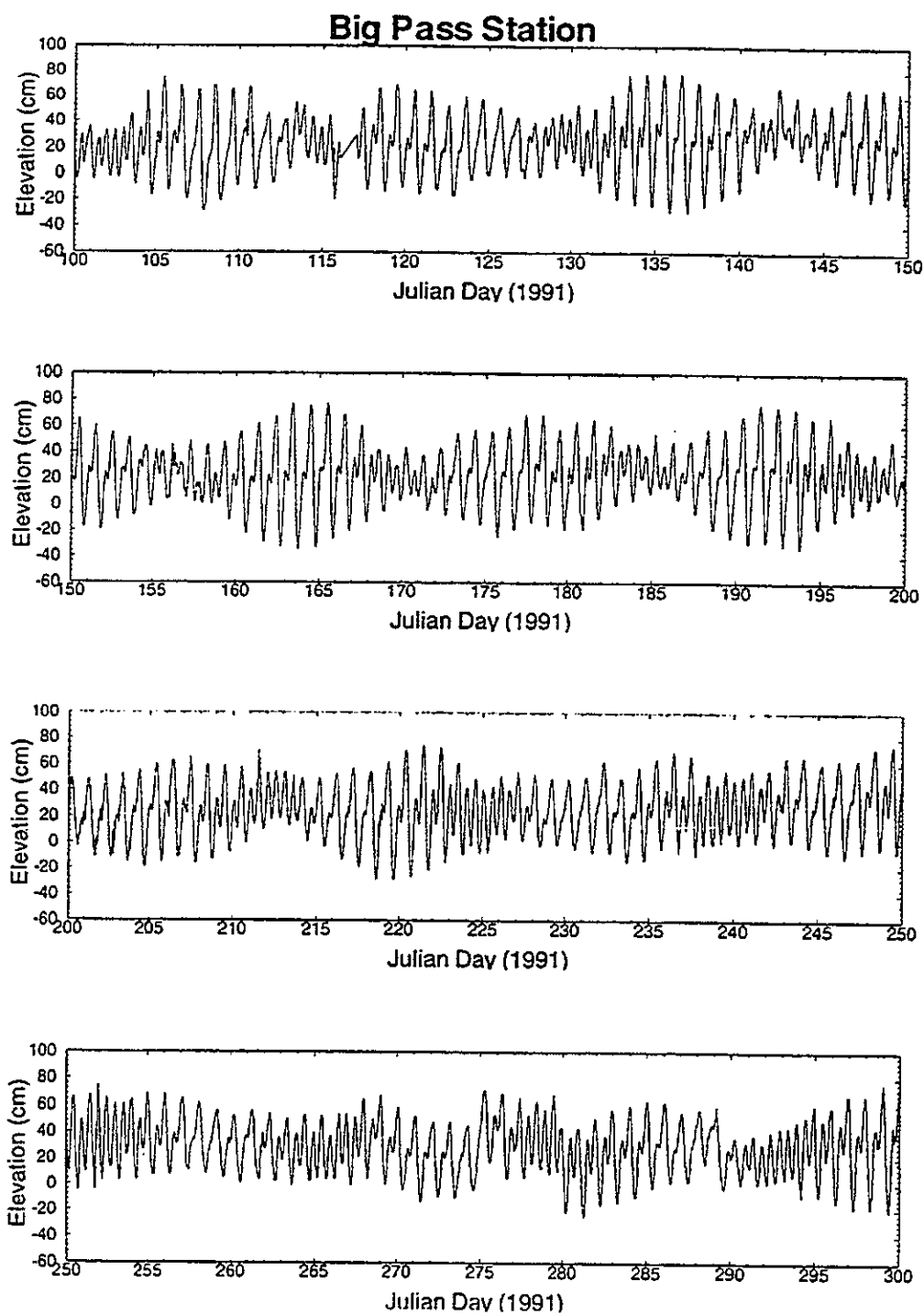
Figure B.13: The Water Surface Elevation Measured at the Big Pass Station (USGS-05) from Julian Day 100, 1991 to Julian Day 300, 1991
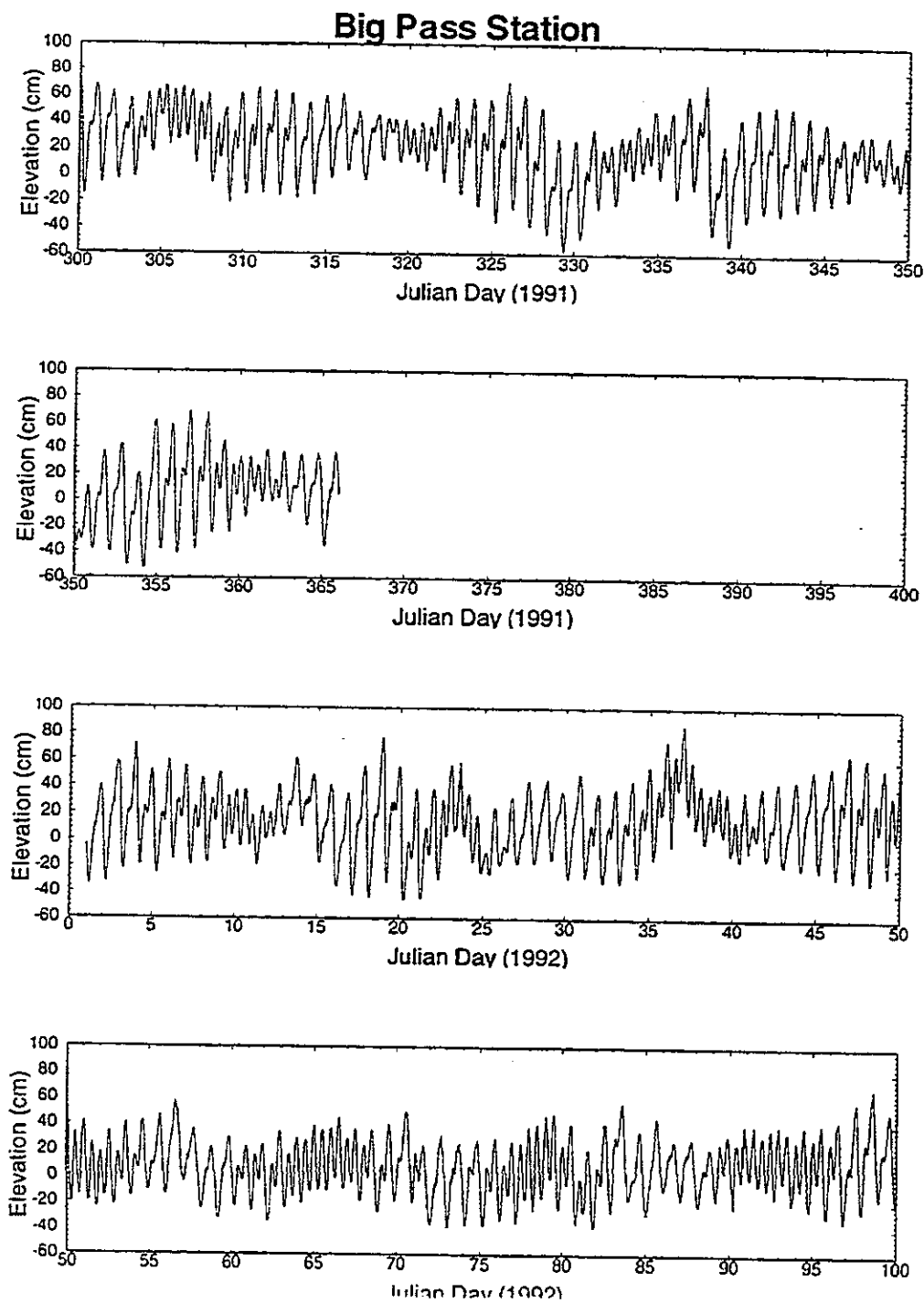
Figure B.14: The Water Surface Elevation Measured at the Big Pass Station (USGS-05) from Julian Day 300, 1991 to Julian Day 100, 1992
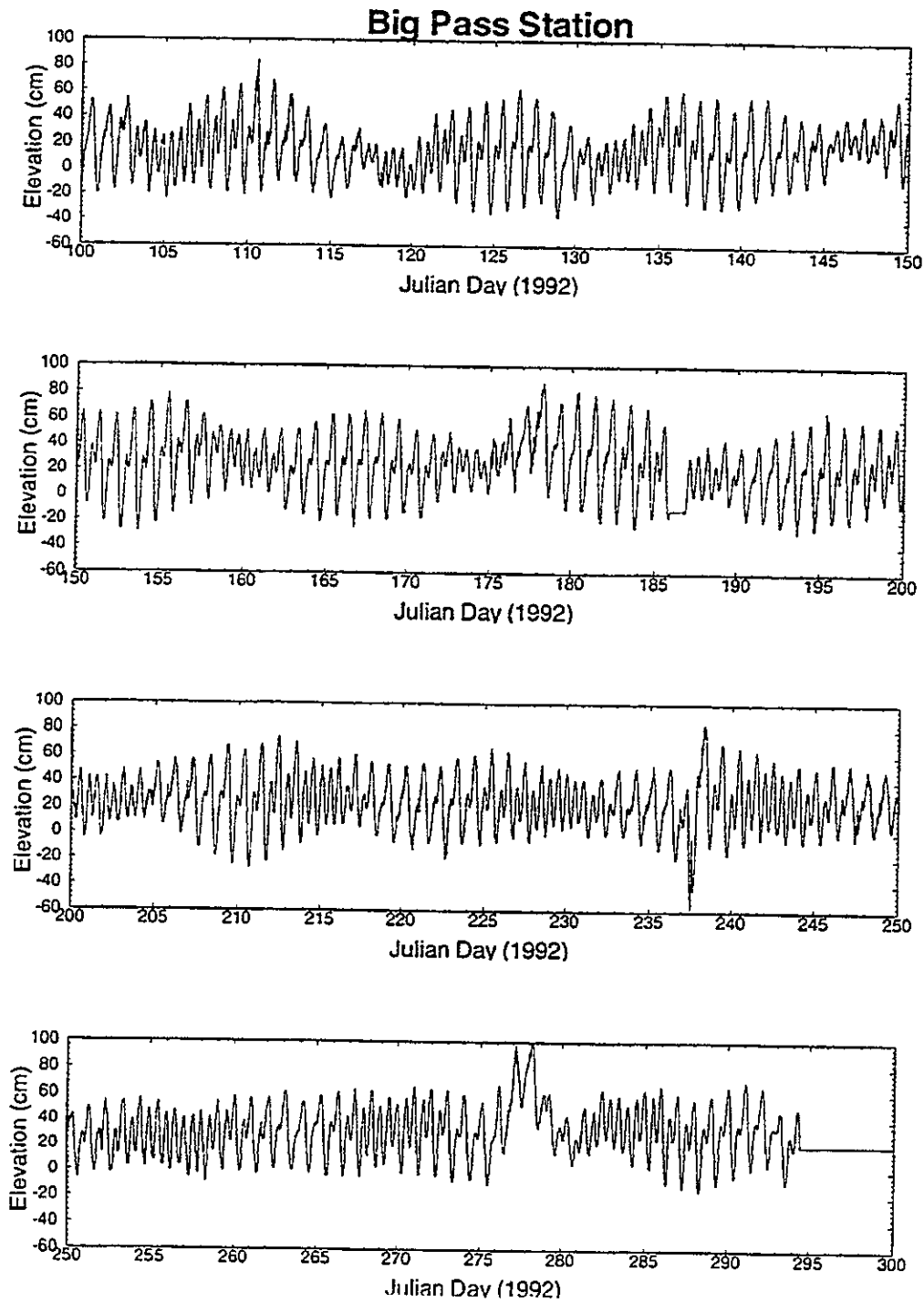
Figure B.15: The Water Surface Elevation Measured at the Big Pass Station (USGS-05) from Julian Day 100, 1992 to Julian Day 300, 1992
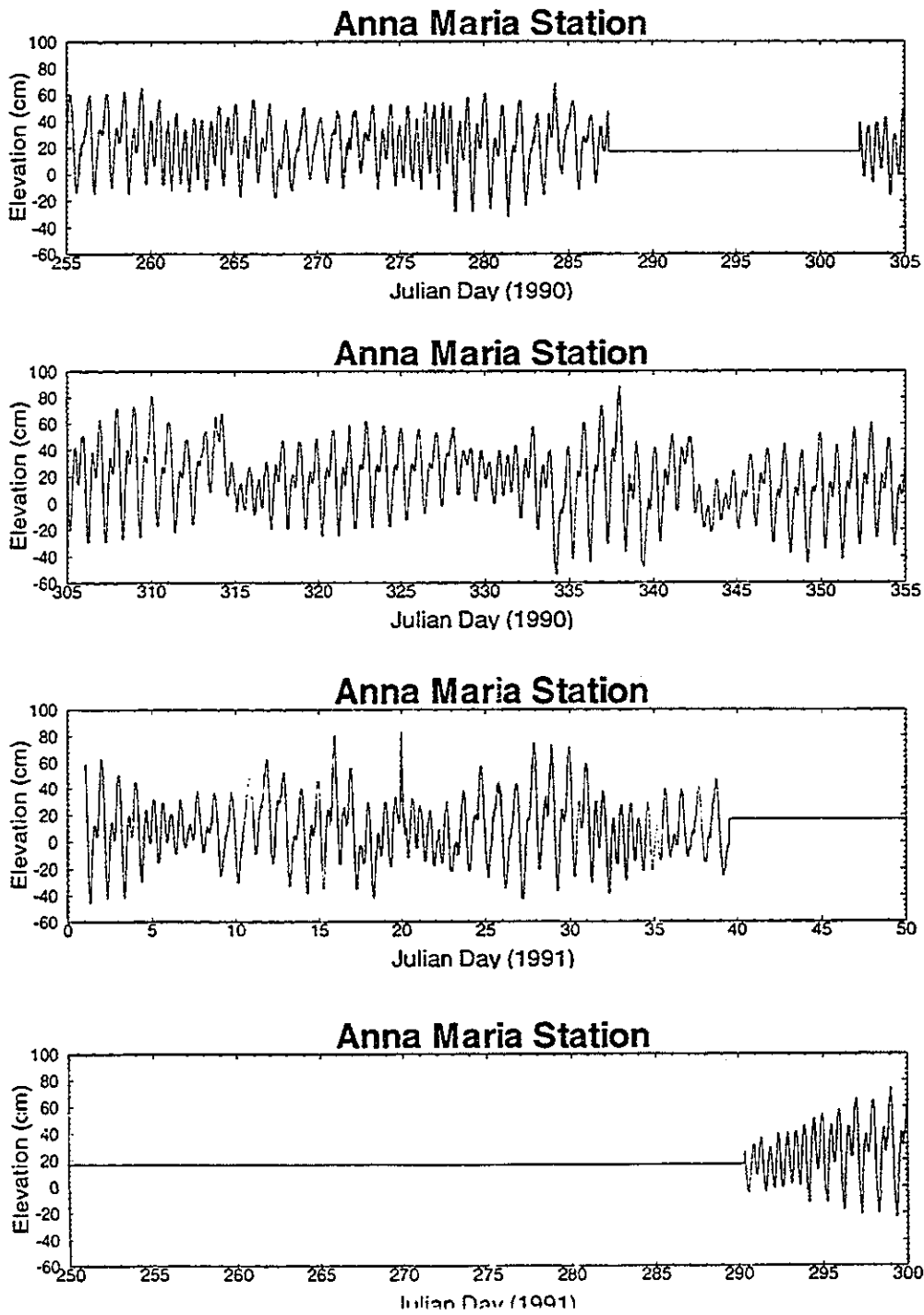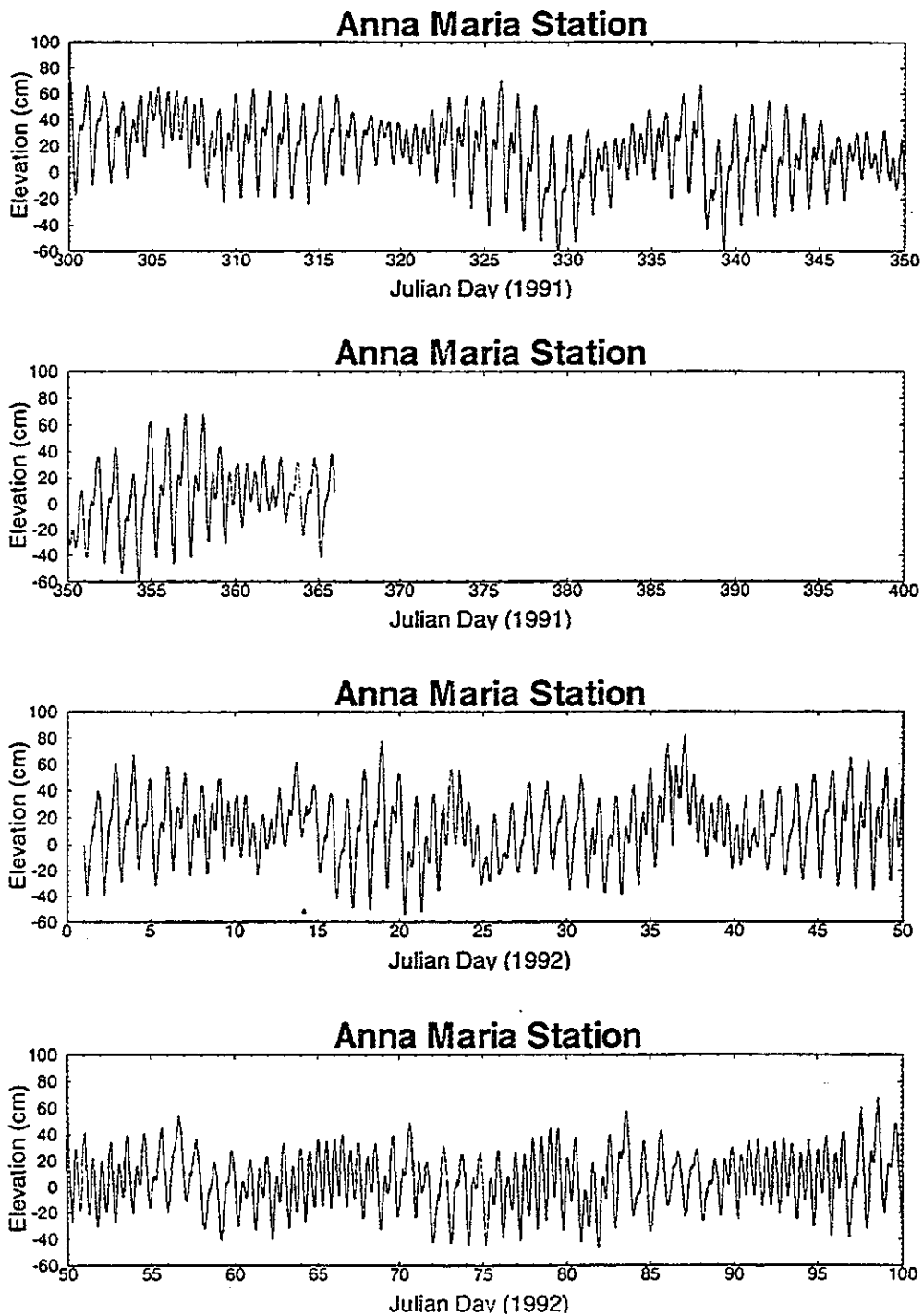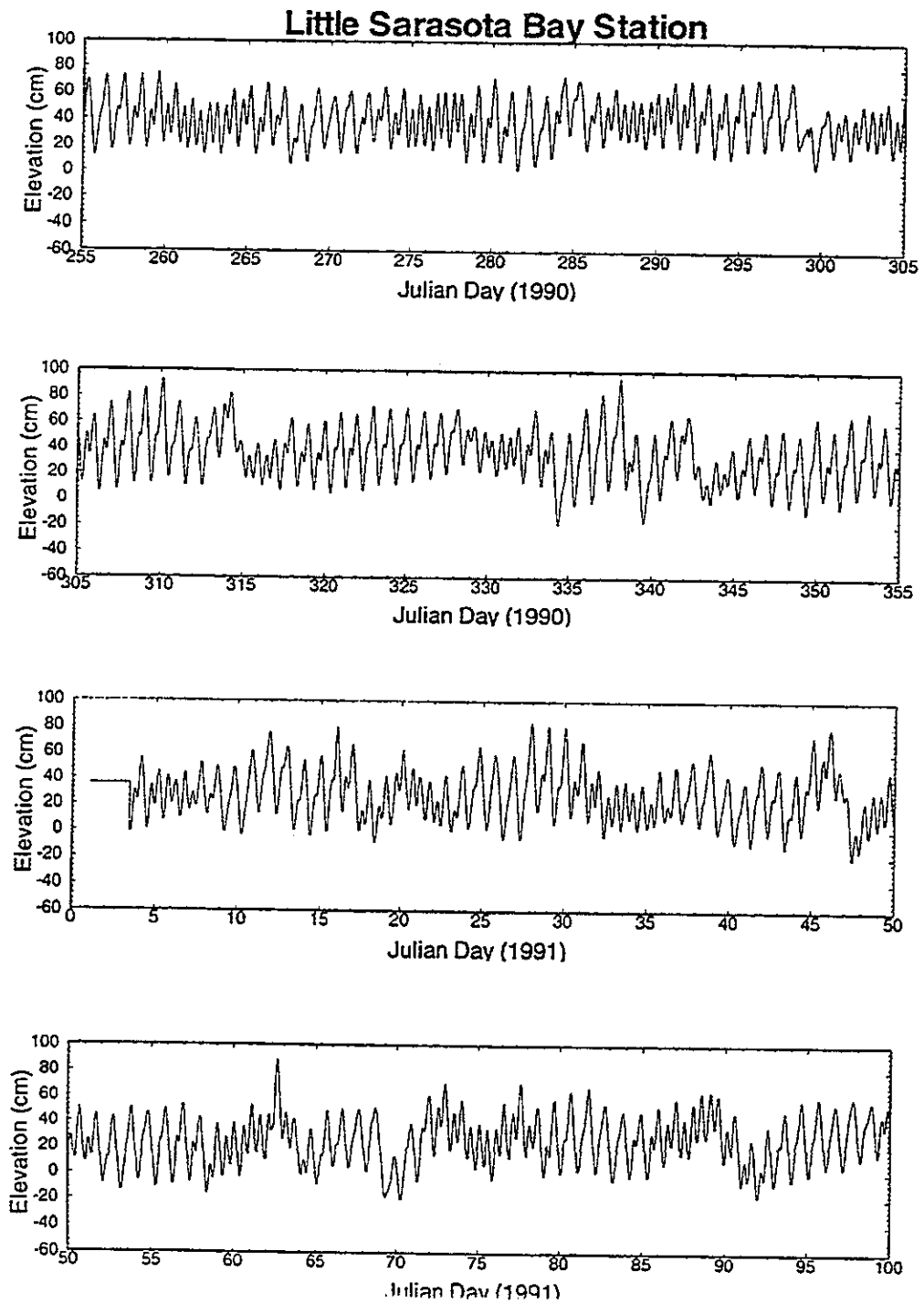
Figure B.16: The Water Surface Elevation Measured at the Little Sarasota Bay Station (USGS-06) from Julian Day 255, 1990 to Julian Day 100, 1991
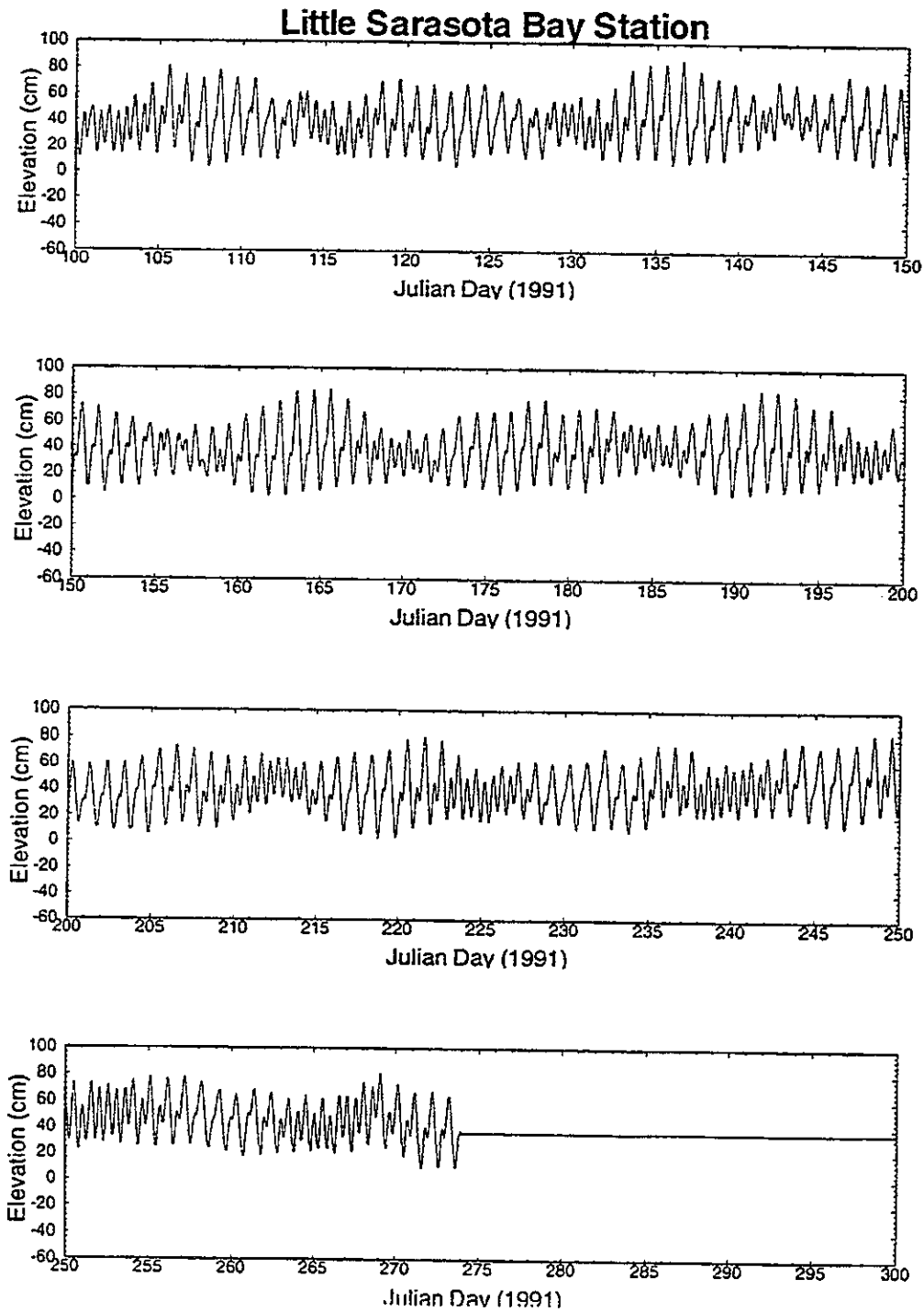
Figure B.17: The Water Surface Elevation Measured at the Little Sarasota Bay Station (USGS-06) from Julian Day 100, 1991 to Julian Day 300, 1991
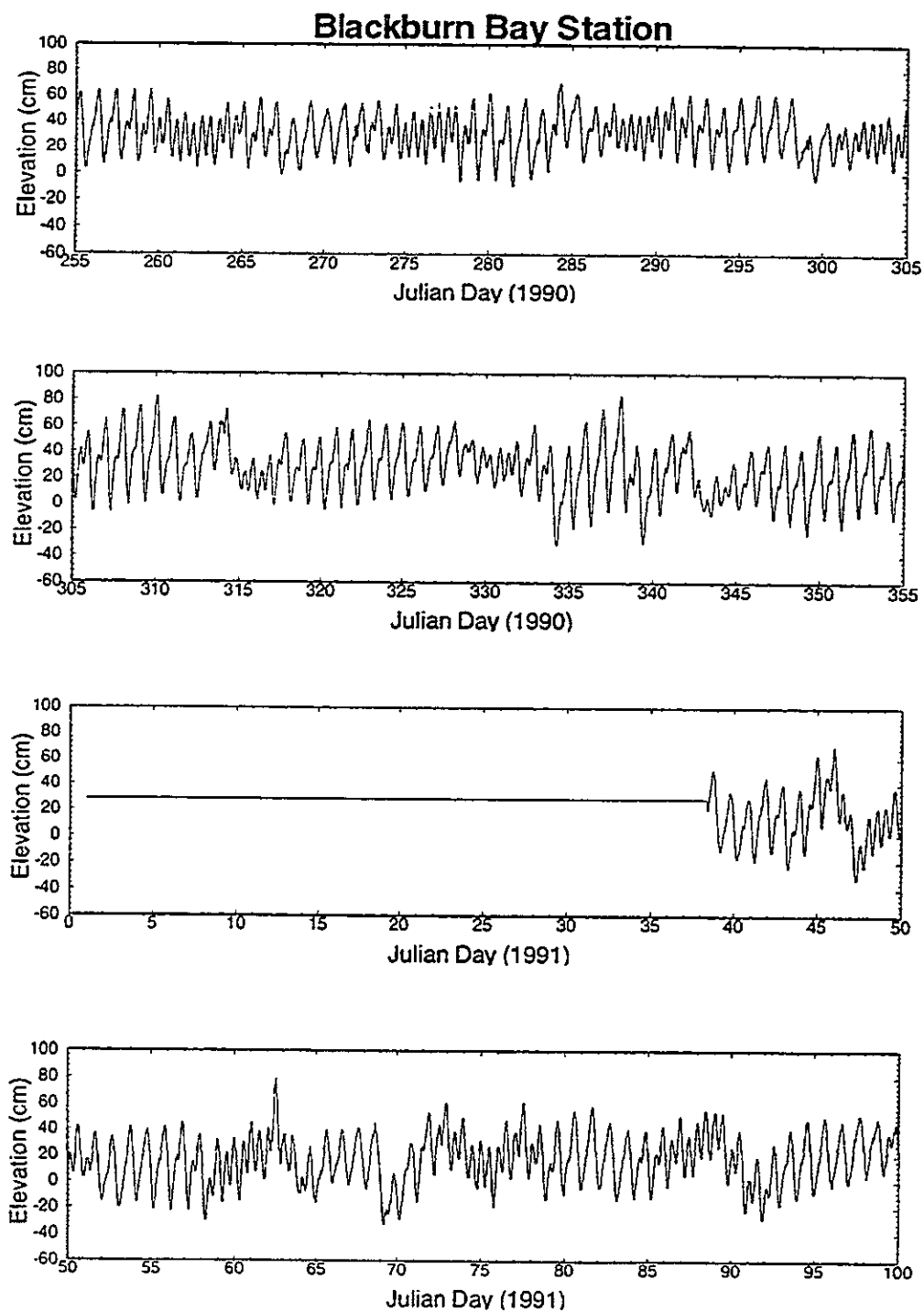
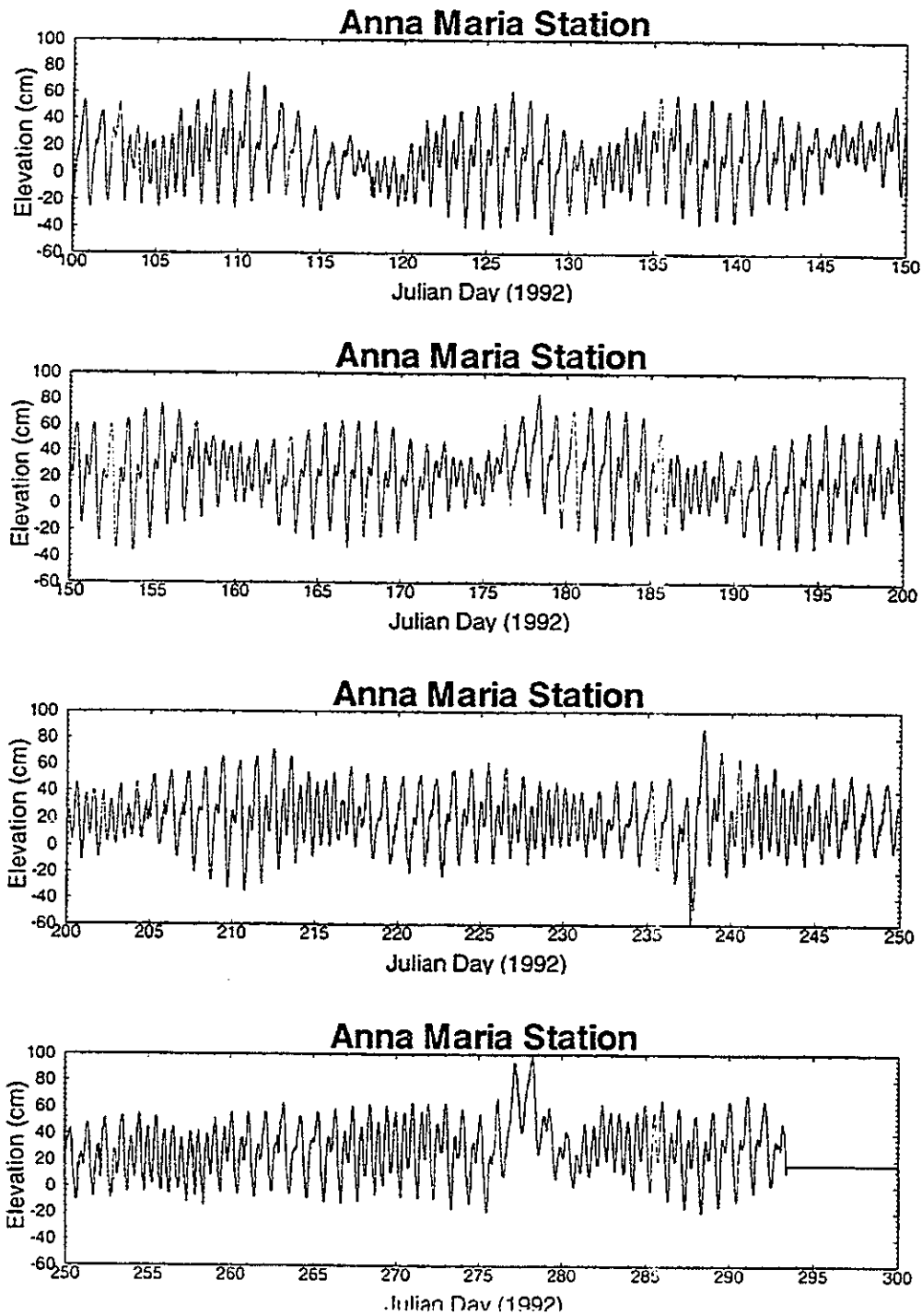Figure B.18: The Water Surface Elevation Measured in Blackburn Bay (USGS-07) from Julian Day 255, 1990 to Julian Day 100, 1991
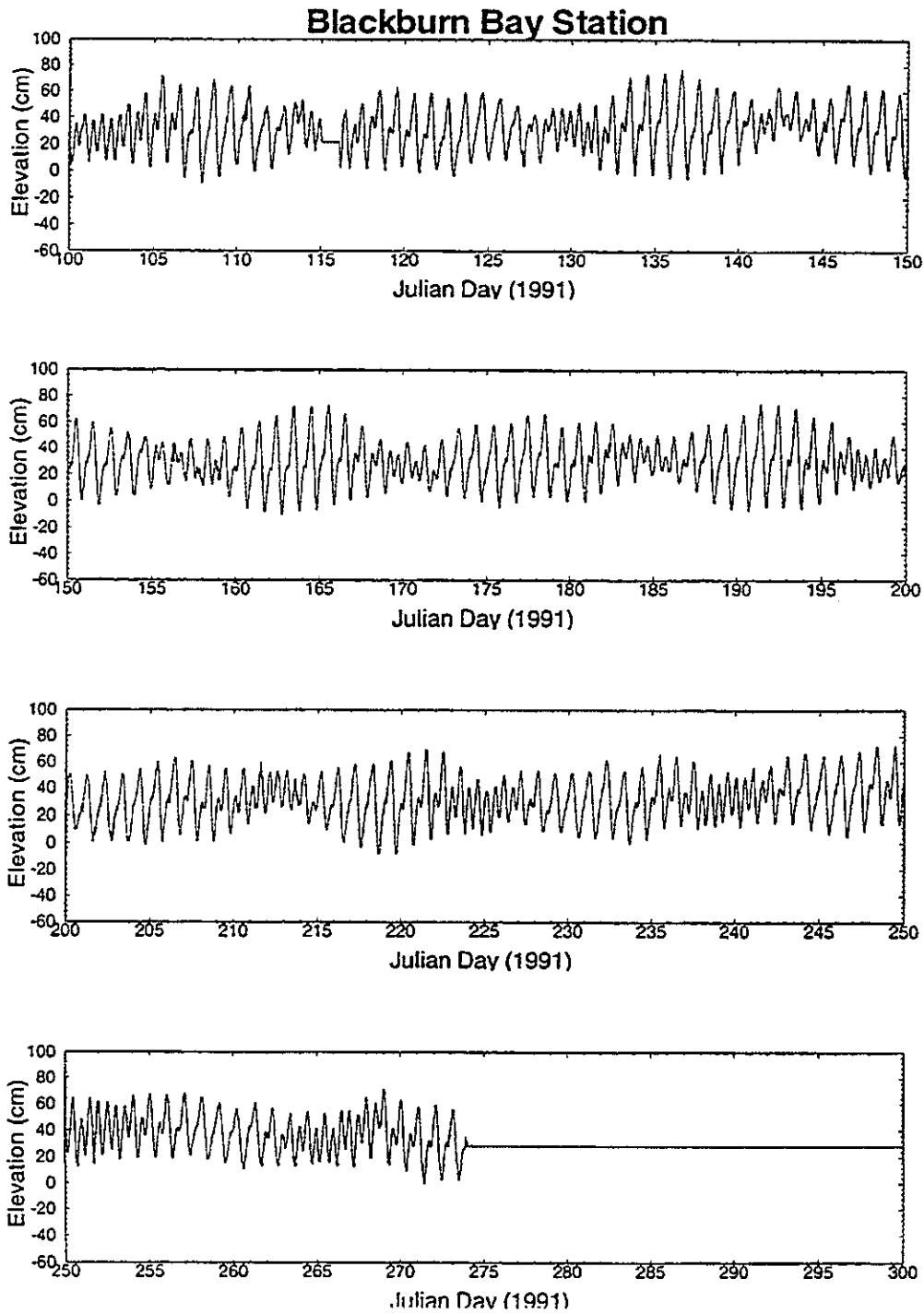
Figure B.19: The Water Surface Elevation Measured in Blackburn Bay (USGS-07) from Julian Day 100, 1991 to Julian Day 300, 1991
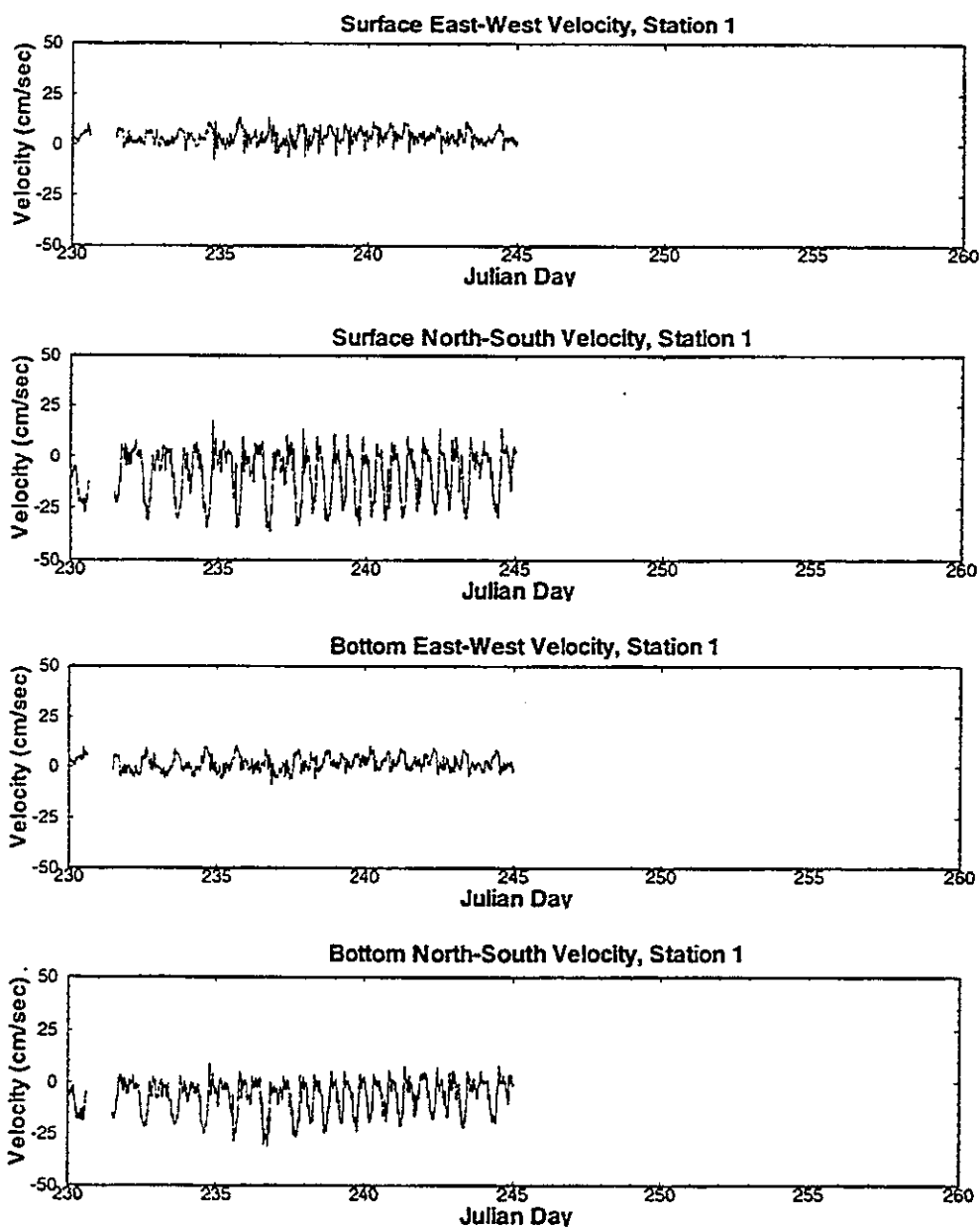
Figure B.20: The Bottom and Surface Water Velocities Measured at Station UFL-B1 from Julian Day 230 to 260, 1991
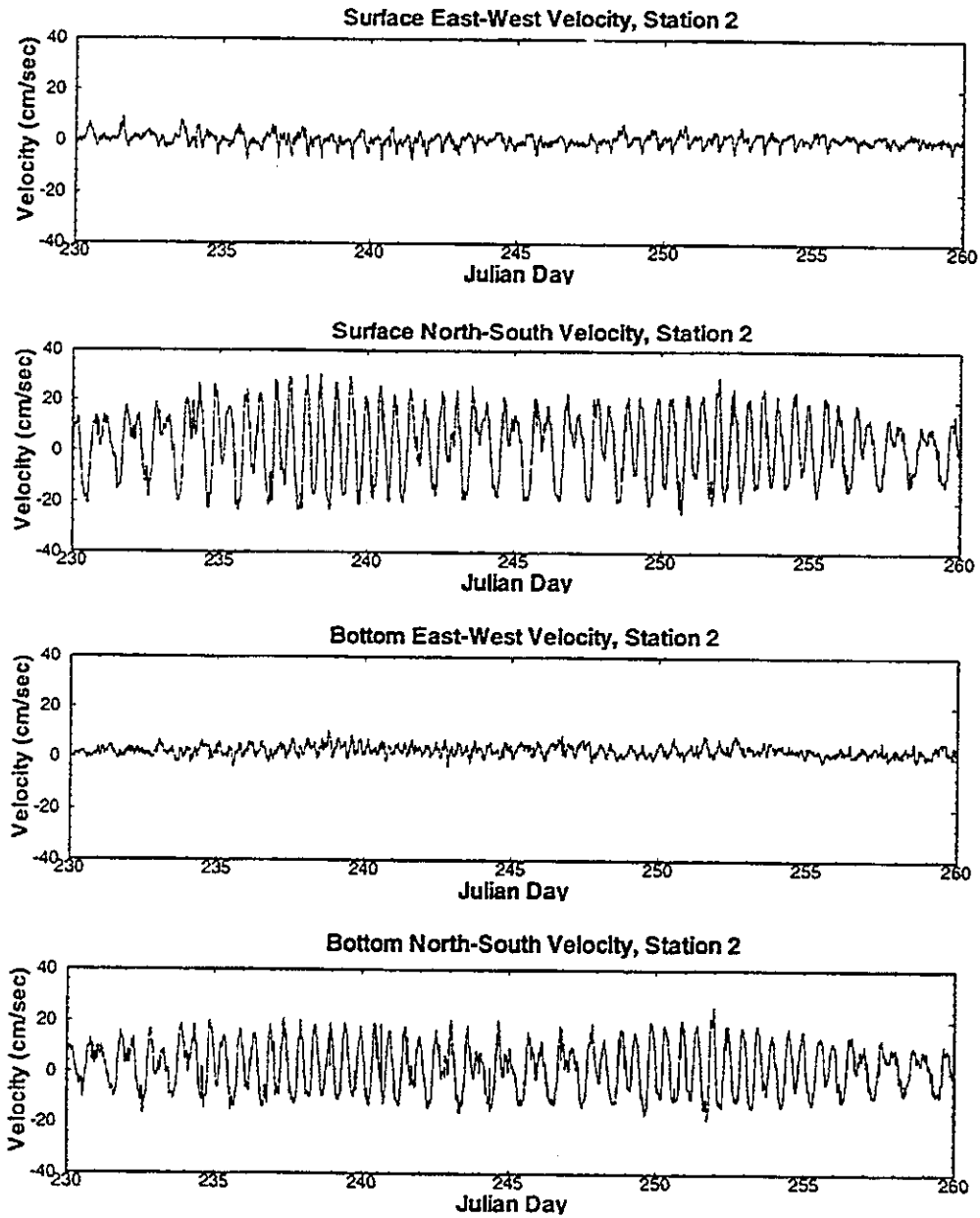
Figure B.21: The Bottom and Surface Water Velocities Measured at Station UFL-B2 from Julian Day 230 to 260, 1991
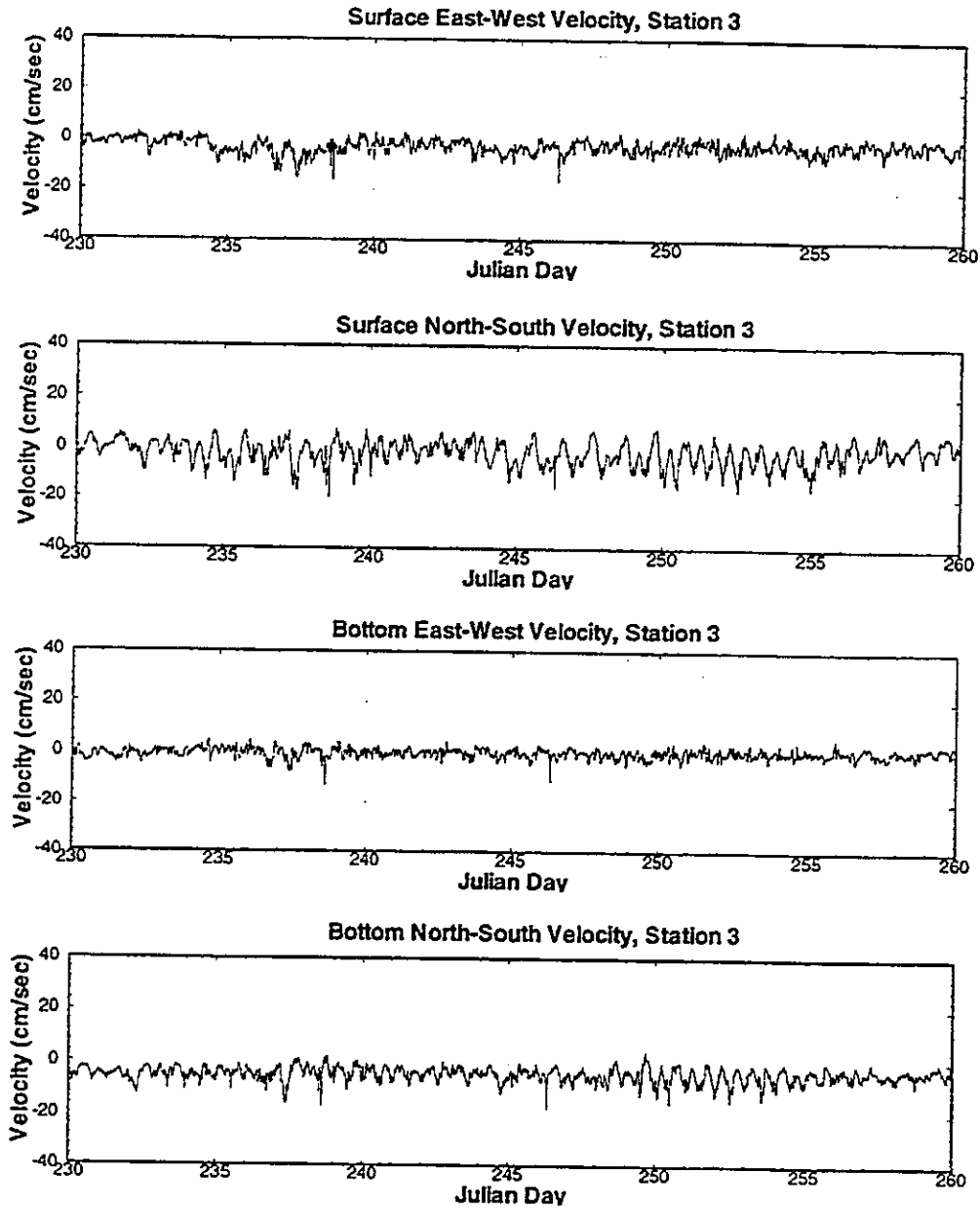
Figure B.22: The Bottom and Surface Water Velocities Measured at Station UFL-B3 from Julian Day 230 to 260, 1991
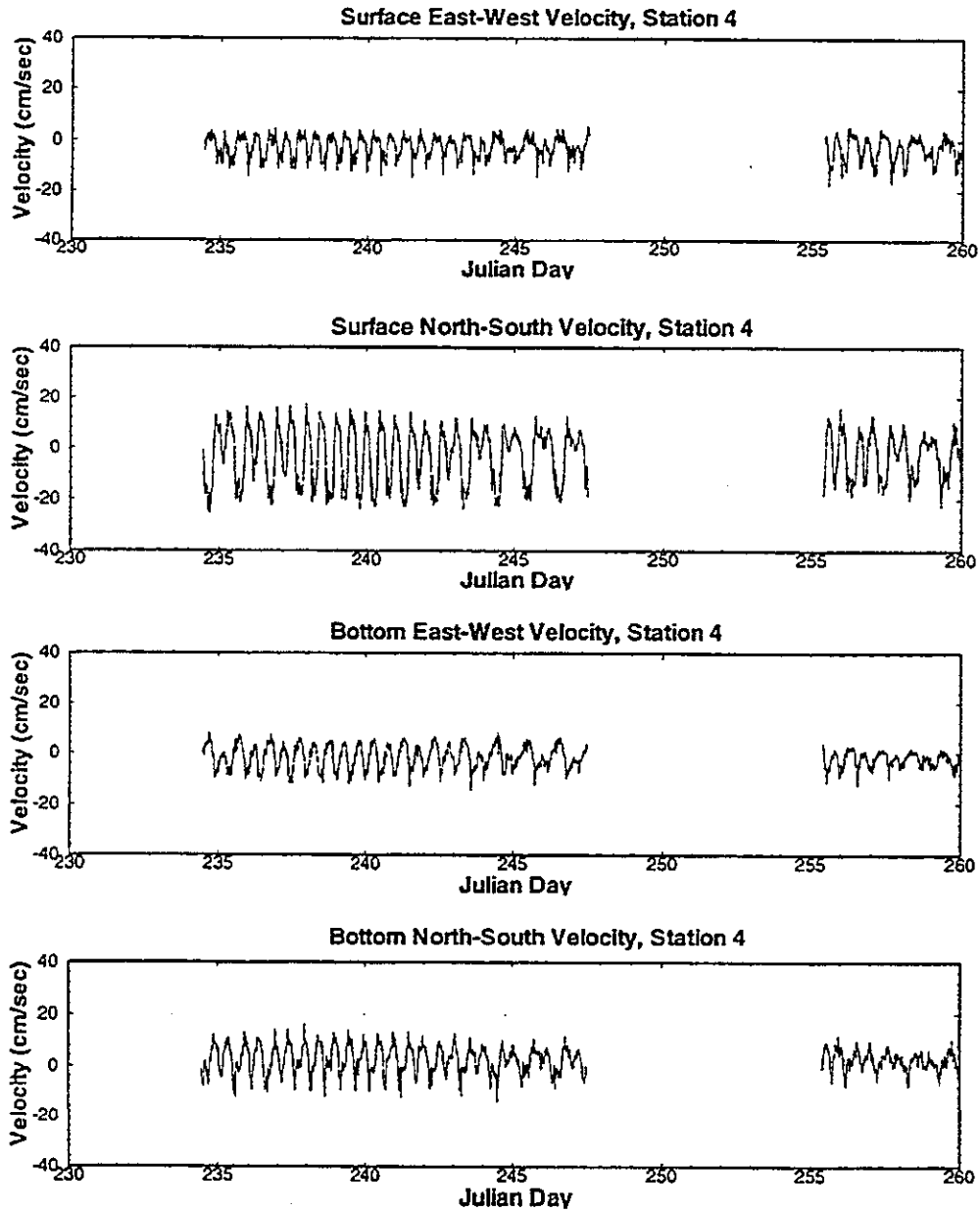
Figure B.23: The Bottom and Surface Water Velocities Measured at Station UFL-B4 from Julian Day 230 to 260, 1991
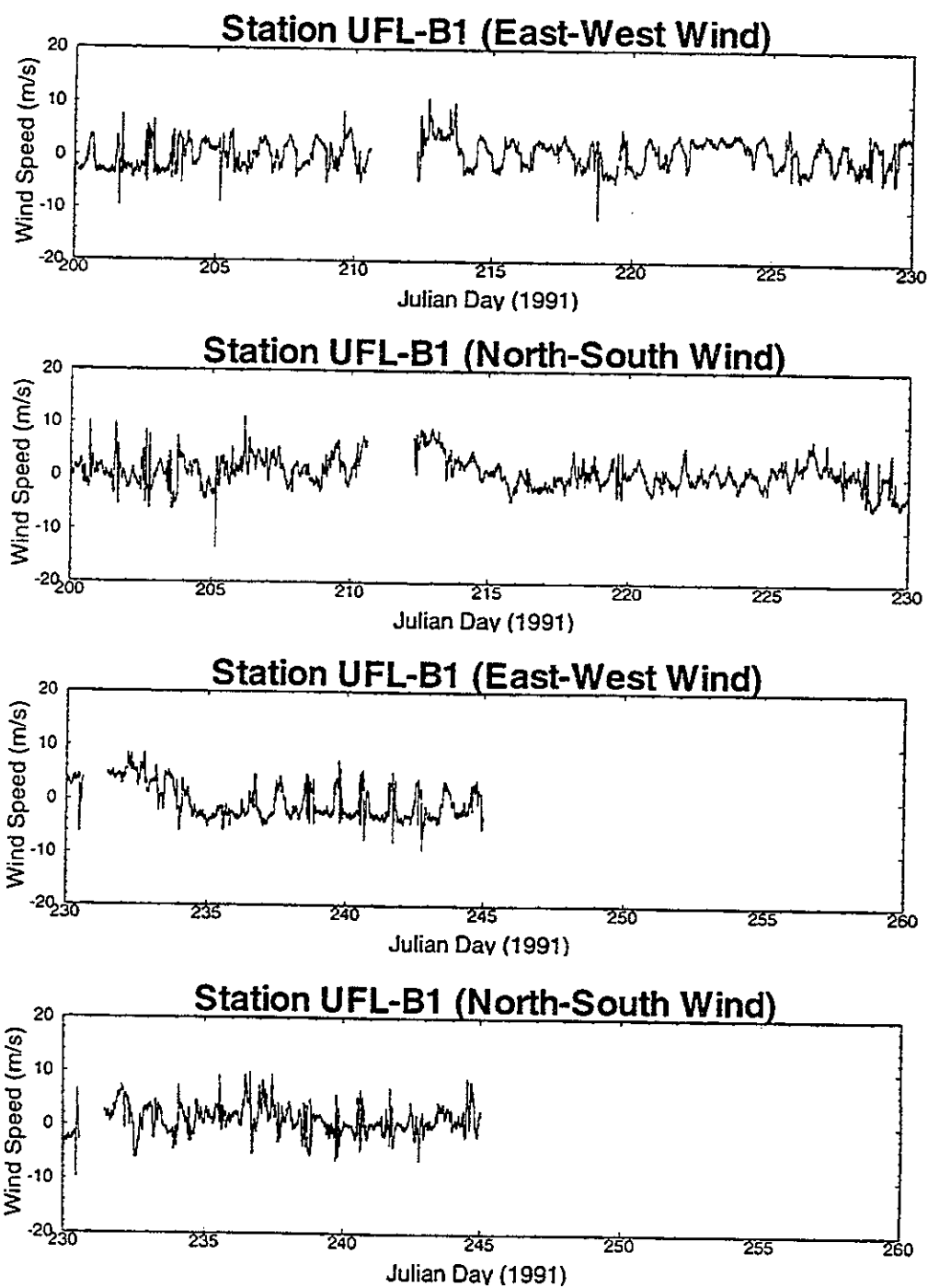
Figure B.24: The East-West and North-South Wind Speed Components Measured at Station UFL-B1 from Julian Day 200 to 260, 1991
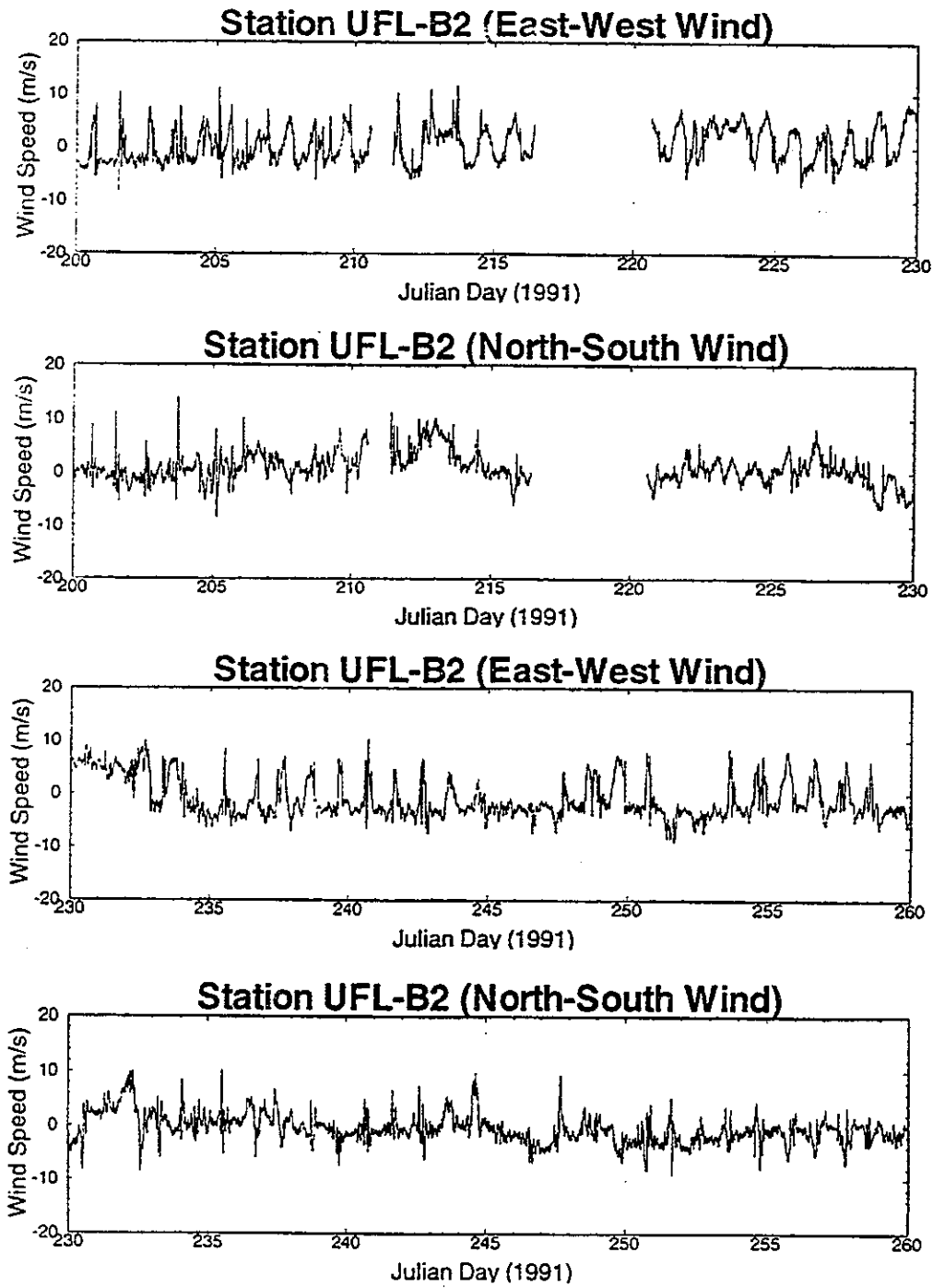
Figure B.25: The East-West and North-South Wind Speed Components Measured at Station UFL-B2 from Julian Day 200 to 260, 1991
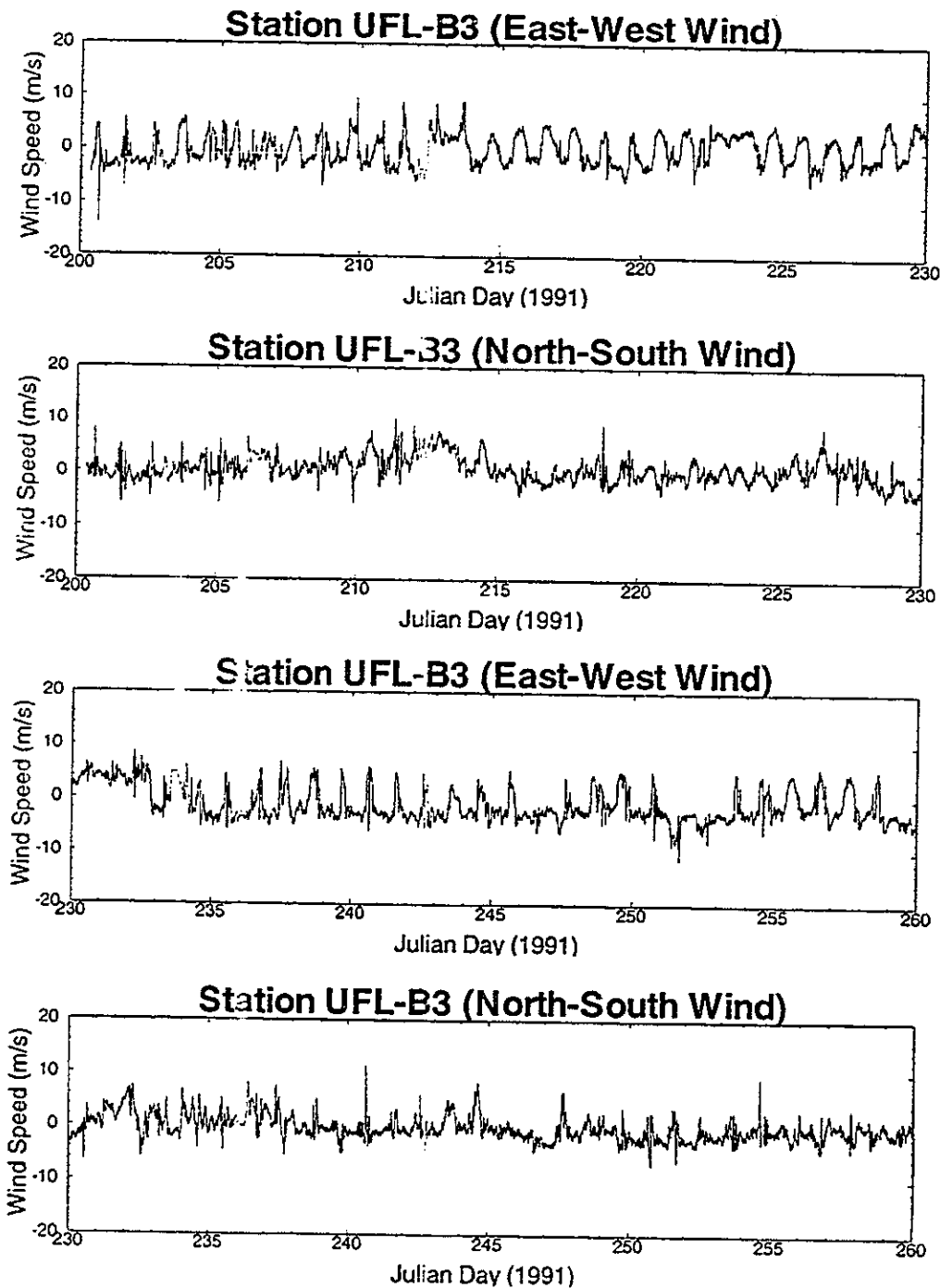
Figure B.26: The East-West and North-South Wind Speed Components Measured at Station UFL-B3 from Julian Day 200 to 260, 1991
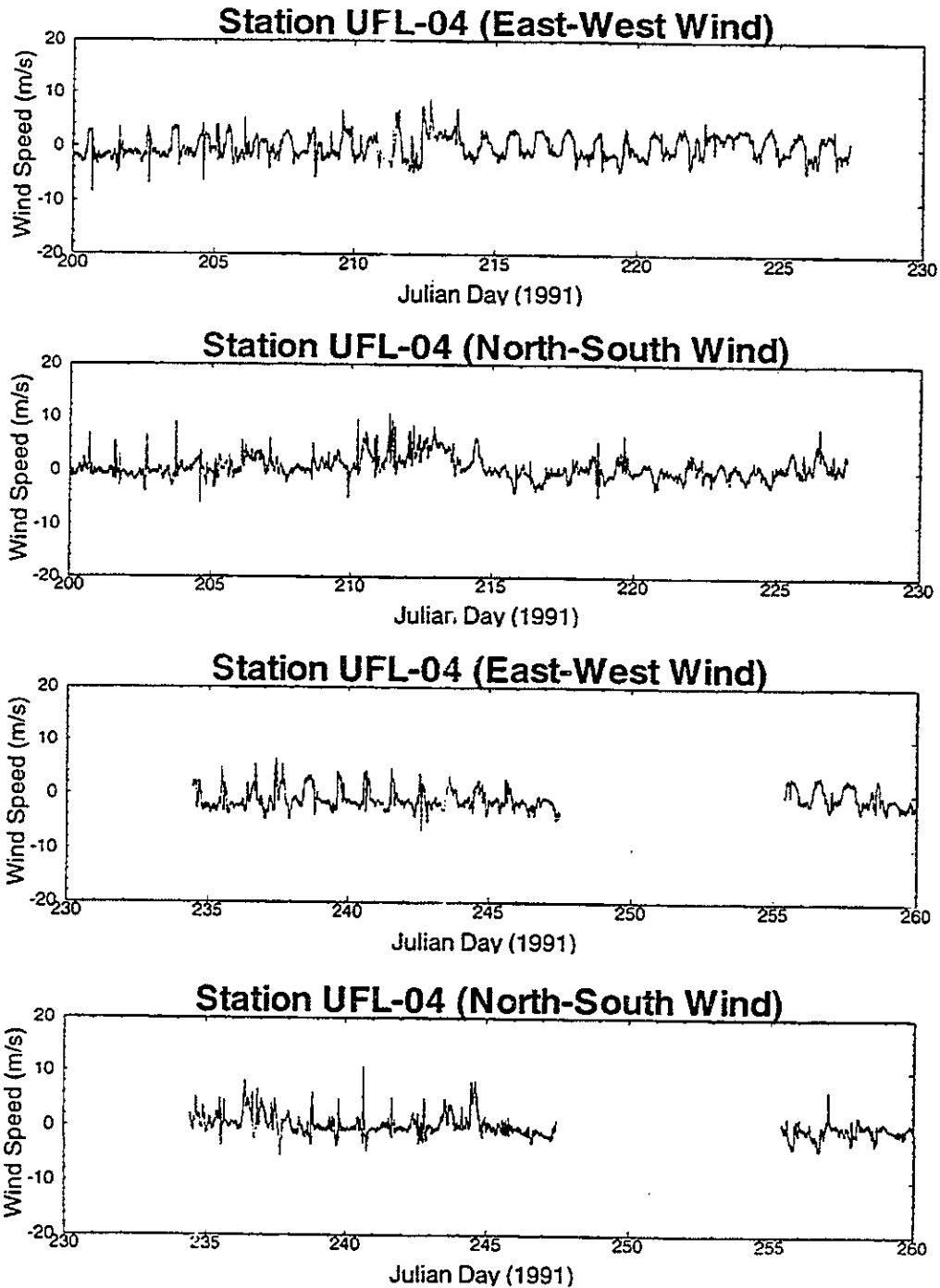
Figure B.27: The East-West and North-South Wind Speed Components Measured at Station UFL-B4 from Julian Day 200 to 260, 1991
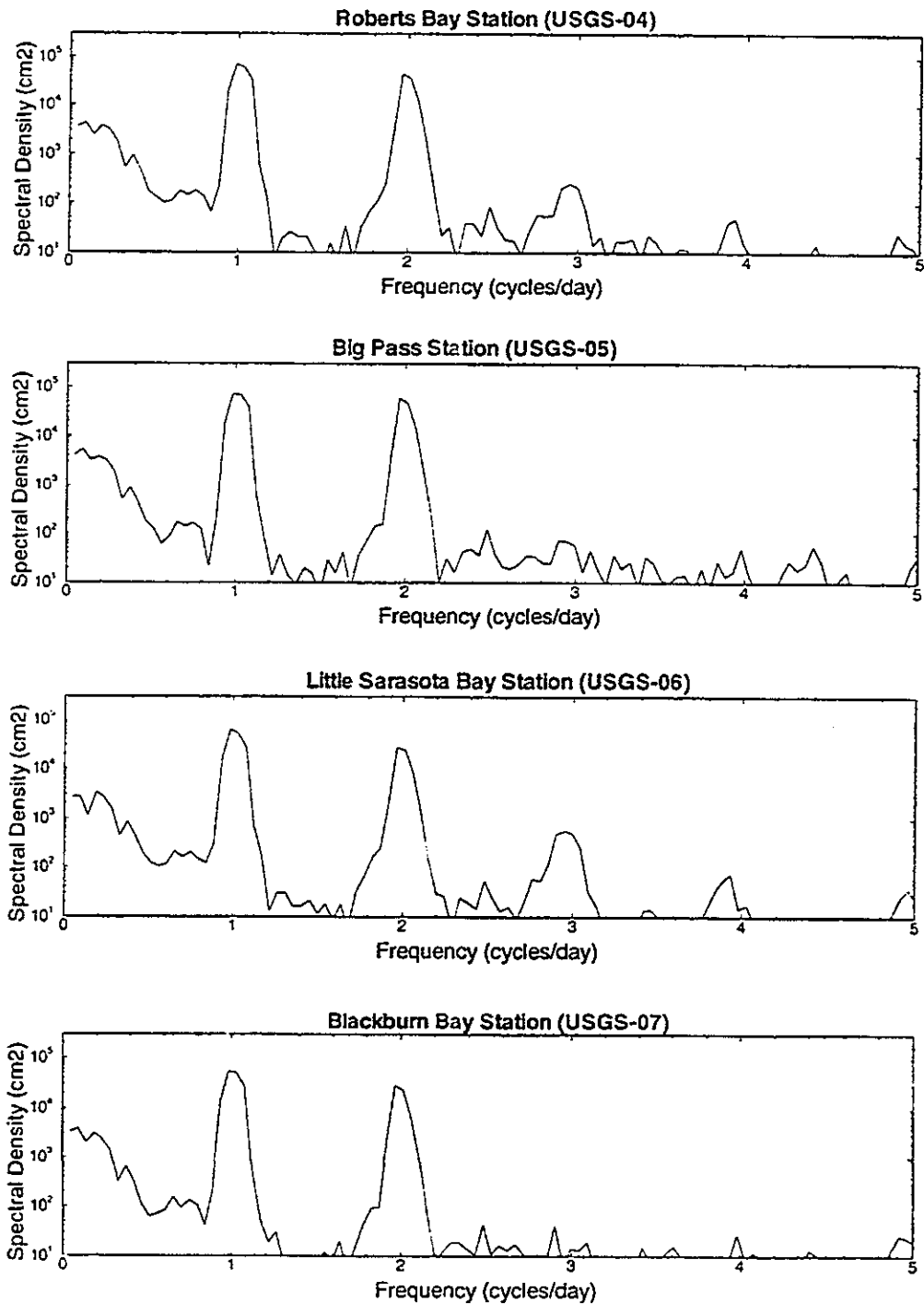
Figure B.28: The Spectral Density versus Frequency for the Water Surface Elevation Data Measured at the Roberts Bay (USGS-04), Big Pass (USGS-05), Little Sarasota Bay (USGS-06) and Blackburn Bay (USGS-07) Stations for Julian Days 200 to 260, 1991
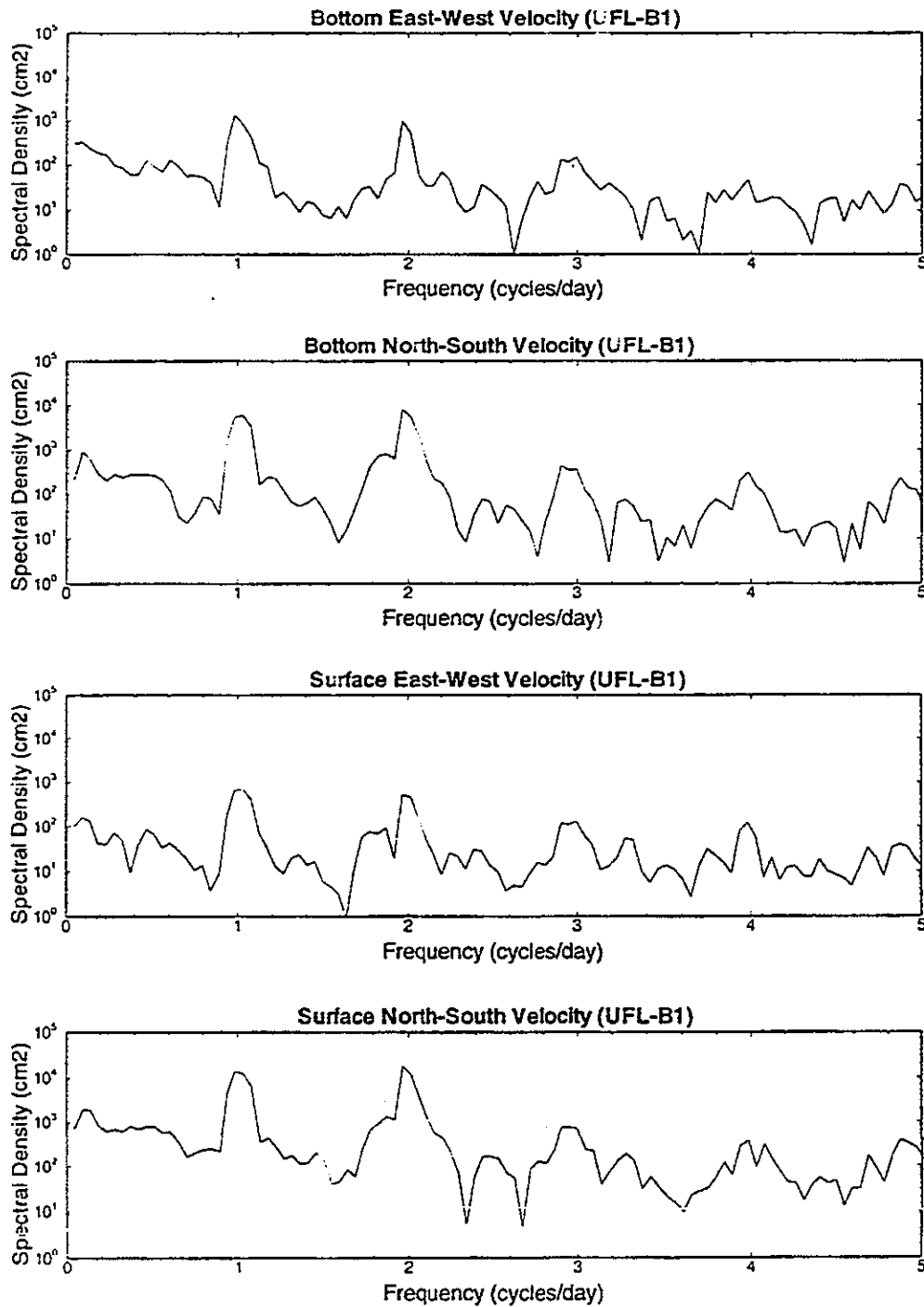
Figure B.29: The Spectral Density versus Frequency for the Surface and Bottom Current Vector Components at the UFL-B1 Station for Julian Days 200 to 260, 1991
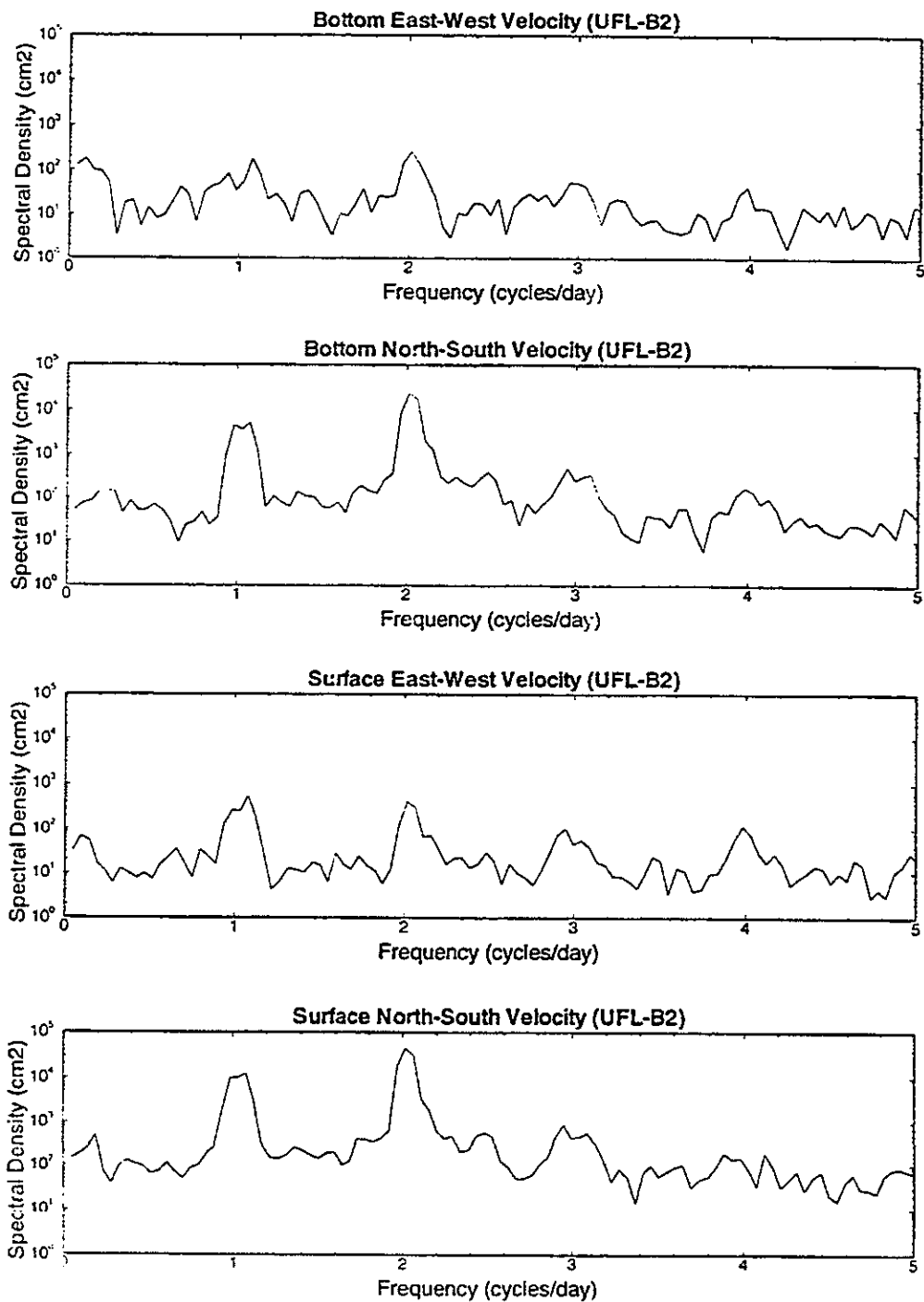
Figure B.30: The Spectral Density versus Frequency for the Surface and Bottom Current Vector Components at the UFL-B2 Station for Julian Days 200 to 260, 1991
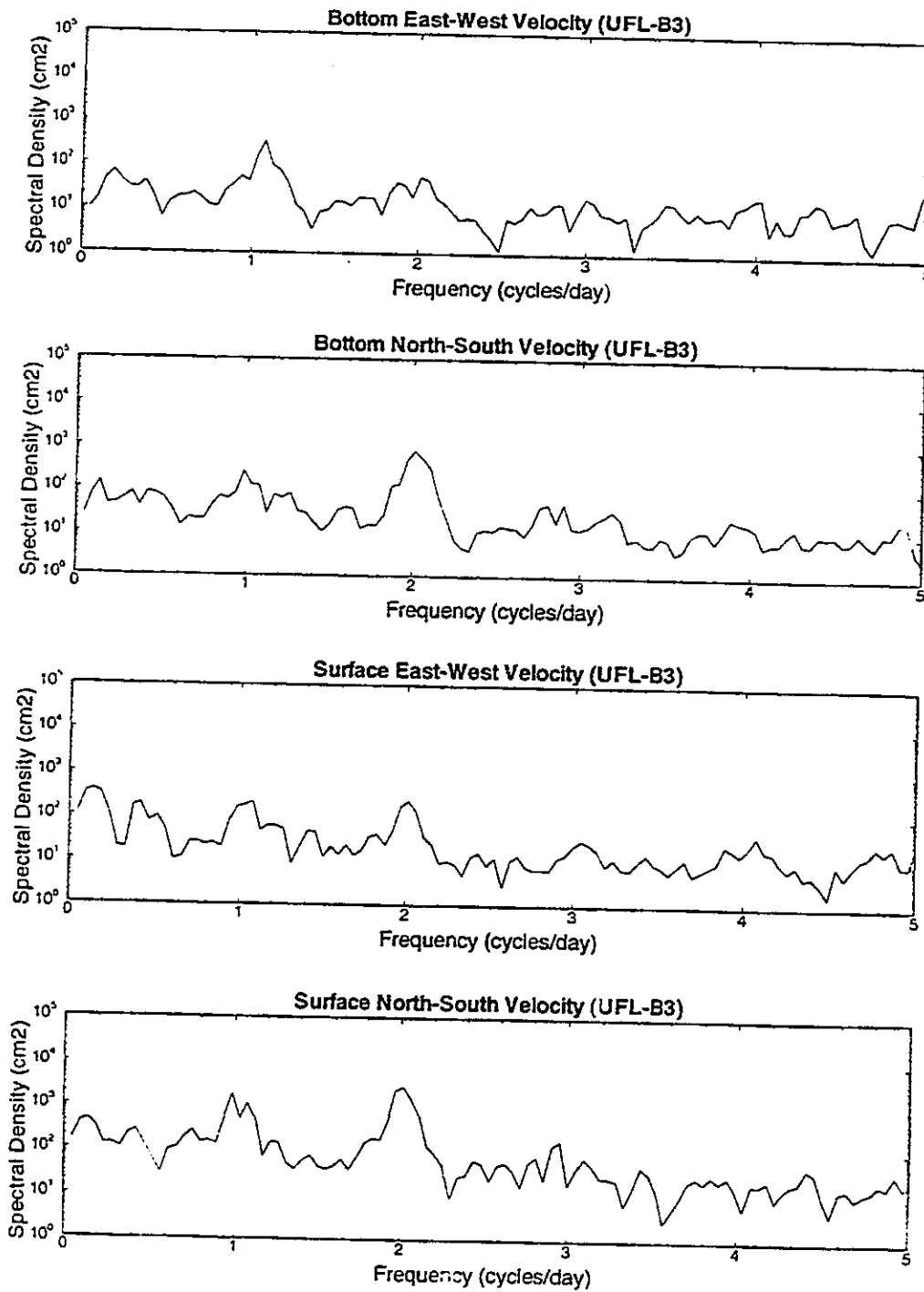
Figure B.31: The Spectral Density versus Frequency for the Surface and Bottom Current Vector Components at the UFL-B3 Station for Julian Days 200 to 260, 1991
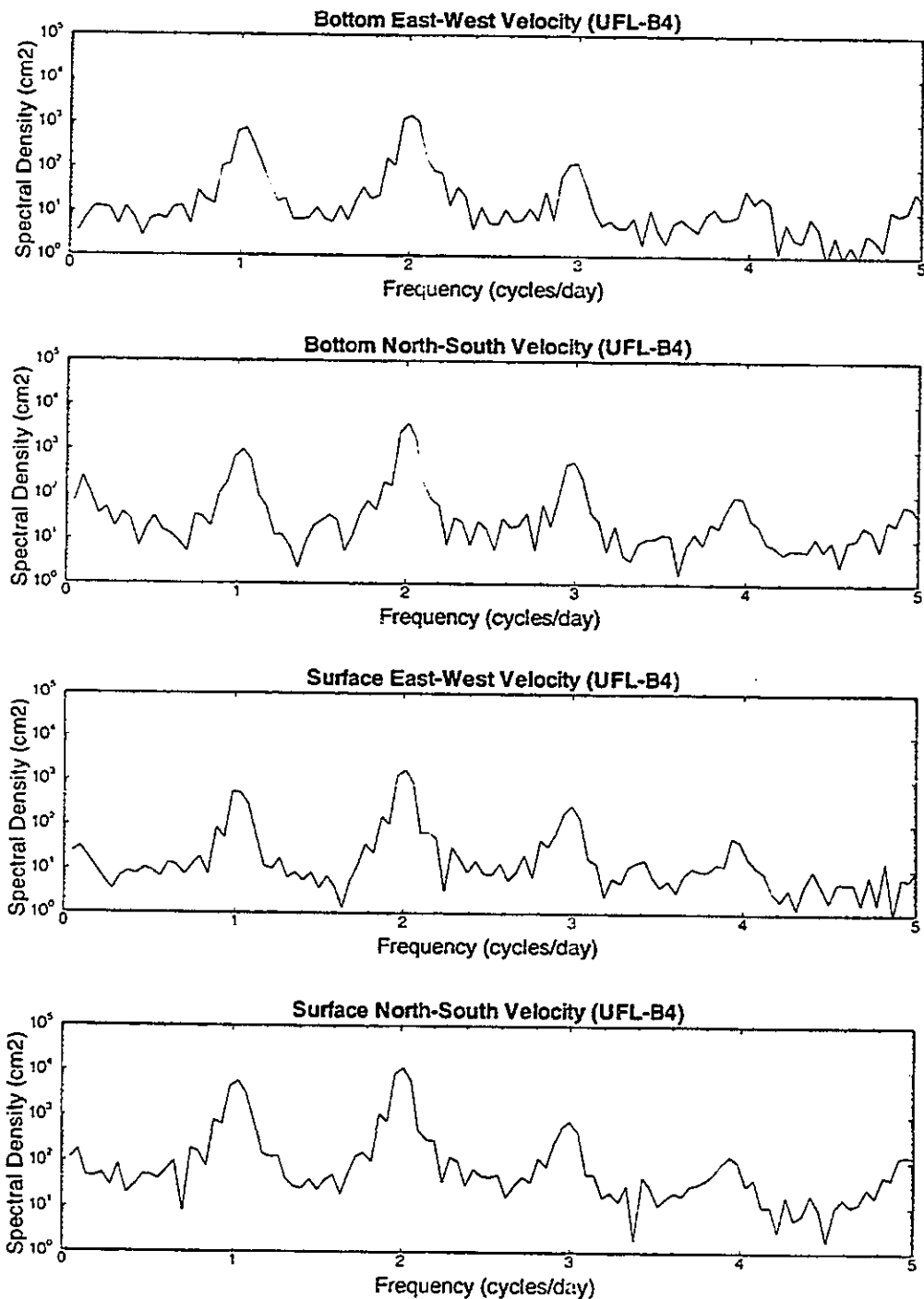
Figure B.32: The Spectral Density versus Frequency for the Surface and Bottom Current Vector Components at the UFL-B4 Station for Julian Days 200 to 260, 1991
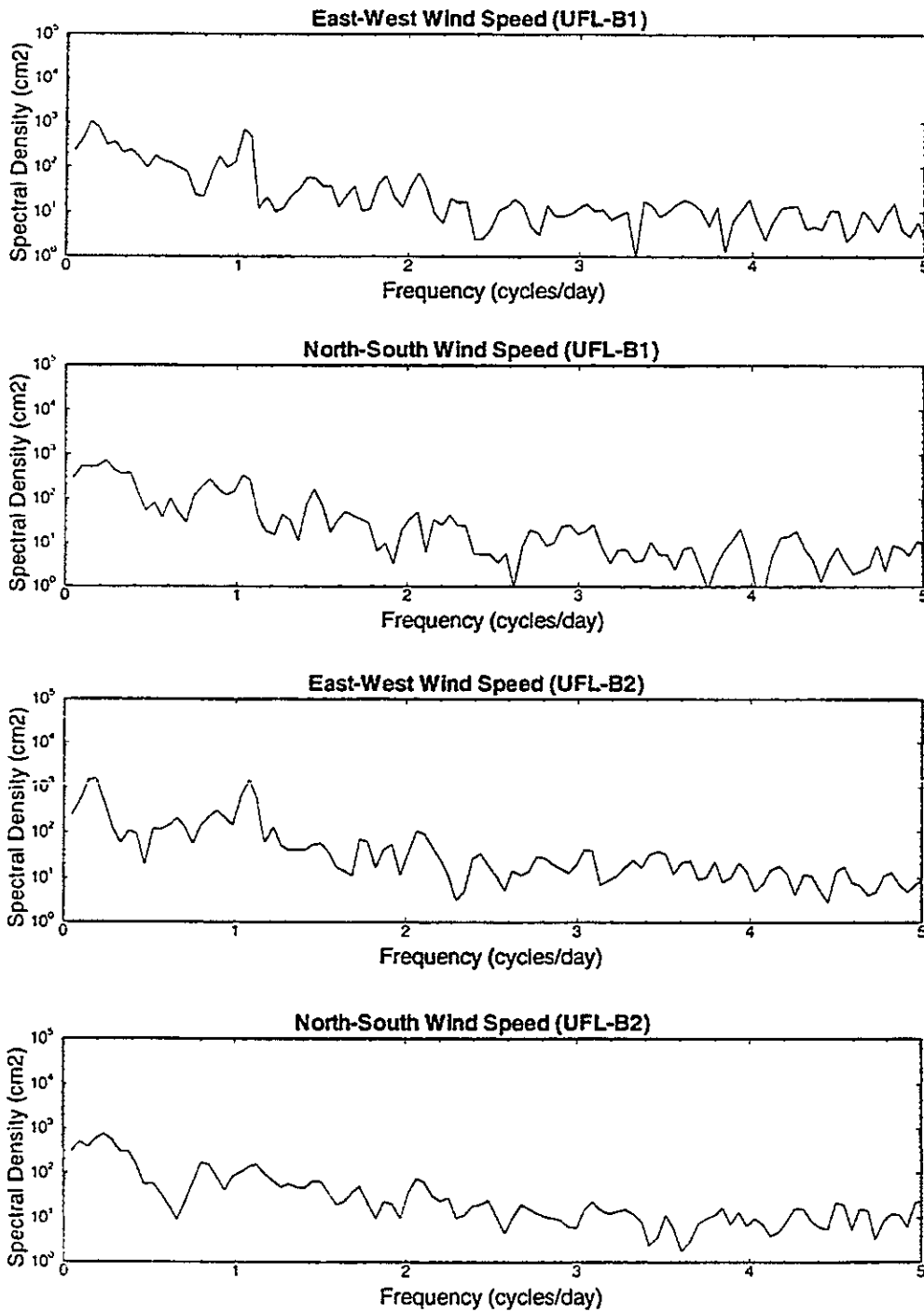
Figure B.33: The Spectral Density versus Frequency for the Wind Speed Components at the UFL-B1 and UFL-B2 Stations for Julian Days 200 to 260, 1991
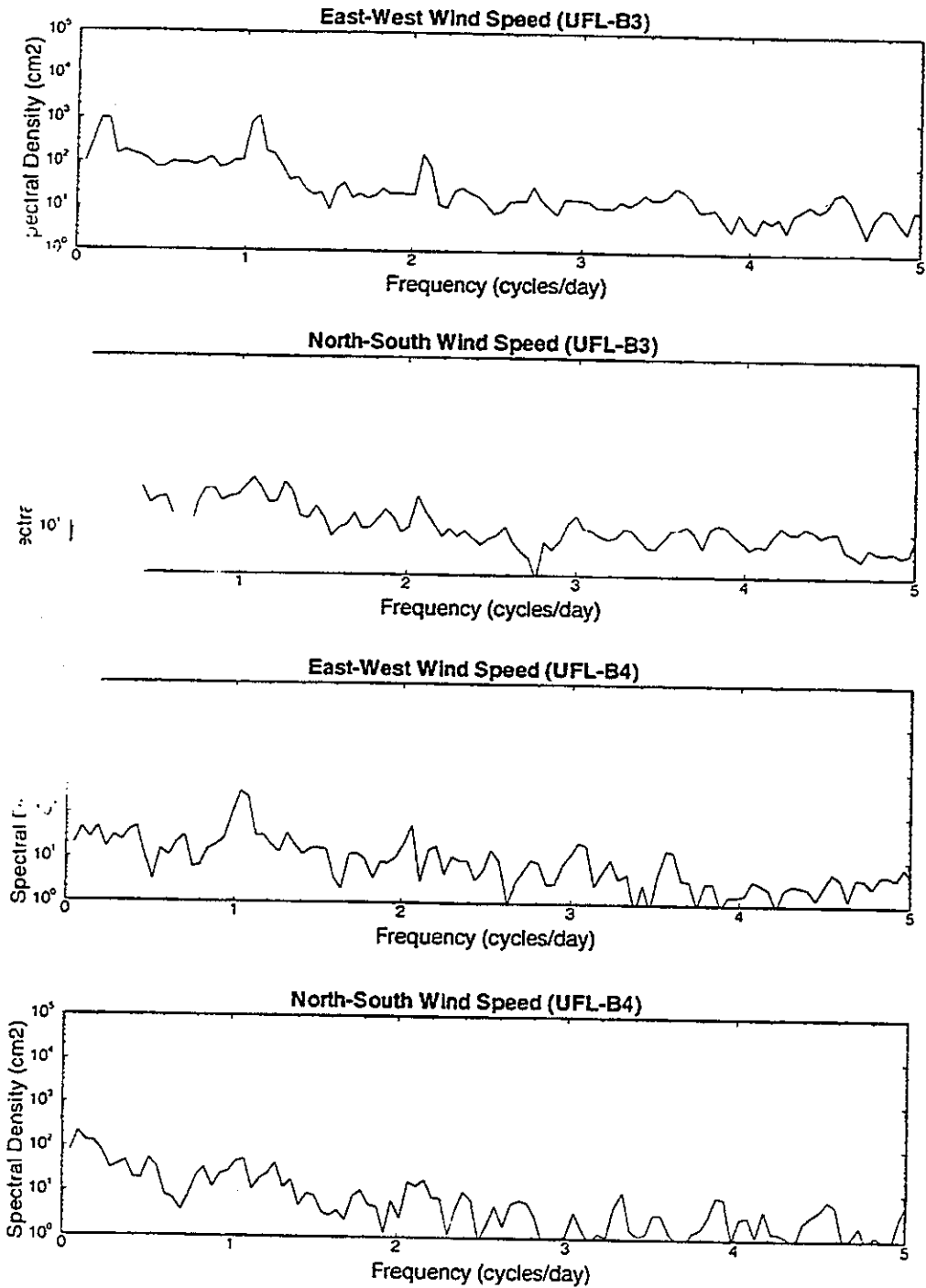
Figure B.34: The Spectral Density versus Frequency for the Wind Speed Components at the UFL-B3 and UFL-B4 Stations for Julian Days 200 to 260, 1991

APPENDIX C
NUMERICAL SOLUTION OF EQUATIONS

C.1 Introduction

Given any one differential equation, a variety of numerical techniques are available to obtain a solution. Each has its own degree of accuracy and stability, and the goal is to choose the method which will obtain the order of accuracy desired with the least complication. This appendix presents the numerical solution techniques used by the model for this study, along with the non-dimensional variables within the model and the tensor invarient equations of motion.

C.2 General Structure of Numerical Solution and Grid

The method used to solve the full three dimensional equations is divided into two parts. The first part, termed the external mode, solves the vertically integrated equations of motion and continuity (Equations 5.43, 5.44 and 5.45), over the entire computational domain simultaneously, this portion of the solution is where conservation is maintained. The second part, termed the internal mode, solves the three-dimensional equations of motion, continuity and transport (Equations 5.38, 5.39, 5.40, 5.41 and 5.42) over depth within each grid cell. The solution techniques for each part of the solution will be presented below.

Prior to attempting a finite difference solution, it is necessary to define the characteristics of the discrete grid over which the solution is obtained. As discussed in chapter 6, the computational domain is within a transformed region, the $\xi - \eta$ plane. From the transformation relationships this new coordinate system is cartesian with
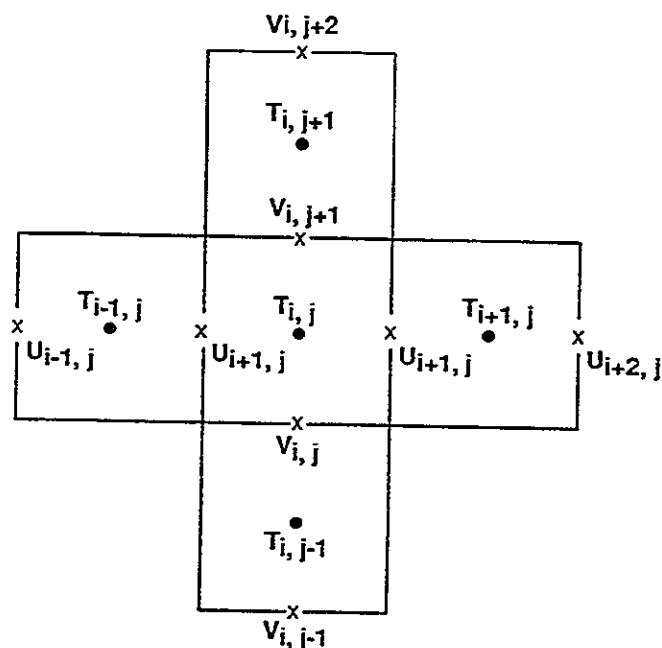
Figure C.1: An Idealized Representation of the Vertical and Horizontal Grid Structure

grids of constant width and depth of value 1. This makes the finite difference solutions fairly simple. Given the nature of the equations of motion and transport, the most logical choice of the grid structure is a staggard grid as shown in Figure C.1, where the scalar quantities such as salinity, water surface elevation, temperature, density, etc. are calculated at the center of the cell (called the ζ node), and the vector quantities are calculated at the sides of the cell (called the u and v nodes). The contravarient velocity components are orthogonal to the local grid lines therefore the contravarient u and v velocities are solved at different sides of the cell. The vertical structure is similar with the Sigma-Stretched vertical velocity ω calculated at the top and bottom of the cell. The advantage of this method is that the spacial derivatives of the velocities are calculated at the ζ node and the spacial derivatives of the scalar quantities are calculated at the u and v nodes thus leading to central differences for each with an order of accuracy of $\Delta\xi^2$.

C.3 Alternating Direction Implicit Solution for the External Mode

Equations 5.43, 5.44 and 5.45 can be rewritten in short form as,

$$\frac{\partial \zeta}{\partial t} + \frac{\beta}{\sqrt{g_o}}\frac{\partial}{\partial \xi}(\sqrt{g_o}U) + \frac{\beta}{\sqrt{g_o}}\frac{\partial}{\partial \eta}(\sqrt{g_o}V) = 0 \tag{C.1}$$

$$\frac{\partial U}{\partial t} + Hg^{11}\frac{\partial \zeta}{\partial \xi} + M_x = 0 \tag{C.2}$$

$$\frac{\partial V}{\partial t} + Hg^{22}\frac{\partial \zeta}{\partial \eta} + M_y = 0 \tag{C.3}$$

where M_x and M_y contain all the terms in the x-direction and y-direction equations of motion which are not shown; the continuity equation is represented fully. The terms which are left in the equations of motion are the time derivatives and the surface slope terms. Multiplying equations C.2 and C.3 by $\sqrt{g_o}$ and rearranging, the equations can be written in matrix form as,

$$W_t + AW_\xi + BW_\eta + M = 0 \tag{C.4}$$

where the matrices and vectors in the equation are,

$$W = \begin{pmatrix} \zeta \\ \sqrt{g_o}U \\ \sqrt{g_o}V \end{pmatrix} \quad A = \begin{pmatrix} 0 & \frac{\beta}{\sqrt{g_o}} & 0 \\ H\sqrt{g_o}g^{11} & 0 & 0 \\ 0 & 0 & 0 \end{pmatrix}$$

$$M = \begin{pmatrix} 0 \\ \sqrt{g_o}M_x \\ \sqrt{g_o}M_x \end{pmatrix} \quad B = \begin{pmatrix} 0 & 0 & \frac{\beta}{\sqrt{g_o}} \\ 0 & 0 & 0 \\ H\sqrt{g_o}g^{22} & 0 & 0 \end{pmatrix}$$

Applying a forward difference to the time derivative in equation C.4, and a central difference to the spacial derivatives gives,

$$\frac{1}{\Delta t}\left(W^{n+1} - W^n\right) + A\delta_\xi\left(\Theta W^{n+1} + (1 - \Theta)W^n\right) \tag{C.5}$$

$$+ B\delta_\eta\left(\Theta W^{n+1} + (1 - \Theta)W^n\right) + M^n = 0$$

where δ is the central space difference operator, and the superscripts indica te the time level. The variable Θ is put into the formulation to allow the solution to be performed in either fully implicit mode, $\Theta = 1$, semi-implicit mode, $1 > \Theta > 0$ or

fully explicit mode, $\Theta = 0$. Many terms are included in the M vector, these are all treated explicitly in the solution.

The ADI solution method splits equation C.5 into two parts and solves for each in separate steps called sweeps. Prior to splitting the equation, terms of similar time level are grouped together such that,

$$W^{n+1}\left(1 + \Theta\lambda_\xi + \Theta\lambda_\eta\right) = W^n\left(1 - (1 - \Theta)\lambda_\xi - (1 - \Theta)\lambda_\eta\right) = \Delta t M^n \qquad \text{(C.6)}$$

The variable λ is a new form of the central difference operator and is defined as, $\lambda_\xi = \Delta t A \delta_\xi$ and $\lambda_\eta = \Delta t B \delta_\eta$. A constant of factorization $\Theta^2 \lambda_\xi \lambda_\eta (W^{n+1} - W^n)$ is added to equation C.6. The addition of this constant does not significantly affect the solution because a forward time difference has a truncation error on the order of Δt^2, which is also the order of the factorization constant. Making this substitution and rearranging allows the equation to be split into two parts,

$$W^* + \Theta\lambda_\xi W^* = W^n - (1 - \Theta)\lambda_\xi W^n - \lambda_\eta W^n - \Delta t M^n \qquad \text{(C.7)}$$
$$W^{n+1} + \Theta\lambda_\eta W^{n+1} = W^* + W^n \Theta\lambda_\eta$$

The first equation termed the ξ-sweep solves for the variables in the W vector at an intermediate time $*$. It is termed the ξ-sweep because only the spacial derivatives in the ξ direction are treated implicitly. The second equation termed the η-sweep solves for the variables at the desired time step $n + 1$ using the results from the solution at the intermediate step. Expanding out the matrix terms gives the detailed finite difference equations which are solved in the External Mode.

$$
\begin{aligned}
\zeta_{i,j}^* + \frac{\Theta\Delta t\beta}{\sqrt{g_o}}\left(\sqrt{g_o}U_{i+1,j}^* - \sqrt{g_o}U_{i,j}^*\right) = {} & \zeta_{i,j}^n \qquad\qquad\qquad\qquad\qquad \text{(C.8)} \\
& - \frac{(1 - \Theta)\Delta t\beta}{\sqrt{g_o}}\left(\sqrt{g_o}U_{i+1,j}^n - \sqrt{g_o}U_{i,j}^n\right) \\
& - \frac{\Delta t\beta}{\sqrt{g_o}}\left(\sqrt{g_o}V_{i,j+1}^n - \sqrt{g_o}V_{i,j}^n\right)
\end{aligned}
$$

$$U_{i,j}^{\tilde{}} + \Theta \Delta t H_{i,j} g^{11} \left(\zeta_{i+1,j}^{\tilde{}} - \zeta_{i,j}^{\tilde{}} \right) \;=\; U_{i,j}^n \tag{C.9}$$

$$-\; (1 - \Theta) \Delta t H_{i,j} g^{11} \left(\zeta_{i+1,j}^n - \zeta_{i,j}^n \right)$$

$$-\; \Delta t M_{\xi_{i,j}}^n$$

$$V_{i,j}^{\tilde{}} \;=\; V_{i,j}^n \tag{C.10}$$

$$-\; \Delta t H_{i,j} g^{22} \left(\zeta_{i,j+1}^n - \zeta_{i,j}^n \right) - \Delta t M_{\eta_{i,j}}^n$$

the ξ-sweep equations and,

$$\zeta_{n+1}^{i,j} + \frac{\Theta \Delta t \beta}{\sqrt{g_o}} \left(\sqrt{g_o} V_{i,j+1}^{n+1} - \sqrt{g_o} V_{i,j}^{n+1} \right) \;=\; \zeta_{i,j}^{\tilde{}} \tag{C.11}$$

$$+\; \frac{\Theta \Delta t \beta}{\sqrt{g_o}} \left(\sqrt{g_o} V_{i,j+1}^n - \sqrt{g_o} V_{i,j}^n \right)$$

$$U_{i,j}^{n+1} \;=\; U_{i,j}^{\tilde{}} \tag{C.12}$$

$$V_{i,j}^{n+1} + \Theta \Delta t H_{i,j} g^{22} \left(\zeta_{i,j+1}^{n+1} - \zeta_{i,j}^{n+1} \right) \;=\; V_{i,j}^{\tilde{}} \tag{C.13}$$

$$+\; \Theta \Delta t H_{i,j} g^{22} \left(\zeta_{i,j+1}^n - \zeta_{i,j}^n \right)$$

the η-sweep equations. By substituting the equation for $V^{\tilde{}}$ from the ξ sweep into the last equation in the η- sweep, each is reduced to 2 equations with two unknowns, $\zeta^{\tilde{}}$ and $U^{\tilde{}}$ in the ξ-direction, and ζ^{n+1} and V^{n+1} in the η-direction. Rewriting the equations back into matrix form leads to the solution of a tridiagonal matrix equation of the form,

$$
\begin{pmatrix}
c_1 & a_1 & & & & & & \\
b_2' & c_2' & a_2' & & & & & \\
& & \cdot & & & & & \\
& & & b_i' & c_i' & a_i' & & \\
& & & & b_i & c_i & a_i & \\
& & & & & \cdot & & \\
& & & & & & b_{n-1}' & c_{n-1}' & a_{n-1}' \\
& & & & & & & b_n & c_n
\end{pmatrix}
\begin{pmatrix}
\zeta_{1,j}^{\tilde{}} \\
U_{2,j}^{\tilde{}} \\
\cdot \\
\cdot \\
U_{i,j}^{\tilde{}} \\
\zeta_{i,j}^{\tilde{}} \\
\cdot \\
U_{n-1,j}^{\tilde{}} \\
\zeta_{n,j}^{\tilde{}}
\end{pmatrix}
=
\begin{pmatrix}
d_1 \\
d_1' \\
\cdot \\
\cdot \\
d_i' \\
d_i \\
\cdot \\
d_{n-1}' \\
d_n
\end{pmatrix}
\tag{C.14}
$$

for the ξ-sweep and,

$$\begin{pmatrix} c_1 & a_1 & & & & & \\ b_2' & c_2' & a_2' & & & & \\ & & \cdot & & & & \\ & & & \cdot & & & \\ & & b_j' & c_j' & a_j' & & \\ & & & b_j & c_j & a_j & \\ & & & & \cdot & & \\ & & & & b_{m-1}' & c_{m-1}' & a_{m-1}' \\ & & & & & b_m & c_m \end{pmatrix} \begin{pmatrix} \zeta_{i,1}^{n+1} \\ V_{i,2}^{n+1} \\ \cdot \\ \cdot \\ V_{i,j}^{n+1} \\ \zeta_{i,j}^{n+1} \\ \cdot \\ V_{i,n-1}^{n+1} \\ \zeta_{i,n}^{n+1} \end{pmatrix} = \begin{pmatrix} d_1 \\ d_1' \\ \cdot \\ \cdot \\ d_j' \\ d_j \\ \cdot \\ d_{m-1}' \\ d_m \end{pmatrix} \qquad (C.15)$$

for the η sweep.

The tridiagonal nature of the matrix makes numerical solution simple through the use of Gaussian Elimination algorithms. This type of a matrix solution is much more computationally efficient as compared with having to invert a complete matrix. This is one of the benefits of the ADI solution technique.

The advantage of allowing the surface slope terms to be treated implicitly is that the limitation on the time step, imposed by the courant condition ($\Delta t < \frac{\Delta x}{\sqrt{gH}}$), is removed. For this study the grid spacing varied from 1 kilometer down to 30 meters over the computational domain, therefore, if the model were purely explicit, the time step limitation imposed by the Courant condition would have made the cpu time excessive.

C.4   Internal Mode Solution

The next step after solving the shallow water wave equations is to solve for the three-dimensional deficit velocity components $\tilde{u}$ and $\tilde{v}$. These are defined by subtracting the vertically integrated velocities from the three-dimensional velocities,

$$\tilde{u} = u - \frac{U}{H} \qquad (C.16)$$

$$\tilde{v} = v - \frac{V}{H} \qquad (C.17)$$

The equations of motion for the deficit velocity can be obtained in a similar manner by multiplying the three-dimensional equations 5.39 and 5.40 by H and subtracting

the Shallow water equations 5.44 and 5.45 to give,

$$\frac{\partial \tilde{u} H}{\partial t} - \frac{E_v}{H}\frac{\partial}{\partial \sigma}\left(A_v \frac{\partial u}{\partial \sigma}\right) = \frac{g_{12}}{\sqrt{g_o}}Hu - \frac{g_{12}}{\sqrt{g_o}}U + \frac{g_{22}}{\sqrt{g_o}}Hv - \frac{g_{22}}{\sqrt{g_o}}V \qquad (C.18)$$

$$- \tau_{s_\xi} + \tau_{b_\xi} - R_o\left[(\xi\text{-dir. inertia}) - \int_{-1}^{0}(\xi\text{-dir. inertia})d\sigma\right]$$

$$- \frac{R_o}{F_{r^2}}\left[(\xi\text{-dir. baroclinic}) - \int_{-1}^{0}(\xi\text{-dir. baroclinic})d\sigma\right]$$

$$- E_h A_h\left[(\xi\text{-dir. horizontal diffusion}) - \int_{-1}^{0}(\xi\text{-dir. horizontal diffusion})d\sigma\right]$$

$$\frac{\partial \tilde{v} H}{\partial t} - \frac{E_v}{H}\frac{\partial}{\partial \sigma}\left(A_v \frac{\partial v}{\partial \sigma}\right) = \frac{g_{11}}{\sqrt{g_o}}Hu - \frac{g_{11}}{\sqrt{g_o}}U + \frac{g_{21}}{\sqrt{g_o}}Hv - \frac{g_{21}}{\sqrt{g_o}}V \qquad (C.19)$$

$$- \tau_{s_\eta} + \tau_{b_\eta} - R_o\left[(\eta\text{-dir. inertia}) - \int_{-1}^{0}(\eta\text{-dir. inertia})d\sigma\right]$$

$$- \frac{R_o}{F_{r^2}}\left[(\eta\text{-dir. baroclinic}) - \int_{-1}^{0}(\eta\text{-dir. baroclinic})d\sigma\right]$$

$$- E_h A_h\left[(\eta\text{-dir. horizontal diffusion}) - \int_{-1}^{0}(\eta\text{-dir. horizontal diffusion})d\sigma\right]$$

Once again all the terms on the right hand side of the equations are lumped into the single terms $\hat{M}_x$ and $\hat{M}_y$. Also the diffusion terms on the left hand side of the equations do not contain the deficit velocities, this is because the vertical integration of the diffusion produces the surface and bottom stresses shown in the 2-Dimensional equations. Incorporating the definition of the deficit velocity and the lumped terms, equations C.18 and C.19 can be rewritten as,

$$\frac{\partial \tilde{u} H}{\partial t} - \frac{E_v}{H}\frac{\partial}{\partial \sigma}\left(A_v \frac{\partial}{\partial \sigma}(\tilde{u} + \frac{U}{H})\right) = \hat{M}_x \qquad (C.20)$$

$$\frac{\partial \tilde{v} H}{\partial t} - \frac{E_v}{H}\frac{\partial}{\partial \sigma}\left(A_v \frac{\partial}{\partial \sigma}(\tilde{v} + \frac{V}{H})\right) = \hat{M}_y \qquad (C.21)$$

The numerical solution of these equations treats the time derivatives and the vertical diffusion terms implicitly in order to avoid instability. The vertically integrated velocities have already been solved for at the $n + 1$ time level and they are knowns in the equations. The terms contained in $\hat{M}_x$ and $\hat{M}_y$ are taken at the n time level. Applying a forward time difference on the time derivative and a central space difference

on the diffusion terms gives,

$$\tilde{u}_{i,j,k}^{n+1} - \frac{E_v}{(H_{i,j}^{n+1})^2} \frac{\Delta t}{\Delta \sigma_{i,j,k}} \left(A_v \frac{(\tilde{u}_{i,j,k+1}^{n+1} - \tilde{u}_{i,j,k}^{n+1})}{\Delta \sigma_{i,j,k+\frac{1}{2}}} - A_v \frac{(\tilde{u}_{i,j,k}^{n+1} - \tilde{u}_{i,j,k-1}^{n+1})}{\Delta \sigma_{i,j,k-\frac{1}{2}}} \right) \quad (C.22)$$

$$= \frac{\tilde{u}_{i,j,k}^{n+1} H_{i,j}^{n+1}}{H_{i,j}^{n+1}} + \frac{\Delta t}{H_{i,j}^{n+1}} M_{x_{i,j,k}}^{\hat{n}}$$

$$\tilde{v}_{i,j,k}^{n+1} - \frac{E_v}{(H_{i,j}^{n+1})^2} \frac{\Delta t}{\Delta \sigma_{i,j,k}} \left(A_v \frac{(\tilde{v}_{i,j,k+1}^{n+1} - \tilde{v}_{i,j,k}^{n+1})}{\Delta \sigma_{i,j,k+\frac{1}{2}}} - A_v \frac{(\tilde{v}_{i,j,k}^{n+1} - \tilde{v}_{i,j,k-1}^{n+1})}{\Delta \sigma_{i,j,k-\frac{1}{2}}} \right) \quad (C.23)$$

$$= \frac{\tilde{v}_{i,j,k}^{n+1} H_{i,j}^{n+1}}{H_{i,j}^{n+1}} + \frac{\Delta t}{H_{i,j}^{n+1}} M_{y_{i,j,k}}^{\hat{n}}$$

These equations can be written in matrix form as was done for the ADI solution. In the case of the deficit velocities the solution is performed over the vertical within a single horizontal cell. The equations are of the form.

$$\begin{pmatrix} c_1 & a_1 & & & & & & \\ b_2 & c_2 & a_2 & & & & & \\ & & \cdot & & & & & \\ & & \cdot & & & & & \\ & b_{k-1} & c_{k-1} & a_{k-1} & & & & \\ & & b_k & c_k & a_k & & & \\ & & & b_{k+1} & c_{k+1} & d_{k+1} & & \\ & & & & \cdot & & & \\ & & & & \cdot & & & \\ & & & & b_{km-1} & c_{km-1} & a_{km-1} & \\ & & & & & b_{km} & c_{km} \end{pmatrix} \begin{pmatrix} \tilde{u}_{i,j,1}^{n+1} \\ \tilde{u}_{i,j,2}^{n+1} \\ \cdot \\ \cdot \\ \tilde{u}_{i,j,k-1}^{n+1} \\ \tilde{u}_{i,j,k}^{n+1} \\ \tilde{u}_{i,j,k+1}^{n+1} \\ \cdot \\ \cdot \\ \tilde{u}_{i,j,km-1}^{n+1} \\ \tilde{u}_{i,j,km}^{n+1} \end{pmatrix} = \begin{pmatrix} d_1 \\ d_2 \\ \cdot \\ \cdot \\ d_{k-1} \\ d_k \\ d_{k+1} \\ \cdot \\ \cdot \\ d_{km-1} \\ d_{km} \end{pmatrix} \quad (C.24)$$

Once again the matrix is tridiagonal and the solutions are computationally efficient.

Once the solution for the deficit velocities is obtained over the entire domain it is neccesary to insure conservation by summing the deficit velocities over the depth. For conservation to be maintained, the sum must be equal to zero. If the sum is not zero, a fix is made on the deficit velocities. Once the corrected solution is obtained, the complete 3-Dimensional velocities are calculated from equations C.16 and C.17.

C.5   Calculation of Vertical Velocities

Thus far only the three-dimensional momentum equations have been solved. The calculation of the vertical velocities completes the solution by using the three-

dimensional continuity equation. 5.38. Applying the forward time difference on the surface slope term and a central time difference on the velocity gradients the finite difference form of the continuity equation can be derived. The equation is presented as a solution of the vertical velocity ω.

$$
\begin{aligned}
\omega_{i,j,k}^{n+1} = \omega_{i,j,k-1}^{n+1} \quad &- \quad \frac{\Delta\sigma}{\beta H_{i,j}^{n+1}} \frac{\zeta_{i,j}^{n+1} - \zeta_{i,j}^{n}}{\Delta t} \\
&- \quad \frac{1}{\sqrt{g_o}H_{i,j}^{n+1}} \left((\sqrt{g_o}Hu)_{i+1,j,k}^{n+1} - (\sqrt{g_o}Hu)_{i,j,k}^{n+1} \right) \\
&+ \quad \left((\sqrt{g_o}Hv)_{i,j+1,k}^{n+1} - (\sqrt{g_o}Hv)_{i,j,k}^{n+1} \right)
\end{aligned} \tag{C.25}
$$

In this equation all the u and v terms at the $n+1$ time level are known from previous solutions. The $\omega_{i,j,k-1}^{n+1}$ value in the bottom cell is equal to zero from the boundary conditions, therefore a solution for each of the vertical velocities can be obtained by stepping the solution from the bottom cell to the surface, in each case the vertical velocities for the next cell up have been calculated from the solution of the cell below.

C.6 Finite Difference Solution of Advection-Diffusion Equations

The finite difference solution of the advection-diffusion equations for salinity and temperature follow closely the method used for the internal mode solution. The time derivatives and the vertical diffusion terms are treated implicitly with the horizontal diffusion and the advection terms treated explicitly. Applying the finite difference techniques to equation 5.41 and grouping the explicit terms gives,

$$
\begin{aligned}
H_{i,j}^{n+1} S_{i,j,k}^{n+1} \quad &- \quad \frac{\Delta t E_v}{H_{i,j}^{n+1} S_{c_v}} \frac{1}{\Delta\sigma_{i,j,k}} \frac{D_v}{\Delta\sigma_{i,j,k+\frac{1}{2}}} \left(S_{i,j,k+1}^{n+1} - S_{i,j,k}^{n+1} \right) \\
&- \quad \frac{D_v}{\Delta\sigma_{i,j,k-\frac{1}{2}}} \left(S_{i,j,k}^{n+1} - S_{i,j,k-1}^{n+1} \right) = H_{i,j}^{n} S_{i,j,k}^{n} + \Delta t N_{i,j,k}^{n}
\end{aligned} \tag{C.26}
$$

where $N_{i,j,k}^{n}$ are the advection and horizontal diffusion terms treated at the n time level. This formulation once again leads to a tridiagonal matrix solution as in the internal mode.

Generally the transport processes within an estuarine system are dominated by turbulent diffusion in the vertical direction and advection in the horizontal. For this reason the choice of the finite difference scheme is important in resolving the advective processes. Within this study a number of numerical advective schemes were employed to try and determine which gave the optimum solution. The following presents the methods tested.

One of the most basic transport schemes is the upwind method. This method takes advantage of the concept that velocity moving out of a cell will tend to transport concentrations equal to the cell concentration. From equation 5.41 the finite difference form for the advection can be written,

$$
\begin{aligned}
\frac{\partial}{\partial \xi} \left(\sqrt{g_o} H u S \right) \;=\; & \frac{1}{2} \left(u_{i+1,j,k} - |u_{i+1,j,k}| \right) S_{i+1,j,k} \\
+ \; & \frac{1}{2} \left(u_{i+1,j,k} + |u_{i+1,j,k}| \right) S_{i,j,k} \sqrt{g_o} H_{i+1,j} \\
- \; & \frac{1}{2} \left(u_{i,j,k} - |u_{i,j,k}| \right) S_{i,j,k} \\
+ \; & \frac{1}{2} \left(u_{i,j,k} + |u_{i,j,k}| \right) S_{i+1,j,k} \sqrt{g_o} H_{i,j}
\end{aligned}
\qquad \text{(C.27)}
$$

This scheme can have problems in maintaining conservation, therefore a modified version was proposed. When the concentration in the upwind cell is greater than the concentration in the downwind cell the transported value is an average of the two values, otherwise the standard upwind applies. This method eliminates some of the non-conservative properties of the basic upwind method.

Both methods described above have numerical diffusion which can tend to smooth out discontinuities within the concentration fields. This can be a problem if advection greatly dominates over diffusion in the physical domain. Additional numerical diffusion can contaminate the solution and reduce accuracy.

A number of higher order advection schemes have been developed to try and reduce the smoothing of discontinuities and give a more realistic representation. One such method is an Adjusted Quadratic Upstream Algorithm or QUICKEST scheme

(Leonard, 1979). This method is a third order accurate scheme which uses cubic upstream-weighted interpolation through the points i-2, i-1, i, i+1 and i+2, along the direction of interest. Because this is a five point interpolation the fluxes near boundaries must be calculated using lower order schemes such as the ones described above.

The finite difference equations for the advection derived using the QUICKEST scheme are,

$$
\begin{aligned}
\frac{\partial}{\partial \xi}\left(HuS\sqrt{g_o}\right) =\ & \left(u_{i+1,j,k} - |u_{i+1,j,k}|\right)\frac{1}{2}\left(S_{i,j,k} + S_{i+1,j,k}\right) \\
& - \frac{1}{6}\left(1 - (u_{i+1,j,k}\Delta t)^2\right)\left(S_{i+2,j,k} - 2S_{i+1,j,k} + S_{i,j,k}\right) \\
& - \frac{1}{2}u_{i+1,j,k}\Delta t\left(S_{i+1,j,k} - S_{i,j,k}\right) \\
& + \left(u_{i+1,j,k} + |u_{i+1,j,k}|\right)\frac{1}{2}\left(S_{i,j,k} + S_{i+1,j,k}\right) \\
& - \frac{1}{6}\left(1 - (u_{i+1,j,k}\Delta t)^2\right)\left(S_{i+1,j,k} - 2S_{i,j,k} + S_{i-1,j,k}\right) \\
& - \frac{1}{2}u_{i+1,j,k}\Delta t\left(S_{i+1,j,k} - S_{i,j,k}\right)\frac{1}{2}\sqrt{g_{o_{i+1,j,U}}}H_{i+1,j,U} \\
& - \left(u_{i,j,k} - |u_{i,j,k}|\right)\frac{1}{2}\left(S_{i-1,j,k} + S_{i,j,k}\right) \\
& - \frac{1}{6}\left(1 - (u_{i,j,k}\Delta t)^2\right)\left(S_{i+1,j,k} - 2S_{i,j,k} + S_{i-1,j,k}\right) \\
& - \frac{1}{2}u_{i,j,k}\Delta t\left(S_{i,j,k} - S_{i-1,j,k}\right) \\
& + \left(u_{i,j,k} + |u_{i,j,k}|\right)\frac{1}{2}\left(S_{i-1,j,k} + S_{i,j,k}\right) \\
& - \frac{1}{6}\left(1 - (u_{i,j,k}\Delta t)^2\right)\left(S_{i,j,k} - 2S_{i-1,j,k} + S_{i-2,j,k}\right) \\
& - \frac{1}{2}u_{i,j,k}\Delta t\left(S_{i,j,k} - S_{i-1,j,k}\right)\frac{1}{2}\sqrt{g_{o_{i,j,U}}}H_{i,j,U}\frac{1}{\sqrt{g_{o_{i,j,\zeta}}}H_{i,j,\zeta}}
\end{aligned}
$$

(C.28)

(C.29)

in the ξ-direction, and;

$$
\begin{aligned}
\frac{\partial}{\partial \xi}\left(HvS\sqrt{g_o}\right) =\ & \left(v_{i+1,j,k} - |v_{i+1,j,k}|\right)\frac{1}{2}\left(S_{i,j,k} + S_{i+1,j,k}\right) \\
& - \frac{1}{6}\left(1 - (v_{i+1,j,k}\Delta t)^2\right)\left(S_{i+2,j,k} - 2S_{i+1,j,k} + S_{i,j,k}\right) \\
& - \frac{1}{2}v_{i+1,j,k}\Delta t\left(S_{i+1,j,k} - S_{i,j,k}\right) \\
& + \left(v_{i+1,j,k} + |v_{i+1,j,k}|\right)\frac{1}{2}\left(S_{i,j,k} + S_{i+1,j,k}\right)
\end{aligned}
$$

(C.30)

$$- \ \frac{1}{6} \left(1 - (v_{i+1,j,k}\Delta t)^2\right) \left(S_{i+1,j,k} - 2S_{i,j,k} + S_{i-1,j,k}\right)$$

$$- \ \frac{1}{2}v_{i+1,j,k}\Delta t \left(S_{i+1,j,k} - S_{i,j,k}\right)\frac{1}{2}\sqrt{g_{o_{i+1,j},v}}H_{i+1,j,V}$$

$$- \ (v_{i,j,k} - |v_{i,j,k}|)\frac{1}{2}\left(S_{i-1,j,k} + S_{i,j,k}\right)$$

$$- \ \frac{1}{6}\left(1 - (v_{i,j,k}\Delta t)^2\right)\left(S_{i+1,j,k} - 2S_{i,j,k} + S_{i-1,j,k}\right)$$

$$- \ \frac{1}{2}v_{i,j,k}\Delta t \left(S_{i,j,k} - S_{i-1,j,k}\right) \hspace{2cm} \text{(C.31)}$$

$$+ \ (v_{i,j,k} + |v_{i,j,k}|)\frac{1}{2}\left(S_{i-1,j,k} + S_{i,j,k}\right)$$

$$- \ \frac{1}{6}\left(1 - (v_{i,j,k}\Delta t)^2\right)\left(S_{i,j,k} - 2S_{i-1,j,k} + S_{i-2,j,k}\right)$$

$$- \ \frac{1}{2}v_{i,j,k}\Delta t \left(S_{i,j,k} - S_{i-1,j,k}\right)\frac{1}{2}\sqrt{g_{o_{i,j},v}}H_{i,j,V}\frac{1}{\sqrt{g_{o_{i,j},\zeta}}H_{i,j,\zeta}}$$

in the η direction. It is clear that additional computational time is required to utilize the higher order schemes.

The horizontal diffusion second derivative terms in the ξ and η directions use a simple three point finite difference approximation which is of order accuracy $\Delta\xi^2$. The equations are;

$$\frac{\partial^2 HS}{\partial\xi^2} \ = \ H^n_{i+1,j,\zeta}S^n_{i+1,j,k} - 2.0H^n_{i,j,\zeta}S^n_{i,j,k} + H^n_{i-1,j,\zeta}S^n_{i-1,j,k}$$

$$\frac{\partial^2 HS}{\partial\eta^2} \ = \ H^n_{i,j+1,\zeta}S^n_{i,j+1,k} - 2.0H^n_{i,j,\zeta}S^n_{i,j,k} + H^n_{i,j-1,\zeta}S^n_{i,j-1,k}$$

The cross derivative term uses a four point averaging to get the salinity at the corner points of the cell, the cross derivative is then evaluated from those averages. The finite difference equation is.

$$\frac{\partial^2 HS}{\partial\xi\partial\eta} \ = \ \frac{1}{4}(S^n_{i,j,k}H^n_{i,j,\zeta} + S^n_{i,j+1,k}H^n_{i,j+1,\zeta} + S^n_{i+1,j+1,k}H^n_{i+1,j+1,\zeta} + S^n_{i+1,j,k}H^n_{i+1,j,\zeta})$$

$$- \ \frac{1}{4}(S^n_{i,j,k}H^n_{i,j,\zeta} + S^n_{i+1,j,k}H^n_{i+1,j,\zeta} + S^n_{i+1,j-1,k}H^n_{i+1,j-1,\zeta} + S^n_{i,j-1,k}H^n_{i,j-1,\zeta})$$

$$- \ \frac{1}{4}(S^n_{i,j,k}H^n_{i,j,\zeta} + S^n_{i-1,j,k}H^n_{i-1,j,\zeta} + S^n_{i-1,j+1,k}H^n_{i-1,j+1,\zeta} + S^n_{i,j+1,k}H^n_{i,j+1,\zeta})$$

$$+ \ \frac{1}{4}(S^n_{i,j,k}H^n_{i,j,\zeta} + S^n_{i-1,j,k}H^n_{i-1,j,\zeta} + S^n_{i-1,j-1,k}H^n_{i-1,j-1,\zeta} + S^n_{i,j-1,k}H^n_{i,j-1,\zeta})$$

C.7 The Non-Dimensional Variables and Parameters

$$x^* = \frac{x}{L}, \quad y^* = \frac{y}{L}, \quad z^* = z\frac{L}{D}\frac{1}{L}$$

$$u^* = \frac{u}{u_r}, \quad v^* = \frac{v}{u_r}, \quad w^* = \frac{w}{u_r}\frac{L}{D}$$

$$t^* = tf, \quad \zeta^* = \frac{g\zeta}{fu_rL}$$

$$\rho^* = \frac{\rho - \rho_0}{\rho_r - \rho_0}, \quad T^* = \frac{T - T_0}{T_r - T_0}$$

$$A_h^* = \frac{A_h}{A_{h_r}}, \quad D_h^* = \frac{D_h}{D_{h_r}}, \quad K_h^* = \frac{K_h}{K_{h_r}}$$

$$A_v^* = \frac{A_v}{A_{v_r}}, \quad D_v^* = \frac{D_v}{D_{v_r}}, \quad K_v^* = \frac{K_v}{K_{v_r}}$$

$$\omega^* = \omega\frac{L}{u_r}, \quad q_s^* = \frac{T_0}{(T_r - T_0)}\frac{q}{\rho_0C_pfDT_0}$$

$$\tau_x^* = \frac{\tau_x}{\rho_0fZ_ru_r}, \quad \tau_y^* = \frac{\tau_y}{\rho_0fZ_ru_r}$$

$$E_v = \frac{A_{vr}}{fZ_r^2} = \text{the vertical Eckman Number}$$

$$E_h = \frac{A_{hr}}{fX_r^2} = \text{the lateral Eckman Number}$$

$$R_o = \frac{U_r}{fX_r} = \text{the Rossby Number}$$

$$F_r = \frac{U_r}{sqrtgZ_r} = \text{the Froude Number}$$

$$S_{c_v} = \frac{A_{vr}}{D_{vr}} = \text{the vertical Schmidt Number}$$

$$S_{c_h} = \frac{A_{hr}}{D_{hr}} = \text{the lateral Schmidt Number}$$

$$P_{r_v} = \frac{A_{vr}}{K_{vr}} = \text{the vertical Prandtl Number}$$

$$P_{r_h} = \frac{A_{hr}}{K_{hr}} = \text{the horizontal Prandtl Number}$$

$$\beta = \frac{gZ_r}{f^2 X_r^2} = \text{a dimensionless parameter}$$

Each parameter has a physical meaning, and when their magnitude is evaluated, it can provide insight into the physics of the flow. The vertical and horizontal Eckman numbers are the ratio of the friction, or diffusive terms, and the corriolis terms. Therefore a large value of the Eckman number would indicate that friction effects are dominant over the corriolis forces. The Rossby number is the ratio of the non-linear terms and the corriolis forcing terms. Therefore, a small value of the Rossby number would indicate that the non-linear terms are negligible in comparison with the corriolis forces. The Schmidt and Prandtl numbers relate the turbulent eddy viscosities with the turbulent eddy diffusivities for salinity and temperature respectively. Values of unity indicate that the diffusivities are assumed equal to the eddy viscosities. The densimetric Froude number represents the ratio of the internal density driven flow with the non-linear forcing. β is the ratio of the Rossby Number with the Froude number and indicates the relative importance between the inertial and gravitational forcing.

The non-dimensional equations allow more intuitive analysis of the relative importance of the terms within the equations of motion and transport. They also give the model a greater sense of generality when applied to water bodies of different scales.

C.8 The Tensor Invarient Equations of Motion

Following the derivations presented in Sokolnikoff, the tensor invariant, 3-Dimensional equations of motion and transport can be derived in terms of the contravarient vector components. These equations are independent of the frame of reference chosen and are the more general form of the Cartesian equations presented earlier.

$$\zeta_t \; + \; \frac{\beta}{\sqrt{g_o}}\frac{\partial}{\partial x^k}(\sqrt{g_o}Hu^k) \tag{C.32}$$

$$\frac{1}{H}\frac{\partial Hu^k}{\partial t} \; = \; -\zeta^{!k} - g_{nj}\epsilon^{kj}u^n \tag{C.33}$$
$$- \; \frac{R_o}{H}\left[(Hu^l u^k)_{,l} + \frac{\partial hu^k\omega}{\partial\sigma}\right]$$
$$+ \; \frac{E_v}{H^2}\frac{\partial}{\partial\sigma}\left(A_v\frac{\partial u^k}{\partial\sigma}\right) + E_h A_h u^k_{,m}{}^{!m}$$
$$- \; \frac{R_o}{F_{r_D^2}}\left[H\int_\sigma^0 \rho^{!k}\,d\,\sigma + H^{!k}\left(\int_\sigma^0 \rho\,d\,\sigma + \sigma\,\rho\right)\right]$$

$$\frac{\partial S}{\partial t} \; + \; \frac{R_o}{H}\left[(Hu^l S)_{,l} + \frac{\partial h\omega S}{\partial\sigma}\right] \tag{C.34}$$
$$= \; \frac{E_h}{S_{c_h}}D_h S_{,m}{}^{!m} + \frac{E_v}{S_{c_v}}\frac{1}{H^2}\frac{\partial}{\partial\sigma}\left(D_v\frac{\partial S}{\partial\sigma}\right)$$

$$\frac{\partial T}{\partial t} \; + \; \frac{R_o}{H}\left[(Hu^l T)_{,l} + \frac{\partial h\omega T}{\partial\sigma}\right] \tag{C.35}$$
$$= \; \frac{E_h}{S_{c_h}}D_h T_{,m}{}^{!m} + \frac{E_v}{S_{c_v}}\frac{1}{H^2}\frac{\partial}{\partial\sigma}\left(D_v\frac{\partial T}{\partial\sigma}\right)$$

where $\frac{\partial}{\partial x^k}$ is the partial derivative, g_{ij} is the metric tensor which in two dimensions is defined as;

$$g_{ij} = \begin{pmatrix} x_\xi^2 + y_\xi^2 & x_\xi\,x_\eta + y_\xi\,y_\eta \\ x_\eta\,x_\xi + y_\eta\,y_\xi & x_\eta^2 + y_\eta^2 \end{pmatrix} = \begin{pmatrix} g_{11} & g_{12} \\ g_{21} & g_{22} \end{pmatrix} \tag{C.36}$$

g_o is the Jacobian and is equal to $x_\xi\,y_\eta - x_\eta\,y_\xi$, ϵ^{kj} is the permutation tensor such that;

$$\epsilon^{12} = -\frac{1}{\sqrt{g_o}}$$
$$\epsilon^{21} = \frac{1}{\sqrt{g_o}} \tag{C.37}$$
$$\epsilon^{11} = \epsilon^{22} = 0$$

Two other derivative operators are given in Equations C.32 through C.35, these are the covariant spatial derivative and the contravarient spatial derivative;

$$u^i_{,j} = u^i_{:j} + D^i_{\alpha j} u^\alpha \tag{C.38}$$

$$S^{!k} = g^{km} S_{,m} \tag{C.39}$$

where : j represents partial differentiation and $D^i_{\alpha j}$ is the Christoffel symbol of the second kind,

$$D^i_{\alpha j} = g^{in} D_{njk} \tag{C.40}$$

where g^{in} is the inverse metric tensor and D_{njk} is the Christoffel symbol of the first kind;

$$D_{ijk} = \frac{1}{2}(g_{ij:k} + g_{ik:j} + g_{jk:i}) \tag{C.41}$$

BIBLIOGRAPHY

Aubrey, D.G. and C.T. Friedrichs (1988), "Seasonal Climatology of Tidal Non- Linearities in a Shallow Estuary", in Hydrodynamics and Sediment Dynamics of Tidal Inlets, Springer-Verlag, New York, pp. 103-124.

Aubrey, D.G. and P.E. Speer (1985), "A Study of Non-Linear Tidal Propagation in Shallow Inlet/Estuarine Systems, Part I: Observations." Estuarine, Coastal and Shelf Science, V.21, pp. 185-205.

Boon, J.D. (1988), "Temporal Variation of Shallow-Water Tides in Basin-Inlet Systems", in Hydrodynamics and Sediment Dynamics of Tidal Inlets, Springer-Verlag, New York, pp. 125-136.

Chiu, T.Y., J. van de Kreeke and R.G. Dean (1970), Residence Times of Water Behind Barrier Islands, Technical Report, Department of Coastal and Oceanographic Engineering, University of Florida, Gainesville, 112 p.

Cotter, D.C. (1974), "Tide-Induced Net Discharge in Lagoon-Inlet Systems", Technical Report 74031, University of Miami, Miami, 40 p.

Dendrou, S.A., C.I. Moore, and R. Walton (1983), "Final Report, Little Sarasota Bay Circulation Study", Technical Report, Camp, Dresser and McKee, 250 p.

Dronkers, J. (1978), "Longitudinal Dispersion in Shallow Well Mixed Estuaries", Proceedings of the 16th Coastal Engineering Conference, V. 3, pp. 2761-2777.

Fischer, H.B., E.J. List, R.C. Koh, Y. Imberger and N.H. Brooks (1979), Mixing in Inland and Coastal Waters, Academic Press, Inc., Florida.

Friedrichs, C.T. and D.G. Aubrey (1988), "Nonlinear Tidal Distortion in Shallow Well-mixed Estuaries: a Synthesis", Estuarine, Coastal and Shelf Science, V. 27, pp. 521-545.

Friedrichs, C.T. and O.S. Madsen (1992), "Nonlinear Diffusion of the Tidal Signal in Frictionally Dominated Embayments", Journal of Geophysical Research, V. 97, No. C4, pp. 5637-5650.

Garrett, J.R. (1977), "Review of Drag Coefficients Over Ocean and Continents", Monthly Weather Review, V. 7, pp. 915-929.

Haney, R.L. (1990), "On the Pressure Gradient Force over Steep Topography in Sigma Coordinate Ocean Models", Journal of Physical Oceanography, V. 21, pp. 610-619.

Hansen, D.V. and M. Rattray (1965), "Gravitational Circulation in Straits and Estuaries", Journal of Marine Resources, V. 23, pp. 104-122.

Hayes, M.O. (1979), "Barrier Island Morphology as a Function of Tidal and Wave Regime", in Barrier Islands, From the Gulf of St. Lawrence to the Gulf of Mexico, Academic Press, New York.

Hoyt, J.H. (1967), "Barrier Island Formation", Geological Society of America Bulletin, V. 78, pp. 1125-1135.

Johnson, D.R. and T.N. Lee (1977), "Density-Induced Motions in Shallow Lagoons", Sea Grant Technical Bulletin No. 38.

Johnson, D.W. (1919), Shore Processes and Shoreline Development, John Wiley and Sons, Inc. New York.

King, C.A.M. (1972), Beaches and Coasts, St. Martin's Press, New York.

Kjerfve, B. (1975), "Tide and Fair-Weather Wind Effects in a Bar-Built Louisiana Estuary", Estuarine Research, V. 2, pp. 47-63.

Little, J.N. and L. Shure (1988), "Signal Processing Toolbox for use with MAT-LAB", The Mathworks, Inc., Natick, MA.

Leonard, B.P. (1979), "Adjusted Quadratic Algorithms for Transient Incompressible Convection", American Institute of Aeronautics and Astronautics.

Moody, J.A. (1988), "Small Scale Inlets as Tidal Filters", In Hydrodynamics and Sediment Dynamics of Tidal Inlets, Springer/Verlag, New York, pp. 137-157.

Peene, S.J., Y.P. Sheng, and S.H. Houston, (1992), "Modeling Tidal and Wind Driven Circulation in Sarasota and Tampa Bay", Estuarine and Coastal Modeling, American Society of Civil Engineers, pp. 112-113.

Pugh, D.T. (1987), Tides, Surges and Mean Sea-Level, John Wiley and Sons, New York.

Seim, H.E. and Sneed, J.E. (1988), "Enhancement of Semidiurnal Tidal Currents in the Tidal Inlets to Mississippi Sound", In Hydrodynamics and Sediment Dynamics of Tidal Inlets, Springer-Verlag, New York, pp. 157-168.

Sheng, Y.P. (1982), "Hydraulic Applications of a Second-Order Closure Model of Turbulent Transport", in Applying Research to Hydraulic Practice, ASCE, New York, pp. 106-119.

Sheng, Y.P. (1983), "Mathematical Modeling of Three-Dimensional Coastal Currents and Sediment Dispersion, 2, User's Manual of CELC3D - A Model of 3-D Coastal, Estuarine, and Lake Currents", Technical Report No. 487, Aeronautical Research Associates of Princeton, Princeton, NJ.

Sheng, Y.P. (1986), "CH3D: A Three-Dimensional Numerical Model of Coastal and Estuarine Circulation and Transport in Generalized Curvilinear Grids", Technical Report No. 587, Aeronautical Research Associates of Princeton, Inc., Princeton, New Jersey.

Sheng, Y.P. (1987), "On Modeling Three-Dimensional Estuarine and Marine Hydrodynamics", In Three-Dimensional Models of Marine and Estuarine Dynamics, Elsevier Oceanographic Series, Elsevier, pp. 35-54.

Sheng, Y.P. (1989), "Evolution of a 3-D Curvilinear-Grid Hydrodynamic Model: CH3D", Estuarine and Coastal Modeling (M.L. Spaulding, Ed.), ASCE, pp. 40-49.

Sheng, Y.P. (1989a), "On Numerical Strategies of Estuarine and Coastal Modeling", Estuarine and Coastal Modeling (M.L. Spaulding, Ed.), ASCE, pp. 291-301.

Sheng, Y.P. (1989b), "Three-Dimensional Numerical Modeling of Tidal Circulation and Salinity Transport in James River Estuary", Estuarine and Coastal Modeling (M.L. Spaulding, Ed.), ASCE, pp. 209-218.

Sheng, Y.P., V. Cook, S. Peene, D. Eliason, S. Schofield, K.M. Ahn and P.F. Wang (1989c), "A Field and Modeling Study of Fine Sediment Transport in Shallow Waters", Estuarine and Coastal Modeling (M.L. Spaulding, Ed.), ASCE, pp. 113-122.

Sheng, Y.P. and W. Lick (1980), "A Two-Mode Free-Surface Numerical Model for the Three-Dimensional Time Dependant Currents in Large Lakes", EPA-600/3-80-047, 62 pp..

Sheng, Y.P. and S.J. Peene (1991), "A Modeling and Field Study of Circulation and Transport in Sarasota Bay", Proceedings of the 1991 EPA/NOAA National Estuary Scientific Symposium, USEPA.

Sheng, Y.P. and S.J. Peene (1992), "Circulation and Its Effect on Water Quality in Sarasota Bay", In Framework for Action, Sarasota Bay, Sarasota Bay National Estuary Program, pp V.2-V.18.

Sheng, Y.P. and S.J. Peene (1993), "A Field and Modeling Study of Residual Circulation in Sarasota Bay and Tampa Bay, Florida", Proceedings of the 3rd International Conference on Coastal and Estuarine Modeling, ASCE.

Sheng, Y.P., T.S. Wu, and P.F. Wang (1988), "Coastal and Estuarine Hydrodynamic Modeling in Curvilinear Grids", Proceedings of the 21st International Conference on Coastal Engineering, ASCE, pp. 2655-2665.

Smith, N.P. (1979), "Tidal Dynamics and Low Frequency Exchanges in the Aransas Pass, Texas", Estuaries, V. 2, No. 4, pp. 218-227.

Smith, N.P. (1980),"A Comparison of Tidal Harmonic Constants Computed at and Near an Inlet", Estuarine and Coastal Marine Science, V. 10, pp. 383-391.

Smith, N.P. (1983), "Tidal and Low-Frequency Net Displacement in a Coastal Lagoon", Estuaries, V. 6, No. 3, pp. 180-189.

Smith, N.P. (1985), "The Decomposition and Simulation of the Longitudinal Circulation in a Coastal Lagoon", Estuarine, Coastal and Shelf Science, V. 21, pp 623-632.

Smith, N.P. (1987), "An Introduction to the Tides of Florida's Indian River Lagoon. I. Water Levels", Oceanographic Sciences, V. 50, No. 1, -p. 49-61.

Smith, N.P. (1990a), "Longitudinal Transport in a Coastal Lagoon", Estuarine, Coastal and Shelf Science, V. 31, No. 6, pp. 835-849.

Smith, N.P. (1990b), "Computer Simulation of Tide Induced Residual Transport in a Coastal Lagoon", Journal of Geophysical Research, V. 95, No. 10, pp 18205-18211.

Sokolnikoff, I.S. (1960), Tensor Analysis, John Wiley and Sons, Inc., New York.

Speer, P.E. and Aubrey, D.G. (1985), "A Study of Non-Linear Tidal Propagation in Shallow Inlet/Estuarine Systems Part II: Theory", Estuarine, Coastal and Shelf Science, V. 21, pp 207-224.

Speer, P.E., Aubrey, D.G. and Friedrichs, C.T. (1991), "Non-linear Hydrodynamics of Shallow Tidal Inlet/Bay Systems", In Tidal Hydrodynamics, John Wiley and Sons, pp. 321-339.

Swakon, E.A., Jr. and Wang, J.D. (1977), "Modeling of Tide and Wind Induced Flow in South Biscayne Bay and Card Sound", Sea Grant Techical Bulletin No. 37.

Thompson, J.E. (1983), "General Curvilinear Coordinate Systems", in Numerical Grid Generation (J.E. Thompson, Ed.), Elsevier Science Publishing Company, Inc., pp. 1-30.

van de Kreeke, J. (1971), "Tide-Induced Mass Transport in Shallow Lagoons", Technical Report No. TR-008, University of Florida, Gainesville, FL.

van de Kreeke, J. and Dean, R.G. (1975), "Tide-Induced Mass Transport in Lagoons", Journal of the Waterways Harbors and Coastal Engineering Division, 101(4), pp. 393-403.

van de Kreeke, J. and Cotter, D.C. (1978), "Tide Induced Mass Transport in Lagoon-Inlet Systems", Proceedings of the 14th Coastal Engineering Conference, V. 3, pp. 2290-2301.

van de Kreeke, J. and Wang, J.D. (1984), "Hydrography of North Biscayne Bay, Part I: Results of Field Measurements", Techical Report, University of Miami, Miami, FL.

—

van de Kreeke, J. and Zimmerman, J. T. F. (1990), "Gravitational Circulation in Well- and Partially-mixed Estuaries", pp. 495-521.

Wong, K.C. and Garvine, R.W. (1984) "Observations of Wind-Induced Subtidal Variability in the Delaware Estuary", Journal of Geophysical Research, V. 89, No. C6, pp. 10,589-10,597.

Wang, J.D. and van de Kreeke, J. (1984), "Hydrography of North Biscayne Bay Part II: Modeling", Technical Report, University of Miami, Miami, FL.

Wang, J.D. and van de Kreeke, J. (1986), "Tidal Circulation in North Biscayne Bay", Journal of the Waterway Port and Ocean Engineering, V. 112, No. 6, pp 615-631.

Zimmerman, J. T. F. "Dispersion by Tide-Induced Residual Current Vortices", in Hydrodynamics of Estuaries and Fjords (J.C.J. Nihoul, ed)., pp. 207-216. Elsevier, Amsterdam.
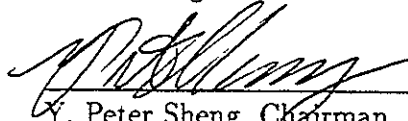
BIOGRAPHICAL SKETCH

The author was born in Westerly, Rhode Island, on December 17, 1960, in a house just 1/2 mile from Long Island Sound. When he was four years old his family moved inland to the town of Amherst, Massachusetts, where he grew up and graduated from high school. During his childhood, a love for the ocean was nurtured by fishing trips with his father to the "race" between Rhode Island and Long Island and Christmas's spent at his grandparents house in Sarasota, Florida.

A chance encounter with a guidance counselor during his senior year in high school piqued the author's interest in the field of coastal engineering. From that time until now, the path toward obtaining a coastal engineering degree was full of side trips. These included time spent at the University of Rhode Island in the Ocean Engineering Department, as a substitute teacher, as a public works employee, as a civil engineer in Brattleboro, Vermont, and finally a move to the University of Florida where the author began his studies in earnest in 1985. He obtained his master's degree in 1987, and after a 4-month exchange trip to Germany, returned to begin his doctoral program.

The most important event which took place in the author's life occurred just prior to leaving for Germany, when he met his wife-to-be, Christina. The two were married on November 7, 1992, in the beautiful town of Charleston, South Carolina, and since then have moved back to Gainesville where the author finally completed his Ph.D. After graduation the author plans on spending a long and happy life with his wife Christina raising a family, sailing, surfing and enjoying life.

I certify that I have read this study and that in my opinion it conforms to acceptable standards of scholarly presentation and is fully adequate, in scope and quality, as a dissertation for the degree of Doctor of Philosophy.
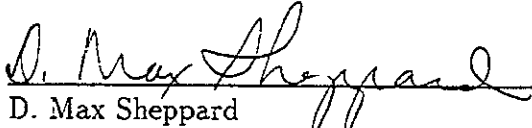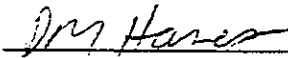
Y. Peter Sheng, Chairman
Professor of Coastal and Oceanographic
Engineering

I certify that I have read this study and that in my opinion it conforms to acceptable standards of scholarly presentation and is fully adequate, in scope and quality, as a dissertation for the degree of Doctor of Philosophy.

Robert G. Dean
Professor of Coastal and Oceanographic
Engineering

I certify that I have read this study and that in my opinion it conforms to acceptable standards of scholarly presentation and is fully adequate, in scope and quality, as a dissertation for the degree of Doctor of Philosophy.
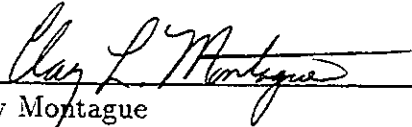
D. Max Sheppard
Professor of Coastal and Oceanographic
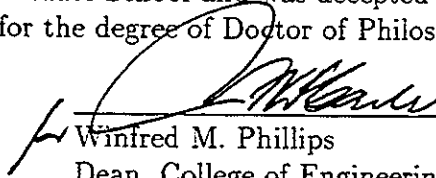Engineering

I certify that I have read this study and that in my opinion it conforms to acceptable standards of scholarly presentation and is fully adequate, in scope and quality, as a dissertation for the degree of Doctor of Philosophy.

Daniel Hanes
Associate Professor of Coastal and
Oceanographic Engineering

I certify that I have read this study and that in my opinion it conforms to acceptable standards of scholarly presentation and is fully adequate, in scope and quality, as a dissertation for the degree of Doctor of Philosophy.
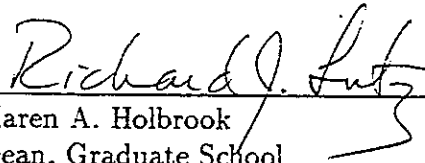
Clay Montague
Associate Professor of Environmental Engineering

This dissertation was submitted to the Graduate Faculty of the College of Engineering and to the Graduate School and was accepted as partial fulfillment of the requirements for the degree of Doctor of Philosophy.

August 1995

Winfred M. Phillips
Dean, College of Engineering

Karen A. Holbrook
Dean, Graduate School